Implementations and applications of Out of Phase Imaging after Optical Modulation (OPIOM) in fluorescence macro-imaging and fluorescence endomicroscopy

Ruikang Zhang

SORBONNE UNIVERSITÉ

École doctorale 388 :
Chimie Physique et Chimie Analytique de Paris Centre

Laboratoire PASTEUR - UMR 8640
Pôle de Chimie Bio-Physique

Implementations and applications of Out of Phase Imaging after Optical Modulation (OPIOM) in fluorescence macro-imaging and fluorescence endomicroscopy

Présentée par

Ruikang Zhang

Thèse de doctorat de Chimie-Physique

Dirigée par

Ludovic Jullien

Soutenance publique prévue le lundi 3 décembre 2018

Devant le jury composé de :

M.	Yves	GOULAS	Rapporteur
Mme.	Nelly	HENRY	Examinatrice
M.	Stéphane	JACQUEMOUD	Examinateur
M.	Ladislav	NEDBAL	Rapporteur
M.	Ludovic	JULLIEN	Examinateur
M.	Jean-Denis	FAURE	Invité
M.	Vincent	CROQUETTE	Invité
M.	Thomas	LE SAUX	Invité

Acknowledgement

First I would like to express my deep gratitude to my supervisors. Pr. Ludovic Jullien, for giving me the chance to join in this interesting project at the very beginning, and for his instructive advice, kind encouragement and valuable guidance during the three years. Especially grateful for his instruction and contribution to my thesis and publications, which have added great value to my PhD work. Dr. Thomas Le Saux, thanks for all the technical supports and intellectual discussions to the construction of the instruments, and the company for the trips to Versailles. I'm continually impressed by his wide-range competence and knowledge, which have greatly facilitated my lab works in all aspects during the 3 years. Dealing with a multidisciplinary subject like this is always a big challenge for me who have little knowledge of chemistry and biology, but their supports have given me the firm courage to overcome the difficulties.

I want to thank Dr. Yves Goulas, Dr. Ladislav Nedbal, Dr. Nelly Henry and Pr. Stéphane Jacquemoud, members of jury for their interest and involvement to the evaluation of my thesis and for taking the time to participate to my PhD defense.

I am sincerely grateful to the biologists of INRA Versailles, Pr. Jean-Denis Faure, Dr. Lionel Gissot and Dr. Zsolt Kelemen for their indispensable contribution to this project, and the rich knowledge in botany that they shared. It was such an honor to work with them during my PhD.

I would also like to offer my thanks to Pr. Vincent Croquette who have developed an easy-to-use software, which has thoroughly changed our ways of working and enormously improved the efficiency in experimental measurements and image processing.

I'd like to express my great appreciation to Mme. Raja Chouket for her contribution in my work from sample supply to data collection, as well as her supports from lab works to daily life. It was such a pleasure to work with her.

I would also like to thank everyone who helped and contributed in my project. Thank Jérome Quérard for his kind assistance in the first year. Thank Agnès Pellissier-Tanon for her technical support in the use of LaTex. Thank Alison Tebo and Marie-Aude Plamont for providing the biological samples.

My special thanks are extended to "les mezzanines" : Louise Hespel, Didier Law-Hine, Julien Dupre-de-Baubigny and Jorge Royes Mir, for creating a lovely ambience in the office, and to all other members in our laboratory, Isabelle Aujard, Agathe Espagne, Jérome Delacotte, Marina Garcia-Jove Navarro, Arnaud Gautier, Chenge Li, Zoher Gueroui, Anne Halloppe, Frederico Milheiro Pimenta, Shunnichi Kashida, Emmanuelle Marie, Hela Benaissa, Fanny Broch, Tiphaine Peresse, Lucas Sixdenier, Christophe Tribet, Wei-An Wang and Xiaojiang Xie for their kindness and all the help they gave to me.

I wish to thank all my friends that I met on my journey in France, for their kind support to my

PhD study and their helps that colored my life. Particular thanks to the group of "Fanfou" for the happy moments that we spent together.

Finally I wish to thank my parents for always being supportive throughout my study.

List of abbreviations

CCD	: Charged-coupled device
PMT	: Photomultiplier tube
SNR	: Signal-to-noise ratio
NAD(P)H	: Nicotinamide adenine dinucleotide phosphate H+
UV	: Ultraviolet
IR	: Infrared
NIR	: Near infrared
FMN	: Flavin mononucleotide
FAD	: Flavin-adenin dinucleotide
UVA	: Ultraviolet A (400-315 nm)
FLD	: Fraunhofer line depth
FP	: Fluorescent protein
GFP	: Green fluorescent protein
EGFP	: Enhanced green fluorescent protein
YFP	: Yellow fluorescent protein
RFP	: Red fluorescent protein
BFP	: Blue fluorescent protein
LED	: Light-emitting diode
AC	: Alternating current
DC	: Direct current
CW	: Continuous wave
ROI	: Region of interest
TRITC	: Tetramethylrhodamine
FITC	: Fluorescein isothiocyanate
DAPI	: 4',6-diamidino-2-phenylindole
PBS	: Phosphate-buffered saline
FLIM	: Fluorescence lifetime imaging microscopy
OLID	: Optical lock-in detection
STD	: Standard deviation
SAFIRe	: Synchronously amplified fluorescence imaging recovery
FFT	: Fast Fourier transform
FCS	: Fluorescence correlation spectroscopy

FRET	: Förster resonance energy transfer
STED	: Stimulated-emission-depletion
RSFP	: Reversibly photoswitchable fluorescent protein
OPIOM	: Out-of-phase imaging after optical modulation
NA	: Numerical aperture
BSA	: Bovine serum albumin
LB	: Lysogeny broth

Contents

I General Introduction **10**

1 Introduction **11**

1.1 Fluorescence: an excellent observable for biological observations 11

1.2 Background light: a major limitation in sensitive and quantitative fluorescence imaging . 12

1.2.1 The ambient light background 13

1.2.2 The autofluorescence background 14

1.3 State-of-the-art for background reduction in fluorescence imaging 18

1.3.1 Strategies against the background of ambient light 18

1.3.2 Strategies against a background of autofluorescence 20

1.3.3 Strategies overcoming interferences of both ambient light and autofluorescence . 24

1.4 Objectives of this PhD work 34

II Macro-imaging **36**

1 Radiometric analysis for Speed OPIOM macro-imaging **37**

1.1 Fluorescence emission from biological media at the macro scale 37

1.1.1 Transparent media 37

1.1.2 Non-transparent media 38

1.2 Speed OPIOM signal at the leaf surface upon modulated resonant dual illumination . . . 40

1.3 Speed OPIOM resonnance conditions for different RSFPs 40

1.4 Illumination strategy 41

1.5 Fluorescence emission detection under ambient light 42

2 A Speed OPIOM macroscope and its applications in fluorescence bio-imaging **43**

2.1 Article: Macroscale fluorescence imaging against autofluorescence under ambient light . 44

2.1.1 Introduction 44

2.1.2 Results 47

2.1.3 Discussion 53

2.1.4 Materials and Methods 55

2.1.5 Acknowledgement 58

2.1.6 Conflicts of interests 58

2.1.7 Contributions 58

2.2 Supporting information . . . 60
2.2.1 Additional Methods . . . 60
2.2.2 Supplementary Figures . . . 64
2.2.3 Supplementary Table . . . 66

3 Speed OPIOM for agronomical applications 68
3.1 Introduction . . . 68
3.2 Results . . . 69
3.2.1 Expression of reversibly photoswitchable fluorescent proteins in plants . . . 69
3.2.2 Reversibly photoswitchable fluorescent proteins as selection markers in plants . . . 69
3.2.3 Quantification of Dronpa-2 expression . . . 71
3.2.4 Live Speed OPIOM monitoring of biotic stresses . . . 77
3.3 Conclusion . . . 79
3.4 Experimental section . . . 80
3.4.1 Methods . . . 80
3.4.2 Acquisition parameters used for the images . . . 82

III Endomicroscopy 83

1 A Speed OPIOM endomicroscope and its applications in fluorescence bio-imaging 84
1.1 Introduction . . . 84
1.2 Results . . . 87
1.2.1 The Speed OPIOM microendoscope . . . 87
1.2.2 Optical characterization . . . 88
1.2.3 Speed OPIOM to improve optical sectioning in fluorescence microendoscopy . . . 88
1.2.4 Speed OPIOM to eliminate autofluorescence in fluorescence microendoscopy . . . 90
1.3 Discussion . . . 96
1.4 Conclusion . . . 97
1.5 Supporting Information and Experimental Section . . . 97
1.5.1 Endoscopic setup for fluorescence imaging . . . 97
1.5.2 Reconstruction of the Pre-OPIOM and OPIOM images by removal of the comb pattern . . . 99
1.5.3 Simulation of the Pre-OPIOM and OPIOM signals in fluorescence microendoscopy 100
1.5.4 Calibration of light intensity . . . 105
1.5.5 Autofluorescence of the fiber bundle . . . 106
1.5.6 Materials . . . 106
1.5.7 Supplementary Figures . . . 108

IV Conclusion and Perspectives **110**

1 General conclusion and perspectives **111**
1.1 Conclusion . . . 111
1.2 Perspectives . . . 112

Bibliography **113**

A Nature Communication Article **135**
A.1 Article: Resonant out-of-phase fluorescence microscopy and remote imaging overcome spectral limitations . . . 135
A.1.1 Summary . . . 136
A.1.2 Results . . . 137
A.1.3 Discussion . . . 140
A.1.4 Methods . . . 140
A.1.5 References . . . 142
A.1.6 Acknowledgements . . . 142
A.1.7 Author contributions . . . 142
A.1.8 Additional information . . . 143
A.2 Electronic Supplementary Material . . . 144
A.2.1 Supplementary Figure 1 . . . 145
A.2.2 Supplementary Figure 2 . . . 146
A.2.3 Supplementary Figure 3 . . . 147
A.2.4 Supplementary Figure 4 . . . 148
A.2.5 Supplementary Figure 5 . . . 149
A.2.6 Supplementary Figure 6 . . . 150
A.2.7 Supplementary Figure 7 . . . 151
A.2.8 Supplementary Figure 8 . . . 152
A.2.9 Supplementary Figure 9 . . . 153
A.2.10 Supplementary Figure 10 . . . 154
A.2.11 Supplementary Methods . . . 155
A.2.12 Supplementary Note 1: Photoswitchable fluorophore responses to dual illuminations 158
A.2.13 Supplementary Note 2: Determination of the RSFP kinetic parameters . . . 179
A.2.14 Supplementary Note 3: Speed OPIOM implementation . . . 179
A.2.15 Supplementary Note 4: Matlab code for OPIOM imaging . . . 192
A.2.16 Supplementary Note 5: Comparison of the selective contrasts obtained with Speed OPIOM, SAFIRe and OLID . . . 193
A.2.17 Supplementary Note 6: Speed OPIOM limitations arising from noise considerations 198
A.2.18 Supplementary References . . . 201

Part I

General Introduction

Chapter 1

Introduction

Fluorescence imaging has proven an essential tool for sensitive observation of species of interest in biological media. In particular, the possibility of fluorescently labeling specific biomolecules by means of genetic fusion has enabled one for locating targets and quantifying them from their probe contents. Nevertheless, fluorescence observation is easily contaminated by the ever-present autofluorescence of the biological media. Moreover fluorescence detection suffers from ambient light, which has mostly limited sensitive and quantitative detection of fluorescent probes to dark environments. In this introduction, we first explain why fluorescence is an attractive observable in biology. We then examine how ambient light and autofluorescence interfere with fluorescence observation and review state-of-art works reporting on their reduction. This introduction ends up with the presentation of the objectives of this PhD work.

1.1 Fluorescence: an excellent observable for biological observations

When it is illuminated with an appropriated wavelength, a fluorophore gets promoted to its first excited electronic state S_1. Fluorescence results from its back relaxation to the fluorophore ground state S_0 by emission of a photon. Both the intensity and the spectral signature of fluorescence have made it attractive as an observable in biological observations. More specifically, fluorescence exhibits three favorable features:

- *Sensitivity*. The observations based on fluorescence are usually highly sensitive, thanks to the high quantum yield of the fluorophore, which enables one for immediate identification of fluorescent probes in complex biological media. Since the emitted photons are red-shifted with respect to the excitation wavelength, the fluorescence signal can be easily separated from the excitation light by spectral filtering. The fluorescence can thus be enhanced by increasing the excitation intensity and be detected over a low background;

- *Specificity*. In animal and plant cells, a few metabolites and biomolecules are intrinsically fluorescent, so as to possibly be used as probes to monitor physiological activities. However these species are in small amounts, with irregular local distributions and complex associations to bio-activities. Therefore exogenous fluorophores are more commonly adopted as probes after associating them by genetic engineering to specific structures or biomolecules,[1] which opened a new door for more

specific biological observations down to the single-molecule level;[2,3]

- *Selectivity*. Several favorable features of the fluorophores have been used to selectively distinguish them from one another and from the background interference. In the spectral domain, fluorophores with distinct absorption or emission spectra can be discriminated by optical filtering or spectral analysis. In the time domain, lifetime imaging, which is based on the fluorescence decay rate from the S_1 to the S_0 state has been developed to retrieve the respective fluorescence signals from different fluorophores. More recently, fluorophores endowed with specific dynamic photochromic features have also found applications in selective imaging (*vide infra*).

Yet, despite all the aforesaid favorable features, fluorescence suffers from several limitations for imaging:

- Light scattering or reflection of ambient light by the sample, as well as autofluorescence originating from endogeneous fluorophores can interfere with the fluorescence of interest;
- Fluorescence usually covers a broad emission over several dozens of nanometers. It correspondingly gives rise to a poor spectral resolution, which limits the number of fluorescent labels to be distinguished in multiplexed imaging;
- Fluorophores tend to fatigue after multiple on-off cycles and they ultimately photobleach upon exposure to continuous and intense excitation light.

In the following, we concentrate on the discussion of the first limitation and the methodologies to overcome it.

1.2 Background light: a major limitation in sensitive and quantitative fluorescence imaging

With the advances of sensitive photo-detectors and digital cameras, and the development of genetically encoded fluorophores, there has been an increasing demand on the sensitive and quantitative detection of fluorescence signals. The quantitative measurement of fluorescence relies on digital recording devices such as charged-coupled devices (CCD), and photomultiplier tubes (PMT).[4] The imaging devices are usually constructed with a two-dimension grid of square-shaped pixels, which individually converts the received photons to voltage signals. Linearly correlated to the received light intensity, these voltage signals are numerized and recorded as a digital image. The digital image provides two fundamental types of information: the spatial information gives us the localization of the fluorescent structure and the intensity information is related to the local concentration of the fluorophore of interest. Film recordings further provide temporal information such as the movement of the target object and the local evolution of the fluorescence intensity.

For a quantitative measurement to be realized, the recorded signal should ideally arise exclusively from the fluorophore of interest contained in the sample. However, in the real world, the intensity values of the digital images are attributed not only to this fluorophore, but also to a background caused by ambient

light or autofluorescence from endogenous fluorophores of the specimen. This unwanted background intensity interferes with the signal of interest, which introduces an uncertainty to the quantification of the fluorescence.[5,6] Furthermore, the inhomogeneity of the background gives rise to artifacts through the image, which can be detrimental to the contrast and the localization of the fluorophore of interest.[7]

In addition to the interference to the absolute intensity value, the background intensity brings an increase of shot noise, causing variance of the intensity value, which adds to imprecision of the measurement. As the noise is positively correlated to the detected intensity, the fluorescence signal has to be significantly stronger than the background noise, so as to yield a satisfactory signal-to-noise ratio (SNR). When the fluorescence signal of interest is so weak that the background overwhelms the image, the presence of a strong noise level makes it impossible or difficult to identify the real fluorescence signal.[8] It is worth noting that while the absolute intensity added by the background can be digitally corrected in one way or another, the shot noise cannot be similarly eliminated.

In general, scattering of ambient light and autofluorescence mostly account for the bothersome background in fluorescence observations. In the following, we describe the sources of ambient light and autofluorescence, as well as their characteristics.

1.2.1 The ambient light background

The interference of ambient light originates from direct reflection or scattering from the specimen exposed to light sources from the environment, which obscures the fluorescence signal in the specimen since it is much stronger than the fluorophore emission. The simplest way to avoid this trouble is to eliminate ambient light from the environment, which explains why fluorescence imaging is usually performed in the dark. However, this radical solution is not always relevant. In the clinical field, fluorescence guided surgery has been used for efficient diagnosis of abnormal tissues. To ensure high contrast fluorescence imaging, the lighting in the operating room has to be turned off and switched on to excitation light during the aquisition,[9,10] which is not practical for real time operation. Fluorescent imaging has also been increasingly used in agronomy for monitoring of photosynthetic performance and environmental stress of the plants. In this case, ambient light in open air results in a background signal 10^3 times more intense than the fluorescence intensity, bringing an even more adverse condition for fluorescence detection.

However the background from ambient light can be distinguished from the fluorescence signal sought for by relying on some distinct features. Firstly, in both indoor and outdoor conditions, ambient light can be considered as constant during acquisition, which makes it easy to eliminate by lock-in or time-gated detection. Secondly, light sources such as the Sun and lamps exhibit broad spectra with relatively flat shape in the visible region, whereas the labelling fluorophores have generally much narrower emission bandwidths of less than 100 nm giving distinct spectral features out of the background. More particularly, sunlight at the sea level exhibits a set of spectral holes (Frauhofer lines) at certain wavelengths originating from the absorption during its passage through atmosphere, which led to develop a series of methods to reduce the contribution of solar radiation during fluorescence measurements. The variety of methods introduced to overcome the interference of ambient light in fluorescence imaging is discussed below.

1.2.2 The autofluorescence background

Source of fluorescence in biological media

Autofluorescence (or natural fluorescence) usually originates from the light emission of intrinsic fluorescent molecules in cells or tissues, when they are exposed to excitation light at certain wavelengths. In imaging, the autofluorescence is distinguished from the emission of exogenous fluorescent markers artificially added to label specific cell and tissue structures.

A variety of substances account for autofluorescence of biological samples. In animals, the cells and tissues contain fluorescent molecules such as NAD(P)H, flavin and lipopigments at different locations and concentrations.[11–14] Many other fluorophores are found in plant cells, such as flavonoid, chlorophyll and the substances of the cell wall.[15–18] The endogenous fluorophores usually have absorption spectra spanning the ultra-violet to the blue wavelength range, and spectral profiles of emission varying from the UV to the visible range (see Fig.1.1,1.2). Some specific fluorophores such as melanin even emit strong IR fluorescence upon NIR excitation.[19] Most of these fluorophores are cellular metabolites that play important roles in the cellular metabolism. As such, some of them are indispensable components in culture media of microorganisms, which cause also intense autofluorescence in such media.[20]

Major endogenous fluorophores: distribution and optical characteristics

Blue-green fluorescence Strong blue-green fluorescence emission has been observed in cells and tissues, especially in cell cytoplasm. NAD(P)H and flavins proved to be the major source of the autofluorescence signal in this wavelength range.[21] NAD(P)H is a coenzyme found in all living cells, in which it plays a vital role as a redox carrier in the reactions of the energetic metabolism. In its reduced state, it exhibits a fluorescence emission in the blue region from 440 to 500 nm upon excitation at 395 nm.[22,23] The two derivatives, NADH and NADPH, show little difference of spectral shape. A blue-shift of the emission maximum and the augmentation of the quantum yield of fluorescence are observed when NAD(P)H is bound to enzyme proteins.[24]

Flavins are important coenzymes existing in animal, plant and fungi. Given their wide distribution in living cells, they are considered to be major sources of intracellular green autofluoescence emission. They act also as redox carriers in a variety of enzymatic reactions. Riboflavin, along with its two derivatives, flavin mononucleotide (FMN) and flavin-adenin dinucleotide (FAD), share similar absorption and emission spectra, peaking at about 440-450 and 525 nm respectively.[25] A red-shift of emission to 540-560 nm has been evidenced when the flavin is bound to proteins.[26]

Structural proteins like collagen and elastin, mostly in the extracellular structures of animal tissues,[27,28] can also give rise to autofluorescence emission in the 470-520 nm range, with excitation maxima at 350-470 nm.

While the major sources of blue-green autofluorescences have been discussed above, one should also consider the contribution of yellow or orange fluorescence emitters such as lipofuscins, which exhibit a broad emission spectrum.[29] Lipofuscins are metabolic products resulting from lipid oxidation. They are accumulated as pigment granules in cytoplasm with aging or pathological changes of the cells.[30–32] Lipofuscins have excitation maxima ranging from 340 to 390 nm, and they exhibit a yellow-orange

fluorescence emission with a broad spectrum covering the blue (480 nm) to the red (600 nm) wavelength range.

Endogenous sources of blue-green fluorescence are much more abundant in the vegetal world. In addition to NAD(P)H and flavins, which are universal in living cells, a lot of other endogenous fluorophores emit in the blue-green wavelength range, such as alkaloids, flavonoids and phenolics.[18,33] However most of the fluorescence generated from the inner leaf structures are reabsorbed by chlorophyll, having limited contribution to the epidermic blue-green emission.[34] At the level of an entire leaf, the main sources of blue-green autofluorescence are the components of the walls of epidermal cells and vascular bundles (mainly ferulic acid, an important element found in organic polymers such as cutin, lignin and suberin, which exhibits emission from 400 to 550 nm upon UVA excitation).[33,35,36]

Red fluorescence Red fluorescence from animal tissues was observed for the first time in rat tumor,[37] which was later attributed to the porphyrins. Porphyrin fluorescence has a distinct emission peak at 635 nm, and an excitation maximum at 400 nm. The intensity of red fluorescence is highly correlated to metabolic disorders and the presence of tumors, which has found applications in diagnosis of cancer.[38] Fluorophores like lipofuscins can also interfere in the red autofluorescence, especially in neoplastic tissues.

In the world of plants, Chlorophyll is the sole source of autofluorescence emission in the red and far-red region,[39] which makes the red autofluorescence an appreciable signal for the physiological state of the plant. Indeed, since the Chlorophyll fluorescence is inversely related to the photosynthetic activity,[40] it has been widely used as a probe for photosynthetic study and stress monitoring of plants.[41–44]

Autofluorescent source	Distribution	Excitation wavelength(nm)	Emission wavelength(nm)
NAD(P)H	Animal and plant cells	360-400	440-510
Flavins	Animal and plant cells	380-490	520-560
Flavonoids	Plant tissues	420-430	490-520
Lipofuscins	Animal organism, nerve cells	390-490	480-680
Elastin and collagen	Animal collective tissues	340-480	470-520
Protoporphyrin	Pathological cells	410-450	600-700
Chlorophyll	Chloroplast	488	680(740)

Table 1.1 – Common biochemical sources of autofluorescence in nature, with their respective emission and excitation maxima. Information summarized from[15,18,45,46]

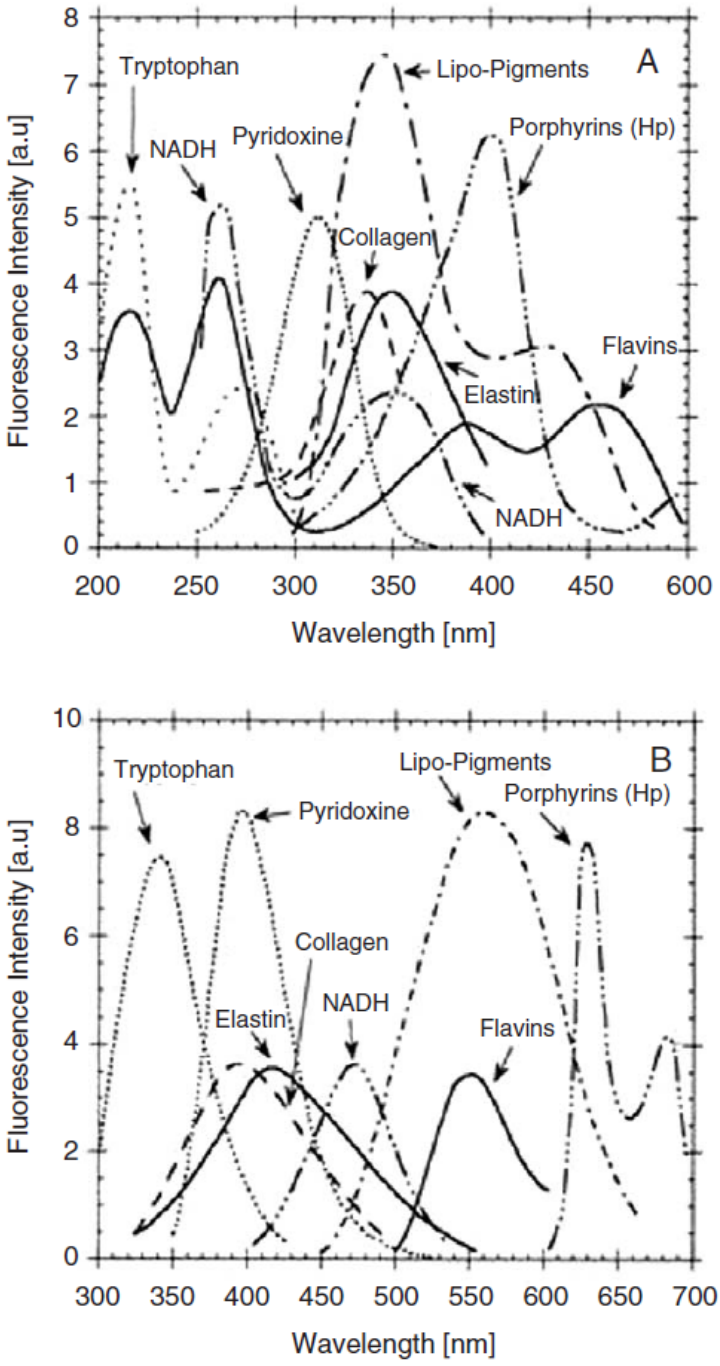

Figure 1.1 – Fluorescence excitation (A) and emission (B) spectra of various endogenous tissue fluorophores. Spectral shapes are shown for the best relative excitation/emission conditions. The figures are derived from.[46]

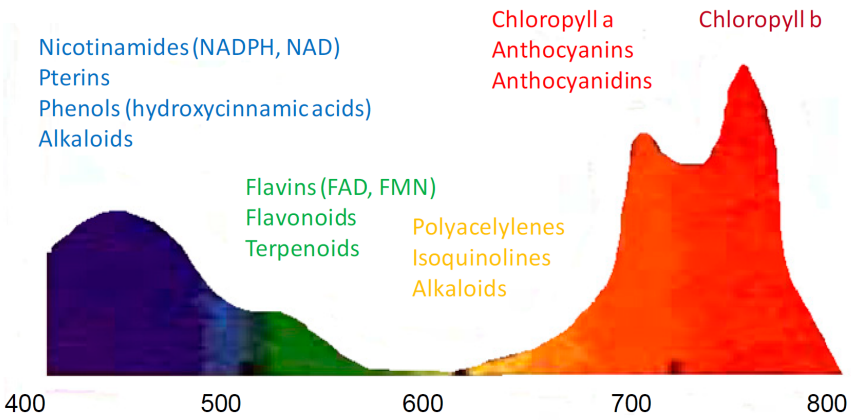

Figure 1.2 – Fluorescence emission spectrum of a typical green leaf under UV-radiation (λ_{exc}=355 nm). The fluorescence peaks are found in blue (430-450 nm), green (520-530 nm), red (680 nm) and far red (740 nm) regions. The figure is derived from.[15]

1.3 State-of-the-art for background reduction in fluorescence imaging

1.3.1 Strategies against the background of ambient light

Spectral analysis

In fluorescence detection, carefully selected optical filters are necessary for discriminating the target fluorescence from the excitation light and the emissions from other ranges of the spectrum. Since the majority of the light sources possess a broad spectrum from UV to IR which covers the emission spectrum of the most commonly used fluorescence probes, spectral filtering has found limited use in elimination of ambient light.

However, the Fraunhofer Line Depth (FLD) method has been exploited to retrieve the red fluorescence signal from the reflected sunlight in sunlight-induced Chlorophyll fluorescence measurements.[47] FLD makes use of the dark lines (so-called Fraunhofer lines) of the solar spectrum resulting from the absorption of solar and earth atmospheres, where the fluorescence signal is relatively stronger than the reflected solar intensity and is in consequence detectable. Indeed three main Fraunhofer Lines are found in the red to far-red wavelength range, in which Chlorophyll fluoresces: one hydrogen (H) absorption band is centered at 656.4 nm whereas two dioxygen (O_2) absorption bands are centered at 687.0 nm and 760.4 nm. FLD relies on intensity measurements inside and outside of the Fraunhofer lines, and the fluorescence signal is deduced by comparison of the two measurements. In particular, the FLD method measures the incident solar irradiation on the ground level and the radiance from the target plants inside the dark line (λ_{in}) and at a wavelength nearby (λ_{out}). The method assumes that the reflectance (r) and the fluorescence intensity (F) from the two measured channels are constant, which may give rise to unreliable results. Several methods aiming at improving the accuracy of the FLD measurement have been proposed in the recent decades. Instead of using only one outside band as a reference, one measures two or more bands and adds correction factors to deal with the change of r and F,[48,49] or uses advanced interpolation to get more precise spectral information around the dark lines.[50,51] Further improvement of this method relies on high resolution spectral measurement devices. FLD is a mature method for Chlorophyll fluorescence measurement under daylight. It is suitable not only for ground-based measurement, but also for airborne and even spaceborne fluorescence imaging. However this method is exclusively adapted to Chlorophyll measurement of vegetation under solar light condition, which limits its applications elsewhere.

Dynamic excitation methods

Difference imaging While it is difficult to find a common way to block out the ambient light, a lot of efforts have been made to enhance the fluorescence intensity itself by playing with the excitation light, so as to reduce the contribution of the ambient light.

The easiest way is to do a subtraction between the images recorded with and without illumination of excitation light. The major disadvantage of this method is due to the fact that the noise induced by the high level ambient light cannot be eliminated by the image subtraction. If the fluorescence intensity is at the same level or even lower than the noise level, the signal would be hard to be detected.

This method has been implemented by using a self-reset complementary metal-oxide-semiconductor image sensor to record the fluorescence image of the Green Fluorescent Protein (GFP) expressed in a

brain slice under indoor background light.[52] The self-reset image sensor enables one to avoid saturation of overexposure by reseting the output value of each pixel when the number of photons received exceeds its threshold. This sensor permits one to collect more fluorescence signal by increasing the exposure time with a reduced noise level of the ambient light. Two images were captured with and without the excitation light under room lighting condition and the difference between them was calculated to retrieve the fluorescence image.

Subtraction has also been applied to detect fluorescence in plants.[53] A reference spectrum was first measured under broad-band artificial light. Then a second spectrum was acquired with an additional excitation UV light. The fluorescence spectrum extracted after subtracting the reference was used to analyze the Chlorophyll fluorescence signal and monitor the water stress.

As simple as it is, the subtraction method has limited interest in fluorescence detection under conditions of high level of ambient light, as well as under a temporally varying lighting environment.

Pulsed-light excitation Pulsed excitation light with gated detection is a more commonly used approach for fluorescence imaging under ambient light. The pulsed excitation light is usually generated with a flash lamp or Light Emitting Diode (LED) source with a duration of millisecond down to microsecond, in order to reach an instantaneous intensity more than 10 times the maximum intensity in continuous mode. The camera is synchronized with the flash at a fast shutter speed. Such a system allows not only to enhance the instantaneous fluorescence response, but it also reduces the exposure time to diminish the input of ambient light intensity, which results in an obvious elevation of the fluorescence to background ratio.[54,55] In practical applications, the image captured during the pulsed excitation is corrected with an image previously recorded in the absence of the excitation pulse, to further eliminate the contribution of the ambient light.[56,57] An optimized strategy was recently proposed to avoid the error signals during the subtraction caused by periodically current-driven ambient light in the operating room.[58] The pulses were synchronized with the frequency of the background light such that the pulses and the acquisitions occured at the lowest point of the background light intensity. Several devices based on this approach have been developed and applied under various lighting environments,[54,55,57–60] from room light to sunlight conditions, performing reliable and sensitive fluorescence imaging ability (see Fig.1.3).

Lock-in detection by light modulation Another approach to distinguish a fluorescence signal from the ambient background relies on lock-in imaging, in which the intensity of the excitation light is modulated at a certain frequency. The fluorescence intensity is consequently modulated with the pace of the excitation light at which any modulation of the ambient light background can be neglected. By applying a time domain Fourier transform, the modulated component of the fluorescence is extracted while the background is filtered.

This method has been successfully applied for fluorescence detection of a bacterial sensor in the soil under daylight condition.[61] A more complicated protocol based on modulating both the excitation light and the ICCD sensor was demonstrated in another work for fluorescence imaging of a living animal.[62] In this imaging system, the recorded images are phase sensitive. Their intensity depends on the phase delay (η) of the modulation signals between the excitation light and the gain of the ICCD. The fluorescence image containing the modulated component was calculated from three images acquired with different η

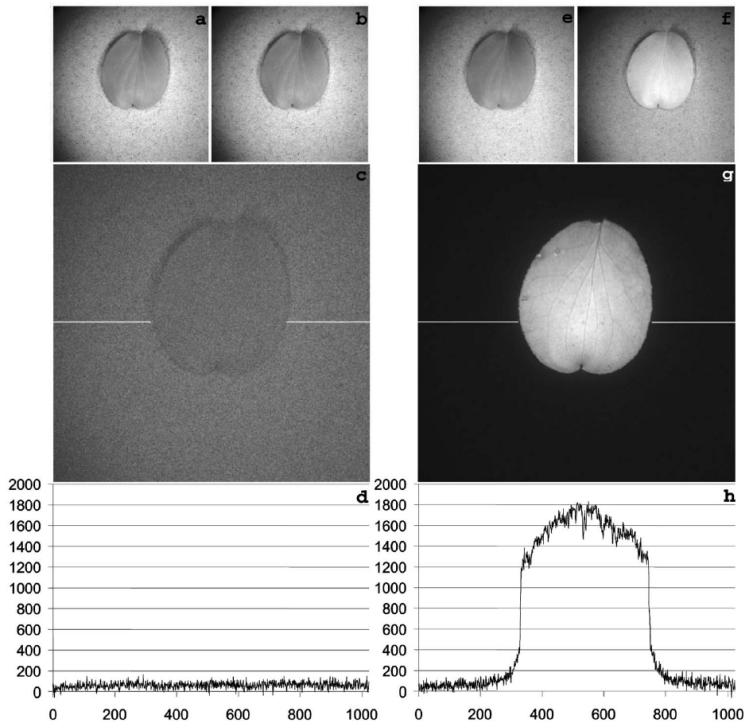

Figure 1.3 – Leaf fluorescence using flash versus continuous illumination (CI). Flash illumination was compared against CI from a 100 W Xenon arc lamp, both equipped with the same bandpass filter as part of the chlorophyll filter set (450/50 excitation filter, 740/140 emission filter). The comparison was done on an equal-exposure-time basis, 25 μs exposures or one 900 μs exposure respectively. Therefore, the light dose for imaging the specimen was approximately 180-fold greater under flash illumination. Artificial shaded sunlight from incandescent lamps was set equal to daylight level (10% of full insolation) in the field of view. Ambient (**a**), and ambient + CI (**b**) images of the test specimen, a leaf on sand; (**c**) digital difference image (**b**) minus (**a**); summed nonflash (**e**) and flash images (**f**); (**g**) digital difference image (**f**) minus (**e**). Graphs (**d**) and (**h**) show line profiles of fluorescence across the leaf image at the position indicated by horizontal white lines in panels (**c**) and (**g**) respectively. Figure derived from.[60]

(see Fig. 1.4). Compared to the pulsed excitation approach, the lock-in strategy enables one to gain higher Signal-to-Noise-Ratio (SNR) thanks to a frequency-domain noise filtering. In addition, this strategy is insensitive to irregular fluctuation of the ambient light, which is an advantageous with respect to the other approaches reported above.

1.3.2 Strategies against a background of autofluorescence

Choice of optical filter sets

A typical fluorescence imaging microscope necessitates a fluorescence filter set, which usually consists of three components: an excitation filter, a dichroic beamsplitter, and an emission filter. The fluorescence filter set is used to separate the excitation and the emission optical pathway, as well as to confine the band pass of both channels in order to avoid the interference of excitation light and enhance the fluorescence intensity from the specific fluorescent reporter. As such, the bandpass of the filters should be particularly

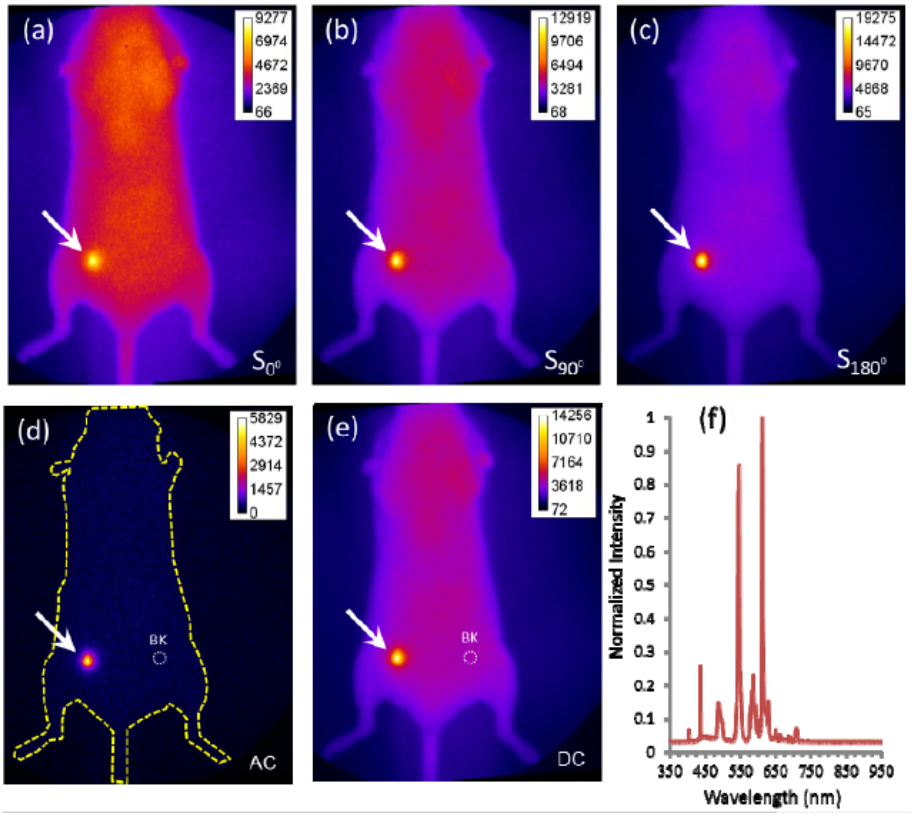

Figure 1.4 – iRFP fluorescence images acquired at the phase delay (**a**) 0°, (**b**) 90°, (**c**) 180° from a representative mouse. (**d**) The extracted image of AC amplitude. (**e**) CW Image of DC. (**f**) Spectra of the fluorescent room lights acquired in the surgical suite showing far red energy. The arrows point to the breast cancer location and the dashed circles represent the background ROIs. Figure derived from.[62]

picked up to match the excitation and emission band of the fluorophores that one wants to observe. In current fluorescence microscopy, the standard filter sets are TRITC, FITC, and DAPI for red, green, and blue fluorescence respectively. These standard filter sets can eliminate autofluorescence in these wavelength ranges, when it is less intense than the reporter fluorescence. However they cannot filter out the whole autofluorescence background since the latter covers the whole visible region (see Fig. 1.1), which overlaps the emission peaks of all the fluorophores.[63]

In practice, one can personalize the filter combinations for more specific observations. Considering that autofluorescence arises from a large gamme of unknown natural molecules, which exhibit different absorption bands, an excitation light with a broad spectrum may lead to a stronger autofluorescence signal since more endogenous fluophores tend to be excited. In this case, excitation filters with narrower bandpasses are ideal to limit the autofluorescence to those whose excitation band overlaps that of the reporter fluorophore.[64–67]

The choice of the emission filter plays a more important role in distinguishing the fluorescence signal. Since the reporter fluorophores exhibit narrow emission spectra with specific peaks, narrow bandpass filters centered around these peaks are often used to augment the contribution of the reporter signals against the non specific broad band autofluorescence. The use of dual bandpass filters has also been reported in fluorescence imaging.[65,67] In a recent work,[67] an optimized filter set was described and used

for GFP imaging in *Caenorhabditis elegans* to overcome the problem of autofluorescence. The proposed filter set used (i) an excitation filter with a very narrow bandwidth of 10 nm centered at the maximum excitation peak of GFP (488 nm) and (ii) more particularly a dual band emission filter with a first pass at 520/20 nm for the GFP emission peak (509 nm) and a second pass at 595/40 nm for the autofluorescence signal. By using a RGB camera, the autofluorescence signal passed through both bands, which appeared yellowish, while the GFP signal was observed mainly through the first pass and remained green (see Fig. 1.5). Compared to broad band filtering, this filter set optimized both the excitation and emission part, firstly to minimize the induced autofluorescence signal from the specimen, secondly to distinguish the color rendering of the GFP signal and autofluorescence signal. Albeit the contrast was enhanced, this method did not truly reduce the autofluorescence background. Moreover it cannot deal with the case when the GFP signal is weaker than the autofluorescence of the same bandpass.

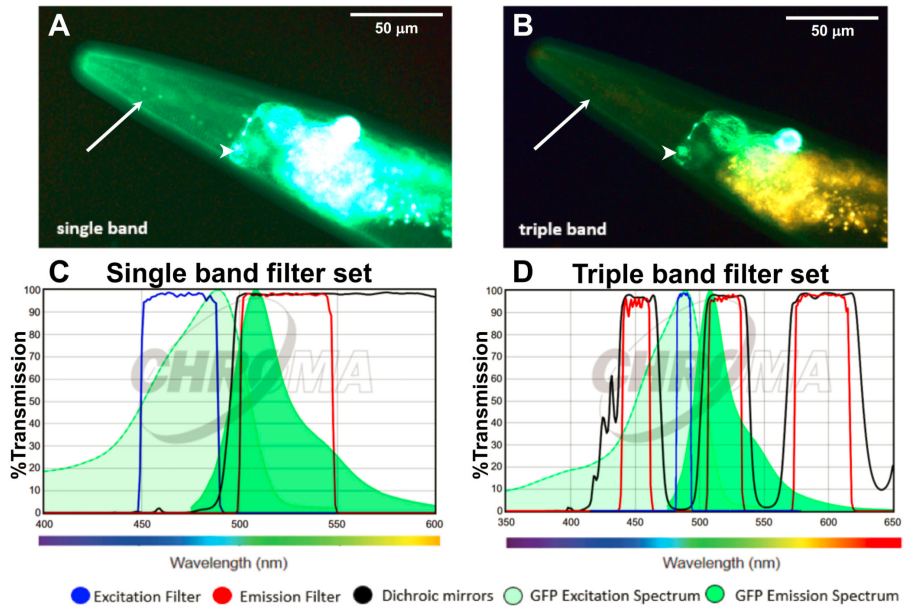

Figure 1.5 – The LSD2022 *C. elegans* strain expresses an integrated collagen::GFP transgene (ROL-6::GFP), which is visible in the cuticle (white arrow). In addition, the strain LSD2022 expresses GFP driven by the *ttx-3* promoter in the AIY interneuron pair (white arrowhead). (A) *C. elegans* worm (LSD2022) imaged with a commonly used single band filter set (C). (B) The same animal imaged with the triple band filter set (D), where Green is GFP and yellow is autofluorescence. The figure is derived from.[67]

.

Instead of remaining in the visible region, near infrared fluorescence (NIR) imaging has been another strategy to get rid of the problem of autofluorescence,[68,69] since very few intrinsic fluorophores emit fluorescence beyond 650 nm in the NIR region.[70] Further studies have shown that the second NIR region (1200-1800 nm) is even more favorable than the NIR region (650-950 nm), since the autofluorescence contribution at the former region is almost negligible.[19,71] Hence fluorescence imaging in the NIR region has been widely adopted to investigate biological systems in order to obtain an autofluorescence-reduced background.[72–76] Although a variety of near infrared dyes such as Indocyanine Green (excitation peak

around 780 nm and emission peak at 820 nm) are currently available,[72,73] it would be favorable to develop new NIR emitting fluorophores with higher quantum yield and biocompatibility.

Choice of the growth medium

Fluorescence detection of cells and microbes can also suffer from autofluorescence interference from the growth media the autofluorescence of which can be intense[20] and sometimes variable due to cell secretion.[77] To generate suitable growth conditions for microbes, growth media are often rich in nutrients, including vitamins such as vitamin A and riboflavin, which are main sources of autofluorescence. The PBS buffer can be used to wash away the fluorescent culture medium right before recording an image. However the medium removal influences the longevity of cells and hampers long-term observation. Various alternatives exhibiting significantly reduced autofluorescence than traditional culture media (E.X. agar gel, LB culture,. . .) have been reported.[45,78,79] Although low autofluorescence culture media are not always available for specific uses, the choice of the culture medium should be considered at first if possible, since it is one of the easiest approaches to circumvent the autofluorescence problem.

Chemical treatment

Autofluorescence from cells or tissues can be diminished by specific chemical treatments. Sodium borohydride has proven useful to quench autofluorescence induced from aldehyde or formalin fixatives.[80–82] Riboflavin can be reduced to a non-fluorescent state by injection of a sodium dithionite solution.[83] Copper sulfate can be used to quench lipofuscin-like autofluorescence[84] and reduce haemosiderin-laden macrophages autofluorescence.[85] A series of diazo dyes like trypan blue[82,86,87] and Sudan black B[88–91] can be used to mask or absorb visible autofluorescence emission in tissues. They are frequentely adopted in immunofluorescence applications.[92,93] However these dyes are usually applied after immunofluorescent labeling, which causes also signal reduction of the labels. Such treatments are often combined for better diminishing of the autofluorescence background.[82,94–97]

Photobleaching treatment

The autofluorescence of biological samples tends to fade after long time UV irradiation, due to photobleaching of the autofluorescent molecules. Photobleaching refers to photo-induced chemical alteration of the fluorescent molecule such that it is permanently disabled to fluoresce.[98] This irreversible destruction of the fluorophore is troublesome in most cases. Nonetheless, it has been an useful tool for diminishing unwanted autofluorescence of animal tissue such as brain, liver and lung.[99–102] It has been evidenced that UV irradiation (20 W) should last for at least 24 h to get a significant autofluorescence reduction through the whole sample, and after a treatment of 48 h, most of the autofluorescent background was faded.[99] In another work,[100] a high power multispectral LED array (240 W) was adopted as the irradiation source, and the process was shortened to 4 h with 80% autofluorescence reduction, which reached 90% after 24 h. Albeit the sample is often photo-treated prior to immunolabeling so as to avoid to affect the label fluorophores, the photo-treatment has also been done after labeling, with cooling during irradiation in order to preserve the quality of the fluorescence marker. It has been additionally shown that fluorescent

proteins like GFP are relatively resistant to photobleaching.[45] Due to the chromophore encapsulation, they exhibit a lower bleaching rate than small fluorophores.[103,104] In any case, one should be aware that UV irradiation can easily jeopardize inner components that are critical to the cell activities, which might not be suitable for real time monitoring *in situ*, not to mention the time consuming pretreatment.

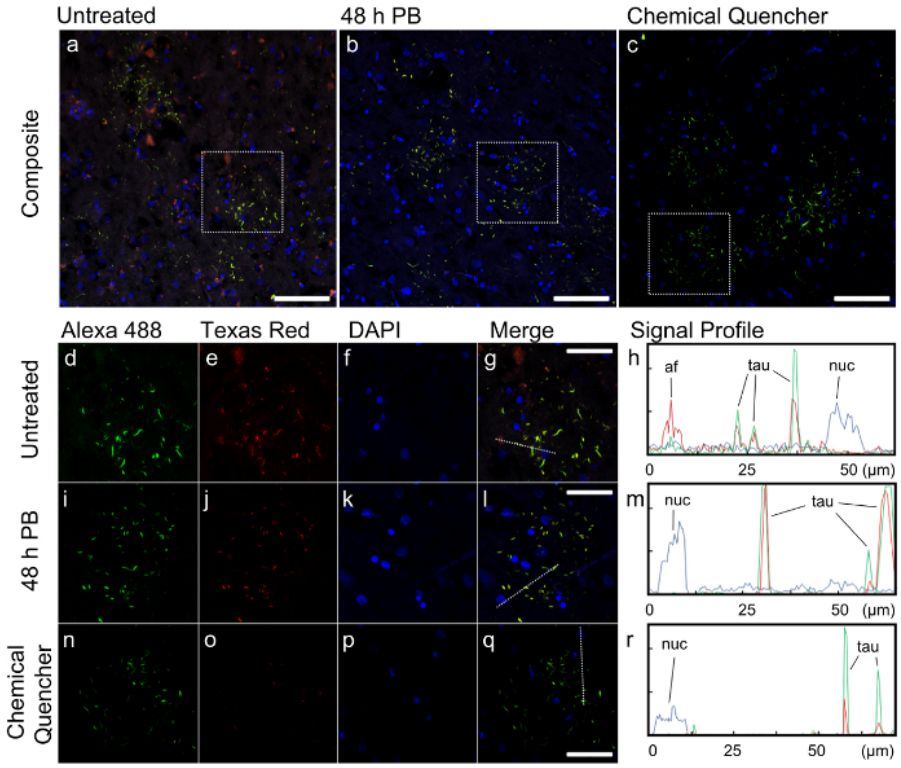

Figure 1.6 – Effect of autofluorescence removal on image quality in the case of FTLD-T tissue with anti-phosphorylated tau immunostaining.(a-c) Low magnification, composite immunofluorescence images of representative fields of view in untreated (a), photobleached for 48 h (b) and chemical quencher treated (c) samples. Colors represent fluorescence in the following channels via excitation by their respective light sources: Alexa 488 (green): λ_{ex} = 488 nm (argon laser) λ_{em} = 493-570 nm; Texas Red (red): λ_{ex} = 561 nm (DPSS 561 nm laser), λ_{em} = 601-635 nm; DAPI (blue): λ_{ex} = 405 nm (Diode 405 laser), λ_{em} = 410-507 nm. Scale bar = 100 μm. (d-r) Higher magnification images of the dotted regions in untreated (d-g), photobleached (i-l) and chemical quencher treated (n-q) samples, with separate fluorescence channels, merged image, and quantified fluorescence signal profiles. Dotted lines in the merged channels (g, l, q) represent the line on which signal profiles (h, m, r) were generated. Scale bar = 50 μm. Autofluorescent particles (af), immunolabeled tau fluorescence (tau) and nucleus signal (nuc) are indicated. The figure is derived from.[102]

1.3.3 Strategies overcoming interferences of both ambient light and autofluorescence

In the previous section, we introduced several methods for reduction of sample autofluorescence by chemical or photochemical treatments. All of them have significant disadvantages: (i) the choice of the biological media is limited for certain specimens, with a compromise for the cell growth condition;

(ii) chemical treatment and photobleaching may reduce the autofluorescence intensity, but at the price of the labeling intensity. Furthermore the chemical or photo-toxicity have to be carefully investigated, which limits their applicability to *in vivo* observations. By contrast, optics-based strategies provide a non-invasive way to investigate biological samples without physical or chemical intrusions. However, intensity detection based on light perturbations have got trouble to eliminate the nuisance of autofluorescence, since both the autofluorescence background and the fluorophore signal are responsive to the excitation light. This section will focus on reviewing several optical imaging techniques exploiting different types of kinetic features of fluorophores,[105] relying on light as a perturbation parameter and signal processing to retrieve the fluorescence of interest from both ambient light scattering and autofluorescence background.

Fluorescence Lifetime Imaging Microscopy (FLIM)

Fluorescence lifetime imaging microscopy (FLIM) is an imaging technology exploiting the differences of lifetime of the excited state of fluorophores.[106,107] When a fluorophore is excited by a photon, it relaxes towards the ground state and its probability of being excited then obeys an exponential decay as a function of time. Therefore the observed fluorescence intensity exhibits also an exponential decay. In FLIM, it is the lifetime rather than the direct intensity, which is used to discriminate fluorophores. Being an intrinsic property of the fluorophore, lifetime is independent of the local concentration and the brightness of the fluorophore, but it may vary with its molecular environment.[108]

Three different ways are generally implemented to extract the lifetime information of the fluorescence. First, time-correlated single-photon counting (TCSPC) relies on the detection of individual emitted photons and the associated delay time of their arrival to build an histogram of the number of photons at different time points.[109] Exponential fitting of the histogram then provides the lifetime(s). Second, the fluorophores are excited with a pulsed laser, and the detection is triggered after a series of time delays. The decay lifetime is reconstructed after analysis of the recorded intensities.[110] While the two former methods rely on pulsed excitation, FLIM can also be implemented with a frequency-domain detection. This approach generates a modulation of the excitation light. As a consequence, the fluorescence intensity is modulated. The fluorescence lifetime can be determined from its modulation depth and phase delay.[107,111]

As FLIM allows one to discriminate fluorescent emitters by the difference of their lifetimes, it has been considered to discriminate autofluorescence as well as the time-independent ambient light. Indeed the background autofluorescence exhibits lifetime ranging from ps to several ns.[112–115] Hence the targeted fluorescence can be collected with time-gated detection after the autofluorescence dies out. This approach has been implemented to eliminate the chloroplast autofluorescence in plant cells.[116] Since the autofluorescence of the chloroplast declines extremely fast(several ps time scale) whereas the lifetime of the common labels like GFP and YFP is to the nanosecond range, the detection started with a delay of 0.3 ns after the pulse excitation, which allowed to completely remove the autofluorescence with only a slight reduction of the label fluorescence. However, autofluorescence has an average lifetime around 4 ns, overlapping the one of most common organic fluorophores. Expanding the detection delay elevates the contrast but at the price of a loss of the fluorescence intensity sought for. For this reason, engineered long-lived fluorescence probes have been designed to ensure complete decline of the autofluorescence while keeping the desired fluorescence at a considerable level. Hence *Jin et al.* used lanthanide-based

luminescence probes with very long lifetime up to μs and ms.[117] Nevertheless these probes have limited photon flux, which lowers the sensitivity. *Ryan et al.* developed azadioxatriangulenium (ADOTA) dye, the 20 ns lifetime of which is three times longer than usual autofluorophores so as to facilitate detection after the autofluorescence has diminished (see Fig. 1.7).[118,119] More recently, Optical Activated Delayed Fluorescence (OADF) extended the lifetime to tens of μs by exploiting the long live dark state of Ag clusters.[120] After a primary pulsed excitation, the Ag cluster is excited to a dark state, which can be depopulated to the excited emissive state by a secondary illumination at longer wavelength with a time delay. Thereby the repumped fluorescence can be activated after fading of the endogenous fluorescence.

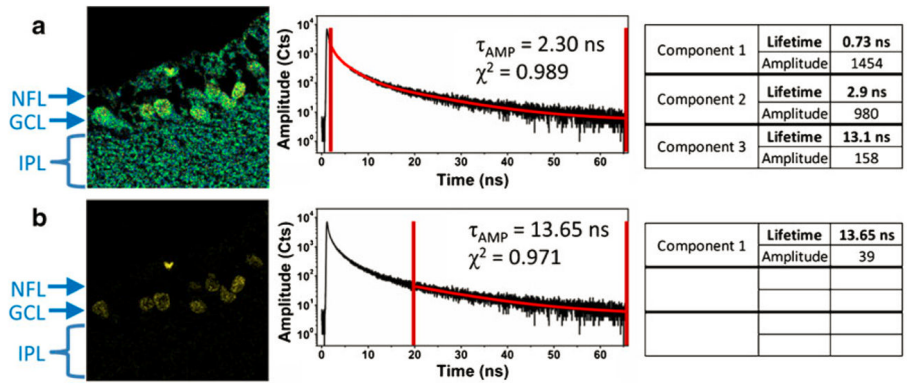

Figure 1.7 – Time-gated FLIM applied to tissue labeled with ADOTA. Panel (a) shows the FLIM equivalent of the steady-state image; data collection starts after 2.5 ns and excludes scattered excitation only. In panel (b) data collection is delayed by 10 ns. All of the data shown in this figure were obtained in one collection of data from a single, 80×80 μm (300 pixels × 300 pixels) area of tissue. The figure is derived from.[118]

By relying on the study of lifetime which is independent of the fluorophore concentration but variable to the molecule context, FLIM is yet not an ideal tool to quantify the local amount of the fluorophore.

Optical Lock-In Detection (OLID)

Several fluorophores exhibit light-driven switch between two states of different brightness, which can be turned on and off reversibly upon illumination of two different wavelengths.[121–123] This specific photo-dynamic feature was exploited by *G. Marriott et al.*[124,125] to isolate the fluorescence signal of the photoswitch from a high level background. Periodic light perturbation drove the fluorophore throughout several cycles of photoswitching and the modulated fluorescence signal of the specific probe was isolated from the constant scattering background as well as the steady autofluorescence background from non-photoswitching sources by what *G. Marriott et al.* named lock-in detection (OLID). More precisely, the probe was first photoswitched from a dark state to a bright state with a short UV light pulse, and a subsequent excitation light was applied to photoswitch it back to the dark state with a much lower rate. After repeated illuminations over several cycles, the acquired signal from the probe exhibited a sawtooth-like modulation. To amplify the desired signal, a cross-correlation was performed between each pixels of the imaging field and a reference waveform picked from a small region where the fluorophore only was present, so as to analyze the temporal similarity. The cross-correlation coefficient $\rho(x, y)$ at a given pixel

was calculated with equation (1.1):

$$\rho(x, y) = \sum_{t} \frac{\{I(x, y, t) - \mu_I\}\{R(t) - \mu_R\}}{\sigma_I \sigma_R} \tag{1.1}$$

where $I(x, y, t)$ is the detected intensity at pixel (x, y) at time t during the cycle, and $R(t)$ is the reference waveform. μ_I and μ_R are the averages, and σ_I and σ_R are the standard deviation values of the pixel intensity and the reference waveform respectively.[124] With this algorithm, the background (including the ambient light-induced scattering and the autofluorescence which is not supposed to present any photoswitching feature) was not correlated to the reference and thus yielded a cross correlation close to zero. In the contrary, any modulated signal exhibiting a response behavior similar to the reference wave was enhanced, which allowed to selectively display the information of the photoswitchable probe.

OLID was first experimentally demonstrated with reversibly photoswitchable small fluorophore (nitrospirobenzopyran; nitroBIPS) and genetically encoded fluorescent protein, Dronpa, used to achieve high contrast imaging of living cells and mammalian tissues (Xenopus spinal cord explant and live Zebrafish) free of the artifacts arising from autofluorescence.[124] OLID imaging was subsequently also validated with a cyanine probe, which can be photoswitched at high light intensity.[126]

Eq. (1.1) shows that the modulation intensity is normalized by the STD of the two signals. Thereby the calculated coefficient is not linearly related to the local concentration of the probe. The same team has proposed an optimized method using the "scope" as a weighting factor.[127,128] The scope value is actually the mean peak-valley measured from each pixel during each local cycle:

$$S(x, y) = \frac{1}{N} \sum_{i=1}^{N} (L_{max}(x, y)_i - L_{min}(x, y)_i) \tag{1.2}$$

where the $L_{max}(x, y)_i$ (respectively $L_{min}(x, y)_i$) is the local maximal (minimal) intensity of the i^{th} cycle, and N is the number of cycles recorded. Meanwhile, the reference point is automatically selected from the pixel possessing the largest scope, without the need of manual process.

The scope values have been used to weight the cross-correlation image[127] (see Fig.1.8). While the addition of the scope has taken into account the switching amplitude and further enhanced the contrast as well as the signal-to-noise ratio, the ability of OLID to quantify the local content of the photoswitching probe is still questioned, especially when the background is so overwhelming that the modulation is at the noise level, where the extracted scope is highly unreliable. An erroneously selected reference point leads to alternative correlation analysis (see Fig.1.12), which fails to yield the right OLID image.[129] In another work, the scope values were used directly as a weight factor to the raw fluorescence intensity image for the sake of an enhanced contrast.[128] Nonetheless, since the final result is coupled with both the scope and the raw intensity (which distorts the real intensity of the fluorescent probe), OLID is not suitable for the quantification of the probe.

Synchronously Amplified Fluorescence Imaging Recovery (SAFIRe)

R. Dickson and his team developed another selective imaging technique called synchronously amplified fluorescence imaging recovery (SAFIRe).[130,131] In their approach, a specific optical modulation strategy is applied so that only the fluorescence of the probe of interest is modulated while the background stays

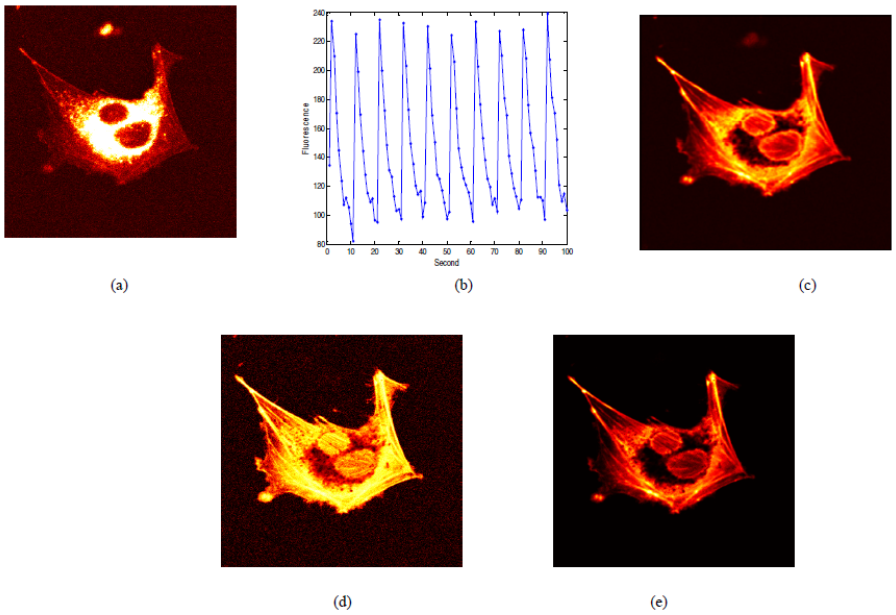

Figure 1.8 – (a) A single image frame of the living cell (labeled with a non-photoswitchable probe Rhodamine 123 and a photoswitchable protein rs-mcherry-rev) representing peak response to switching; (b) Reference waveform obtained from the fluorescence intensity profile at the selected reference point; (c) Scope image; (d) Results from the correlation image; and (e) Results from the scope-weighted correlation image. The figure is derived from.[127]

steady. This discrimination exploits a few specific fluorescent molecules, which possess long-lived dark states. When a fluorophore is promoted by light from its ground-state S_0 to its excited state S_1, it has a certain probability to transit to a dark state T_1. When the dark state is long-lived, fluorescence drops even at rather low light intensity. However the population of the dark state can be interestingly reduced upon a secondary illumination with high energy. It regenerates the emissive state S_1 faster than the natural decay rate from T_1, which thus elevates the fluorescence signal. SAFIRe has implemented this scheme by exploiting several fluorophores in which the depopulation of the dark state occured upon illumination at a wavelength longer than that of the fluorescence emission. While maintaining a constant primary excitation light, optical modulation of the secondary light allowed to dynamically control the population of the emissive state, resulting in a modulated fluorescence intensity. Meanwhile, the collected background was free of the crosstalk from the secondary light with a longer wavelength, therefore remained unmodulated. After performing a time-domain Fourier transformation of the signal from each pixel, the SAFIRe image was reconstructed, where the modulatable probe was amplified whereas the background was removed. Similar to a lock-in amplifier, this scheme allowed to eliminate both autofluorescence and ambient light.

SAFIRe was first validated with Ag nanodots,[130] and then with organic fluorophores like xanthene[131] and Cy5.[132] It was later implemented in bioimaging using specific genetically encoded fluorescent proteins, which were able to be photoswitched with the mechanism discussed above. In the first attempt, AcGFP was used to label mitochondria in NIH 3T3 cells while labeling EGFP was introduced elsewhere as a background interference. The image was obtained with a confocal scanning system using an optical

fiber as a pinhole. The demodulated image recovered the location of the AcGFP against the EGFP background.[133] In another work, SAFIRe was applied in wide field imaging, where a series of engineered BFP mutants modBFP/H148K were found attractive as modulatable labels to enhance the imaging contrast against autofluroescence (see Fig.1.9).[134]

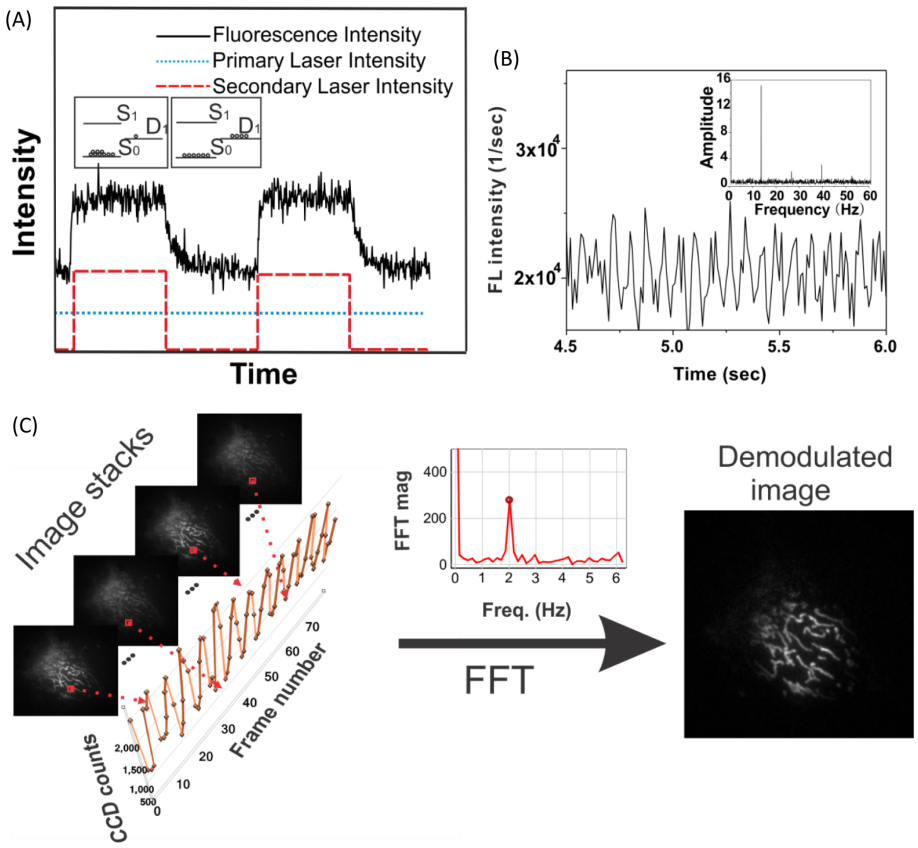

Figure 1.9 – (A) Fluorescence response of an optically modulatable blue fluorescent protein (modBFP/H148K) with constant primary excitation and modulated secondary excitation. The insets show Jablonski diagrams representing dark/bright populations; (B) Time trace of aqueous modBFP/H148K with 372 nm primary excitation and 514 nm secondary excitation modulated at 13 Hz. The inset shows the fast Fourier transform (FFT) of the bulk intensity trajectory, recovering the modulation frequency encoded in the fluorescence signal. (C) Analysis of optically modulated image stacks acquired with SAFIRe by taking the Fourier transform of each pixel's intensity trajectory. The demodulated image is formed from the FFT amplitude at each pixel. The figure is derived from.[135]

Quantitative measurement of fluorophore concentrations in the presence of an high background was validated by *Hsiang et al.*,[135] using diluted Cy5 solution at varying concentrations with and without a Texas Red fluorescence background. Fig. 1.10A shows the number of Cy5 molecules measured by FCS, respectively in a Texas Red solution and fluorescence-free water. The curve exhibits a non-linearity at low Cy5 numbers, due to the interference of the fluorescence background. In contrast, the FFT amplitude in Figure1.10B reconstructed a quasi-identical linear dependence on the Cy5 concentration in both solutions, devoid of any contribution from the non-modulated background. SAFIRe has also been successfully used in fluorescence correlation spectroscopy (FCS) for background-free quantification of Ag nanocluster.[136]

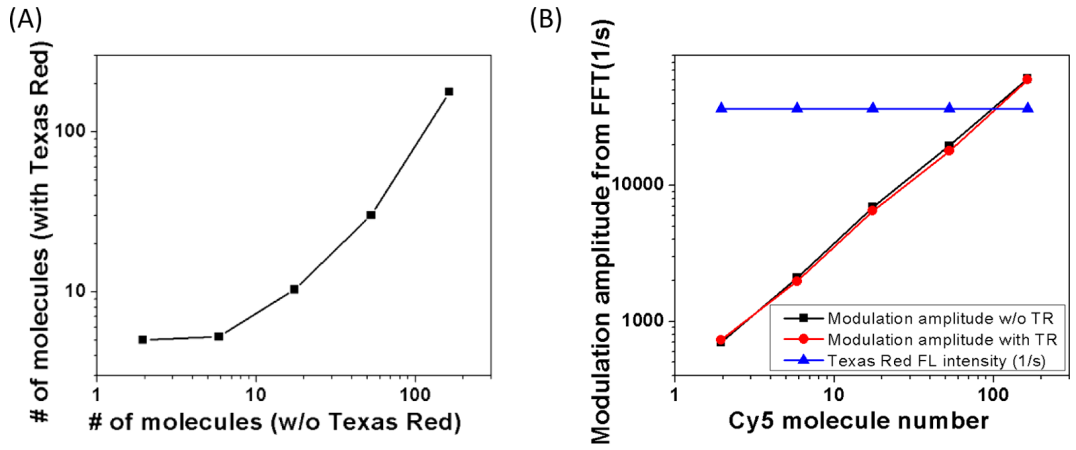

Figure 1.10 – (A) Highly nonlinear correlation between the numbers of Cy5 molecules measured by FCS with and without a constant Texas Red background; (B) Plots of the SAFIRe signal (FFT amplitude) *vs* the number of Cy5 molecules, showing that the modulation amplitude is independent of the presence of the unmodulatable Texas Red background. The figure is derived from.[135]

A first limitation of SAFIRe originates from constraining the fluorophores to rely on a red-shifted illumination for dark state depopulation to avoid crosstalk. To overcome this limit, Dickson's research group has proposed a smart approach combining SAFIRe and FRET.[137] The primary excitation light was applied to the donor, that transfers its energy to the acceptor. Meanwhile a secondary light of longer wavelength than the emission peak of the donor excited the acceptor, giving rise to a competition against the FRET transfer. As a consequence, the intensity of the secondary light was negatively correlated to the fluorescence emission of the donor.

A second SAFIRe limitation originates from constraining the fluorophores to exhibit a long-lived dark state. To avoid seeking dark state fluorophores, Dickson's research group introduced an all-optical method utilizing simulated emission depletion.[138] It exploits the depletion of the fluorescence state by stimulated emission induced by a secondary depletion laser at a longer wavelength than the fluorescence emission, which could be modulated by modulating the depletion laser. The selectivity of this protocol relies on an higher STED efficiency of the targeted fluorophore than the one of the background emitters. Moreover this approach requires high intensities of both primary and secondary lights (mostly attainable in a confocal system), which may generate photobleaching and phototoxicity to the sample and limit its use in real time living cell observations.

A recent work evaluated reversibly photoswitchable fluorescent proteins as labels for SAFIRe imaging.[129] To avoid the generation of a modulated autofluorescence background which would originate from the high energy secondary light with short wavelength required to depopulate the dark state of RSFPs such as rsFastLime, this work introduced a dual modulation system (DM-SAFIRe), where both the primary and the secondary lights were modulated, but at different frequencies. While the non-photoswitching background independently followed the modulation of the two photoswitching-driving lights, the rsFastLime emission was selectively modulated at both frequencies, which gave rise to a pair of sideband signals (see Fig.1.11) in the Fourier domain completely excluding the background. The superiority of DM-SAFIRe with regards to OLID and SM-SAFIRe in RSFP imaging was established in live NIH-3T3 cells (see

Fig.1.12).

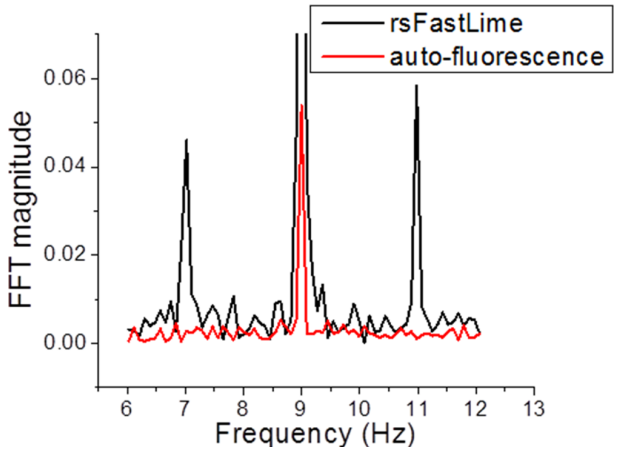

Figure 1.11 – Dual modulation enables background-free rsFastLime detection. rsFastLime interacts with both 405 and 488 nm lasers, while the autofluorescence background is excited independently by each laser. The Fourier transform shows that only rsFastLime presents sideband signals (at 7 and 11 Hz) when the 488 and 405 nm lasers are respectively modulated at 9 and 2 Hz. The figure is derived from.[129]

Out-of-Phase Imaging after Optical Modulation (OPIOM)

In order to get a more selective kinetic signature of reversibly photoswitchable fluorescent probes, Out-of-Phase Imaging after Optical Modulation (OPIOM) has added the phase lag of the modulated signal to the frequency-dependent modulation depth exploited by SAFIRe for selective imaging. Indeed, OPIOM acts as a band-pass filter for the RSFP signal whereas SAFIRe acts as a low pass filter. As a consequence, OPIOM is more easily prone to direct multiplexed observations of several RSFPs. Moreover OPIOM relies on an exhaustive theoretical frame, which led to extract analytic conditions for its optimal implementation.

The OPIOM theoretical framework was first illustrated by *Quérard et al.*[139] It is based on a thorough analysis of the photo-induced switching behavior of a reversibly photoswitchable probe between two states **1** and **2**, bright or dark, where the thermodynamically stable state **1** can be photochemically depopulated to the thermodynamically unstable state **2** with a rate constant

$$k_{12}(t) = \sigma_{12} I(t), \tag{1.3}$$

whereas it is populated back either by photochemical induction or slow thermal recovery at a rate constant

$$k_{21}(t) = \sigma_{21} I(t) + k_{21}^{\Delta}, \tag{1.4}$$

where $\sigma_{21} I(t)$ and k_{21}^{Δ} are respectively the photochemically-driven and the thermally-driven contributions. Since the exchanging rates between the two states depend on the light intensity $I(t)$, a slight sinusoidal modulation of the light intensity generates a modulation of the population of the two states, but with a phase delay due to the relaxation time of the switch.

$$i(t) = i^0 + \varepsilon[i^{1,in} \sin(\omega t) + i^{1,out} \cos(\omega t)] \tag{1.5}$$

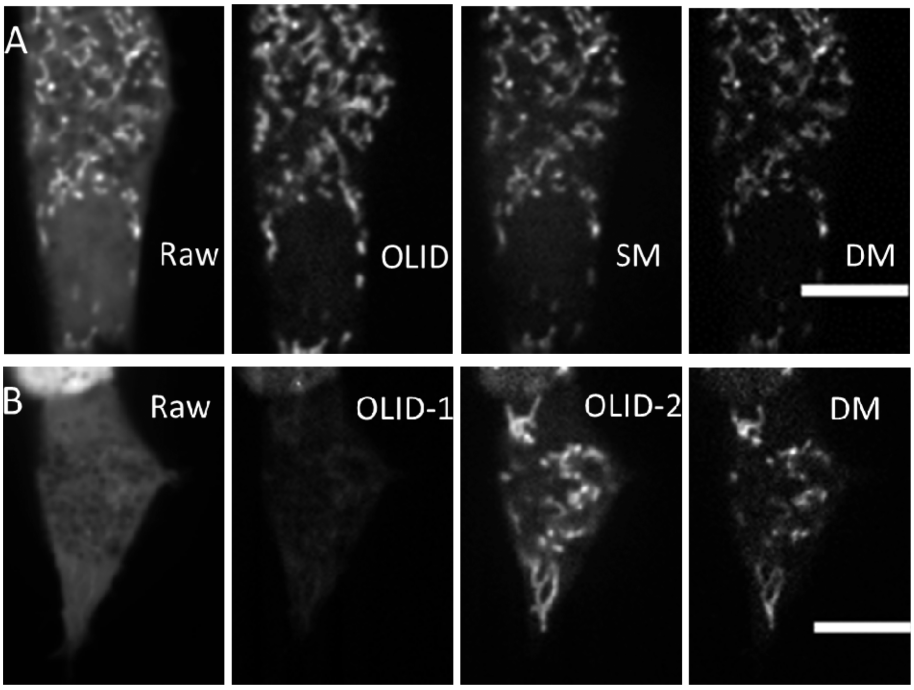

Figure 1.12 – (A) Signal/background (S/B) comparison of SM- and DM-SAFIRe vs OLID in live NIH-3T3 cells co-expressing untargeted EGFP and mitochondria-targeted rsFastLime: (left to right) raw image, S/B≈1.4; OLID, S/B≈6; demodulated image at 405 nm frequency (SM-SAFIRe), S/B≈5; demodulation at the sideband frequencies (DM-SAFIRe), S/B≈9. (B) S/B comparison in the presence of bright non-rsFastLime background: (left to right) raw live cell image as in (A), S/B≈1; OLID using automatic selection of brightest feature for reference waveform, S/B≈1.6; OLID with manual selection of reference point, S/B≈5; demodulation image upon DM-SAFIRe, S/B≈9. Scale bars = 10 μm. OLID and SM-SAFIRe give similar contrast improvements, and DM-SAFIRe gives a further 2-fold improvement. The figure is derived from.[129]

where $\varepsilon i^{1,in} \sin(\omega t)$ and $\varepsilon i^{1,out} \cos(\omega t)$ are respectively the in-phase and out-of-phase components of the concentrations at the modulation frequency. Interestingly, further calculation revealed that the $i^{1,in}$ and $i^{1,out}$ values are tunable with two modulation parameters: the offset intensity I_0 and the angular frequency ω. In particular, the amplitude of the out-of-phase term $i^{1,out}$ exhibits a resonant behavior with a single optimum when the parameters matches:

$$I^0 = \frac{k_{21}^{\Delta}}{\sigma_{12} + \sigma_{21}} \tag{1.6}$$

$$\omega = 2k_{21}^{\Delta} \tag{1.7}$$

where σ_{12} and σ_{21} are the photoswitching action cross-sections of the probe. The optimal conditions are exclusively related to the kinetic features of the probe itself. Since the fluorescence emission is directly related to the population of the bright state, the out-of-phase signal can be extracted from the fluorescence modulation of each pixel simply by temporal Fourier transformation, and used for quantification of the RSFP concentration.

OPIOM has been then experimentally implemented for selective imaging of two mutants of Dronpa

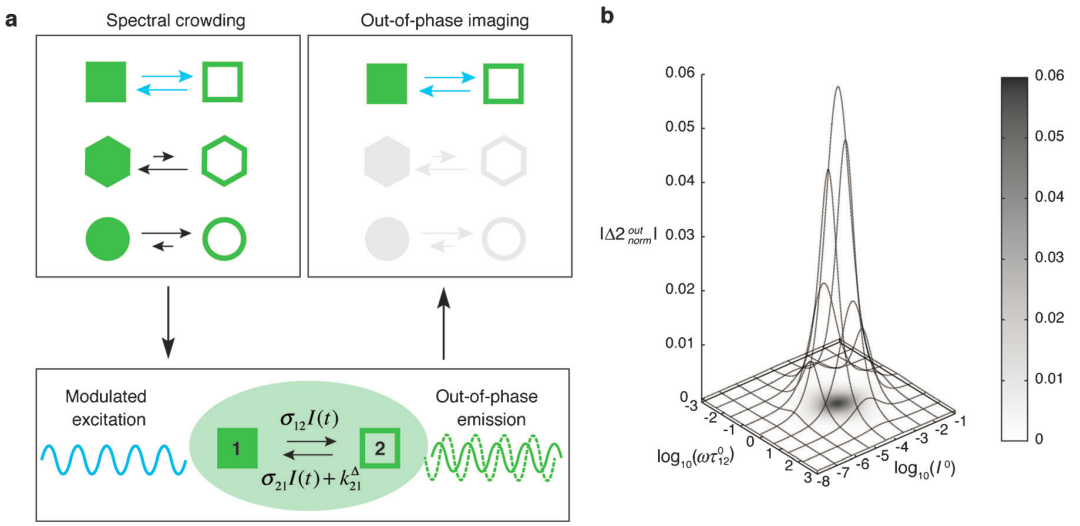

Figure 1.13 – (a) Out-of-phase imaging after optical modulation (OPIOM). A periodically modulated light generates modulation of the signal from reversibly photoswitchable fluorescent probes exchanging between two states (**1** and **2**), each having a different brightness. The image of a targeted probe is selectively and quantitatively retrieved from the amplitude of the out-of-phase component of the fluorescence emission at angular frequency (ω) upon matching I_0 and ω to its dynamic parameters (σ_{12}, σ_{21}, k_{21}^{Δ}). (b) Theoretical response of a reversibly photoswitchable fluorophore, **1**⇋**2**, submitted to light harmonic forcing of small amplitude. The absolute value of the normalized amplitude of the out-of-phase oscillations in concentration of **2**, $|\Delta 2^{out}_{norm}|$, is plotted versus the light intensity I_0 (in ein.s^{-1}.m^{-2}) and the adimensional relaxation time $\omega\tau_{12}^0$. σ_{12} = 73 m^2.mol^{-1}, σ_{21} = 84 m^2. mol^{-1}, k_{21}^{Δ} = 1.5 × 10^{-2} s^{-1}. The figure is derived from.[140]

(Dronpa-2 and Dronpa-3[141]) in mammalian cells and zebrafish.[140] The images were obtained with a wide field epifluorescence microscope or a single plane illumination microscope by modulating the excitation light from a LED source with a central wavelength of 480 nm. To get the maximal OPIOM response, the modulation parameters $[I^0, \omega]$ were tuned to match the resonance conditions (Eqs. (1.7)). OPIOM selectively visualized the Dronpa-3 labeled structures in the cells, completely rejecting the autofluorescence and EGFP signal which did not exhibit any out-of-phase response (see Fig.1.14). Moreover OPIOM bandpass discrimination enabled to independently image both Dronpa-2 and Dronpa-3 in systems containing both RSFPs.

With a single excitation light at 480 nm, OPIOM relies on repetitive exchange between state **1** and **2** (**1** being bright state and **2** being dark state in the case of the Dronpa mutants used), where the population of state **2** is light-driven and recovery of the state **1** occurs with a slow thermal resetting rate of up to several minutes. Under this circumstance, low modulation frequency had to be used to match the resonance. The image acquisition required more than 2 minutes.[140] *Chen et al.* combined SAFIRe[131] and OPIOM[140] to achieve a faster imaging rate by introducing a secondary continuous wave light at 405 nm which accelerated the recovery process from **2** to **1**.[142] The low intensity co-illumination light allowed to drastically increase the light modulation frequency and speeded up the imaging rate to a sub-second time scale.

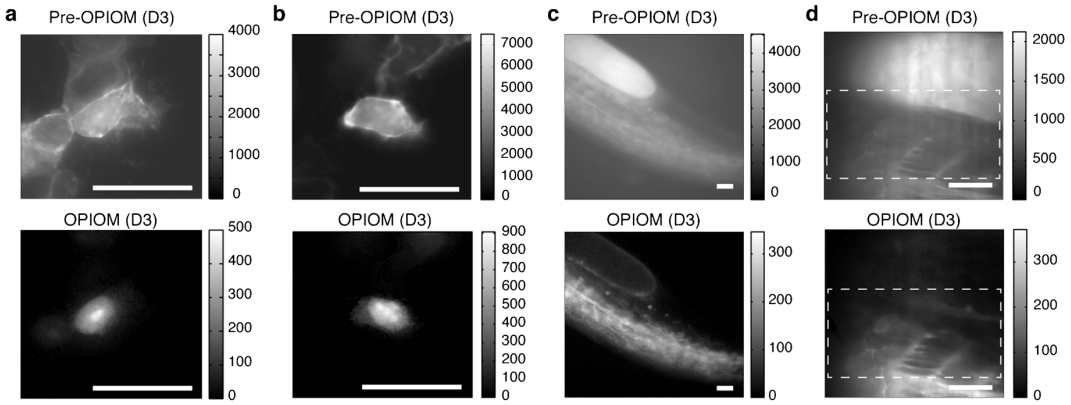

Figure 1.14 – OPIOM application in mammalian HEK293 cells and in 24 hpf zebrafish embryos. (a,b) Selective imaging of nuclear Dronpa-3 against membrane-localized EGFP. (c,d) Selective imaging of Lifeact-Dronpa-3 against autofluorescence. Fixed (a) or live (b) cells, and zebrafish embryo (c,d) were imaged by epifluorescence (a–c) or single plane illumination microscope (d) (the dashed rectangles indicate the zone illuminated by the thinnest part of the light sheet) upon illuminating with sinusoidal (a–c) or square wave (d) light modulation of large amplitude tuned on the resonance of Dronpa-3. Images labeled Pre-OPIOM and OPIOM correspond to the unfiltered and OPIOM-filtered, respectively, images. Scale bars: 50 mm. The figure is derived from.[140]

An advanced OPIOM protocol exploiting dual illumination, named Speed OPIOM, was independently introduced by *Quérard et al.* to increase the frequency of the periodic illumination.[143] In Speed OPIOM, both light sources at 480 and 405 nm are modulated in antiphase, leading to a photoswitching between the bright and dark states of the RSFP which is both much faster and of larger amplitude than in OPIOM. Following the theoretical analysis, the fluorescence signal of the RSFP also exhibits a tunable out-of-phase response with a single resonance in the space of the illumination parameters. Interestingly, instead of tailoring the absolute average intensity I^0 and the radial frequency ω, one can maximize the Speed OPIOM amplitude only by adjusting the ratios I_2/I_1 and ω/I_1 to specific values determined by the kinetic photoswitching properties of the RSFP, where I_1 and I_2 are the average light intensities at 480 and 405 nm respectively. Moreover, the maximum Speed OPIOM response is twice that in the original one color OPIOM.[143] In particular, the resonance conditions show that we can modulate the light sources at higher frequency by increasing both light intensities while keeping constant their ratio, allowing to shorten the imaging time down to the millisecond timescale. Experimental validations have evidenced that Speed OPIOM is a powerful tool for quantitative imaging of reversible photoswitching fluorescent probes, overcoming the autofluorescence background under adverse lighting conditions.

1.4 Objectives of this PhD work

Our group theoretically introduced and experimentally validated the Speed OPIOM protocol for cell observations in fluorescence imaging in works performed before the beginning of this PhD. A simple and cheap homemade epi-fluorescence microscope and a light-sheet fluorescence microscope were respectively developed, with modified illumination systems embedding dual LED or laser sources to achieve two-color

light modulations. Equipped with Speed OPIOM, these microscopes have overcome the limitations of autofluorescence in providing high contrast fluorescence images of different types of RSFP-labeled cells from Hela cells, U2OS cells, and zebrafish embryo. Moreover, Speed OPIOM enabled to discriminate up to 4 different fluorophores in complex biological mixtures, which is promising for multiplexed fluorescence imaging. However the application of Speed OPIOM was restricted to microscopic observations of cells, which forbidded to illustrate all its potential in other optical configurations. The general goal of this PhD work was precisely to extend the implementation of Speed OPIOM to new instruments for macro-scale and endoscopic fluorescence imaging. In particular, we were willing to illustrate that Speed OPIOM could be highly relevant to overcome the limitations of ambient light and autofluorescence in these imaging modalities. Moreover, we also aimed at enlarging the Speed OPIOM scope and precise its potential in new applications.

The manuscript reporting on this PhD work correspondingly contains four chapters:

- In the first introductive chapter, we examined autofluorescence and ambient light as limitations in fluorescence imaging and reported on state-of-the-art strategies to overcome them;
- In the second chapter, we report on a homemade macroscope exploiting the Speed OPIOM protocol. By benefiting from optimized illumination and a thoroughly imaging system, it could achieve efficient fluorescence imaging overcoming autofluorescence and strong ambient light (e.g. sunlight). More specifically, this macroscope was experimentally validated for selective fluorescence observation of diverse biological media, such as fluorescent blotting membranes, microbial growth plates, and living plant leaves under outdoor conditions. This macroscope also proved a powerful and sensitive tool for quantification of reversible photoswitchable fluorophores, with a drastic improvement of sensitivity and signal-to-background ratio, even under sunlight;
- The third chapter reports on a collaborative work with agronomists, which aimed at applying the macroscope for quantitative fluorescence detection of living plant leaves in the context of stress monitoring. A series of genetically transfected or transformed plant leaves expressing targeted reversibly photoswitchable fluorescent probes were imaged under indoor or outdoor conditions, and the expression level of the target probe was successfully retrieved. Our system allowed us also to monitor in real-time the stresses of genetically engineered plants;
- The fourth chapter reports on a fiber bundle-based endo-microscope, which integrates the Speed OPIOM protocol. With its ability for selective imaging, this endoscope allowed us to realize specific observations such as imaging plant roots in a soil, or real-time monitoring of a bio-process in a bioreactor. Furthermore, this optical setup has been used to evidence the ability of the Speed OPIOM protocol for optical sectioning, which is promising for fiber-based deep tissue imaging;
- The last chapter concludes the PhD work and discusses a few perspectives.

This manuscript also integrates in an Annex the paper in which Speed OPIOM has been introduced for which I contributed to validations with the macroscope.

Part II

Macro-imaging

Chapter 1

Radiometric analysis for Speed OPIOM macro-imaging

The fluorescence of biological samples is observed under the illumination of an excitation light. In the case of large samples such as plant leaf and animal tissue, the excitation light has a complicated interaction with the system. Moreover, the detectable fluorescence is generated only from the surface of the sample. In this chapter, we evaluated the surface fluorescence emission of a scattering model, taking into account the penetration length of the excitation intensity. This analysis helped us to define the excitation system and the image collection system required for the macroscope implementing Speed OPIOM.

1.1 Fluorescence emission from biological media at the macro scale

1.1.1 Transparent media

To estimate the fluorescence emission of an object at the macro level, we first consider a simple model: a thin layer of fluorophore solution under perpendicular illumination of the excitation light using 480 nm wavelength for illustration.

We assume that the thickness of the layer is $\delta \leqslant 200\ \mu$m (less than the depth of field of the macroscope) and the concentration of the fluorophore is low ($c \sim 10^{-6}$ M), which is a representative concentration of a fluorescent protein for labeling biological media. For the molar absorption coefficient at λ = 480 nm, we take $\varepsilon = 5 \times 10^4$ $M^{-1}cm^{-1}$, a typical value for most green fluorescent proteins. When the excitation light at λ = 480 nm passes through the layer perpendicularly, the absorbance of the light is estimated as $A = \varepsilon c\delta \sim 10^{-3} \ll 1$, which indicates that the attenuation of the excitation light owing to the absorption of the fluorophore is negligible. Hence the layer can be considered transparent, and I_{ex} is constant through the solution. The intensity of the fluorescence emission I_{em} is proportional to the absorbed intensity I_{abs} of the excitation light and

$$I_{em} \quad = \quad \Phi_F I_{abs} = \Phi_F I_{ex}(1 - 10^{-\varepsilon c\delta}) \approx \Phi_F \varepsilon c\delta I_{ex} ln10 \tag{1.1}$$

where Φ_F is the quantum yield of the fluorophore in the layer. The equation suggests that the emission is linearly dependent on the thickness of the solution.

1.1.2 Non-transparent media

The biological tissues have more complicated interaction with light than transparent solutions. Light intensity attenuates rapidly through the tissue due to scattering and molecular absorption, which greatly limits the depth of penetration. Here we take the leaf of a living plant as a model and analyze its epidermic fluorescence emission under excitation light.

Decay of light intensity through living leaves

The interaction of light with plant leaves depends on the chemical and physical properties of the leaves. Generally two main factors contribute to the decay of light through leaves: light absorption of the pigments (chlorophyll and carotenoids) and light scattering by the tissue structure. To evaluate the light penetration through the leaf, we used the **PROSPECT** model, which has been developed by S. Jacquemoud et F. Baret to analyze the spectral transmission by *Arabidopsis thaliana*.[144] As displayed in Fig.1.1, the transmission through the total leaf is 14 % at λ_{fluo} = 525 nm, 1.17 % at λ_1 = 480 nm and 0.2 % at λ_2 = 405 nm, which are the emission wavelength and the excitation wavelengths to be used to photoswitch our reversible photoswitchable fluorescent proteins.

a **b**

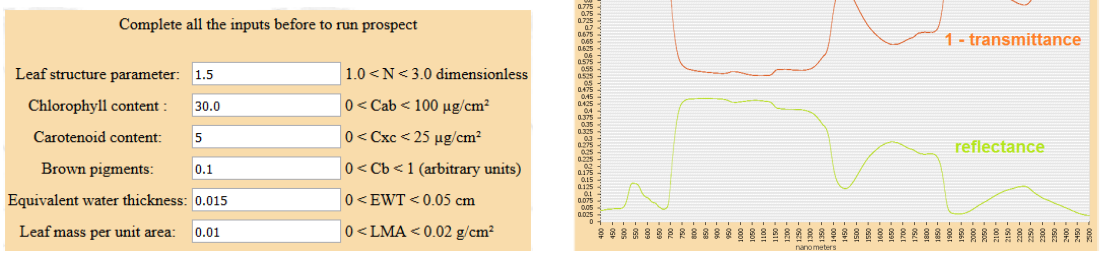

Figure 1.1 – Application of the PROSPECT Model to the leaf of Arabidopsis thaliana. **a**: Inputs of Arabidopsis leaf data : typical leaf parameters extracted from literatures[145–148]; **b**: Evaluation of the spectral reflectance and transmission through the total thickness of the leaf.

We then assumed that the light decay through the leaf was exponential as a function of the depth (see Equation (1.2) and Fig.1.2)

$$I_{ex}(z) = I_0 10^{-\frac{z}{\delta_\lambda}} \tag{1.2}$$

where δ_λ is the typical penetration depth at wavelength λ and I_0 is the light intensity on the leaf surface. Considering that the typical thickness of the leaves is 220 μm, we could first derive δ_{525} = 258 μm, δ_{480} = 114 μm and δ_{405} = 85 μm. Then we could deduce the length z_λ over which the light intensity decays by a factor 10 since $z_\lambda = \delta_\lambda$. These values agree with the measurements reported in literature.[149,150]

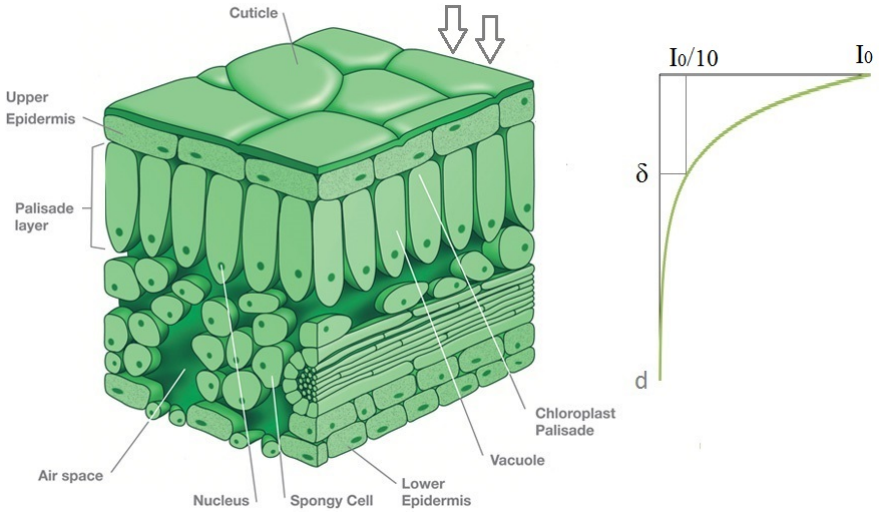

Figure 1.2 – Leaf structure (left) and light excitation profile through the leaf (right).

Epidermic fluorescence emission on the leaves

Taking into account the light decay through the tissue, the detectable fluorescence emission on the surface of the leaf could be estimated. The fluorophore concentration in the tissue was considered spatially homogeneous. The light absorption by the fluorescent protein through a thin layer dz is

$$\mathrm{d}I_{abs}(z) = -\mathrm{d}I_{ex}(z) = I_{ex}(z)(1-10^{-\varepsilon c \mathrm{d}z}) = \varepsilon c I_{ex}(z) ln10\,\mathrm{d}z \tag{1.3}$$

The emitted fluorescence from the deeper layers also suffers from light reabsorption by the tissue before being finally detected at the leaf surface. Hence the total detected fluorescence intensity at the leaf surface I_{em} is:

$$I_{em} = \int_0^{\delta_{leaf}} \Phi_F \mathrm{d}I_{abs} 10^{-z/\delta_{525nm}} \tag{1.4}$$

$$= \Phi_F \varepsilon c I_0 ln10 \int_0^{\delta_{leaf}} 10^{-z/\delta_{480nm}} \cdot 10^{-z/\delta_{525nm}} \mathrm{d}z \tag{1.5}$$

$$= \Phi_F \varepsilon c I_0 \delta_\gamma (1-10^{-\frac{\delta_{leaf}}{\delta_\gamma}}) \tag{1.6}$$

When $\delta_{leaf} > \delta_\gamma$, Eq.(1.6) yields Eq.(1.7)

$$I_{em} \rightarrow \Phi_F \varepsilon c I_0 \delta_\gamma \tag{1.7}$$

where $\delta_\gamma = \frac{\delta_{480}\delta_{525}}{\delta_{480}+\delta_{525}} = 79\ \mu$m is related to the absorption property of the light through the tissue.

Hence, in contrast to the case of the transparent solution, when the thickness of the leaf δ_{leaf} is higher than δ_γ (which is always the case), the actual leaf thickness has little influence on the fluorescence intensity detected at the surface. In another word, the surface fluorescence emission is mainly generated by the fluorophores within a shallow layer of δ_γ at the surface of the leaf.

1.2 Speed OPIOM signal at the leaf surface upon modulated resonant dual illumination

Speed OPIOM exploits resonant sinusoidally modulated dual illumination at two wavelengths λ_1 and λ_2.[143] At resonance, the average light intensities I_1^0 and I_2^0 and angular frequency ω of the modulated lights should fulfil the conditions given in Eqs.(1.8,1.9)

$$(\sigma_{12,1} + \sigma_{21,1})\, I_1^0 = (\sigma_{12,2} + \sigma_{21,2})\, I_2^0 \tag{1.8}$$

$$\omega = 2\,(\sigma_{12,1} + \sigma_{21,1})\, I_1^0. \tag{1.9}$$

which involve the photoswitching cross sections at λ_1 and λ_2, $\sigma_{12,1}$, $\sigma_{12,2}$, $\sigma_{21,1}$, and $\sigma_{21,2}$, between the states **1** and **2** of the reversibly photoswitching fluorophores.

During this work, we decided to fix illumination to fulfill the resonance conditions at the leaf surface. However, since the light intensity decreases through penetrating the leaf, the resonance conditions could not be met anymore below the leaf surface. Since the transmission of UV and blue lights by leaves are very close (*vide supra*), we assumed that the first resonance condition (1.8) was satisfied within δ_γ. In contrast, the second resonance condition would be violated when going deep into the leaf due to the decays of the light intensities. This violation results in a drop of the Speed OPIOM signal, which can be evaluated from the expression of the Speed OPIOM response given in Eqs.(97) and (100) of the Supporting Information from reference.[143] It yields

$$I_F^{OPIOM} = \int_0^{\delta_{leaf}} \Phi_F \mathrm{d}I_{abs} 10^{-z/\delta_{525nm}} \frac{I_0/I(z)}{1 + (I_0/I(z))^2} \tag{1.10}$$

$$= \Phi_F \varepsilon c I_0 ln10 \int_0^{\delta_{leaf}} 10^{-\frac{z}{\delta_\gamma}} \frac{1}{10^{\frac{z}{\delta_{480nm}}} + 10^{-\frac{z}{\delta_{480nm}}}} \mathrm{d}z \tag{1.11}$$

The term $\frac{1}{10^{\frac{z}{\delta_{480nm}}} + 10^{-\frac{z}{\delta_{480nm}}}}$ decreases from 0.5 to around 0.2 from the surface to the depth δ_γ beyond which essentially no further fluorescence signal is collected. Hence Eq.(1.11) shows that the Speed OPIOM is between 0.2 and 0.5 times lower than the average fluorescence signal (instead of 0.5 times lower in the case of a transparent solution).

1.3 Speed OPIOM resonnance conditions for different RSFPs

In the case of green RSFPs, illumination has to be modulated at λ_1=480 and λ_2=405 nm under resonant conditions to enable selective fluorescence imaging. Table 1.1 provides the relevant datas to set resonance for a series of previously investigated green RSFPs.[143]

Figure 1.3 displays the resonant illuminations for the six proteins above. At resonance, the intensity of the blue light is always higher than that of the UV light. At the same I_{480}^0, the modulation frequency ω is notably higher for Dronpa-2 than other proteins, which means that the detection of Dronpa-2 is at the fastest at a given excitation intensity.

Table 1.2 provides the average light intensities I_1^0 and I_2^0 needed to be at resonance for the different RSFPs to modulate illumination at an angular frequency of 1 Hz: The resonance condition is easier to reach for Dronpa-2, which needs a lower level of blue light intensity with respect to the other RSFPs.

RSFP	$\sigma_{12,480} + \sigma_{21,480}$ ($m^2 \cdot s^{-1}$)	$\sigma_{12,405} + \sigma_{21,405}$ ($m^2 \cdot s^{-1}$)
Dronpa	5.1	354.5
Dronpa-2	196	413
Dronpa-3	29	331
rsFastLime	36	648
Padron	36	96.8
Kohinoor	56	233

Table 1.1 – Values of $\sigma_{12,480} + \sigma_{21,480}$ and $\sigma_{12,405} + \sigma_{21,405}$ for previously investigated RSFPs.[143]

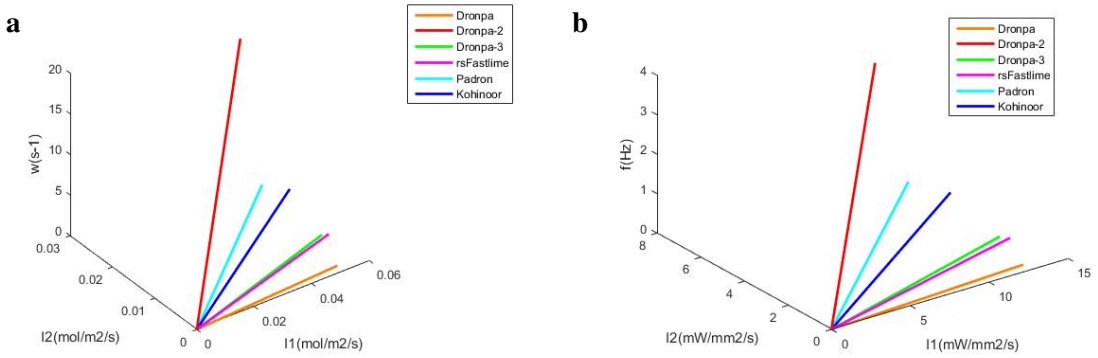

Figure 1.3 – Evolution of the Speed OPIOM resonance condition for I_1 (blue light), I_2 (UV light), and angular frequency of modulated illumination for different RSFPs. **a**: Intensities in $mol \cdot m^{-2} \cdot s^{-1}$; **b**: Intensities in $mW \cdot mm^2$.

	Dronpa	Dronpa-2	Dronpa-3	rsFastLime	Padron	Kohinoor
$I_1(mW \cdot mm^{-2})$	154	4.01	27.5	21.8	21.8	14.0
$I_2(mW \cdot mm^{-2})$	2.62	2.25	2.86	1.43	9.58	3.98

Table 1.2 – I_1, I_2 at 1 Hz under the Speed OPIOM resonance conditions.

1.4 Illumination strategy

From examining the resonance condition, we first deduced that high intensity excitation lights were necessary to accelerate the modulation frequency in order to shorten the duration of the detection. Moreover, we should obtain a uniform illumination to ensure that the Speed OPIOM resonance occurs over the whole imaged area, which can be extended from mm to m in macro scale observations.

At such scale, it is difficult to deliver a powerful and uniform illumination. Laser sources are ideal for remote illumination since they are stable, powerful, and well-collimated. However, high power laser light is dangerous, which requires supplementary safety precautions. They are not practical for agronomic uses, which have been considered in this work. LEDs are alternative candidates as sources of excitation light. High power colored LED chips can emit light with high flux and narrow spectra with a bandwidth

of only several tens of nanometers. Since the LED chip is extremely small (1×1 mm^2 minimum), and with no need of complicated operating modules, it is highly suitable for miniaturized optical design. Moreover, with a robust longevity, LED sources permit reliable and long-lasting light modulation.

The macroscope designed in this work uses two high power colored LED chips as excitation sources. The blue color LED(LXZ1-PB01, Lumileds) gives a luminance of $L = 105 \sim 170$ mW$\cdot$ $mm^{-2}\cdot$ sr^{-1} @ 500 mA, and the UV LED (LHUV-0400,Lumileds) has a luminance of $L = 135 \sim 170$ mW$\cdot$ $mm^{-2}\cdot$ sr^{-1} @ 500 mA. Thanks to a condensing system, the two color lights are focused to the sample at 120 mm away with an illumination area of 4×4 mm^2. The light irradiance on the sample can be up to 10 mW/mm^2, with which we could be able to reach a modulation frequency of more than 1 Hz (Fig. 1.3).

1.5 Fluorescence emission detection under ambient light

According to Eq.(1.6), we could estimate the fluorescence emission from the leaf surface to be $I_{em} = \Phi_F \varepsilon c I_0 \delta_\gamma = 0.00032 I_0$ by assuming $c = 10^{-6}$M, $\Phi_F = 0.8$, and $\varepsilon = 5 \times 10^4 M^{-1}cm^{-1}$. Hence the fluorescence light flux would be extremely low with respect to the excitation, with only 0.03% of the excitation energy being converted to fluorescence. With the illumination system of the macroscope, the order of magnitude of the epidermic fluorescence emission from the leaf was estimated around 1 μW/mm^2.

Such a weak fluorescence intensity could be easily overwhelmed when the leaf is exposed to strong ambient light. To design the setup we took into account an extreme case, direct sunlight. The typical irradiation of the sunlight on Earth surface is $I_\lambda = 1.3 W/m^2/nm$ around 525 nm, which is the peak of the fluorescence emission of the reversibly photoswitchable fluorescent proteins to be used in this work. Assuming that the light is filtered by an optical filter with bandwidth of Δ_λ=40 nm around 525 nm before been imaged onto the CCD, most of the green fluorescence and only the green part of the reflected sunlight are involved in the imaging. The reflected sunlight intensity on the leaf was estimated as $I_{sun} = R \cdot I_\lambda \Delta_\lambda \sim 6\mu W/mm^2$, where R=12% is the reflectance of the leaf for the green light (see Fig. 1.1). From this derivation, we could conclude that the signal from the reflection of sunlight on the leaf would be higher than the fluorescence signal from the leaf, but would remain at the same order of magnitude. However, Speed OPIOM will use a lock-in detection scheme, allowing to extract the modulated fluorescence signal from a constant background of about 3000 times higher (*vide infra*), which would make it possible to extract the fluorescence signal under sunlight.

Chapter 2

A Speed OPIOM macroscope and its applications in fluorescence bio-imaging

Fluorescence imaging is increasingly being considered to observe large biological samples such as microbial colonies, tissues, organs, up to living plants and animals. In contrast to microscopic imaging which is concerned with observations of the micro world, macro imaging deals with a global view of the objects at much larger scale, which requires specific imaging devices and more complex imaging conditions.

Macro-scale fluorescence imaging is quite different from microscopic imaging in various aspects. Firstly, while micro-imaging is normally performed in a dark room with enclosed environment to eliminate the interference of the light from outside, macro-scale observations are sensitive to ambient light. At a technological level, macroscopes are designed to establish distance of at least several centimeters between the specimen and the objective, in order to get a large imaging area; at such a scale, the specimen is easily exposed to environmental light. At a practical level, human eye observation is often involved in macro imaging to facilitate the manipulation, which necessitates a bright working environment. Secondly, macroscopes offer a global vision of the sample at a large scale of more than 1 mm, regardless of the sub-cellular structures. While the targeted fluorescent probe might be discriminated at the sub-cellular scale, it should be totally mixed with autofluorescence in macro images due to a much weaker image resolution. Moreover, compared to microscopic objectives which possess a depth of field of less then 10 μm, macroscopic objectives have a deeper focal depth of more than 200 μm on the sample, collecting more autofluorescence signal owing to the thickness of the imaged object.

Speed OPIOM has been proved to be an efficient protocol in microscopic imaging to selectively eliminate autofluorescence. In order to exploit the same protocol for macro-scale imaging, I developed a cheap and compact macroscope with compatible illumination and image collection systems, which aimed to get high contrast fluorescence imaging of various macro samples under versatile applicative environments. In this work, I first designed and constructed a simple macroscope. I elaborated the illumination system of the excitation light in order to optimize the light intensity on the image plan. I also redesigned the imaging system to correct possible aberrations through the field of view. I synchronized the modulation signal and the image acquisition with a teensy card controlled by a PC, and I implemented a matlab code to process the collected images and properly extract the final OPIOM image. Then I used

the macroscope for selective imaging of several different biological samples originating from our group or from collaborators. First I used it for fluorescence western blot imaging on nitrocellulose membrane, that emits a strong autofluorescence interfering with the targeted signal of the fluorescent probe. A series of blots with different Dronpa-2 content from 500 to 2.5 pg were deposited onto the membrane and imaged under the macroscope. From totally removing the background autofluorescence from the membrane, the Speed OPIOM image highly enhanced the blot-to-background ratio, and drastically lowered the limit of detection from around 100 pg (under constant illumination) to 2.5 pg, which enabled high sensitivity detection and quantification of the probe. Second, I applied the setup for screening microbial colonies growing on agar culture plates. *E. Coli* colonies expressing different fluorescent proteins (Dronpa-2 or Padron) were successfully discriminated in Speed OPIOM images, and the autofluorescent background from the culture medium was totally removed. Finally, I imaged living leaves of genetically engineered *Camelina sativa* expressing Dronpa-2 with my setup. This time, imaging was done under an adverse condition where the plant was exposed to direct sunlight. My results evidenced that the setup could extract the weak fluorescence emission from the leaves under a 200 times stronger sunlight radiation.

This work led to the publication of an article entitled "Macroscale fluorescence imaging against autofluorescence under ambient light'" by Ruikang Zhang,[a] Raja Chouket,[a] Marie-Aude Plamont,[a] Zsolt Kelemen,[b] Agathe Espagne,[a] Alison G. Tebo,[a] Arnaud Gautier,[a] Lionel Gissot,[b] Jean-Denis Faure,[b] Ludovic Jullien,[a] Vincent Croquette,[c] and Thomas Le Saux,[a] to appear in *Light: Science and Applications*, the contents of which are provided below.

2.1 Article: Macroscale fluorescence imaging against autofluorescence under ambient light

2.1.1 Introduction

Macro-imaging has become an essential tool to study various types of samples of biological origin (plate readers, microorganism or cell cultures, tissues, organs, up to plants and animals). Among the observables, fluorescence has proven particularly attractive in view of its sensitivity[105] and the possibility to fluorescently tag many biomolecules of interest with absolute specificity through genetic fusion.[151,152] Despite these advantages, macroscale fluorescence imaging has encountered specific limitations for biological applications. First many samples exhibit a significant background fluorescence, which can originate from the samples themselves (containing autofluorescence or spectrally interfering fluorescent labels) but as well from the vessels and substrates, or the imaging media (due to additives such as nutrients, drugs,. . .). As a consequence, one can encounter a loss of sensitivity together with a reduction of opportunities for multiplexed imaging, which is often claimed as an advantage of fluorescence

[a]PASTEUR , Département de Chimie, Ecole normale supérieure, PSL University, Sorbonne Université, CNRS 75005 Paris, France

[b]Institut Jean-Pierre Bourgin, INRA, AgroParisTech, CNRS, Saclay Plant Science (SPS), Université Paris-Saclay, Versailles, France

[c]Laboratoire de Physique Statistique, Ecole normale supérieure, PSL Research University, Université Paris Diderot Sorbonne Paris-Cité, Sorbonne Université, CNRS 75005 Paris, France and Institut de biologie de l'Ecole normale supérieure (IBENS), Ecole normale supérieure, CNRS, INSERM, PSL Research University, 75005 Paris, France

over other observables such as chemiluminescence for instance. Macroscale fluorescence imaging can additionally suffer from ambient light (up to sunlight in the case of outdoor observations), which has mostly restricted applications to light-tight enclosures or darkrooms. In macroscale fluorescence imaging, modulated illumination and image acquisition operated in homodyne detection[55,62] or pulsed excitation and time-gated detection[56,60] have been already proposed to retrieve fluorescence signals against ambient light. In contrast, there is still a demand for reliable strategies to eliminate the detrimental effects of autofluorescence in this imaging modality.

In fluorescence bioimaging, spectral discrimination has been generally favoured to generate contrast of a fluorescent label against an interfering background. Specific spectral properties have correspondingly been sought for. Hence labels with (near-infra)red emission have been often favored since the autofluorescence of biological media is generally less pronounced in this wavelength range. However, the corresponding narrow wavelength window intrinsically limits the opportunities for multiplexed observations. Alternatively, spectral discrimination of autofluorescence has been achieved with fluorescence unmixing protocols[153,154] but this relied on the assumption that it exhibits an homogeneous spectrum over the whole sample. Engaging a label in reactions provides a complementary dimension to overcome the limitations encountered with spectral discrimination. In particular, the dynamic response of a fluorescent label to light modulation has been exploited since kinetics brings as many discriminative dimensions as the number of rate constants involved in the label reactions.[105] This discriminative strategy has been explored early in fluorescence spectroscopy whose signal precisely originates from the relaxation of an excited label after light absorption by its ground state. Hence lifetimes of excited states have been extensively used to discriminate spectrally overlapping labels.[155] However, except in specific favorable cases,[156] the range of lifetimes of the fluorescent labels is narrow (the same few nanoseconds) and mostly overlaps the lifetime range of the components giving rise to autofluorescence; thus deconvolutions[153,157] or subtractions[107] have to be performed to extract individual contributions, which is detrimental to the signal-to-noise ratio.

Reversibly photoswitchable fluorescent labels which can exchange between an ON (bright) state and an OFF (dark) state[121–123,158–160] do not suffer from this drawback since their photoswitching relaxation times cover a much broader range than fluorescence lifetimes. For instance, we recently showed that the photoswitching relaxation time of genetically-encoded green emissive, reversibly photoswitchable fluorescent proteins (RSFPs) spans over three orders of magnitude.[143] Hence several microscopy protocols (e.g. OLID,[124] SAFIRe,[135] and OPIOM – Out-of-Phase Imaging after Optical Modulation[139,140,143]) have been recently introduced to kinetically discriminate reversibly photoswitchable fluorescent labels against several types of spectrally interfering backgrounds without any deconvolution nor subtraction scheme. In OPIOM,[139,140,143] kinetic information of a targeted fluorescent label is uncovered by driving its reversible photoswitching between states of contrasted brightness. Subsequent filtering enables one to selectively extract the contribution of this label from the overall signal, even in the presence of interfering species. More specifically, Speed OPIOM drives photoswitching with two modulated light sources synchronized in antiphase at two wavelengths (Fig. 2.1a). After acquisition of tens to hundreds of images for at least two periods of light modulation, the Speed OPIOM signal $\mathcal{S}$ – the out-of-phase component of the modulated fluorescence signal – is directly retrieved by Fourier transform of the acquired images (Fig. 2.1b); no

further processing is needed and lock-in detection secures efficient noise rejection. $\mathcal{S}$ exhibits a narrow resonance when light intensities are tuned to balance the average concentrations of the ON and OFF states (in order to maximize the photoswitching amplitude on the changes of light intensities) and the angular frequency is matched with the inverse of the photoswitching relaxation time[143] (in order to generate the phase lag optimizing the out-of-phase amplitude of the fluorescence response; see reference[143] for the complete description). Since a reversible photoswitchable fluorescent label has singular photochemical and kinetic properties (and correspondingly its own resonant conditions), simply tuning the illumination control parameters to the resonant values enables one to selectively image a targeted label, filtering out the contribution of non-resonant fluorophores as well as ambient light (Fig. 2.1b).

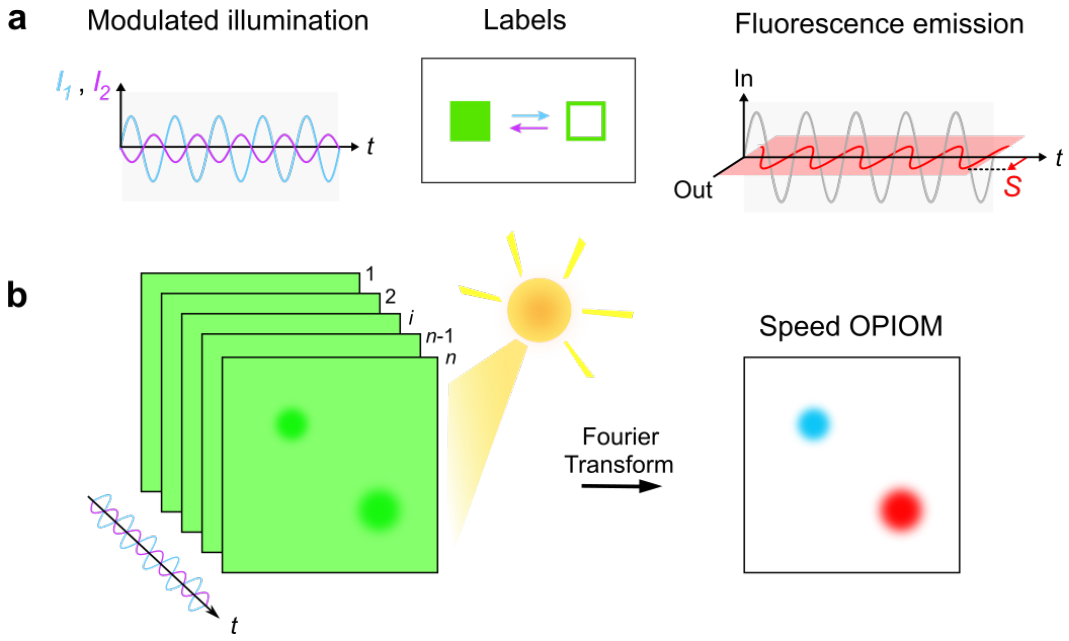

Figure 2.1 – *Principle of Speed OPIOM*. **a**: Sinusoidally modulated light sources synchronized in antiphase at two wavelengths generate the quadrature-delayed component $\mathcal{S}$ (in red) of the fluorescent emission from the reversibly photoswitchable fluorescent labels used for selective Speed OPIOM imaging; **b**: A dynamic video is recorded upon modulated illumination and the series of images is demodulated to extract $\mathcal{S}$ from a complex background including spectrally interfering auto-fluorescence and ambient light.

In the present manuscript, we implement Speed OPIOM in macroscale fluorescence imaging. We build a simple and cheap macroscope and thoroughly evaluate its efficiency to eliminate the interference of autofluorescence and ambient light when observing targeted RSFPs in three types of biologically-relevant samples. We first examine its application to improve the sensitivity of blot assays. Most commercially available porous membranes used for protein transfer (nitrocellulose, polyvinylidene difluoride – PVDF,. . .) emit a significant fluorescence in the blue–yellow wavelength range of the visible spectrum, which worsens the analytical performance after revelation with fluorescently labelled antibodies.[161–164] We show that our macroscope enhances sensitivity and signal-to-noise ratio for fluorescence detection on nitrocellulose membranes by a factor of 50 and 10 respectively, over direct fluorescence observation under constant illumination. We then apply our setup for imaging colonies and lawns of fluorescent bacteria

growing on agar plates. Fluorescence plates are widely used to analyze the level of protein production[165] or the organization of microbial biofilm communities,[166] as well as in screening for compounds that select against antibiotic resistance[167]; however they often suffer from a significant autofluorescence originating from the plate material or the growth media.[78] We evidence that our macroscope overcomes the strong autofluorescence of growth media used in microbiology and that it enables multiplexed fluorescence observation with the same configuration of excitation and emission wavelengths. Finally we address macroscale fluorescence imaging of fluorescently labelled leaves under conditions of strong external illumination. Leaves are strongly reflective and autofluorescent heterogenous media, in which macroimaging of fluorescent proteins has been hampered by endogenous fluorophores[168,169] (e.g. the photosynthetic apparatus) and has necessitated sophisticated time-gated detection schemes.[170] We demonstrate that our setup for macroscale imaging easily discriminates fluorescent labels from the autofluorescent background even at light intensities comparable to sunlight.

2.1.2 Results

The Speed OPIOM macroscope

Speed OPIOM imaging requires a well controlled illumination homogeneity to enable one for selective imaging of a targeted reversibly photoswitchable fluorophore over the whole image. More precisely the average intensities I_1^0 and I_2^0 of the light sources modulated at angular frequency ω have to be maintained constant over the whole imaged field since the Speed OPIOM resonance conditions fix both I_1^0/I_2^0 and I_1^0/ω ratios.[143] One should additionally adopt powerful light sources in order to record the images at the highest possible acquisition frequency. We have chosen Light Emitting Diode (LEDs) as light sources for our macroscope, since they are compact, inexpensive, robust, easy to modulate and flexible for optical design.

Hence our macroscope integrates three 500 mW colored LEDs with center wavelengths at 405, 480, and 550 nm (Fig. 2.2a,b); whereas the two LEDs emitting at 405 and 480 nm are directly involved in the implementation of Speed OPIOM with RSFPs (*vide infra*), the last LED emitting at 550 nm has been added to excite red fluorescent proteins in view of agronomic applications to be published elsewhere.[171] After collimation by high NA condensers and bandpass filtering, the excitation lights are combined by three beamsplitters and refocused by a beam expanding system (composed of three optical elements; see Fig. 2.2b, Electronic supplementary material and Fig. S2.1) onto the sample located 120 mm away, so as to generate uniform illumination within a square-shape area of 4×4 mm^2 with high irradiance for the three excitation wavelengths: maximum irradiance is estimated to exceed 1000 mW/cm^2 at each wavelength and the distribution of light intensity is essentially uniform with a deviation of less than 25% throughout the square (Fig. 2.2c), which is fully compatible with Speed OPIOM requirements. The fluorescence emission is collected by the same optical system and filtered by bandpass filters centered at 525 or 585 nm for green or red fluorescent labels respectively. The image is formed by an achromatic lens system (composed of three spherical singlet lenses with optimized air spaces and an effective focal length of f = 30 mm; see Fig. 2.2b, Electronic supplementary material and Fig. S2.2) onto the camera, which allows us to get sharp images for both green and red channels from 500 to 650 nm (Fig. 2.2d,e, S2.3, S2.4 and S2.5). The modulation reference signal and the acquisition of the camera are synchronized by

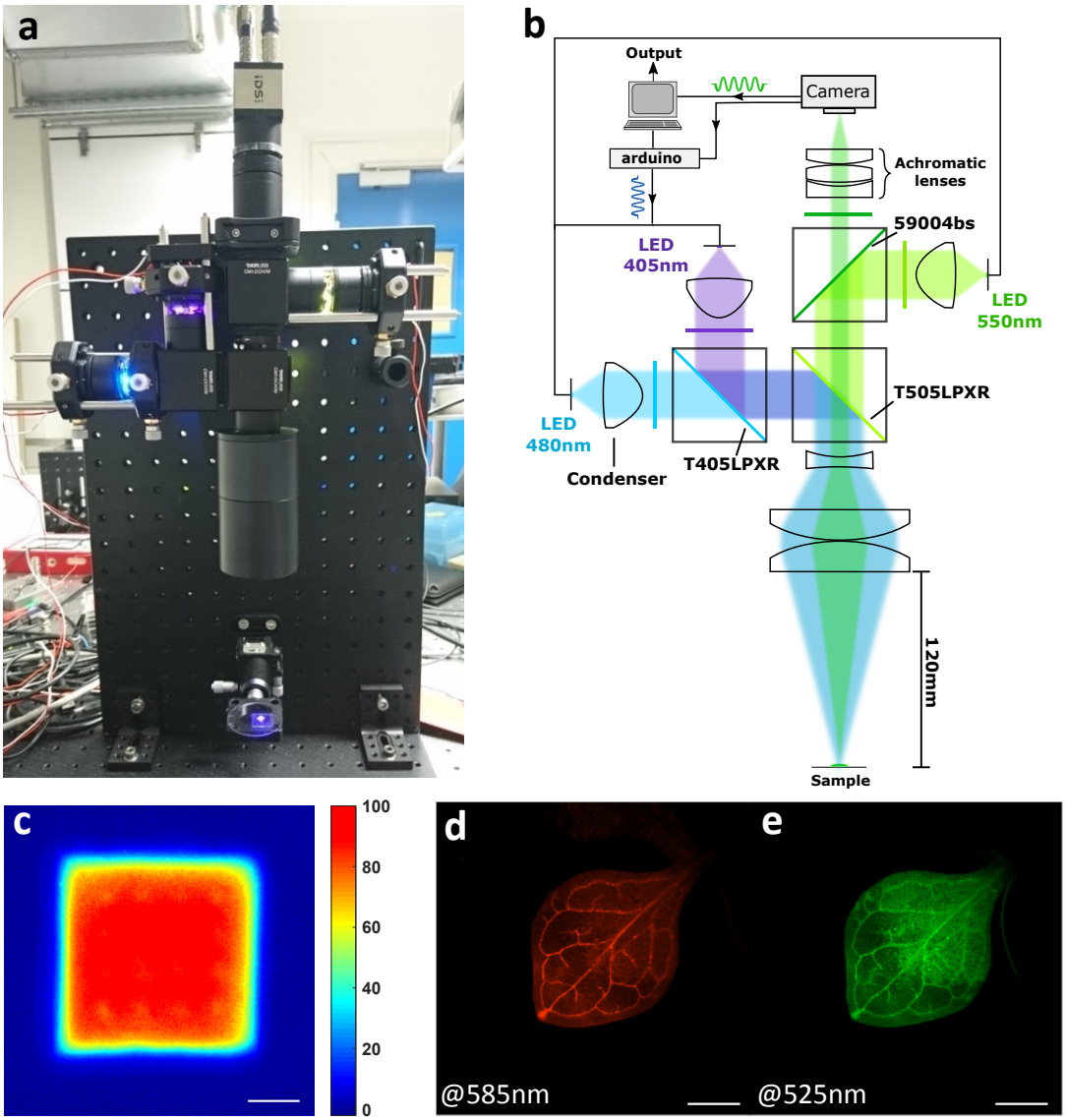

Figure 2.2 – **a**: Optical setup for Speed OPIOM macroscale fluorescence imaging; **b**: Scheme of the setup showing the optical layout and the interface to a PC-based synchronized modulation and image acquisition system; **c**: Normalized light illumination is homogeneous at the sample; **d**,**e**: Chromatic correction yields sharp images of leaves of Dronpa-2 and DsRed-double-labeled *Arabidopsis thaliana* in both red (585 nm) and green channels (525 nm). *Scale bars*: 1 mm.

an Arduino compatible card (Teensy 3.5), and the series of acquired images is subsequently processed by a computer. After preliminary correction of any photo-bleaching occurring during the illumination sequence, the time domain Fourier transform is applied to the series of captured images to yield the average and out-of-phase images subsequently denoted as Pre-OPIOM and OPIOM respectively. It is worth noting that the Pre-OPIOM image compares fairly well with the fluorescence image, which would be classically recorded under constant illumination.

Enhancing contrast and sensitivity in blot analysis

Blots are among the most important analytical tools in cell biology, immunogenetics and other biological fields. Fluorescence has attracted increasing attention for quantitative reading out of protein amounts since it provides opportunities for multiplexed observations. However, its sensitivity has been limited by the auto-fluorescence of the transferring membranes[162]: Upon excitation with UV or blue light, these membranes emit significant fluorescence from the blue to the yellow regions of the visible spectrum, which overlaps the emission spectrum of the most commonly used fluorescent probes so as to limit the reliable detection of targeted proteins to no less than 0.5 ng.[164]

To evaluate the ability of our imaging setup to overcome the interference of the membrane auto-fluorescence and to improve the contrast and the sensitivity of the fluorescent blotting, we adopted the 28 kDa Dronpa-2[141,172] RSFP as the targeted reversibly photoswitchable fluorescent label and a commercially available and widely used nitrocellulose membrane as a representative transferring substrate on which different Dronpa-2 amounts have been blotted. Fig. 2.3 displays the Pre-OPIOM and OPIOM images of the membrane recorded in a dark room. In Pre-OPIOM images (Fig. 2.3a-e), the 250 pg blot can be clearly detected, the 25 pg blot is still perceptible although with a significantly lower contrast, but the blot cannot be observed anymore below 5 pg against the overwhelming membrane auto-fluorescence. In contrast, the blot is reliably evidenced in OPIOM images down to an amount of 2.5 pg with an excellent contrast and image resolution by total elimination of the auto-fluorescence (Fig. 2.3f-j).

We further analyzed the collected Pre-OPIOM and OPIOM images to quantitatively estimate the contrast and sensitivity improvements achieved by applying the Speed OPIOM protocol in blot analyses. We computed the values of the mean signals and the standard deviations in each 5×5 pixels^2 areas and subsequently computed the signal-to-noise ratios. The analyses have been performed along three lines: one crosses the middle of the blot whereas the two others are located on the homogeneous membrane area away from it as controls (see Fig. S2.6). Fig. 2.4a displays the dependence on Dronpa-2 amount of the average intensity at the blotted spot in both Pre-OPIOM and OPIOM images. In Pre-OPIOM, the dependence is linear down to 25 pg. Below this amount, the membrane auto-fluorescence dominates the signal so as to forbid the reliable quantification of the Dronpa-2 content. In contrast, OPIOM restores the linearity between the signal and the amount of Dronpa-2 in the whole 500–2.5 pg range. In fact, this linearity is still observed down to 0.5 pg but only for the average signal over three measurements.

The signal-to-noise ratios of the Pre-OPIOM and OPIOM images of the 250 pg blot are respectively equal to 30 and 800 upon estimating the background contribution over a homogeneous area on the membrane (Fig. 2.4b-c). The large improvement of the signal-to-noise ratio brought by the OPIOM protocol is the result of filtering out a large amount of shot noise by the lock-in demodulation and

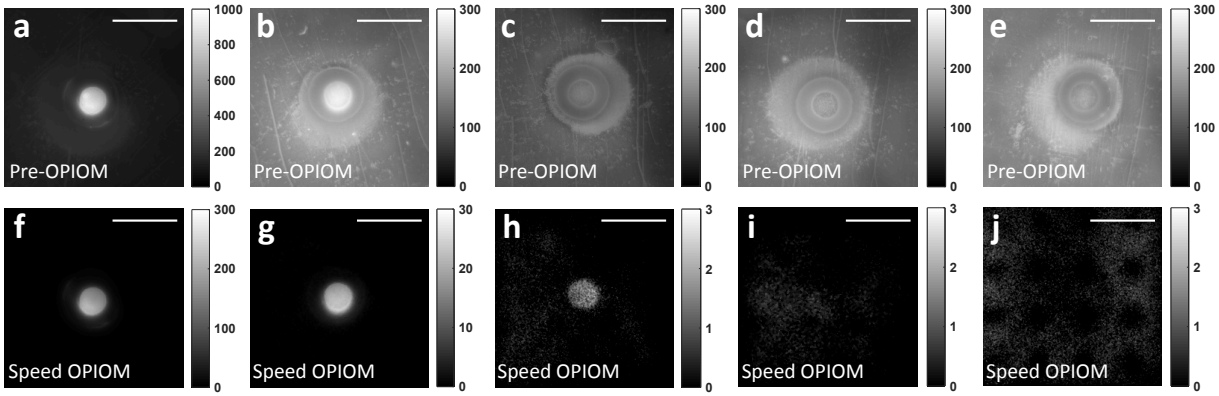

Figure 2.3 – Pre-OPIOM **(a-e)** and OPIOM **(f-j)** images of the nitrocellulose membrane on which various amounts of Dronpa-2 (in pg) have been percolated within the deposited 400 μm-diameter blot: **(a,f)**: 250; **(b,g)**: 25; **(c,h)**: 2.5; **(d,i)**: 0.5; **(e,j)**: 0 (control). The images have been recorded at resonance for Dronpa-2. The conditions of image acquisition are given in Table S2.1. *Scale bars*: 1 mm.

from fluorescent background annihilation providing an average null contribution of the membrane to the OPIOM signal. The Pre-OPIOM signal-to-noise ratio could not be reliably evaluated at 2.5 pg since the observed signal of the blotted Dronpa-2 was lower than the standard deviation over the autofluorescent membrane (Fig. 2.4d; see also the control in Fig. S2.6 where only the buffer has been deposited on the membrane). In contrast the 2.5 pg deposit of Dronpa-2 was clearly observable in the OPIOM image with a signal-to-noise ratio equal to 6 (Fig. 2.4e).

These observations suggested that our macroscope can selectively extract the signal of interest and enhance the sensitivity of fluorescence blotting by 1–2 orders of magnitude and the signal-to-noise ratio by at least a factor 10 over the whole relevant concentration range (see Fig. S2.6).

Multiplexed macroscale fluorescence imaging

Beyond eliminating autofluorescence, Speed OPIOM is compatible with the discrimination of spectrally similar reversibly photoswitchable fluorescent labels, which exhibit distinct photoswitching dynamics.[143] To illustrate this attractive feature for multiplexed macroscale fluorescence observations, we imaged colonies of *E.Coli* bacteria respectively expressing two different green fluorescent RSFPs, Dronpa-2[141,172] and Padron,[173] growing on a strongly autofluorescent growth medium (Fig. 2.5a-j). Again we could efficiently eliminate the strong autofluorescent background arising from the solid growth medium. Moreover, since both RSFPs exhibit Speed OPIOM resonances for different values of the illumination parameters, we could selectively retrieve their individual fluorescence contributions. At resonance for Dronpa-2, Fig. 2.5b,e show that Dronpa-2-labeled bacteria exhibit a strong OPIOM signal, whereas the signal from Padron-labeled bacteria is turned off. In contrast, at resonance for Padron, Fig. 2.5h,j selectively evidence the Padron-labeled bacteria without any interference from Dronpa-2-labeled bacteria. Interestingly, discrimination is here additionally facilitated by opposite signs of the algebraic Speed OPIOM observables for Dronpa-2 and Padron, which are governed by opposite signs of their photochromism.

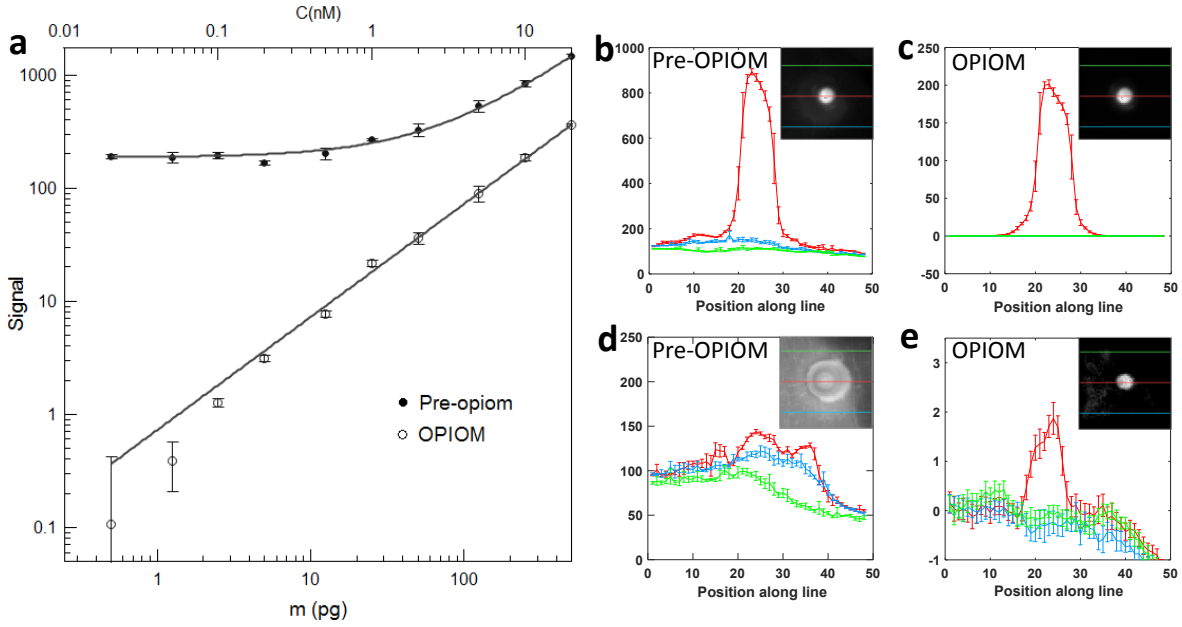

Figure 2.4 – Dependence of the mean signal (**a**) and of the signal profiles (**b–e**) on the Dronpa-2 amount in Pre-OPIOM and OPIOM images. **a**: Pre-OPIOM (disk), OPIOM (circle); the error bar measures the standard deviation over three independent measurements. **b,c**: 250 pg, **d,e**: 2.5 pg. In **b–e**, the analyses of both Pre-OPIOM and OPIOM have been performed along three lines: one crosses the middle of the blot (displayed in red) whereas the two others (shown in green and blue) are located out of it (see also Fig. S2.6).

Fluorescence imaging under sunlight conditions

Fluorescence is used to image not only cells, but also increasingly whole living organisms like plants[170] and animals.[174] For the latter observations, ambient light is always interfering and it correspondingly degrades the contrast and the sensitivity of the images acquired. In particular, although fluorescence imaging techniques against adverse lighting conditions such as room light or shaded sunlight have been proposed,[60] fluorescent detection under strong direct sunlight in outdoor conditions has not yet been reported.

Unlike cells or animal tissues which are transparent or semi-transparent, plant leaves reflect around 5% to 20% of the sunlight in the visible wavelength range,[175] which makes them especially difficult to image with fluorescence macroscopy; in particular, 15–20 % of the incident light is reflected around 525 nm, making it even harder to shade the reflected sunlight, even with a narrow band pass filter designed for green fluorescence. To evidence the relevance of our setup for accurate fluorescent imaging of plants under direct sunlight, we imaged Dronpa-2-expressing *Camelina sativa* leaves using wild type plants as control. To be even more quantitative, we used a LED to simulate the interference of the sunlight in the wavelength range of the emitted RSFP fluorescence collected by our macroscope. Fig. 2.6 displays the images of leaves recorded in the dark and under artificial sunlight conditions matching the optical power actually sent to the sample under real sunlight. In the dark (Fig. 2.6a-d), both wild type and Dronpa-2-expressing leaves are clearly seen in the Pre-OPIOM images, which underlines the significant autofluorescence emission of the sample; in contrast, Speed OPIOM provides a non-vanishing signal

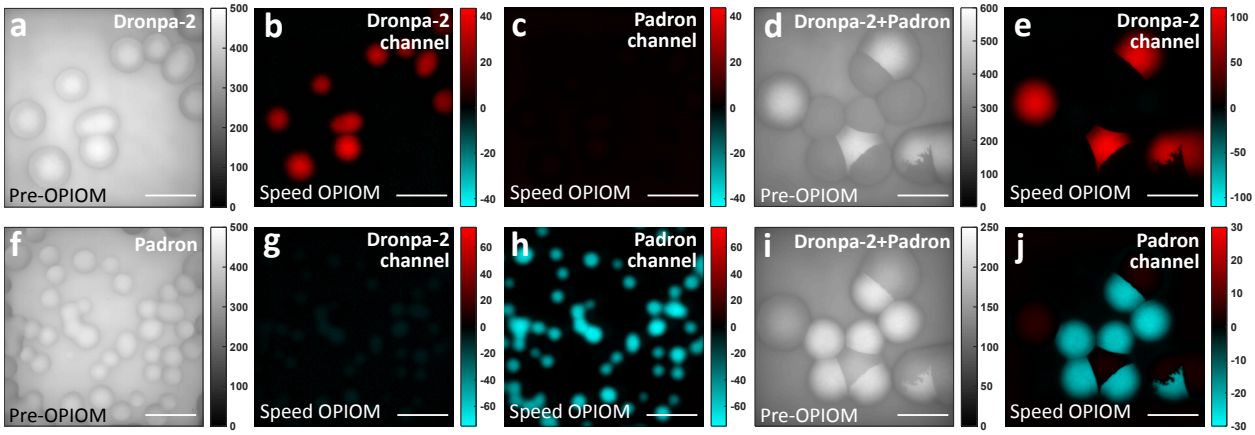

Figure 2.5 – Pre-OPIOM (**a**,**d**,**f**,**i**) and Speed OPIOM (**b**,**c**,**e**,**g**,**h**,**j**) images of *E. Coli* bacteria growing on agar plates and expressing Dronpa-2 (**a–c**), Padron (**f–h**) or a co-culture of *E. Coli* bacteria expressing Dronpa-2 or Padron respectively (**d,e,i,j**). The images have been recorded at resonance of Dronpa-2 (**a**,**b**,**d–g**) and Padron (**c**,**h**,**i**,**j**). The conditions of image acquisition are given in Table S2.1. *Scale bars*: 1 mm.

only for the leaf of the Dronpa-2-expressing plant. When the leaves are exposed to artificial sunlight (Fig. 2.6e-h), the Pre-OPIOM signal of both wild type and Dronpa-2 expressing leaves is about 20 times stronger than in the dark where autofluorescence is ubiquitously detected (Fig. 2.6a,c): sunlight reflection on the leaf epiderm dominates any fluorescence signal. In contrast, the OPIOM images (Fig. 2.6f,h) retain the Dronpa-2 signal of the Dronpa-2-expressing leaf measured in the darkroom. Hence our macroscope provides accurate information on the fluorescence signal of the Dronpa-2 label without any interference from ambient light even at high intensity.

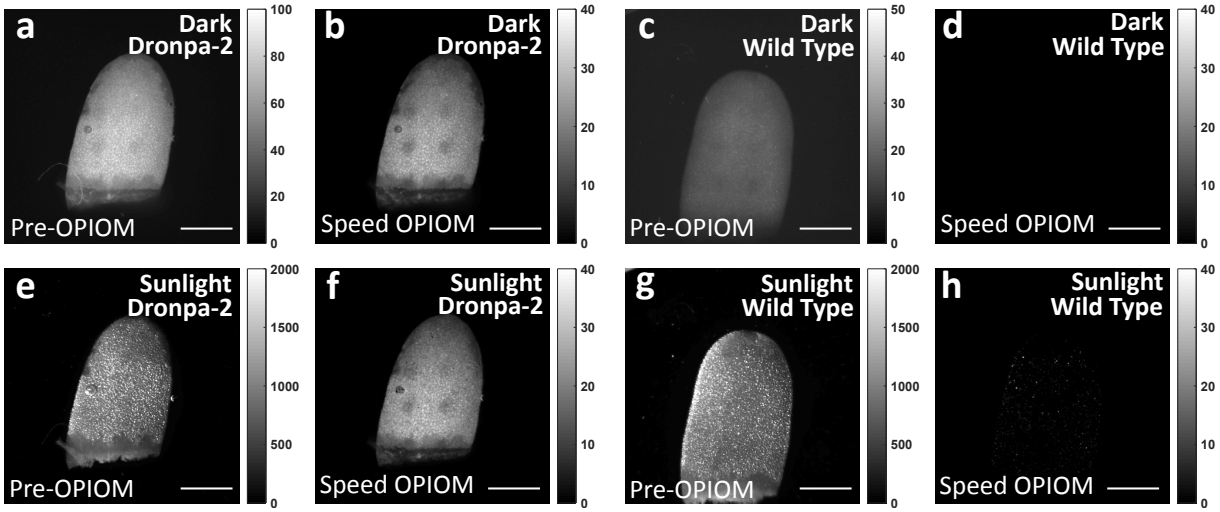

Figure 2.6 – Pre-OPIOM (**a**, **c**, **e**, **g**) and Speed OPIOM (**b**, **d**, **f**, **h**) imaging of Dronpa-2-expressing (**a**, **b**, **e**, **f**) and wild type (**c**, **d**, **g**, **h**) *Camelina sativa* in the darkroom (**a–d**) and under artificial sunlight (**e–h**) conditions. The conditions of image acquisition are given in Table S2.1. *Scale bars*: 1 mm.

2.1.3 Discussion

The preceding series of experiments has demonstrated the relevance of the Speed OPIOM protocol implemented in our simple optical setup to overcome the limitations of spectrally interfering (auto)fluorescence and ambient light for fluorescence macroscale imaging. The following paragraphs recapitulate its scope and limitations with respect to the fluorescent labels to be used and the maximal achievable contrast against spectral interferences.

In the present account, we relied on RSFPs for the experimental validations. In fact numerous categories of fluorophores exhibit a photochemical behavior which can be exploited by our setup broadening the application of the OPIOM protocols. Hence numerous molecular backbones exhibit reversible photoswitching when they are exposed to light.[122,160,176] When the backward isomerization following forward photoswitching is thermally-driven, one can use the original OPIOM protocol exploiting resonant modulation of monochromatic light to eliminate spectral interferences.[140] Alternatively, when the forward and backward photoswitching processes are photochemically governed at two distinct wavelengths as in many reversibly photoswitchable labels (e.g. reversibly photoswitchable fluorescent proteins – RSFPs,[123,159] azobenzenes,[177–179] cyanines,[121,132,180] diarylethenes,[158,181] and spirobenzopyrans[182]), one should preferentially rely on the Speed OPIOM protocol used in this study since it gives rise an amplitude twice that of the collected signal and accordingly a better signal-to-noise ratio. It is eventually important to recognize that our approach can also be applied to non-photoswitching fluorophores, provided that their photophysical scheme can be dynamically reduced to a two-state model at a long enough time scale. In particular, we have already shown that OPIOM can be adapted to three-state models involving a reaction in the excited state (e.g. intersystem crossing).[140]

OPIOM application requires the tuning of the control parameters of illumination (angular frequency of light modulation and average photon flux per unit of surface at the sample) in order to match the resonance conditions of the targeted fluorophore. Whereas in OPIOM the resonant angular frequency only depends on the rate constant for thermal relaxation after photoswitching,[140] it can be tuned with more flexibility in the two-color Speed OPIOM approach: one can increase it by increasing the mean intensities of both light sources provided that their ratio remains constant. The nature of the light sources to be used accordingly depends on the time scale at which the scheme for reversible fluorophore photoactivation can be reliably reduced to a two-state model and on the sample distance: both shorter time scale and larger distance necessitate higher light powers. Since the relevant reversibly photoswitchable fluorescent labels[121–123,158–160] exhibit photoswitching relaxation times in the μs–s range, easily modulatable LEDs could be most often used as excitation light sources to meet the resonance conditions in fluorescence macroscopy at 0.1–1 m imaging distance; modulatable lasers should have to be used at longer imaging distances. In principle, it is then advantageous to adopt the highest possible value of the angular frequency of light modulation (and correspondingly the light sources with the highest possible intensity) in order to shorten the measurement (which must last at least two periods of light modulation) and avoid noise (which is generally more abundant at low frequency). With delivered irradiance over 1000 mW/cm^2 at both 405 and 480 nm wavelengths which largely exceeds the maximum solar radiation ($\approx$ 10 mW/cm^2 for 40 nm bandwidth at both excitation wavelengths), our optical design can drive and image the photoswitching of Dronpa-2 at Speed OPIOM resonance up to 3 Hz with full amplitude modulation. One may note

that the photoswitching features of Dronpa-2 enable its Speed OPIOM imaging up to 50 Hz modulation frequency[143] by focusing light emitted from the LEDs over a smaller area or using more powerful light sources such as lasers.

Elimination of autofluorescence and ambient light in our setup intrinsically suffers from two limitations. Our first limitation arises from the limited precision on phase retrieval when extracting the out-of-phase component of the fluorescence modulation. We generally rely on preliminary calibrations to retrieve the phase information by analyzing the response of the attenuated light source or of a fast responding fluorophore (e.g. fluorescein). Alternatively one could tune the phase lag for signal detection in order to eliminate the contribution of autofluorescence or ambient light under the experimental conditions. Any error on phase retrieval will introduce a contribution from the in-phase component of the fluorescence modulation, which contains the interfering contribution of autofluorescence and ambient light. With a present precision in the 3 10^{-3} rad range, we could typically enhance the contrast of the targeted fluorophore against the spectrally interfering signal by a factor 10^2-10^3. A second limitation originates from the enhanced and intrinsic noise of the detector. Indeed any strong signal from the spectrally interfering species will generate a photon noise interfering with the extraction of the OPIOM signal. For instance, the minimal OPIOM signal detectable against ambient light scales as the square root of the photon flux of the latter,[143] which typically enables one to specifically detect the OPIOM signal even in the presence of a 10^3 times stronger non-modulated photon source.

Finally, we may underline the limited cost (less than 10 k€, see Supporting electronic material) of our prototype, which only includes standard optical equipment and a camera for industrial vision. This cost could be even optimized by using the reflecting properties of the bandpass filters and a special arrangement of LED chips would also make possible to combine the lights from the colored LEDs with a single dichroic mirror for short range imaging (0.1 - 1 m). For Speed OPIOM imaging at longer distances, modulatable lasers (roughly 6 k€ per color) should have to be used. Eventually, with rapidly evolving performances (lower dark and read noises, higher quantum yield, higher saturation capacities), the next generation of CMOS sensor integrated in such cameras (including backside illumination configuration) should allow to reach even better performance in terms of signal-to-noise ratio and dynamic range.

To conclude, this study has demonstrated the relevance of a simple and cheap fluorescence macroscope to overcome the detrimental limitations of autofluorescence and strong ambient light for macro-imaging. Beyond the preceding achievement, this setup combined with a powerful reference-free dynamic contrast protocol considerably enhances sensitivity and signal-to-noise ratio for fluorescence detection. Compatible with a large collection of fluorophores, it also gives access to further opportunities for multiplexed fluorescence observations by overcoming the limitations encountered with spectral discrimination. Thus this macroscope is expected to find multiple applications in areas as diverse as quantitative bioanalysis and diagnostics (multiplexed Western blots, ELISAs, cytometry...), bioassays, microorganism selection, plant research, or environmental monitoring.

2.1.4 Materials and Methods

Setup for macro fluorescent imaging

Excitation system Our setup uses three high power color LED chips (LXZ1-PB01, LHUV-0400, LXZ1-PX01; Lumileds, NL) as excitation lights for the green (such as the RSFPs used in this work) and red (such as DsRed, subsequently used in an applicative development[171]) fluorescent emitters. The sources are respectively collimated by high NA condensers (ACL25416U-A, f=16 mm, Thorlabs, NJ, US) and filtered by band pass filters (ET470/40X, ET402/15X, ET550/15x; Chroma, VT, US) to avoid spectral overlaps. The three quasi-parallel beams are combined by three dichroic mirrors (T425LPXR, T505LPXR, 59004bs; Chroma, VT, US). An optimized beam expander system integrating one divergent lens (ACN254-040-A, f = -40 mm, Thorlabs, NJ, US) and two convergent lenses (AC508-100-A, f = 100 mm, Thorlabs, NJ, US) is used to clearly refocus the lights at a distance of 120 mm away onto the sample (see Supplementary electronic material).

Imaging system To obtain the fluorescence image of the illuminated area, the fluorescent light emitted from the sample is collected by the expander system and imaged to infinity. Band-pass filter (ET525/36m or ET585/20m, Chroma, VT, US) is used for green emission or red emission. Light is then focused onto the camera (iDS 3060cp) to get the image of the fluorescent sample. As the detectable sample is the same size of the illumination area (4×4 mm^2), an extra lens system is designed for macroimaging of small size objects, which requires high resolution and well-corrected chromatic aberration from red to green, a spectral range that cannot be corrected by regular lens or even achromatic lens. The elaborated achromatic system (see Fig. 2.2), with an effective focal length of f = 30 mm is composed of three spherical singlet lenses (LC2679-A, LB1757-A, LA1422-A, Thorlabs, NJ, US) and the air spaces are optimized (see Supplementary electronic material).

Video acquisition In the imaging experiments, we record films for m periods of light modulation (m is an integer). The acquisition frequency of the camera is set so as to obtain $2N$(N is an integer) frames per period of modulation. Thus the acquisition frequency is $f_s = 2Nf_m$, where f_m is the modulation frequency of the excitation light. The fluorescence emission acquired at pixel(x,y) of the k^{th} frame is equal to

$$I_{\text{F}}(x,y,k) = T_s\left\{\Im_{\text{F}}^{0}(x,y) + \sum_{n=1}^{N}\left\{\Im_{\text{F}}^{n,\sin}(x,y)\sin\left[\frac{\pi n f_s}{N}\left(\frac{k}{f_s}+\phi_{\text{acq}}\right)\right] + \Im_{\text{F}}^{n,\cos}(x,y)\cos\left[\frac{\pi n f_s}{N}\left(\frac{k}{f_s}+\phi_{\text{acq}}\right)\right]\right\}\right\} \quad (2.1)$$

where $T_s = \frac{1}{f_s}$ refers to the exposure time of one frame, $\Im_{\text{F}}^{n,\sin}(x,y)$ and $\Im_{\text{F}}^{n,\cos}(x,y)$ are respectively the sinus and cosinus components of the fluorescence signal at harmonic n around the average value $\Im_{\text{F}}^{0}(x,y)$, and ϕ_{acq} is a time lag which may originate from distinct starting times for the light modulation and the acquisition of the camera.

Pre-processing has been performed over the video to compensate for possible photobleaching of the fluorophores. By assuming the photobleaching to exhibit a linear decay, the compensation factor has been calculated from the average of two successive periods:

$$K(x,y) = \frac{\langle I_{\text{F}}(x,y,k)\rangle_{k=2N}^{4N-1} - \langle I_{\text{F}}(x,y,k)\rangle_{k=0}^{2N-1}}{2N} \quad (2.2)$$

Then all the frames over the two periods are corrected as in Eq.(2.3)

$$I_{\mathrm{F}}^{\mathrm{corr}}(x, y, k) = I_{\mathrm{F}}(x, y, k) - K(x, y) \times k \tag{2.3}$$

All the frames over the whole video have been corrected for photobleaching by applying the same algorithm for all the successive pairs of two periods.

ϕ_{acq} can be easily calibrated by using the fluorescence emission from instantaneously responding fluorophores (such as EGFP or Fluorescein). The Pre-OPIOM image is calculated by averaging the frames over the whole film and normalizing to unit time to yield $\Im_{\mathrm{F}}(x, y)$

$$\Im_{\mathrm{F}}^{0}(x, y) = \frac{f_s}{2mN} \sum_{k=0}^{2\mathrm{mN}-1} I_{\mathrm{F}}^{\mathrm{corr}}(x, y, k) \tag{2.4}$$

The demodulation is done by multiplying the k^{th} frame $I_{\mathrm{F}}^{corr}(x, y, k)$ with $\cos\left[\frac{\pi n f_s}{N}\left(\frac{k}{f_s} + \phi_{\mathrm{acq}}\right)\right]$ and by averaging over the whole film to get the first order cosinus component, namely the Speed OPIOM image:

$$\Im_{\mathrm{F}}^{1,\cos} = \frac{f_s}{mN} \sum_{k=0}^{2\mathrm{mN}-1} \left\{ I_{\mathrm{F}}^{\mathrm{corr}}(x, y, k) \times \cos\left[\frac{\pi n f_s}{N}\left(\frac{k}{f_s} + \phi_{\mathrm{acq}}\right)\right]\right\} \tag{2.5}$$

Calibration of light intensity Speed OPIOM implementation requires to determine the intensity of the two excitation lights at the sample (typically at 480 and 405 nm) so as to fulfill the resonant illumination conditions for the desired reversibly photoswitchable fluorescent proteins. Instead of using a powermeter which is not accurate enough for our intensity measurement, we prefered to directly exploit the dynamical photochemical properties of the RSFPs. The principle of the calibration experiments is to measure the relaxation time associated to the conversion between the ON and OFF RSFPs states by applying light jumps on a RSFP-containing sample. We typically used a thin layer of RSFP solution spread on the coverslip as the calibrating sample. In the first step, the sample was submitted to a light jump at 480 nm with constant light intensity I_1^0, in which the current of the LED source was set around 500 mA to give the maximal power. Upon illumination, the RSFP switched from its thermodynamically stable state (denoted **1**) to its photoisomerized state (denoted **2**), and the fluorescence image was recorded as a function of time. The fluorescent signal (usually obtained by averaging over the image) was then plotted as a function of time (Fig. S2.7a, S2.8a) and was fitted with Eq.(2.6):

$$I_{\mathrm{F}}(t) = I_{\mathrm{F}}(0, \lambda_1) + \mathcal{A}_{\lambda_1}\left[1 - \exp\left(-\frac{t}{\tau_{\lambda_1}}\right)\right] \tag{2.6}$$

where $\mathcal{A}_{\lambda_1}$ is a pre-exponential term which accounts for the molecular brightnesses of the ON and OFF states as well as their relative proportions (see[143]). τ_{λ_1} was extracted from the fit and I_1^0 could be then retrieved from Eq.(2.7):

$$\frac{1}{\tau_{\lambda_1}} = k_{21}^{\Delta} + (\sigma_{12,\lambda_1} + \sigma_{21,\lambda_1})I_1^0 \tag{2.7}$$

where σ_{12,λ_1} and σ_{21,λ_1} are respectively the molecular action cross-sections for photoisomerization which converts **1** to **2** and **2** to **1** (see[143]). In the second step, while I_1^0 was still maintained at its original value, the sample was subsequently submitted to a light jump at 405 nm at constant light intensity I_2^0. A

reversed switch took place, the temporal evolution of the fluorescence emission was again recorded (Fig. S2.7b,S2.8b) and fitted with Eq.(2.9):

$$I_F(t) = I_F(0, \lambda_1, \lambda_2) + \mathcal{A}_{\lambda_1\lambda_2}\left[1 - \exp\left(-\frac{t}{\tau_{\lambda_1\lambda_2}}\right)\right] \tag{2.8}$$

where $\mathcal{A}_{\lambda_1\lambda_2}$ is a pre-exponential term which accounts for the molecular brightnesses of the ON and OFF states as well as their relative proportions (see[143]). $\tau_{\lambda_1\lambda_2}$ was extracted from the fit and I_2^0 could be then retrieved from Eq.(2.9):

$$\frac{1}{\tau_{\lambda_1\lambda_2}} = k_{21}^{\Delta} + (\sigma_{12,\lambda_1} + \sigma_{21,\lambda_1})I_1^0 + (\sigma_{12,\lambda_2} + \sigma_{21,\lambda_2})I_2^0 \tag{2.9}$$

where $\sigma_{12,\lambda_1} + \sigma_{21,\lambda_1}$ and $\sigma_{12,\lambda_2} + \sigma_{21,\lambda_2}$ are respectively the molecular action cross-sections for photoisomerization at wavelength λ_1 or λ_2 which converts **1** to **2** and **2** to **1**. After repeating this experiment for several values of I_1^0 and I_2^0, we could use the reported values of $\sigma_{12,\lambda_1} + \sigma_{21,\lambda_1} = 196$ m^{2}mol^{-1} and $\sigma_{12,\lambda_2} + \sigma_{21,\lambda_2} = 413$ m^{2}mol^{-1} for Dronpa-2,[143] to finalize the calibration linking the current intensities applied to the LEDs with I_1^0 and I_2^0.

Speed OPIOM macroimaging

Blot samples

Image recording The Dronpa-2-blotted membrane was placed on a cover slip and put on the focal plan under the macro-imaging device. The measurement was done at 24°C while the blotted area was still wet. The LED lights at 480 ($I_1^0 = 4 \times 10^{-2}$ ein.m^{-2}.s^{-1}) and 405 ($I_2^0 = 1.9 \times 10^{-2}$ ein.m^{-2}.s^{-1}) nm synchronized in antiphase and sinusoidally modulated at 2.5 Hz were applied to irradiate the membrane and a series of fluorescence images of the membrane was simultaneously captured by the CCD camera with a sampling rate of $f_s = 50$ Hz. For each measurement in this series of experiments, the excitation lights were modulated for 8 cycles leading to capture 160 images in less than 4 s. For each Dronpa-2 concentration, 3 samples have been independently measured to evaluate the reliability of the results.

Estimation of signal-to-noise ratios The Pre-OPIOM and OPIOM images have been first averaged over 5×5 pixel^2. Then we computed the mean and standard deviation values for each pixel. We subsequently chose three lines in the pixelized Pre-OPIOM and OPIOM images (indicated by the colored lines in Fig. 2.4 and Fig. S2.6): a first line crossing the area where Dronpa-2 was deposited and two additional lines departing from the deposition area and where the fluorescence background was at the most homogeneous. The maximum value S_{D2} in the blot area of Dronpa-2 was obtained from the first profile line. Mean value $\langle bg \rangle$ and standard deviation σ_{bg} along the two other profile lines were calculated to estimate the background contributions. The signal-to-noise ratios were estimated as: SNR=$(S_{D2} - \langle bg \rangle)/\sigma_{bg}$ using the data from both profile lines taken in the membrane zone. We eventually retained the lowest calculated value as SNR (See Fig. S2.6).

***E.coli* bacteria on solid growth medium** The agar plates on which the bacteria grew were placed on the focal plan under the macro-imaging setup. The bacteria samples (colonies of bacteria labeled either with Dronpa-2 or with Padron, or coexisting colonies from both later strains) were successively imaged under two different illumination conditions associated to the respective resonance of Dronpa-2 and Padron. For Dronpa-2 imaging, we adopted a sampling rate of f_s = 50 Hz with a light modulation at 5 Hz for 8 periods. For Padron imaging, we used a light modulation at 0.02 Hz for 2 periods at a sampling rate of f_s = 4 Hz. Imaging has been performed in the dark room at 24°C.

Plant leaves The leaves of *Camelina sativa* were placed on a cover slip immersed with water. Light from a LED with a green emission centered at 530 nm (LXZ1-PM01, lumileds, NL) was collimated and delivered to the sample in order to simulate the interference of the sunlight in the wavelength range analyzed with our macroscope. To match the optical power actually sent to the sample with the real sunlight power, a photo-diode power meter (PM100A, Thorlabs, DE) has been used to measure the sunlight and the intensity of the LED on the sample. Since the recorded green fluorescent emission is detected after band pass filtering (ET525/36m Chroma, USA) in our setup, we applied the same filter to record the irradiance of the direct sunlight in the same green waveband (525 ± 18 nm). We measured 10 mW/cm^2 (λ = 525 nm, $\Delta\lambda$ = 36 nm). We correspondingly adjusted the power of the green LED to deliver the same power in our experiments. The images of the leaves have been recorded under both darkroom and artificial sunlight conditions at a sampling rate of f_s = 200 Hz by modulating the excitation lights at 2.5 Hz for 8 periods.

2.1.5 Acknowledgement

The authors thank S. Jakobs for providing the Dronpa-2 cDNA. This work was supported by the ANR (France BioImaging - ANR-10-INBS-04, Morphoscope2 - ANR-11-EQPX-0029), the SATT Lutech (OPIOM), the Fondation de la Recherche Médicale (FRM), the LabEx Saclay Plant Sciences-SPS (ANR-10-LABX-0040-SPS) from the "Investments for the Future" program (ANR-11-IDEX-0003-02), the Mission Interdisciplinarité du CNRS, and the Domaine d'Intérêt Majeur Analytics de la Région Ile de France (DREAM).

2.1.6 Conflicts of interests

The authors declare no competing interests.

2.1.7 Contributions

L. J. and T. L. S. supervised the project. L. J., T. L. S., and R. Z. wrote the manuscript. M. A. P, Z. K., L. G., A. G. T., A. G., and J. - D. F. designed and prepared the biological samples. R. Z., R. C., A. E., V. C., T. L. S., and L. J. designed and performed the experiments, and analyzed the results.

Electronic supplementary material

Additional Materials (Reversibly photoswitchable fluorescent proteins, Plasmids, Protein production and purification, Preparation of the Dronpa-2 solutions at different concentrations, Blot samples, Mixed bacterial culture, Plant transformation and growth, Optical design of the Speed OPIOM macroscope), Figures (Validations of the chromatic correction, Dependence of the Pre-OPIOM and OPIOM images, of the signal profiles, and the associated signal-to-noise ratios of the nitrocellulose membrane on the Dronpa-2 amount, Calibration of light intensities), and Table (Parameters for Speed OPIOM macroimaging, Parameters for simulations of optical designs) are provided as Electronic Supplementary material.

2.2 Supporting information

2.2.1 Additional Methods

Materials

Reversibly photoswitchable fluorescent proteins The RSFPs used in this study are Dronpa-2[141,172] and Padron,[173] which belong to the Dronpa[183] family. Dronpa-2 contains only one mutation M159T and Padron contains eight mutations: T59M, V60A, N94I, P141L, G155S, V157G, M159Y and F190S.

Plasmids The plasmids for bacterial expression of Dronpa-2, Padron and EGFP, and the plants (*Camelina* and *Arabidopsis*) expression vector expressing p35S::Dronpa-2; pCVMV::DsRED construct have been previously described.[143]

Protein production and purification The plasmid expressing Dronpa-2 carrying an N-terminal hexahistidine tag was transformed in *E. coli* DH10B strain. Cells were grown in Terrific Broth (TB). Expression was induced by addition of isopropyl β-D-1-thiogalactopyranoside (IPTG) to a final concentration of 1 mM at OD(600 nm)=0.6. Cells were harvested after 16 h of expression and lysed by sonication in Lysis buffer (30/40 mM imidazole, 50 mM Tris/HCl at pH 7.5, 400 μM 1-(2-Aminoethyl) benzenesulfonyl fluoride hydrochloride, 5 mg/mL DNAse, 5 mM $MgCl_2$ and 1 mM dithiothreitol). Insoluble materials were removed by centrifugation and the soluble protein extract was batch-absorbed onto Ni-NTA agarose resin (Thermofisher). The protein loaded Ni-NTA column was washed with 20 column volumes of 50 mM TRIS/HCl pH 7.5, 20 mM imidazole, 150 mM NaCl. Bound protein was eluted in 50 mM TRIS/HCl pH 7.5, 500 mM imidazole, 150 mM NaCl. Protein fractions were dialyzed on cassette Slide-A-Lyzer Dialysis Cassettes (Thermofisher) against 50 mM TRIS/H_2SO_4 pH 8.0.

Preparation of the Dronpa-2 solutions at different concentrations The actual concentration of the purified Dronpa-2 stock solution was determined with a spectrophotometer (Agilent Technologies, Santa Clara, CA). Its UV-Vis absorption spectrum was recorded from 400 to 600 nm in a 55 μL quartz cuvette with 1.5 mm light path (Hellma Optics, Jena, Germany). The absorbance (0.16) at 480 nm yielded 29 μM concentration using $\varepsilon(480)$=37000 $M^{-1}\cdot cm^{-1}$ (evaluated after recording the absorbance at 447 nm of a denaturated Dronpa-2 solution in 1 M NaOH by using 44000 $M^{-1}\cdot cm^{-1}$ for the molar absorption coefficient of the deprotonated chromophore[184]). The Dronpa-2 stock solution was diluted with a BSA buffer (50 mM phosphate, 150 mM NaCl, 0.1 mM BSA, pH=7.4 measured with a Standard pH meter PHM210, equipped with a Radiometer Analytical PHC3359-8 combination pH electrode (Hach, Loveland, CO)) to generate a series of Dronpa-2 solutions at concentrations 20, 10, 5, 2, 1, 0.5, 0.2, 0.1, 0.05, and 0.02 nM.

Blot samples 1 μL aliquots of Dronpa-2 solutions in 0.1 mM BSA (Bovine Serum Albumin)–50 mM pH=7.4 PBS buffer at concentrations ranging from 20 to 0.02 nM were deposited on a nitrocellulose membrane (0.2 μm pore-size, 7× 8.5 cm; Bio-Rad, Hercules, CA, USA) by slightly pressing the micropipette tip onto the membrane. As the nitrocellulose membrane is hydrophilic, the Dronpa-2 solution

permeates the membrane within a few seconds leading to the formation of a spot delimited by the tip area (diameter=0.4 mm).

Mixed bacterial culture Dronpa-2 and Padron were expressed in *E. coli* DH10B strain. Cells were grown into 2 mL of lysogeny broth (LB) at 37°C, 220 RPM for 1 h. Cells were platted at low density on LB agar plates, and plates were incubated overnight at 37°C. Dronpa-2 and Padron single colonies were then separately transfered to LB-ampicillin media and incubated at 37°C, 220 RPM for 4 h. The pre-cultures were diluted to reach OD(600 nm)=0.6, then mixed at the same concentrations, and were finally plated onto LB agar and incubated at 37°C.

Plant transformation and growth *Arabidopsis thaliana* and *Camelina sattiva*(cv Celine) were transformed with *Arabidopsis* floral-dip method and transgenic were selected as described previously.[185] *Arabidopsis* and *Camelina* seeds were sown respectively on sucrose-supplemented medium[186] or water-soaked paper and grown for 7 days in a growth chamber under cycles of 16 h light / 8 h dark at 22°C.

Optical design of the Speed OPIOM macroscope

Illumination system The illumination system aims at increasing the distance between the last optical surface of our device and the sample without significant loss of light intensities delivered to the sample. The optical layout of the illumination system is shown in Fig.S2.1. Our design integrates one divergent doublet (ACN254-040-A, f = -40 mm, Thorlabs, NJ, US) and two convergent doublets (AC508-100-A, f = 100 mm, Thorlabs, NJ, US), which were chosen to minimize the spherical aberration at both 405 and 480 nm wavelengths and maximize the numerical aperture of the illumination system. The air spaces between the three elements (which define the size of the illuminated zone and the numerical aperture of the optical system) were optimized with the OSLO software (Lambda Research Corporation, Littleton, MA). Our final optical design allowed us to focus light emitted from the LEDs to a small area of 4×4 mm^2 at 120 mm away from the last optical surface, with powerful intensity (NA = 0.19) and excellent uniformity.

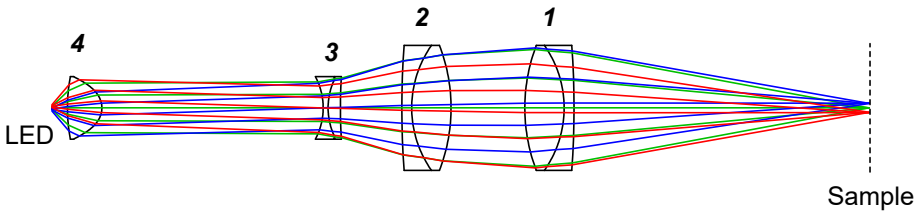

Figure S2.1 – Optical layout of the illumination system. Optical elements denoted from ***1*** to ***4*** are given in Supplementary Table S2.2.

Imaging system The macroscope aims at observing fluorescence emission from a small area within 4×4 mm^2 with both green (525 nm) and red (585 nm) channels. Before being imaged by the objective, the fluorescence emission is first collected by the beam-expanding system used for excitation, through which optical aberrations (especially the chromatic one) are introduced. Our objective consists of three lenses with different glass materials (BK7, SF11) to correct for chromatic aberration. The shape of each lens minimizing the spherical aberration at large NA and off-axis aberrations up to 2 mm from the optical axis was optimized using the OSLO software. Commercial lenses shapes and focal lengths at the closest to the optimized elements were chosen and the air space between each element was optimized to yield the final design (Fig. S2.2), which surpasses the imaging performances of singlet or achromatic doublet lenses (Fig. S2.3 and Fig. S2.4) for generating high quality images (Fig. S2.5).

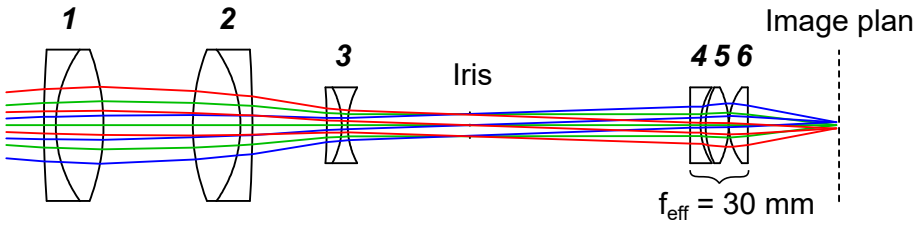

Figure S2.2 – Optical layout of the imaging system. The final objective has an effective focal length of 30 mm, giving a magnification of 0.5× with a maximal usable aperture of F/4.0 (NA=0.125). The optical elements denoted from ***1*** to ***6*** are given in Supplementary Table S2.3.

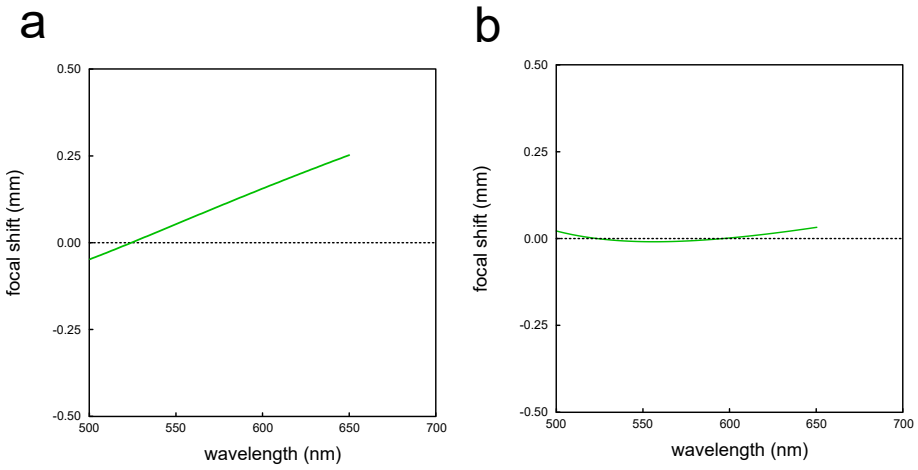

Figure S2.3 – Simulated chromatic aberrations of the imaging system with an imaging objective composed of an achromatic doublet lens (f = 30 mm; **a**) or our designed lens system (**b**). Our optical design lowers by a factor ten the chromatic aberration.

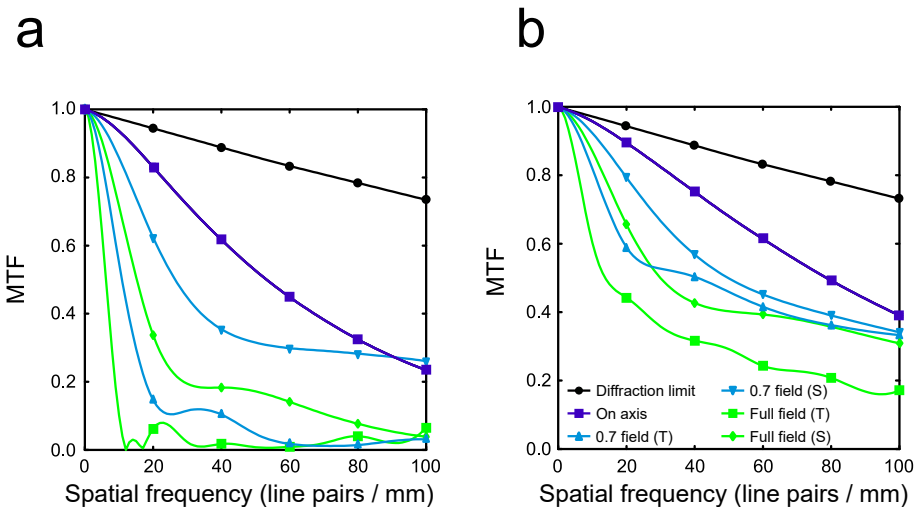

Figure S2.4 – Modulation transfer function (MTF) in image space computed with an imaging objective composed of an achromatic doublet lens (f = 30 mm; **a**) or our designed lens system (**b**). Our optical design improves the overall resolution of the imaging system.

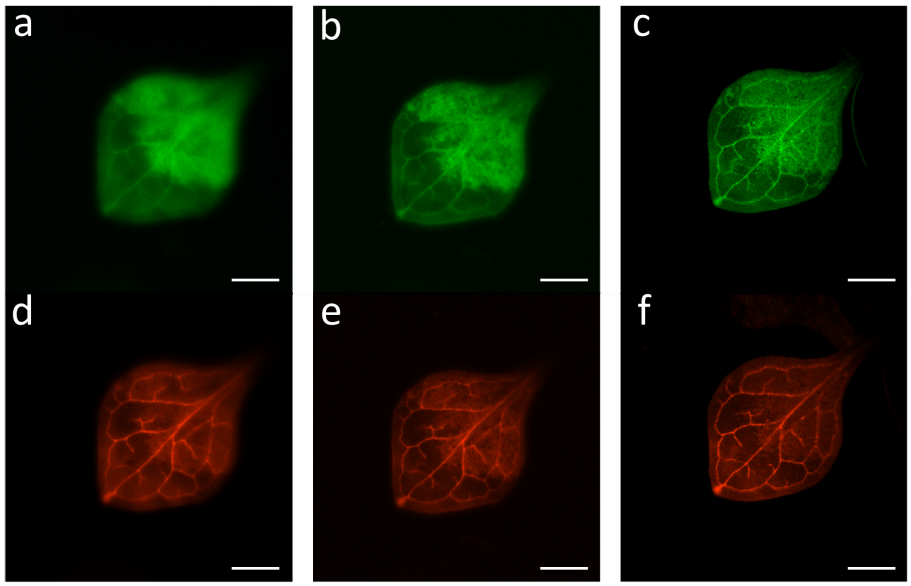

Figure S2.5 – Quality of images of *Arabidopsis Thaliana* leaves observed in the red and green channels. **a,d**: Singlet lens; **b,e**: Achromatic lens (doublets); **c,f**: Designed lens system. Images taken with green filter ET525/36m and red filter ET585/20m, aperture F/4.0, focusing in the red channel. The system succeeds to improve the sharpness for both channels and corrected the defocus in the green channel. *Scale bars*: 1 mm.

Estimated cost of the Speed OPIOM macroscope We currently estimate the cost of our imaging macroscope in the lower 10 k€ range as follows: camera 0.8 k€ , optomechanical parts /filters 7 k€, electronics (Teensy 3.5, LEDs and printed circuits boards) 0.2 k€, computer 1 k€.

2.2.2 Supplementary Figures

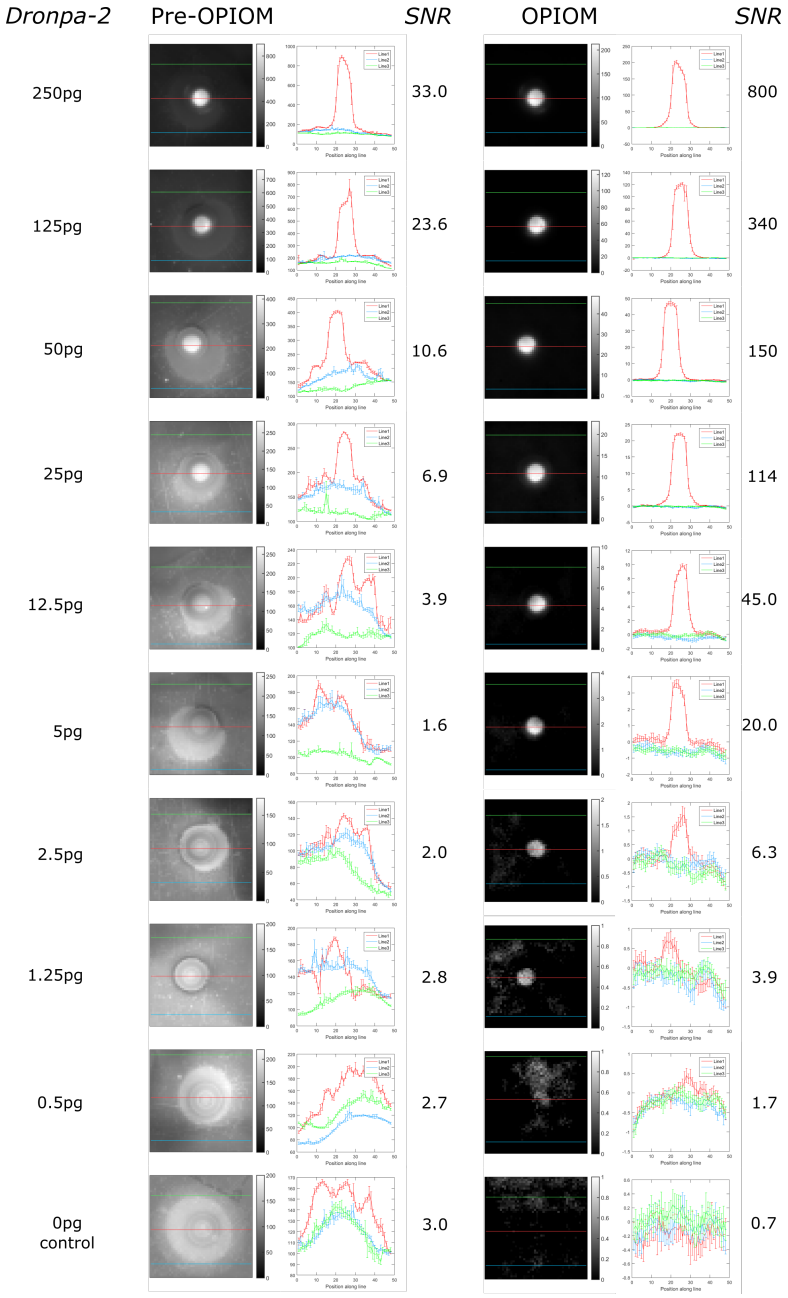

Figure S2.6 – Dependence of the Pre-OPIOM and OPIOM images, of the signal profiles, and the associated signal-to-noise ratios of the nitrocellulose membrane on the Dronpa-2 amount (in pg) deposited on a 400 μm-diameter blot. In the signal profiles, the error bar measures the standard deviation over three independent measurements. The analyses have been performed along three lines: one crosses the middle of the blot (displayed in red) whereas the two others (shown in green and blue) are located out of it. The images have been recorded at resonance for Dronpa-2 (see also Table S2.1). One should notice that at low concentrations, the signal-to-noise analysis of the Pre-OPIOM images is no longer reliable since the signal observed at the blotted area is lower than the observed standard deviation of the membrane signal and much similar to the Pre-OPIOM signal observed for the control.

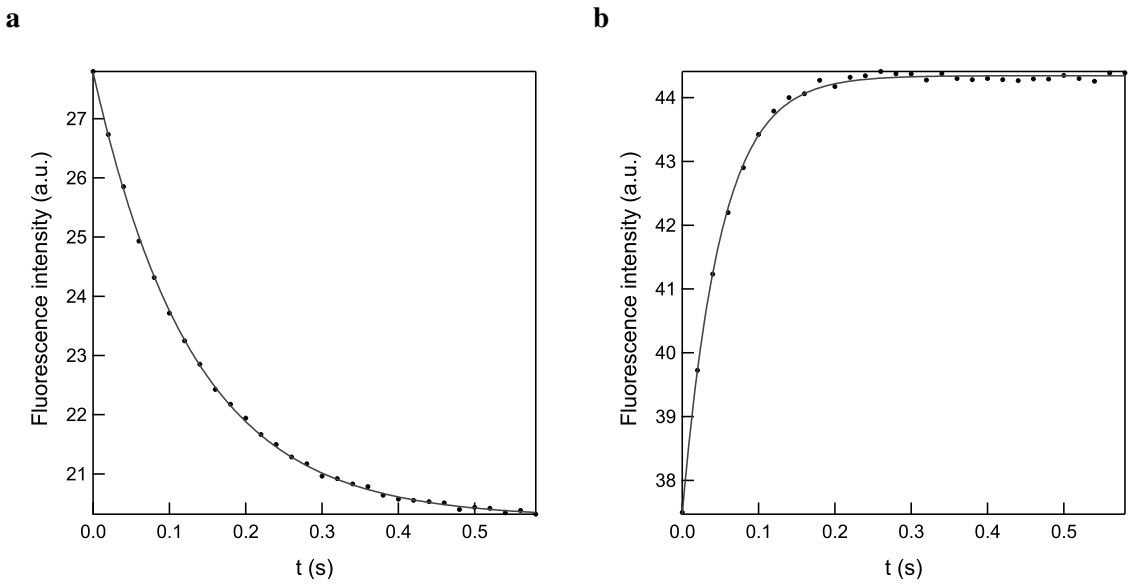

Figure S2.7 – Photoisomerization kinetics of Dronpa-2. **a**: Evolution of the fluorescence emission of Dronpa-2 upon illumination at 480 nm ($I_1^0 = 4 \times 10^{-2}$ Ein.m^{-2}s^{-1}); **b**: Evolution of the fluorescence emission of Dronpa-2 upon illumination at both 480 and 405 nm ($I_1^0 = 4 \times 10^{-2}$ Ein.m^{-2}s^{-1} and $I_2^0 = 1.9 \times 10^{-2}$ Ein.m^{-2}s^{-1}).

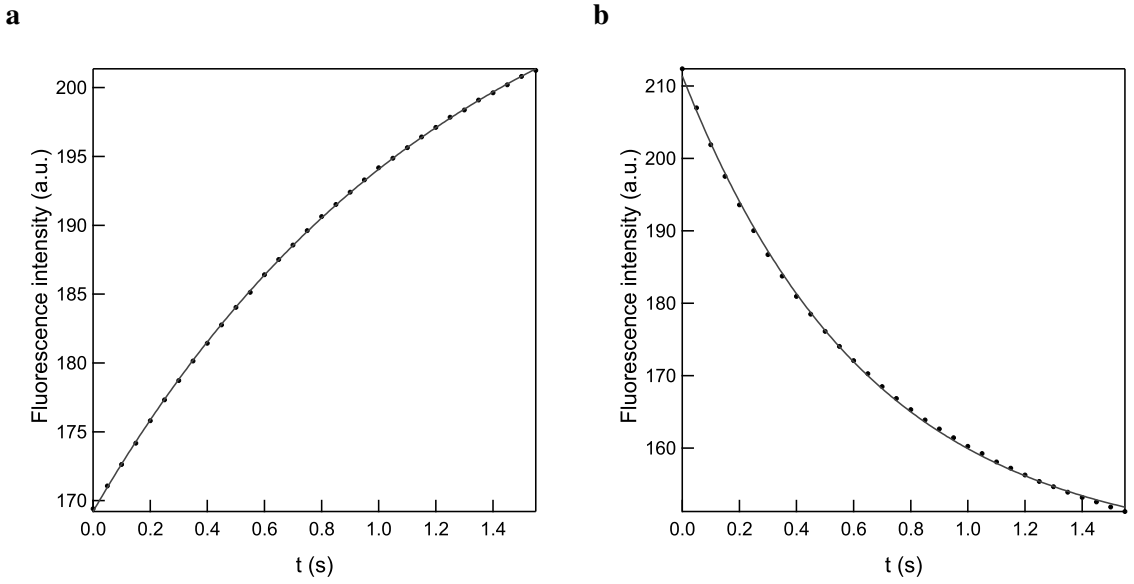

Figure S2.8 – Photoisomerization kinetics of Padron. **a**: Evolution of the fluorescence emission of Padron upon illumination at 480 nm ($I_1^0 = 1.75 \times 10^{-2}$ Ein.m^{-2}s^{-1}); **b**: Evolution of the fluorescence emission of Padron upon illumination at both 480 and 405 nm ($I_1^0 = 4.2 \times 10^{-2}$ Ein.m^{-2}s^{-1} and $I_2^0 = 6.5 \times 10^{-3}$ Ein.m^{-2}s^{-1}).

2.2.3 Supplementary Table

Figure	Aperture	Periods	f_s (Hz)	f_m (Hz)	$\lambda_{exc,1}$ nm	I_1^0 Ein.m^{-2}.s^{-1}	$\lambda_{exc,2}$ nm	I_2^0 Ein.m^{-2}.s^{-1}
2.3a-j	F/4.0	8	50	2.5	480	4×10^{-2}	405	1.9×10^{-2}
2.5a,b,d-g	F/5.6	8	50	5	480	4×10^{-2}	405	1.9×10^{-2}
2.5c,h-j	F/5.6	2	4	0.02	480	4.2×10^{-2}	405	6.5×10^{-3}
2.6a-h	F/5.6	8	200	2.5	480	4×10^{-2}	405	1.9×10^{-2}

Table S2.1 – Acquisition parameters used for Speed OPIOM imaging in Figures 2.3,2.5,2.6 of the Main Text, where f_s refers to the sampling rate and f_m refers to the modulation frequency of the excitation lights.

Surface	Optical element	Radius (mm)	Thickness (mm)	Aperture Radius (mm)	Material
Object	LED	–	6.973/6.787[a]	0.5	air
1	(***4***)	69.999	14	12.7	B270
2		-8.818 (aspheric[b])	90	12.7	air
3	(***3***)	-27.05	2.00	12.7	N-BAF10
4		27.05	5	12.7	N-SF11
5		189.23	25.0	12.7	air
6	(***2***)	363.10	4	25.4	SF10
7		44.17	16.00	25.4	N-BAF10
8		-71.12	30.00	25.4	air
9	(***1***)	71.12	16.00	25.4	N-BAF10
10		-44.17	4.00	25.4	SF10
11		-363.1	120	25.4	air
Image		–	0	2.13	

Table S2.2 – Optical surfaces introduced in simulation of the illumination system.

[a]The radius were set at 6.973 and 6.787 mm for LED emitting light at 405 and 480 nm respectively.

[b]Aspheric coefficient for the $Z(r) = r^2/(R(1+\sqrt{1-(1+k)\frac{r^2}{R^2}}) + A_4 r^4 + A_6 r^6 + A_8 r^8 + A_{10} r^{10}$ surface profile (sag) of the condenser: $R = 8.818$ $k = 0.9991715$, $A_4 = -8.6821674 \times 10^{-05}$, $A_6 = -6.3760123 \times 10^{-08}$, $A_8 = -2.4073084 \times 10^{-09}$ and $A_{10} = -1.7189021 \times 10^{-11}$, where r is the radial distance from the optical axis, R is the radius, k is the conic constant and A_4, A_6, A_8 and A_{10} are respectively the 4^{th}, 6^{th}, 8^{th} and 10^{th} order aspheric coefficients.

Surface	Optical element	Radius (mm)	Thickness (mm)	Aperture Radius (mm)	Material
Object	Sample	–	120.00	2	air
1	(***1***)	363.10	4	25.4	SF10
2		44.17	16.00	25.4	N-BAF10
3		-71.12	30.00	25.4	air
4	(***2***)	71.12	16.00	25.4	N-BAF10
5		-44.17	4.00	25.4	SF10
6		-363.10	25.00	25.4	air
7	(***3***)	-189.23	5.00	12.7	N-SF11
8		-27.05	2.00	12.7	N-SF11
9		27.05	41.00	12.7	air
10	Iris	–	74.00	3.79	air
11	(***4***)	–	3.50	12.7	N-SF11
12		23.4	1.648	12.7	air
13	(***5***)	29.50	7.70	12.7	N-BK7
14		-29.50	0.1	12.7	air
15	(***6***)	20.60	6.4	12.7	N-BK7
16		–	29.767	12.7	air
Image		–	0	1.02	

Table S2.3 – Optical surfaces introduced in simulation of the imaging system.

Chapter 3

Speed OPIOM for agronomical applications

3.1 Introduction

A major challenge in agriculture is to adapt the resources to the actual physiological state of the plant in a context of an ever changing environment. Electronic monitoring of plant environment (i.e. hygrometry, temperature, soil humidity,...) allows to obtain precise, rapid and quantitative parameters. However it does not provide any information on the actual physiological state of crops. Plant status is currently assessed visually, by monitoring biomass parameters, or by chemical analysis. Visual evaluation of plants is immediate but clearly not specific, not quantitative and very dependent on the evaluating expert. Biomass or biometric analysis of plants or organs is quantitative but it does not provide a specific answer to the nature of stress involved. Finally, metabolic, enzymatic or molecular analyses are sensitive and specific but they require extraction with time-consuming and/or costly procedures that involve manpower which hampers real time feedback in crop management. In fact, an immediate and quantitative evaluation of plant physiological state is still in demand to provide a rapid and appropriate management of crop culture.[187]

The use of fluorescence is here advantageous since it is not invasive, requires minimal handling and provides an immediate response. Endogenous fluorescence emission can provide information on biochemical and anatomical status down to individual plants through the canopy, up to the field or even regional scales.[188–191] Under constant illumination, it increases markedly in response to stress[192] and this observable has been correspondingly proposed to extract physiological information on plants.[57,193,194] This approach has nonetheless been questioned for its possible limited specificity.[195–197] Fluorescent proteins (FPs)[198] have further expanded opportunities upon visualizing physiological processes and reporting on gene expression under the control of inducible promoters acting as non-invasive sensors to stress situations.[199–202] However, FP reporters suffer from two main drawbacks. FP imaging of plants is limited by endogenous fluorescence emission from several compounds (chlorophyls, carotenoids, polyphenols) that produce a significant background within a broad range of wavelength (from UV to IR). Secondly, the observation of FP fluorescence - as well as endogenous fluorescence - requires either low light environment for imaging or light-proof devices, which limits its use for live recording of

plants. The possibility to selectively record fluorescent emission with minimal contribution from the autofluorescence background or ambient light (artificial or natural) would definitively open new avenues for plant phenotyping.

Our group recently introduced the Speed OPIOM fluorescence imaging protocol, which is endowed with such capabilities.[139,140,143] Speed OPIOM exploits modulated illumination under resonant conditions of light intensities and angular frequency in order to image reversibly photoswitchable fluorescent labels such as Reversibly Photoswitchable Fluorescent Proteins (RSFPs).[123,159] In particular, I developed a Speed OPIOM macroscope, which has been designed to image macro scale samples, making possible to detect RSFP whole seedlings and individual adult leaves in plants with minimal preparation. In this chapter, I demonstrate that Speed OPIOM can be used to image several RSFPs in transient as well as in stable plant systems produced by our collaborators at INRA Versailles (Zsolt Kelemen, Lionel Gissot, and Jean-Denis Faure).[a] We first showed that several RSFPs are compatible with the plant environment. Dronpa-2 was subsequently used as a sensor of physiological status of the plants by efficiently reporting on different transcriptional activities, both in a qualitative and quantitative manner. In particular, we showed that Speed OPIOM can reliably monitor early plant response to biotic stresses, even in the presence of endogenous fluorescence under exogenous light. This work is in collaboration with the agronomists, who designed and constructed the sensor plant system and provides all the transgenic plant samples.

3.2 Results

3.2.1 Expression of reversibly photoswitchable fluorescent proteins in plants

RSFPs have been rarely expressed in plants.[203,204] In this work, a total of four different RSFPs: Dronpa-2, Dronpa-3, rsFastlime, and Padron were expressed under the control of the 35S promoter in tobacco. The plant leaves have been imaged in the dark with our Speed OPIOM macroscope by setting the parameters of excitation to resonance for each RSFP (see subsection 1.3 and Table 3.1). As expected, Fig. 3.1a–h shows that Speed OPIOM selectively retrieved the fluorescence emission of the four RSFPs without any interference from autofluorescence. Interestingly, Dronpa-2, Dronpa-3, and rsFastlime on one hand, and Padron on the other hand exhibit Speed OPIOM observables of opposite signs due to their opposite change of brightness upon light-induced photoswitching. Since Dronpa-2 turned out to allow the fastest acquisitions with our experimental set-up, it was subsequently used in our subsequent observations (see Table 3.1).

3.2.2 Reversibly photoswitchable fluorescent proteins as selection markers in plants

Transgenic species are often selected by adding a gene coding for a fluorescent protein acting as a reporter to a transfected gene(s) of interest. As an illustration of such a situation, we generated and selected transgenic camelina plants using DsRed as a selection marker. Whereas a first strain was expressing DsRed only as a fluorescent protein, the second produced Dronpa-2 from further expressing p35S:DRONPA-2.

[a] Institut Jean-Pierre Bourgin, INRA, AgroParisTech, CNRS, Saclay Plant Science (SPS), Université Paris-Saclay, Versailles, France

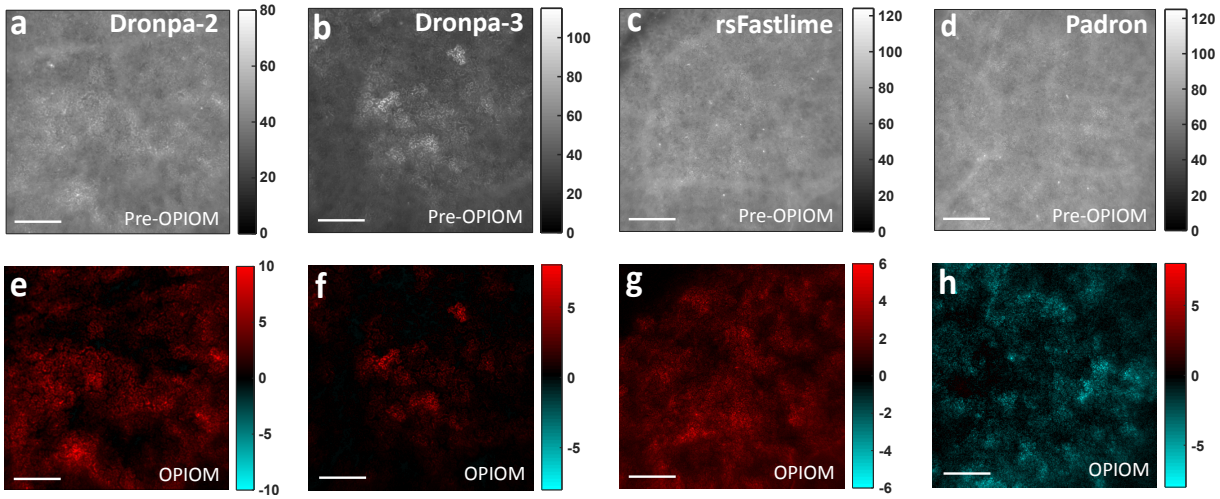

Figure 3.1 – Selective Speed OPIOM imaging of RSFPs against autofluorescence in *N. benthamiana* leaves. Pre-OPIOM (**a-d**) and Speed OPIOM (**e-h**) images of constructs expressing RSFPs in *N. benthamiana* leaves (**a**,**e**: Dronpa-2; **b**,**f**: Dronpa-3; **c**,**g**: rsFastlime; **d**,**h**: Padron. Illumination conditions: see Table 3.1. Images acquired in the dark.*Scaling bars*: 1 mm.

.

To image DsRed under ambient light, we first considered to use fluorescence imaging under constant illumination at 550 nm or similarly to exploit the fluorescence image resulting from averaging the images collected under an integer number of periods of 550 nm light modulation. Fig. 3.2a shows that the averaged image can hardly evidence the presence of DsRed against the background signal generated by interference of ambient light (indirect sunlight). Hence we imaged the amplitude of the modulated fluorescence of the leaves in order to benefit from lock-in amplification, which eliminates any contribution of light varying at a frequency range differing from the applied one on the light source. As evidenced by the dark background, we could overcome the interference of ambient light in both plant strains (Fig. 3.2b). Eventually the corresponding out-of-phase amplitude of the fluorescence modulation was vanishing in both plants, as expected from the instantaneous response of DsRed fluorescence to any light change (Fig. 3.2c).

Speed OPIOM proved more satisfactory to evidence the presence of Dronpa-2 in the labeled plant. Both Dronpa-2 labeled and unlabeled plants exhibit comparable signals and poor contrast against the background with the averaged Pre-OPIOM image using modulated light at Speed OPIOM resonance for Dronpa-2 (Fig. 3.2a). The in-phase image showed a stronger signal in the Dronpa-2-labelled plant than in the other one (Fig. 3.2b). However it could not be generally used for quantification since both Dronpa-2 and autofluorescence can contribute to the in-phase image. In contrast, Speed OPIOM unambiguously imaged Dronpa-2 in the Dronpa-2-labelled plant since the out-of-phase image eliminates the contribution of both ambient light and autofluorescence (Fig. 3.2c).

The preceding paragraph has illustrated how spectral discrimination can be used to select transgenic plants. However this approach reduces the accessible wavelength window, which can be exploited for subsequent fluorescence imaging investigations. Thus in the preceding case, the red emission channel would be not anymore accessible for imaging due to the presence of DsRed. Hence we evaluated whether

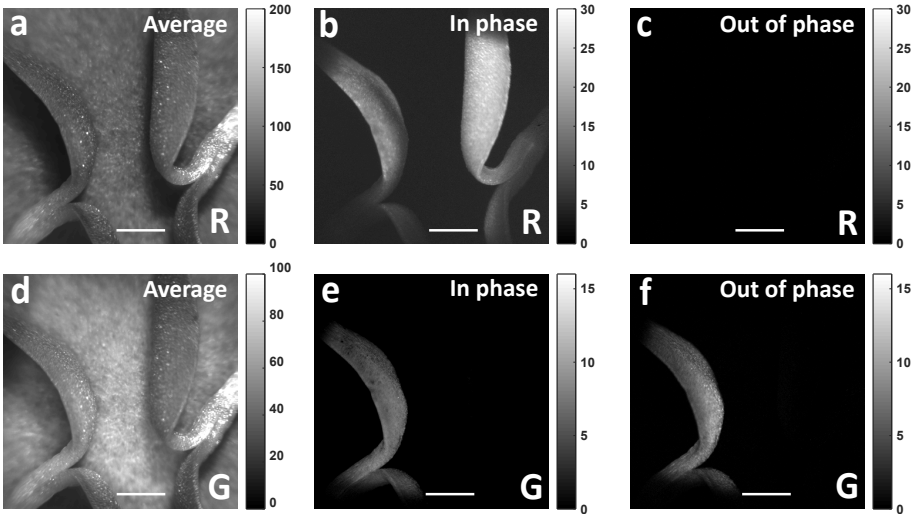

Figure 3.2 – Selective imaging of DsRed (R channel) and Dronpa-2 (G channel) against autofluorescence and ambient light in *Camelina sativa* leaves (left: labelled plant expressing both DsRed and Dronpa-2 under the control of the p35S promotor; right: plant only expressing DsRed as a control). Images were taken under modulated light at 550 nm (**a-c**) and at 480 & 405 nm (**d-f**) respectively. Averaged images: **a**, **d**, in-phase (**b**, **e**), and out-of-phase (Speed OPIOM; **c**, **f**) images. Illumination conditions: see Table 3.1. Images acquired in outdoor condition under indirect sunlight. *Scaling bars*: 1 mm.

Speed OPIOM could be implemented to select plants by using a RSFP as a reporter in the presence of a FP exhibiting similar excitation/emission properties. Using the p35S promoter in tobacco leaves, we first co-expressed nuclear localized Dronpa-2 (Fbr-Dronpa-2) with EGFP either at the plasma membrane (PMA4-GFP) or at the endoplasmic reticulum (PAS1-EGFP). Dronpa-2- and EGFP-expressing leaves were analyzed with Speed OPIOM implemented on an epifluorescence microscope in the dark. We could easily discriminate the transgenic plants with cells expressing both EGFP and Dronpa-2 fusions, which were unambiguously evidenced by their specific and non-overlapping subcellular distribution. Whereas Pre-OPIOM simultaneously imaged both EGFP and Dronpa-2 (Fig. 3.3a–e), only Dronpa-2 could be selectively imaged with Speed OPIOM (Fig. 3.3f–j).

3.2.3 Quantification of Dronpa-2 expression

In the perspective of using fluorescence imaging for selecting transgenic plants, we then evaluated the ability of the Speed OPIOM protocol to quantify gene expression in transient as well as in stable expression plant systems. We designed three constructs in which Dronpa-2 was expressed under the control of promoters with various strengths:[205] pNOS:DRONPA-2, pACTIN2:DRONPA2, and p35S:DRONPA2. In addition, all the constructs carried pCVMV:DsRED as a selection marker. These constructs have been tested for both transient and stable expression with our fluorescence macroscope.

In *N. benthamiana* leaves transiently expressing Dronpa-2

The constructs were first tested in transient expression in *N. benthamiana* leaves. The leaves have been imaged with both Pre-OPIOM and Speed OPIOM to selectively image Dronpa-2 in the Speed OPIOM

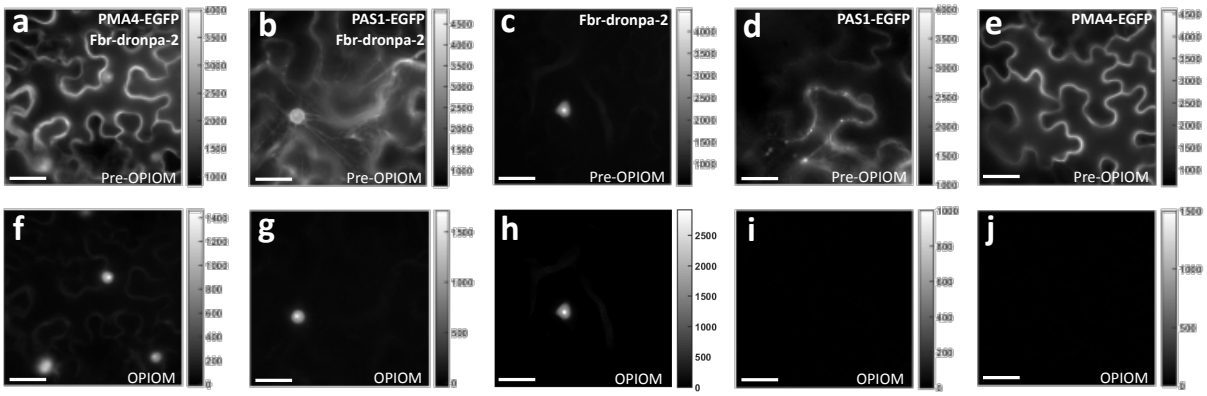

Figure 3.3 – Selective Speed OPIOM imaging of Dronpa-2 against EGFP in *N. benthamiana* leaves. Pre-OPIOM (**a-e**) and Speed OPIOM (**f-j**) images of constructs expressing Dronpa-2 and/or EGFP in N. benthamiana leaves (**a**,**f**: ; PMA4-EGFP and Fbr-Dronpa-2; **b**,**g**: PAS1-EGFP and Fbr-Dronpa-2; **c**,**h**: Fbr-Dronpa-2; **d**,**i**: PAS1-EGFP; **e**,**j**: PMA4-EGFP). PAS1-EGFP, PMA4-EGFP and Fbr-Dronpa-2 are respectively localized in the endoplasmic reticulum, the plasma membrane and the nucleus. Images acquired in the dark *Scaling bars*: 50 μm.

480/405 nm channel and to evidence DsRed in the in-phase 550 nm channel. Fig. 3.4 displays the results. The images exhibit a rather heterogeneous fluorescence. Beyond evidencing that our imaging protocol was efficient to overcome the interferences of autofluorescence, the main conclusion of this preliminary investigation was that the level of fluorescence was significantly larger with the p35S:DRONPA2 construct than with the pACTIN2:DRONPA-2 and pNOS:DRONPA2 ones, which demonstrates the ability of Speed OPIOM for quantitative measurement of fluorescence expression.

In *Camelina* leaves stably expressing Dronpa-2

Since transient expression could lead to artificially higher expression levels, we carried out the same analysis in stable transgenic camelina lines. Three independent T1 lines were selected and Speed OPIOM imaging was performed on leaves of independent T2 plants selected for their DsRed fluorescence. In order to define the most reliable protocol for analyzing the level of transcriptional activity, we analyzed not one but several individual seedlings (including wild type seedlings as negative controls). Fig. 3.5 displays representative results. In contrast to the images collected in *N. benthamiana* leaves, the images of Dronpa-2 and DsRed exhibited a rather homogeneous fluorescence. Nevertheless, we noticed that the image of DsRed displayed a more heterogeneous fluorescence, with the brightest level at the leave veins. As in *N. benthamiana* leaves, we noticed that the Dronpa-2 Speed OPIOM signal was significantly larger with the p35S:DRONPA2 construct than with the pACTIN2:DRONPA-2 and pNOS:DRONPA2 ones.

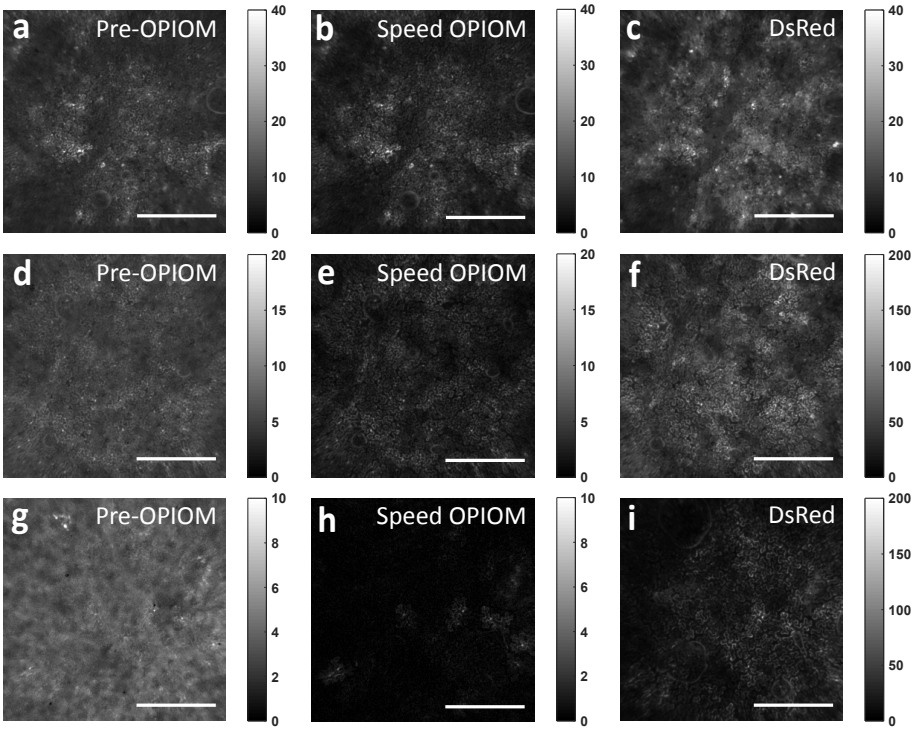

Figure 3.4 – Fluorescence imaging of *N. benthamiana* leaves transiently expressing Dronpa-2 (imaged with Pre-OPIOM and Speed OPIOM) and DsRed (imaged with in-phase fluorescence imaging) constructs. Promoters: p35S **a-c**, pACTIN2 **d-f**, pNOS **g-i**. Images acquired in the dark.*Scaling bars*: 1 mm.

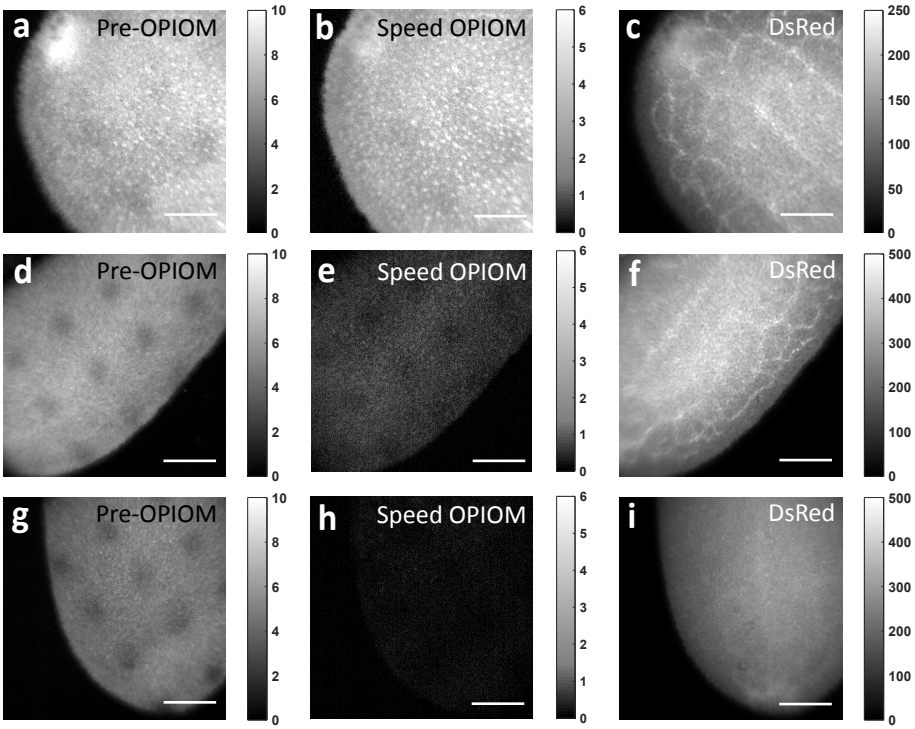

Figure 3.5 – Fluorescence imaging of *Camelina Sativa* leaves stably expressing Dronpa-2 (imaged with Pre-OPIOM and Speed OPIOM) and DsRed (imaged with in-phase fluorescence imaging) constructs. Promoters: p35S **a-c**, pACTIN2 **d-f**, pNOS **g-i**. Images acquired in the dark. *Scaling bars*: 1 mm.

Data analysis

Data analysis at the single pixel level We first analyzed the collected images at the single pixel level. More specifically we plotted the intensity of the Speed OPIOM signal as a function of the DsRed one.[b] In the case of the p35S:DRONPA2 constructs, we observed rather linear correlations (see Fig.3.6). Furthermore the slope of the linear fitting was always found close to the ratio of the integrated signals over the whole leaf surface (see Fig.3.6). Interestingly, whereas we noticed a significant dispersion of the fluorescence levels among the seedlings, the slopes of the linear correlations were fairly constant for all the observed seedlings. In contrast, we obtained poor correlations and much variability for the pNOS:DRONPA-2 and pACTIN2:DRONPA2 constructs, which suggested that we were at the noise level for those samples.

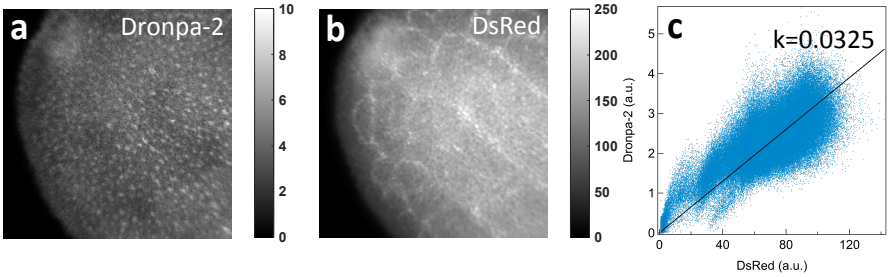

Figure 3.6 – Correlations of the Speed OPIOM signals of Dronpa-2 and in phase fluorescence signals of DsRed collected at each pixel of the image of a *Camelina sativa* leaf permanently expressing Dronpa-2 and DsRed constructs under the control of the p35S promoter. The slope of the linear fitting (0.0325) is close to the ratio of the integrated signals over the whole leaf surface, which equals to 0.0317.

Data analysis at the whole leaf level Taking into account the preceding result, we subsequently decided to integrate the Speed OPIOM signals over the whole leaf surface for quantification. We subsequently explored various analyses to determine the most robust way to exploit our data to evidence the expression level of Dronpa-2. We first proceeded by analyzing the distribution of the Pre-OPIOM and Speed OPIOM signals with 480/405 nm illumination, and the in-phase DsRed signal with 550 nm illumination, both acquired on the preceding *N. benthamiana* and *Camelina sativa* leaves observed in the dark.

Fig. 3.7 displays the results obtained in *N. benthamiana*. We could make several conclusions:

- The Pre-OPIOM signals were essentially similar and moderately dispersed in all the plants, either containing pNOS:DRONPA-2, pACTIN2:DRONPA2, or p35S:DRONPA2, or no Dronpa-2-coding gene (see Fig. 3.7a). This result probably originates from the significant plant autofluorescence, which dominates the Pre-OPIOM signal;

- In contrast, the Speed OPIOM signals proved discriminating although upon exhibiting dispersion (see Fig. 3.7b). First Speed OPIOM could clearly discriminate the Dronpa-2 expressing lines from

[b]This correlation has been also established by removing singular pixels exhibiting an abnormally high level of fluorescence without markedly altering the conclusions retrieved from the correlations with the non-corrected datas (data not shown).

the wild type plants. Moreover the Speed OPIOM signals were decaying in the expected order p35S:DRONPA2>pACTIN2:DRONPA2>pNOS:DRONPA-2≫ Wild type;

- Eventually we analyzed the in-phase DsRed reporting signal (see Fig. 3.7c). It was much lower in the wild type than in the Dronpa-2 expressing lines. Furthermore, it was found essentially similar in the three Dronpa-2 expressing lines albeit with a significant dispersion.

As originally planned, we also computed the ratio of the Speed OPIOM signal over the in-phase DsRed signal in a purpose of normalization (see Fig. 3.7d). The observed behavior of this ratio was essentially similar to the behavior observed from directly analyzing the Speed OPIOM.

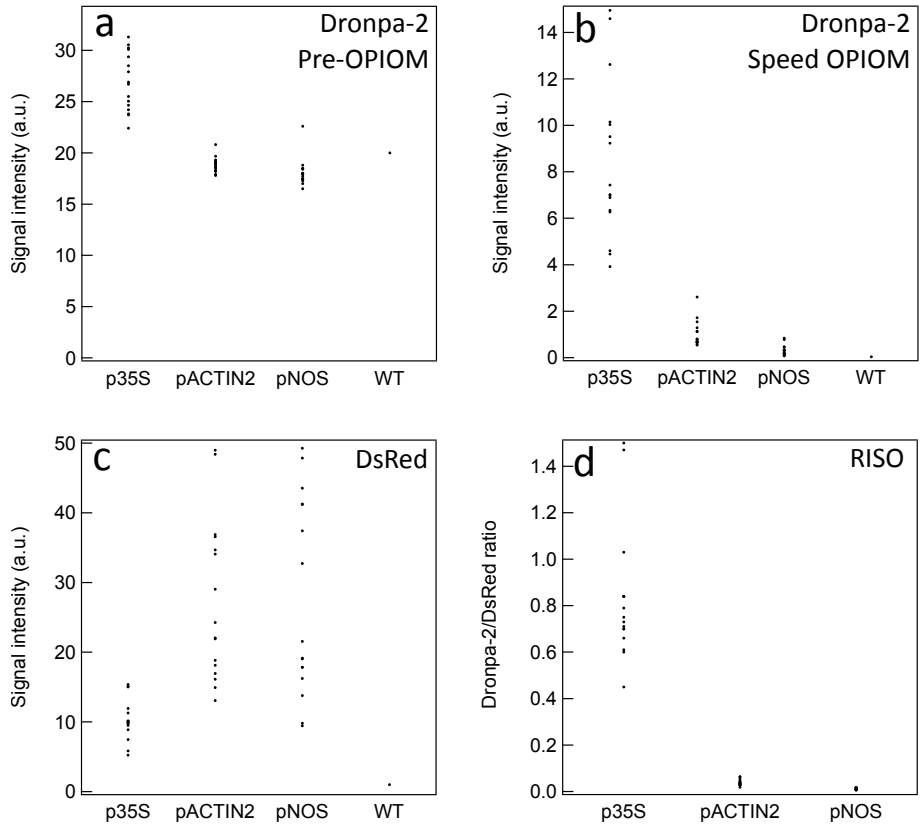

Figure 3.7 – Signals of *N. benthamiana* leaves from different imaging channels: Pre-OPIOM and Speed OPIOM signals with 480/405 nm illumination, and in-phase DsRed signal with 550 nm illumination, for the three constructs p35S, pACTIN and pNOS. Signals have been extracted from integration over the whole surface of the leaf. 16 samples have been measured for each promoter construct.

We essentially made similar observations in *Camelina sativa* seedlings (see Fig.3.8a–d). One should notice that the three investigated lines exhibited different levels of Dronpa-2 expression. One should refine the plant choice for agronomic purposes.

We eventually ended up our analysis by examining whether ambient light would anyhow interfere to measure the Dronpa-2 expression level. We proceeded by comparing the results obtained in the dark and under ambient light after normalizing the Speed OPIOM signal of Dronpa-2 by the DsRed signal to define a ratiometric index of Speed OPIOM imaging (RISO) (see Fig. 3.9). The analysis of independent transformation events in *N. benthamiana* showed an average RISO index of 0.8, 0.06 and

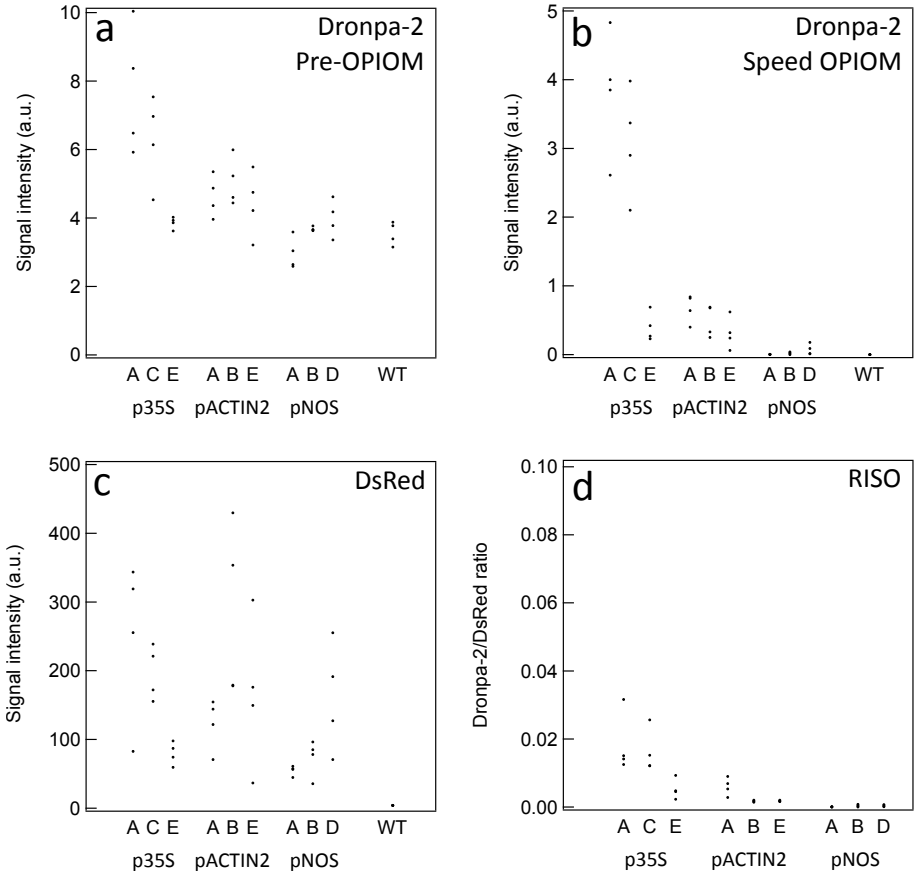

Figure 3.8 – Signals of *Camelina sativa* seedlings from different imaging channels: Pre-OPIOM and Speed OPIOM signals with 480/405 nm illumination, and in-phase DsRed signal with 550 nm illumination, for the three constructs p35S, pACTIN and pNOS. Signals have been extracted from integration over the whole surface of the leaf. For each construct, three lines of seedlings have been studied and in each line four individual samples have been measured.

0.02 for respectively p35S, pACTIN and pNOS promoters when Speed OPIOM recording was carried out in the dark (Fig. 3.9a). Independent leaf samples were analyzed with the presence of ambient light under indoor lighting condition providing RISO index of 0.45, 0.04 and 0.02 for p35S, pACTIN and pNOS (Fig. 3.9a). There was no statistical differences between the two sets of data, which indicated that the ambient light had no influence on quantitative analysis of gene expression by Speed OPIOM. We then turned to monitoring seedlings of *Camelina sativa*. We first observed that the RISO index varied between the different lines expressing the same construct. The pNOS:DRONPA-2 construct showed little trace of expression, which remained below the noise level. The pACTIN2:DRONPA-2 constructs showed a range of expression varying from 0.002 to 0.01 in the dark, and 0.002 to 0.006 in the ambient light. It is worth noting that a line of the pACTIN2:DRONPA-2 construct showed higher RISO in both conditions. Finally the p35S:DRONPA-2 showed the highest expression centered around 0.015 in the dark and 0.01 in ambient light but also the most variable.

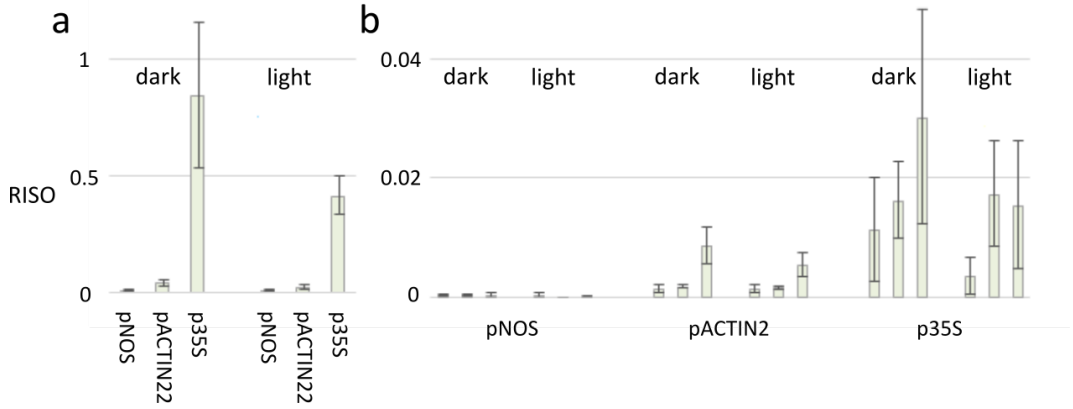

Figure 3.9 – Quantitative assessment of transcriptional activity in transient *N. benthamiana* (**a**; statistic data based on 16 samples for each promoter) and *Camelina sativa* (**b**; three independent lines have been measured for each construct and four samples were measured for each lines) leaf assays.

Conclusion

As a whole, we could conclude that Speed OPIOM was able to directly quantify Dronpa-2 expression levels both in transient and stable systems with comparable expression range. More importantly, Dronpa-2 monitoring could be carried out under ambient light, which provides an unique tool to quantify fluorescent reporter activity with minimal impact on plant growth conditions.

3.2.4 Live Speed OPIOM monitoring of biotic stresses

Reporter genes were frequently used to monitor plant response to biotic or abiotic environmental changes. Fluorescence provides a non invasive way to monitor gene expression but it is susceptible to the environmental light interference and the autofluorescence of the plant, which obscure the sensoring of the gene-related fluorescence. Speed OPIOM macro imaging system, with the series of validations demonstrated above, could surely open a new way for stress detection via reporter genes.

To illustrate that Speed OPIOM could provide a non invasive tool to monitor stress responses in real time with minimal interference, we expressed Dronpa-2 in *Arabidopsis thaliana* plants under the control of the VSP2 and AtNRAMP4 promoters respectively. VSP2 is coding acidic phosphatase, the expression of which is regulated by several biotic and abiotic stresses including water deficiency.[206] AtNRAMP4 is coding for a vacuolar metal transporter the expression of which is regulated by iron limitation.[207] Water stress was controlled with an automated large-scale phenotyping platform.[208] Plants expressing pVSP2:Dronpa-2 were grown for 15 days at 60% soil water content (no stress) and submitted to moderate (30%, Stress +) or high (25%, Stress ++) water limitation for 8 more days before being imaged with Speed OPIOM. Soil-drying conditions induced Dronpa-2 expression mainly in petioles of older leaves and cotyledons that could be monitored even for moderate stress (Fig. 3.10). Iron starvation was monitored by growing pAtNRAMP4:Dronpa2 expressing plants for 12 days in the presence of 50 μM FeHBED (no stress), in the presence of traces of iron (Stress +), and in the absence of iron with 100 μM Ferrozine (Stress ++). Speed OPIOM detected Dronpa-2 expression specifically in young leaves of iron-starved plants (Fig. 3.11). In both cases Speed OPIOM was able to selectively discriminate the organs expressing Dronpa-2 reporters even under moderate conditions of stress. In conclusion, Dronpa-2 monitoring allows non destructive real time identification of stress occurrence at the level of individual plants and even to specific organs.

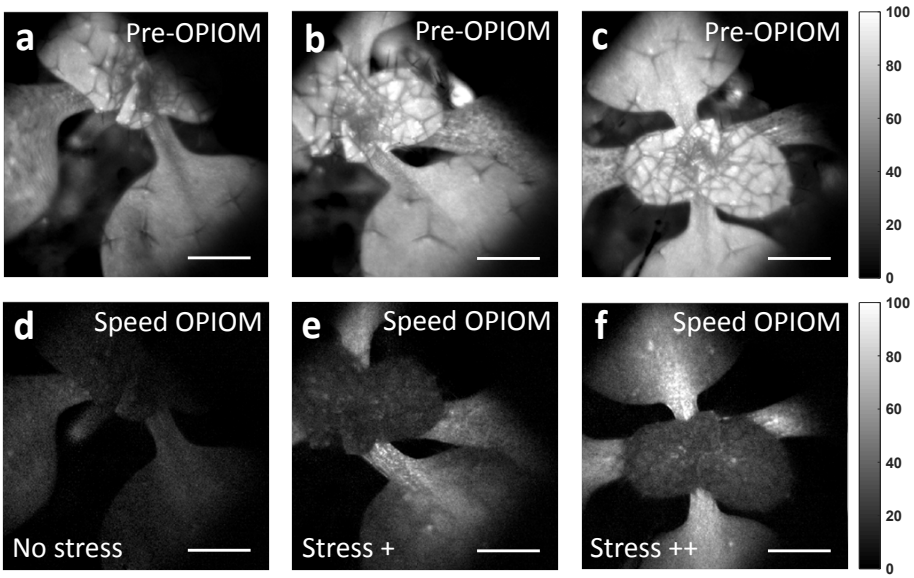

Figure 3.10 – Dronpa-2 labeled *Arabidopsis thaliana* plants cultivated in soils with different water contents, **a,d**: 60%, **b,e**: 30%, **c,f**: 20%. The Pre-OPIOM images (**a-c**) show no visible difference between the three individuals in terms of fluorescence signal. In contrast, the comparison of the Speed OPIOM images **d-f** reveal the suffering of the plants lacking water.

.

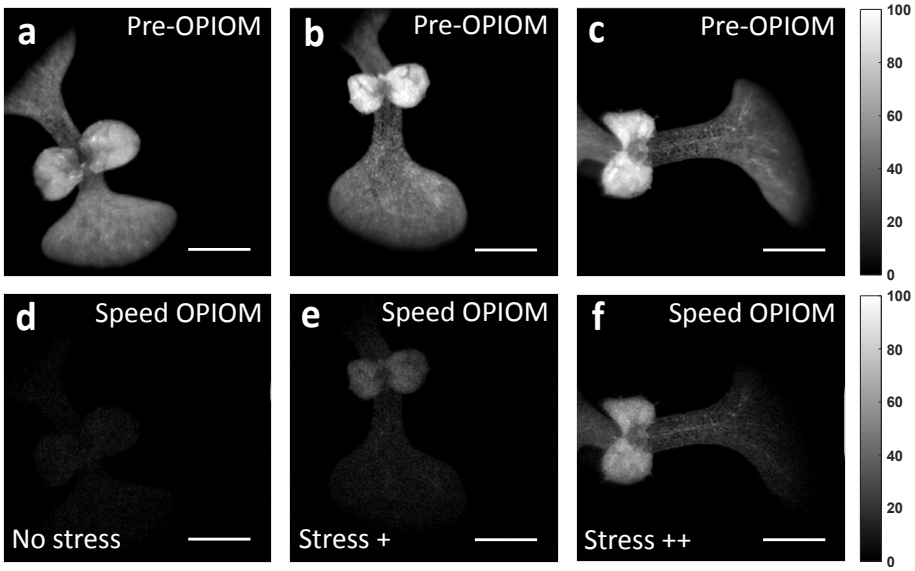

Figure 3.11 – Dronpa-2 labeled *Arabidopsis thaliana* plants cultivated in soils with different iron availability, **a,d**: Fe abundant, **b,e**: trace of Fe mineral, **c,f**: no Fe mineral. The Pre-OPIOM images (**a-c**) show a minor difference of expression between the three individuals, while the Speed OPIOM images **d-f** give direct expression levels of Dronpa-2 without the inteference of autofluorescence.

3.3 Conclusion

This work demonstrated the use of the Speed OPIOM detection system to remotely image the Dronpa-2 signals in plants, which are challenging objects for fluorescent imaging. First, plants accumulate a large diversity of endogenous fluorescent compounds, in particular upon stress conditions. Speed OPIOM was able to efficiently discriminate the Dronpa-2 signals from autofluorescence and the signals from other fluorescent reporters like GFP and DsRed. The combination of Speed OPIOM and Dronpa-2 also allowed us to quantitatively assess the reporter gene even for weak expression. The system was also validated in high expressing transient as well as in stable gene expression systems. Second, plant physiology is strongly dependent to its light environment. Speed OPIOM demonstrated that quantitative fluorescent acquisition was as sensitive and robust in dark as well as in bright light conditions. This is a remarkable achievements compared to the existing fluorescent acquisition set-ups. Finally, we demonstrated that OPIOM technology could be used to record abiotic stress responses like water or iron limitations in real time. It now provides the possibility to monitor plant physiological status even in natural conditions.

The use of Speed OPIOM for plant monitoring offers unique opportunities. First, the original set up presented here could be used to monitor different plant responses to abiotic and biotic stresses but also to developmental cues in real time and under normal growth conditions. It requires only the identification of genes, the transcriptional regulation of which changes in leaves. However, application of Speed OPIOM in plants will require further validations. First, the absolute quantification of the Dronpa-2 responses has to be correlated with endogenous gene expression, which has to be validated for each reporting system. Second, the turn over of the Dronpa-2 protein will also have to be determined to define the time window in which the Dronpa-2 signal remains stable. Such parameter will be important for transient gene induction but also to define the robustness of the signal to multiple monitoring evaluation. Third, Speed OPIOM

detection devices will have to be adapted to the plant environment that includes, heat or cold, humidity and dust.

Speed OPIOM could eventually be used for different applications. The Speed OPIOM set up could be installed in phenotyping platform to monitor plant responses to changing environment but also to help defining the best growth conditions for instance to implement controlled stress conditions. It could also provide significant information to breeders to identify the best lines in a selection program by using gene expression as a proxy of an expected phenotype and eventually design predictive markers for specific traits. A third possible use of Speed OPIOM technology could be to turn plants into environmental sensors. Plants have large leaf and root exchange surface and also the possibility to accumulate metabolite turning them in sensitive environmentally connected organisms. Speed OPIOM could therefore be used to monitor gene expression associated with pollutants (soil or air), the presence of pathogens, water or nitrogen content. Individual sentinels plants could be used with crops in fields or glass houses, in contaminated industrial area, along roads or even within buildings to detect environmental changes. Such use of Speed OPIOM will only need 3 minimal requirements: an optimized Speed OPIOM set up adapted to individual or population of plants, a selected plant species, and the transcriptional regulation of specific genes.

3.4 Experimental section

3.4.1 Methods

Constructs

Expression of Dronpa-2, Dronpa-3, rsFastlime, and Padron under the control of the 35S promoter in tobacco PCR were performed with primers LG403DRONPAgtwFOR (GGGGACAAGTTTGTACAAAAAAGCAGGCTTCATGGTGAGTGTGATTAAACC) and LG404DRONPAgtwREV (GGGGACCACTTTGTACAAGAAAGCTGGGTCttaCTTGGCCTGCCTCGGCA) to amplify the gateway modified DRONPA, DRONPA-2 and DRONPA-3 coding sequence using respectively the corresponding DNA template. Same procedure was used to amplify the PADRON and rsFastLime gateway modified coding sequence using respectively the LG890PADRONgtwFOR (GGGGACAAGTTTGTACAAAAAAGCAGGCTTCatgagtgtgattaaaccaga) and LG891PADRONgtwREV (GGGGACCACTTTGTACAAGAAAGCTGGGTCttagttggcctgcctcggca) primers or LG895rsFastLimegtwFOR (GGGGACAAGTTTGTACAAAAAAGCAGGCTTCatgagtgtgattaaaccaga) or LG896rsFastLimegtwREV (GGGGACCACTTTGTACAAGAAAGCTGGGTCttacttggcctgcctcggca) primers. These CDS were then cloned into the pDONR207 plasmid and then transferred into the pB2GW7 vector to obtain the final p35S::Fluorescent Protein constructs.[209]

Camelina expression vector expressing p35S::Dronpa2 constructs The Camelina expression vector expressing p35S::Dronpa2 construct was achieved as follow. The gateway-cassette from pUBN-GFP-Dest[210] amplified by PCR using primers:

- 5'-tgacgcgtaaggggatctagaatcacaagtttgtacaaaaaagctg-3' and
- 5'-ttaatcacactcaccatctcgaggatcaccactttgtacaagaaag-3'

and Dronpa-2 coding sequence amplified from Dronpa-2pDONR207 with primers

- 5'-atggtgagtgtgattaaaccagaca-3' and
- 5'-ggctgcggccgcctcgactacttggcctgcctcggcagctcag-3'

were cloned in one step in BamHI XhoI-digested pBinGlyRed vector,[211] creating pD2. The doubled CaMV 35 S promoter was amplified from pMDC83[212] with primers

- 5'-ggggacaagtttgtacaaaaaagcaggcttccagtgccaagcttggcgtgcct-3' and
- 5'-ggggaccactttgtacaagaaagctgggtcgtcgaggtcctctccaaatgaaatg-3',

recombined into pDONR207 (Invitrogen) and eventually recombined into pD2.

pACTIN2:DRONPA2; pCMV:DsRED The actin promoter was amplified from Arabidopsis thaliana Col-0 genomic DNA with primers

- 5'-GGGGACAAGTTTGTACAAAAAAGCAGGCTTCaccatagaatagctagctaactaatac-3' and
- 5'-GGGGACCACTTTGTACAAGAAAGCTGGGTCtttttatgagctgcaaacacacaaaaagag -3',

recombined into pDONR207 and eventually recombined into pD2.

pNOS:DRONPA2; pCMV:DsRED The nos promoter was amplified from pGWB1[213] with primers

- 5'-GGGGACAAGTTTGTACAAAAAAGCAGGCTTCgatcatgagcggagaattaagggag-3' and
- 5'-GGGGACCACTTTGTACAAGAAAGCTGGGTCgcgaaacgatccagatccggtgcag-3',

recombined into pDONR207 and eventually recombined into pD2.

prVSP2:DRONPA2; pCMV:DsRED The VSP2 promoter (AT5G24770) was amplified from Arabidopsis thaliana Col-0 genomic DNA with primers

- 5'-GGGGACAAGTTTGTACAAAAAAGCAGGCTTCgctgcttggacgattttgtgaatga-3' and
- 5'-GGGGACCACTTTGTACAAGAAAGCTGGGTCgttttttatggtatggtttattgtt-3',

recombined into pDONR207 and eventually recombined into pD2.

prNRAMP4:DRONPA2; pCMV:DsRED The AtNRAMP4 promoter (AT5G67330) was amplified from Arabidopsis thaliana Col-0 genomic DNA with primers

- 5'-GGGGACAAGTTTGTACAAAAAAGCAGGCTTCttttcttaattgtagtcctaataac-3' and
- 5'-GGGGACCACTTTGTACAAGAAAGCTGGGTCatttcccggtaaccgccgattctcag-3',

recombined into pDONR207 and eventually recombined into pD2.

Plant transformation

Transient expression in Nicotiana benthamiana leaves The vectors were transformed into Agrobacterium tumefaciens and inoculated in Nicotiana benthamiana leaves of one month-old plants. Agrobacterium carrying clones of interest were grown overnight at 28°C in 5 mL LB medium with appropriate antibiotics. Aliquots from the overnight cultures were resuspended in 10 mM $MgCl_2$ and 1 mM 2-(N-morpholine)-ethanesulphonic acid (MES) to obtain a final OD(600 nm) of 0,5 for tobacco leaf infiltration. Two individual leaves of two independent plants were infiltrated.

Permanent expression in Camelina and Arabidopsis Camelina and Arabidopsis flower dip transformation was carried out as described previously.[185]

Plant culture Plant culture Tobacco, Arabidopsis and camelina were grown on soil in glasshouse and were imaged directly with Speed OPIOM at about 15 cm distance. The water stress experiment was carried out in phenoscope.[208] The plants were germinated and grown in soil in the glass house for 8 days, then adapted to 60% soil water content in the phenoscope for 8 days 8h/16h day/night cycle at 21/18°C and 65% humidity. Plants were then cultured for 8 days at 30 or 25% soil water content before being imaged. For iron stress, plants were cultivated for 12 days in 16/8h light/dark cycle at 22°C, in ABIS medium[214] with 50 μM FeHBED (Strem Chemicals) for the control condition (media with Fe) or without any iron supplement (trace of iron) or supplemented with 10 μM Ferrozine (Sigma) to remove any trace of iron.

3.4.2 Acquisition parameters used for the images

Figure	Periods	f_s (Hz)	f_m (Hz)	$I_1^0(\lambda_{480nm})$ Ein.m^{-2}.s^{-1}	$I_2^0(\lambda_{405nm})$ Ein.m^{-2}.s^{-1}	$I_3^0(\lambda_{550nm})$	Lighting condition
3.1a,e	8	50	2.5	4.0×10^{-2}	1.9×10^{-2}	-	dark
3.1b,f	3	50	0.5	5.3×10^{-2}	4.7×10^{-3}	-	dark
3.1c,g	4	40	0.5	4.4×10^{-2}	2.4×10^{-3}	-	dark
3.1d,h	4	20	0.5	4.3×10^{-2}	1.6×10^{-2}	-	dark
3.2a-c	8	50	2.5	-	-	On	Outdoor
3.2d-f	8	50	2.5	4.0×10^{-2}	1.9×10^{-2}	-	Outdoor
3.3a-j	8	10	1	1.5×10^{-2}	8.8×10^{-3}	-	dark
3.4a,b,d,e,g,h	8	50	2.5	4.0×10^{-2}	1.9×10^{-2}	-	dark
3.4c,f,i	8	50	2.5	-	-	On	dark
3.5a,b,d,e,g,h	8	50	2.5	4.0×10^{-2}	1.9×10^{-2}	-	dark
3.5c,f,i	8	50	2.5	-	-	On	dark
3.10,3.11	8	50	2.5	4.0×10^{-2}	1.9×10^{-2}	-	lab light

Table 3.1 – Acquisition parameters used for all the images shown in this chapter. f_s and f_m respectively refer to the sampling rate and to the modulation frequency of the excitation lights.

Part III

Endomicroscopy

Chapter 1

A Speed OPIOM endomicroscope and its applications in fluorescence bio-imaging

1.1 Introduction

Fiber-optic based fluorescence microendoscopes are versatile devices, which have found numerous biological and medical applications.[215–219] In contrast to conventional imaging tools, they permit to non-invasively image cells within hollow tissue tracts or deeply embedded within solid organs.[220] They are also convenient to observe plant roots in the soil[221,222] or the brain of freely moving animals.[223] Beyond being geometrically demanding, such samples often exhibit significant light scattering and autofluorescence, which are both detrimental for the quality of the image contrast.

Standard fiber-optic epifluorescence imaging with one-photon excitation is easy of use, benefits from cheap light source and full-frame acquisition for high-speed imaging. However, it is unable to reject the out-of-focus background (generally providing low signal contrast images; see[224]) and it is not robust to light scattering when imaging thick samples.[215] To deal with optical sectioning in fiber bundle microendoscopy, various strategies coming from microscopy have been transposed including confocal, multi-photon and structured illumination imaging.[225–227] However, due to the inherent characteristics of the bundle, these methods have encountered several limitations. In confocal microscopes, the axial resolution of the system strongly relies on the use of both high NA objective to image the specimen and a pinhole of small diameter, which selects for the collection of fluorescence emission at the focal plane. In fiber bundle-based endoscopes, confocal scanning is performed at the proximal end of the fiber bundle and a single fiber core serve as both a point-like excitation source and a pinhole. With typical core size around 5 μm and NA of the fiber of 0.4, the axial fluorescence intensity decays only slowly out of the focal plan and lessens the confinement of the collected fluorescence.[225,227–229] To improve the sectioning ability, additional high NA objectives have been used to tightly refocus the excitation beam exiting from the fiber onto the specimen.[230,231] While efficient, these approaches require specialized optics for the endoscope. Whereas confocal detection eliminates the background caused by out-of-focus light and scatter by introducing a spatial filter along the optical pathway, multiphoton–excited fluorescence imaging overcomes this limitation by restricting significant fluorescence emission to the focus of the light source.[227,232,233] However the broadening of the pulsed excitation when it propagates

through the fiber cores degrades the performance of multiphoton excitation. Importantly both confocal detection and multiphoton excitation strategies use punctual illumination. They correspondingly require scanning and focusing mechanisms to build the final image, which both hinder miniaturization and reduce the frequency for image acquisition. Alternatively, out-of-focus background has been rejected in non-scanning wide-field endoscopes by using structured illumination microscopy.[226,234–238] Although this approach provides wide-field images after minimal computation, it may suffer from the lack of axial optical sectioning mentionned above in confocal microscopy. Moreover it relies on a spatial light modulator the refreshing of which ultimately limits the frequency of image acquisition to a few Hz.[226]

There are multiple causes of interfering fluorescence in microendoscopy. First, the biological samples may intrinsically emit fluorescence originating from endogeneous (e.g. flavins) or added (e.g. vitamins contained in culture media) components. Second the sample may contain several fluorescent labels exhibiting spectral overlap. Eventually the imaging fiber itself is autofluorescent and its emission results in a significant loss of image constrast.[239] To circumvent these issues, various strategies including background subtraction[240] and un-mixing spectral analysis[153] have been proposed. However they rely on assumptions on the autofluorescence patterns and may fail when dealing with low levels of targeted fluorescence signals with poor signal-to-noise ratios. Thus reliable strategies to eliminate the detrimental effects of autofluorescence in this imaging modality are still demanded.

The preceding analysis led us to implement Speed-OPIOM in fluorescence microendoscopy. Unlike regular fluorescence imaging which exploits the spectral dimension to generate contrast in images, Speed-OPIOM discriminates reversibly photoswitchable fluorescent labels against spectrally interfering backgrounds by exploiting their dynamic photoswitching properties, without any deconvolution nor subtraction scheme.[143] More specifically, Speed OPIOM uses two modulated light sources synchronized in antiphase at two wavelengths in order to drive photoswitching (Fig. 1.1a). The Speed OPIOM signal $\mathcal{S}$ – the out-of-phase component of the modulated fluorescence signal – is directly retrieved by Fourier transform of tens to hundreds of images for at least two periods of light modulation. No further processing is necessitated and lock-in detection secures efficient noise rejection. Interestingly $\mathcal{S}$ exhibits a narrow resonance in the space of the control parameters of illumination (light intensities and angular frequency) (Fig. 1.1b). It is non-vanishing only when the average light intensities are tuned to maximize the photoswitching amplitude on the changes of light intensities, and the angular frequency matches with the inverse of the photoswitching relaxation time. For a given set of the control parameters of illumination, $\mathcal{S}$ exhibits as well a narrow resonance in the space of the rate constants, which govern forward and backward photoswitching of the labels (Fig. 1.1c).

At a given radial frequency of light modulation ω, the spatial dependence of the Speed OPIOM resonance on the light intensities I_1^0 and I_2^0 opens an unprecedented avenue to improve the axial resolution and to remove the out-of-focus fluorescence in fiber-optic epifluorescence imaging with one-photon excitation. Indeed the spatial light profile does not exhibit a cylindrical symmetry at the fiber end (*vide infra*). As a consequence, the Speed OPIOM resonance condition can only be met in a restricted region of space for a given set of intensities and angular frequency of the modulated light sources, which eliminates the fluorescence contributions from out-of-resonance locations. As an aditional benefit of Speed OPIOM, a reversible photoswitchable fluorescent label has singular photochemical and kinetic properties (and

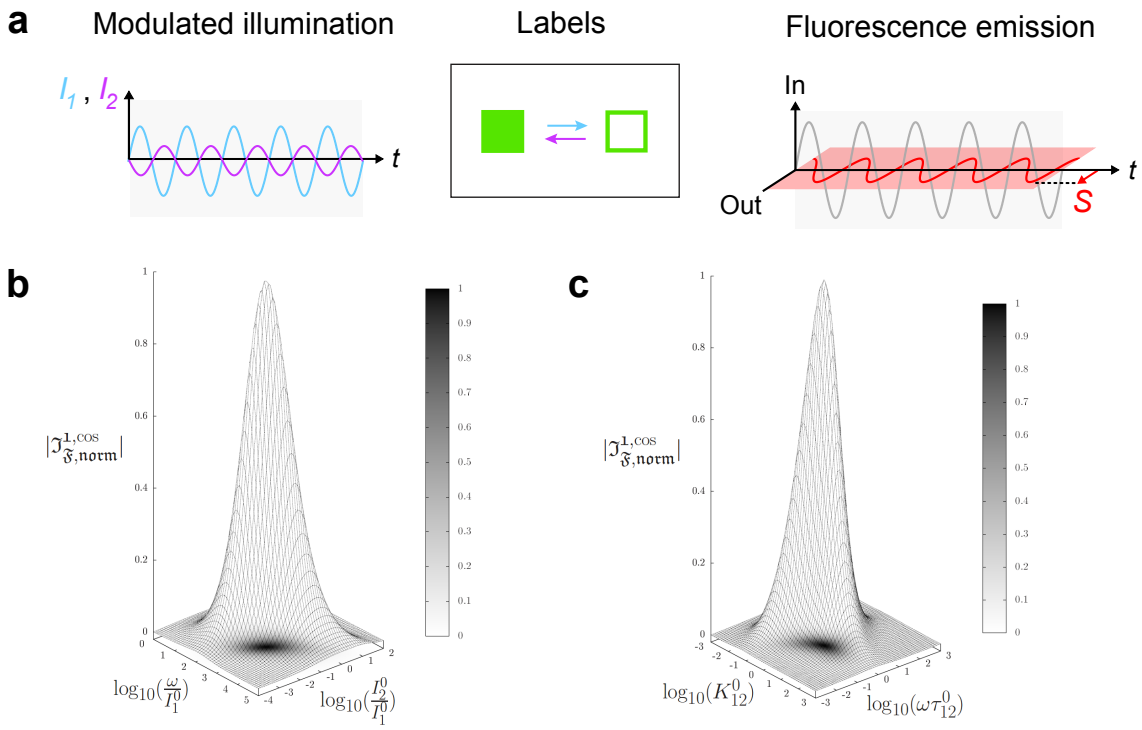

Figure 1.1 – **a**: *Principle of Speed OPIOM*. Sinusoidally modulated light sources synchronized in antiphase at two wavelengths generate the quadrature-delayed component S (in red) of the fluorescent emission from the reversibly photoswitchable fluorescent labels used in Speed OPIOM; **b**,**c**: *Speed OPIOM for optical sectioning and selective imaging*. $\mathcal{S}$ exhibits a narrow resonance both in the space of the control parameters of illumination (**b**; here parametered by I_1^0/I_2^0 and ω/I_1^0 where I_1^0 and I_2^0, and ω respectively designate the average light intensities at both wavelengths, and the angular frequency of the modulated lights) and in the space of the rate constants, which govern forward and backward photoswitching of the labels (**c**; parametered by K_{12}^0 and $\omega\tau_{12}^0$ where K_{12}^0 and τ_{12}^0 respectively designate the ratio of the average rate constants associated to forward and backward photoswitching and the photoswitching relaxation time at steady-state).

correspondingly its own resonant conditions). Hence simply tuning the illumination control parameters to its resonant values enables one for its selective imaging, filtering out the contribution of spectrally interfering fluorophores (non-photoswitching or non-resonant reversibly photoswitching fluorophores) as well as autofluorescence.

In the present chapter, I implemented Speed OPIOM in wide-field fluorescence microendoscopy with one-photon excitation. I built a simple and cheap optical-fiber bundle-based microendoscope integrating modulatable light sources. I first demonstrated that it provides intrinsic optical sectioning, which facilitates the observation of fluorescent labels at targeted positions within the sample. Then I thoroughly evaluated its efficiency to eliminate the interference of autofluorescence arising from both the fiber bundle and the specimen when observing targeted reversibly photoswitchable fluorescent proteins (RSFPs[123,159]) in several biological samples. Finally, I demonstrated that it enables multiplexed observations of two spectrally similar RSFPs, which differ by their photoswitching dynamics. The biological samples measured in this work were kindly offered by my collegues in our group, who prepared the Hela cells and the

bacterial culture, and the plant sample were provided by the agronomists.

1.2 Results

1.2.1 The Speed OPIOM microendoscope

Flexible fiber-optic based fluorescence microendoscopes have been mainly built around two designs.[241] In the first one, excitation light and fluorescence emission are transmitted through a single optical fiber. Scanning of the fiber over the sample allows one to collect fluorescence signals from each point of the specimen. To reconstruct the final images, one therefore needs additional micromechanical actuators to accurately drive the pathway followed by the fiber end.[242–245] In the second approach, flexible fiber bundles are used to deliver the excitation lights and send back the fluorescent images of the specimen. Although the lateral resolution is limited by the number of microfibers composing the bundle, large areas of the sample can be directly imaged without the need of scanning.[246] Our Speed OPIOM microendoscope exploits this second strategy with the epifluorescent fiber imaging configuration by using one-photon excitation, which enables full-frame image capture with a camera (Fig.1.2a).[247]

To implement Speed OPIOM imaging, the average intensities I_1^0 and I_2^0 of the excitation light modulated at angular frequency ω have to be constant over the whole imaged area and match the Speed OPIOM resonance condition where both I_2^0/I_1^0 and ω/I_1^0 ratios are fixed. In addition, intense excitation lights should be preferentially delivered at the sample in order to increase the modulation frequency and shorten the acquisition duration. Hence we adopted Light Emitting Diode (LEDs) as light sources since they are stable, inexpensive, easy to modulate, and suitable for the miniaturization of the device.

Our endoscope integrates two 500 mW colored LEDs with peak wavelengths at 405 and 480 nm. To insure an homogeneous illumination pattern at both wavelengths, we designed a Köhler illumination system instead of directly focusing the image of the LED chip through the objective onto the distal end of the fiber as previously described.[246] The lights emitted from the two LEDs are first collimated by a high NA condenser, band-pass filtered, and combined together with an appropriate dichroic mirror before passing through an afocal system to provide an even illumination of circular shape thanks to a round iris. Such an illumination system is particularly suited to reduce the contributions of inhomogeneities of the LED chips and of possible misalignment between both light sources. The iris is imaged at the focal plan of a 10× objective (NA=0.5), where the distal end of the fiber bundle composed of 30000 cores (average core-to-core distance of around 7μm) was placed. The excitation pathway of the endoscope terminates with a needle graded-index (GRIN) lens optically cemented at the end of the fiber bundle to deport the illumination pattern over the sample at a working distance of 50 μm with a 1× magnification.

The fluorescence image of the specimen is sent back through both the GRIN-lens and the fiber bundle and the proximal end of the bundle is further imaged by the objective. After fluorescence emission has been filtered by a bandpass filter centered at 525 nm, a tube lens permits to reconstruct the image of the proximal end onto the CMOS sensor of a cheap camera for industrial vision, which yields a 3× magnified image with an effective field of view of up to 790 μm in diameter. To further minimize instrument complexity and costs, modulation of lights and triggering of the acquisition by the camera are synchronized by an Arduino compatible card (Teensy 3.5). The series of acquired fluorescence images

are processed on PC by applying a time-domain Fourier transform in order to yield the time-averaged and out-of-phase images (subsequently denoted as Pre-OPIOM and Speed OPIOM respectively), in which the honeycomb pattern from the bundle is removed by an interpolation algorithm[248] (see section 1.5.2 in Supporting Information and Fig.S1). It is worth noting that the Pre-OPIOM image essentially compares with the fluorescence image, which would be classically recorded under constant illumination.

1.2.2 Optical characterization

Several measurements and theoretical computations have been performed to reveal the optical properties of our fluorescence microendoscope. We first analyzed the emergent light at the distal end of the fiber. Fig. 1.2b displays the experimental light intensity profile visualized by autofluorescence of a medium subsequently used for bacteria growth. It is axially symmetric and exhibits a conical shape. The emergent light at the distal end of the fiber has been simulated to further analyze the spatial evolution of the light intensity along the optical axis (see Supporting Information). Fig. 1.2c shows that the light intensity remains strictly constant within a cone up to a 1.2 mm depth. It then rapidly decays both radially and along the optical axis.

We then proceeded to calibrate the light intensities delivered by the fiber bundle by analyzing the kinetics of photoswitching of two RSFPs, Dronpa-2[141,172] and Padron,[173] which we investigated in a previous investigation[143] (see Supporting Information). Although the maximum light flux transferred by the fiber bundle is limited by the low numerical aperture of a fiber core (NA = 0.39), our optimized configuration enabled us to reach a maximal irradiance of more than 10 mW/mm^2 at the distal end of the fiber. Such an irradiance allowed us to image Dronpa-2 within a few seconds with the Speed OPIOM protocol (*vide infra*).

Fig. 1.2d and e image the normalized excitation light intensities at 480 and 405 nm across the distal end of the fiber. Both light distributions exhibit excellent spatial uniformity, with a fluctuation of less than 10% in line with the Speed OPIOM requirement discussed above.

We eventually evidenced the fiber autofluorescence under dual illumination at 480 and 405 nm. Fig. 1.2f is a fluorescence image of the proximal end of the fiber by circumventing the illuminated zone to the central area of the fiber bundle. It shows that the individual microfibers are intrinsically autofluorescent, which is usually detrimental to the image contrast and sensitivity.

1.2.3 Speed OPIOM to improve optical sectioning in fluorescence microendoscopy

To evidence the optical sectioning resulting from Speed OPIOM implementation in fluorescence microendoscopy with one-photon excitation, we collected the Pre-OPIOM and Speed-OPIOM signals in a series of Dronpa-2-labeled samples as a function of their thickness under illumination of our endoscope, which was restricted by varying the distance z between the GRIN lens and the bottom of a quartz cuvette.

We first recorded the signals from a 1 μM Dronpa-2 solution (see Fig. 1.3a). From 0 to 1 mm sample thickness, both Pre-OPIOM and Speed OPIOM signals increased linearly due to the quasi-homogeneous distribution of the excitation light within a cone extending up to 1.2 mm from the focal plan (see Fig. 1.2c). Beyond 2 mm the light distribution exiting from the fiber bundle (see Fig. 1.2c) exhibits a significant spatial decay along the optical axis. As a consequence, the Pre-OPIOM signal increases more slowly

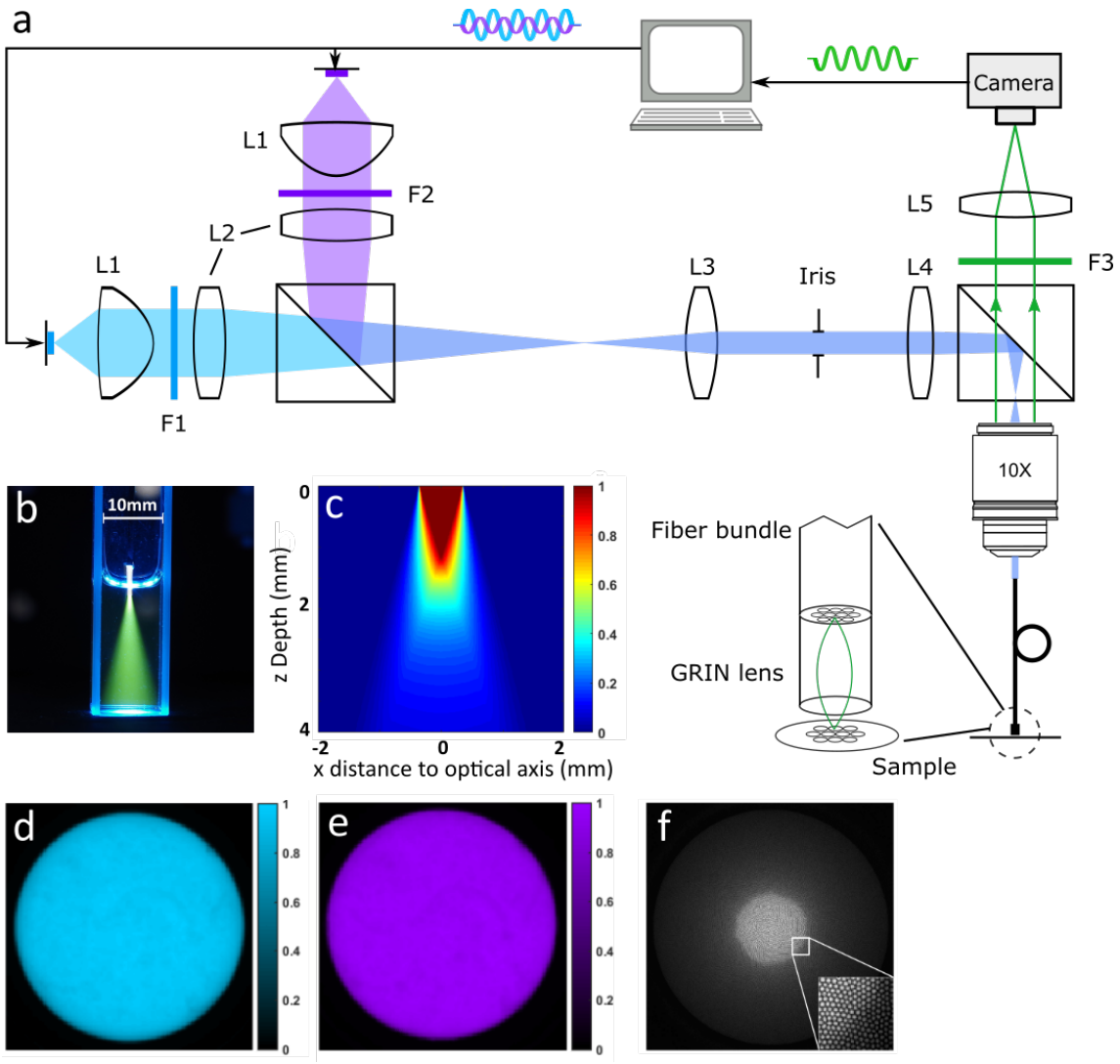

Figure 1.2 – *Fluorescence endoscopy setup for Speed OPIOM imaging*. **a**: Optical layout of the endoscope and its interface to a PC-based synchronized modulation and imaging acquisition system; **b**: Experimental light intensity profile visualized by autofluorescence of a lysogeny broth (LB) solution along the pathway of 405 nm UV light emitted from the fiber; **c**: Simulation of the excitation light intensity at the distal end of the fiber as a function of the sample depth. The computation was performed for a multimode fiber of 0.72 mm in diameter and 0.39 NA plunging into water (n=1.34); **d,e**: Normalized light intensity pattern at 480 (**d**) and 405 (**e**) nm measured at the distal end of the fiber bundle by microscopy. A uniformity better than 90% was observed over the whole surface of the fiber bundle; **f**: Autofluorescence of the fiber bundle recorded under constant illumination at 480 and 405 nm upon filtering at 525 nm. The zoomed image depicts the detail of the cores and cladding giving rise to a honeycomb artifact, and the slight core-to-core coupling.

with increasing the sample depth. In contrast, the Speed-OPIOM intensity experiences more strongly the change of light intensity by departing from resonance at constant angular frequency so that the zone at lower light intensities vanishingly contribute to the Speed OPIOM signal. Thus beyond 2 mm, the Speed-OPIOM intensity reached a plateau as if the Speed OPIOM response was originating from a spatially

restricted section of the sample, a phenomenon which is not observed in conventional fluorescence endoscopy. These conclusions could be confirmed with numerical simulations of the Pre-OPIOM and Speed OPIOM responses to the spatial profiles of exiting light intensity at the distal end of the fiber bundle. Fig. 1.3b,c show that the Speed OPIOM response is much less spatially extended laterally and along the fiber axis than the Pre-OPIOM one, which evidences the optical sectioning provided by Speed OPIOM over an imaging protocol with constant illumination.

A similar experiment has been performed on a dense suspension of Dronpa-2-expressing bacteria. In this sample, the absorption and scattering of the incident light further contribute to shaping the spatial profile of light intensity at the end of the fiber bundle. More specifically, absorption and scattering introduce an attenuation length λ_c, which restricts the spatial extension of the light profile within the sample. Fig. 1.3d shows that this phenomenon causes (i) the change of regime of the growth of the Pre-OPIOM signal to occur at a lower path length and (ii) the Pre-OPIOM signal to grow more slowly in the regime of large z than in the Dronpa-2 solution. It also explains that the saturation of the Speed OPIOM signals takes place at half the distance z observed in the Dronpa-2 solution. This trend was further observed by analyzing the behavior of Dronpa-2-containing samples of increasing opacities: The larger the sample opacity, the earlier the saturation of the Speed OPIOM signal (see Fig. S5). It was also in line with the results of numerical simulations, which demonstrated that both Pre-OPIOM and Speed OPIOM responses are spatially less extended in the bacteria suspension than in the Dronpa-2 solution (see Fig. 1.3e,f) due to the attenuation length (estimated to λ_c=3 mm), which further contributes to the spatial decay of the light profile.

We further explored the optical sectioning ability of the Speed OPIOM protocol by replacing the iris in the setup shown in Fig. 1.2a with a pinhole of 150 μm diameter in order to illuminate only a small area (a few fiber cores of the bundle; 25 μm diameter) at the proximal end of the fiber bundle. The resulting point-like source exiting the fiber was used to illuminate the 1 μM Dronpa-2 solution, and the fluorescence intensity from different locations was collected by the fiber bundle. In the corresponding Pre-OPIOM image, we observed a broad signal originating from integration of the fluorescence response over the whole illumination profile (see Fig. 1.3g). Conversely, the signal exhibited a much narrower width in the Speed OPIOM image as only a restricted portion of the illumination profile generated a significant Speed OPIOM signal (Fig.1.3j). These observations have been satisfactorily accounted for by the simulation of the spatial profiles of the Pre-OPIOM and Speed OPIOM response to single fiber illumination (see Fig. 1.3h,k) as well as of the Pre-OPIOM and Speed OPIOM signals gather by the fiber bundle (see Fig.1.3i,l).

All together, this series of experiments suggest that Speed OPIOM can selectively enhance the in-focus fluorescent signal while minimizing the out-of-focus background fluorescent signal, which results in an improvement of axial resolution for optical sectioning.

1.2.4 Speed OPIOM to eliminate autofluorescence in fluorescence microendoscopy

Two different series of experiments have been performed to illustrate the relevance of the Speed OPIOM protocol to overcome the interference of autofluorescence originating from the specimen and the fiber bundle materials, which can severly degrade image constrast in fluorescence microendoscopy.[239]

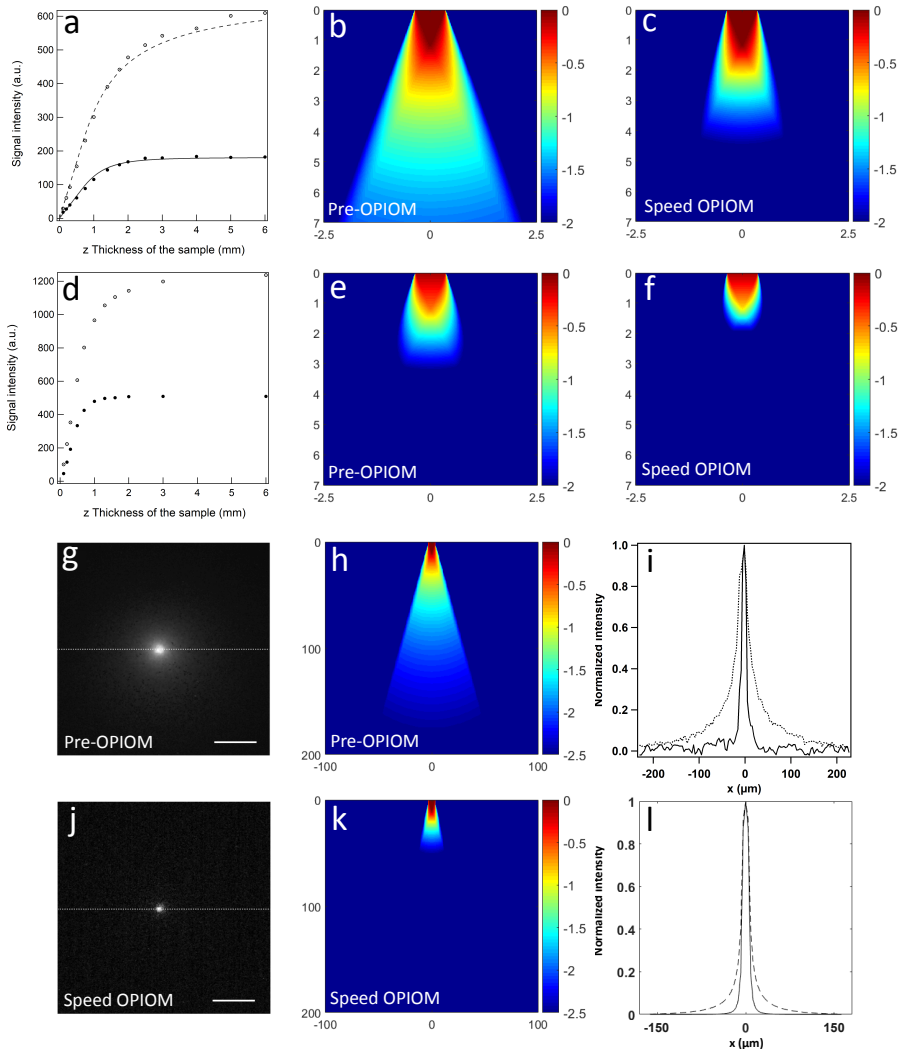

Figure 1.3 – *Speed OPIOM for optical sectioning*. **a**,**d**: Pre-OPIOM (circles) and Speed OPIOM (disks) signals collected from a 1 μM Dronpa-2 solution (**a**) and a dense suspension of Dronpa-2-expressing bacteria (**d**) as a function of the thickness z of the sample under illumination. The Pre-OPIOM and Speed OPIOM signals have been obtained after spatial averaging over a disk of 50 pixels (equivalent to a disk 60 μm in the sample) of the Pre-OPIOM and Speed OPIOM images. In **a**, the theoretical calculations of the Pre-OPIOM and Speed OPIOM signals based on the simulated illumination pattern displayed in Fig.1.2c are shown as dashed and solid lines respectively (see Supporting information for the detailed calculations); **b**,**c**,**e**,**f**: Normalized Pre-OPIOM (**b**,**e**) and Speed OPIOM (**c**,**f**) responses to the spatial profiles of exiting light intensity at the distal end of the fiber bundle based on simulated illumination pattern through the Dronpa-2 solution (**b**,**c**) and a scattering medium with a penetration length of λ_c=3 mm (**e**,**f**). Intensities are displayed in common decimal logarithmic scale. *Axis unity: mm*; **g**,**j**: Pre-OPIOM (**g**) and Speed OPIOM (**j**) images of 1 μM Dronpa-2 solution observed by fluorescence microendoscopy upon illuminating a small area (a few fiber cores of the bundle; 25 μm diameter) at the proximal end of the fiber bundle; **h**,**k**: Normalized Pre-OPIOM (**h**) and Speed OPIOM (**k**) responses to the spatial profiles of exiting light intensity at the distal end of a single microfiber based on simulated illumination pattern through the Dronpa-2 solution. Intensities are displayed in common decimal logarithmic scale. *Axis unity: μm*; **i**,**l**: Experimental (**i**) and simulated (**l**; for a single illuminated fiber) signal profiles along the dashed line in **g** and **j** (dotted and solid lines correspond to Pre-OPIOM and Speed OPIOM respectively). *Scale bar*: 100 μm.

A sensitive tool to monitor gene expression in bioreactors

In situ monitoring of cellular health in bioreactors is a challenge for industrial bioprocessing to ensure batch-to-batch reproducibility, maximize the yield of production and reduce the risk of contamination associated to sampling procedures.[249–251] In addition to the measurement of metabolites in the culture medium such as O_2, CO_2 or pH, production of fluorescent proteins (FPs) such as GFP have been recently introduced as a reporter of the status of cells or bacteria in bioreactors, which allows in turn to feedback control the culture conditions when needed[250,252] using e.g. optogenetic tools.[77,253] As a challenge to be tackled, the contribution of a strong autofluorescence due to both the complex nature of the culture broth and the number of fluorescent species with overlapping spectra[250] has to be quantitatively separated from the fluorescence signals of the reporter. A first proposed method was to extract the fluorescence signal of a reporting FP by substracting the background signal obtained from a synchronized culture of non expressing cells.[254,255] Another strategy retrieves the fluorescence signal of the reporting FP by analyzing the spectral difference between FP and the background.[157] In addition to increasing the overall complexity of the monitoring protocol, both methods require high levels of reporter expression to secure sufficient signal-to-noise ratio.

Our Speed OPIOM fluorescence microendoscope provides an efficient and minimally invasive way to accurately sense in real-time and *in situ* the production of a weakly expressed RSFP in culture medium. For illustration, Dronpa-2 was genetically encoded into *E. coli* BL21 strains with its expression under control of the lac operator. After cells were primarily grown in LB culture at 37°C, expression of Dronpa-2 was monitored every 30 or 60 minutes by plunging the fiber in 2 mL of the growth medium and acquiring Pre-OPIOM and Speed-OPIOM images. It is worthy of note that we fixed the optical path length between the fiber tip and the bottom of the vessel to 500 μm in order to circumscribe the influence of the optical density (OD) variation of the culture medium during cell growth. Fig. 1.4 displays the temporal evolution of the Pre-OPIOM and Speed OPIOM signals resulting from spatial averaging over a disk containing 50 pixels at the center of the collected images. Before induction to trigger the Dronpa-2 production by addition of isopropyl-β-D-1-thiogalactopyranoside (IPTG), it was impossible to detect the basal expression of Dronpa-2 with Pre-OPIOM since the autofluorescence arising from the fiber bundle and the culture medium (see Fig. 1.2f) exceeded the Pre-OPIOM signal from Dronpa-2 and prevented its accurate monitoring (Fig. 1.4a). In contrast, the weak Dronpa-2 expression before induction was easily detected with Speed OPIOM (Fig. 1.4b). Similarly, although we could early detect the exponential increase of the Dronpa-2 production from 6 to 12 h after IPTG addition at 5.1 h with Speed OPIOM, accurate monitoring of this increase required a further 3 h delay with Pre-OPIOM since Dronpa-2 fluorescence had first to emerge from the autofluorescence background. Hence Speed OPIOM readily enlarges the dynamic range of fluorescent reporter that can be monitored by microendoscopy. As such it is well-suited for real time monitoring of cultures of cells even at low levels of expression of the fluorescent labels.

Imaging fluorophores in plant roots under the soil with wide-field microendoscopy

In a second series of experiments, we imaged the root of a living plant (*Camelina sativa*) directly in the soil, either ubiquituously expressing Dronpa-2 or as a wild-type specimen used as a control. Both plants exhibit

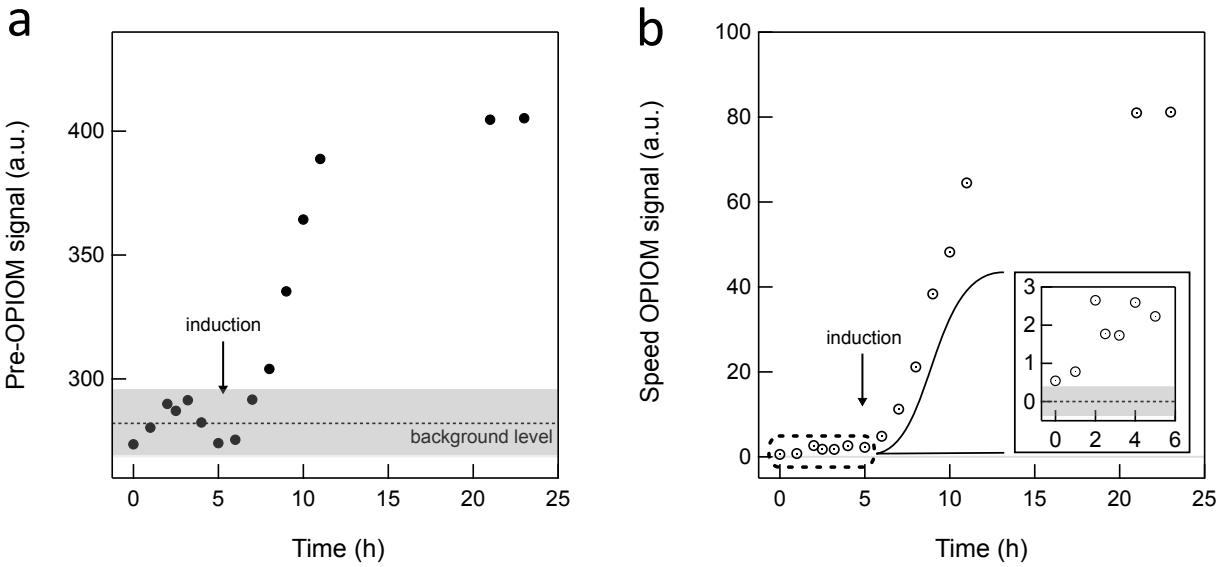

Figure 1.4 – *In situ* monitoring of Dronpa-2 expression in *E. coli* cultured in LB for 24 h using Pre-OPIOM (**a**) and Speed-OPIOM (**b**). In **b**, the insert zooms on the 0–5 h temporal window. Spatial averaging over a disk of 50 pixels at the center of the Pre-OPIOM and Speed OPIOM images yielded the signals represented in the figures. For each imaging protocol, the average background level and its incertitude ($\pm 1\sigma$) were measured with non-transfected *E. coli* BL21 strains cultured in LB (n=8). They are displayed in the figures as dashed lines and gray areas respectively. See Supporting Information for the acquisition conditions.

similar Pre-OPIOM images, which results from the high level of root autofluorescence (Fig.1.5a,b). In particular, one cannot clearly evidence Dronpa-2 expression in the labeled plant. Furthermore the contrast between the root and the background is poor, which originates from the signifiant autofluorescence of the fiber bundle. In contrast, the Speed OPIOM images are strongly different in the labeled plant and in the wild type. The Dronpa-2 expressing root is selectively imaged with a sharp contrast against the background, as expected from elimination of the autofluorescence from the root and from the fiber bundle (Fig.1.5c). This outcome is confirmed by Speed OPIOM imaging of the wild type root, which provided a black image.

Multiplexed fluorescence imaging in wide-field microendoscopy

In addition to optical sectioning and elimination of autofluorescence, Speed OPIOM is also endowed with discriminating reversibly photoswitchable fluorophores by their photoswitching dynamics. To illustrate this attractive feature, we imaged fixed Hela cells expressing green fluorescent proteins: two RSFPs, Dronpa-2 and Padron, tagging cell nucleus and mitochondria respectively, and EGFP as a spectrally interfering fluorophore, localized at the membrane. In the Pre-OPIOM images, the cells could be hardly distinguished from the fluorescent background originating from the autofluorescence of the fiber bundle, which precluded to visualize the inner structures labeled with Dronpa-2 or Padron (Fig.1.6a–c). In contrast, Speed OPIOM efficiently cancelled out the contributions of the autofluorescence background and EGFP fluorescence. Hence the RSFP signals could be selectively imaged with high contrast and reveal

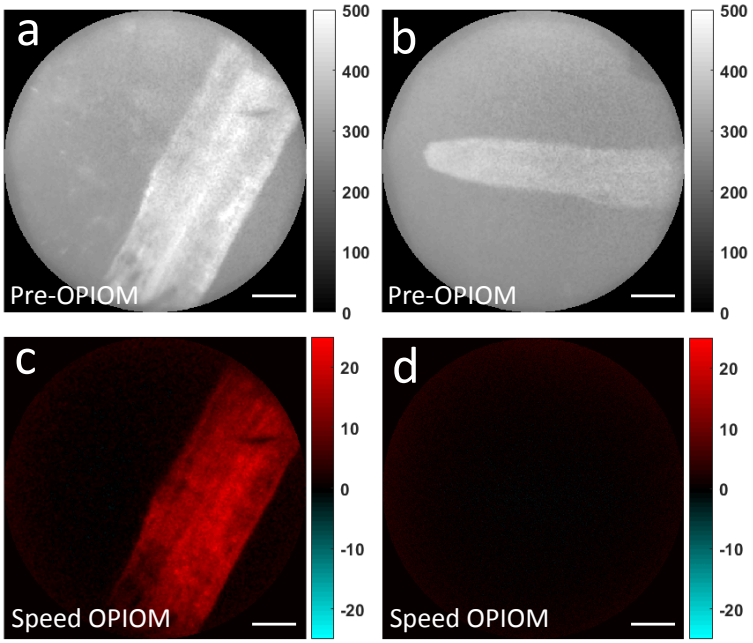

Figure 1.5 – *Images of Camelina sativa roots in soil obtained by fluorescence microendoscopy*. Pre-OPIOM (**a**,**b**) and Speed OPIOM (**c**,**d**) images of a root from a genetically transformed plant expressing Dronpa-2 (**a**,**c**) or a wild type plant as a control (**b**,**d**). *Scale bar*: 100 μm. See Supporting Information for the acquisition conditions.

the location of the RSFP-labeled structures. Furthermore, at Dronpa-2 resonance, the cell nuclei labeled with Dronpa-2 were unambiguously imaged while the structures tagged with Padron were not visible (Fig. 1.6d–f). Similarly, the mitochondria labeled with Padron were selectively imaged (Fig. 1.6g–i) without interference from the contribution of Dronpa-2 when the illumination parameters were tuned to Padron resonance. It is interesting to notice that the opposite signs of the Speed OPIOM signals associated to Dronpa-2 and Padron reflected their opposite photochromic behavior: Dronpa-2 turns dark (respectively bright) upon illumination at 480 (respectively 405) nm, whereas Padron becomes bright (respectively dark) upon illumination at 480 (respectively 405) nm. Thus Speed OPIOM emerges as an attractive protocol for multiplexed fluorescence imaging with excellent contrast in wide-field microendoscopy.

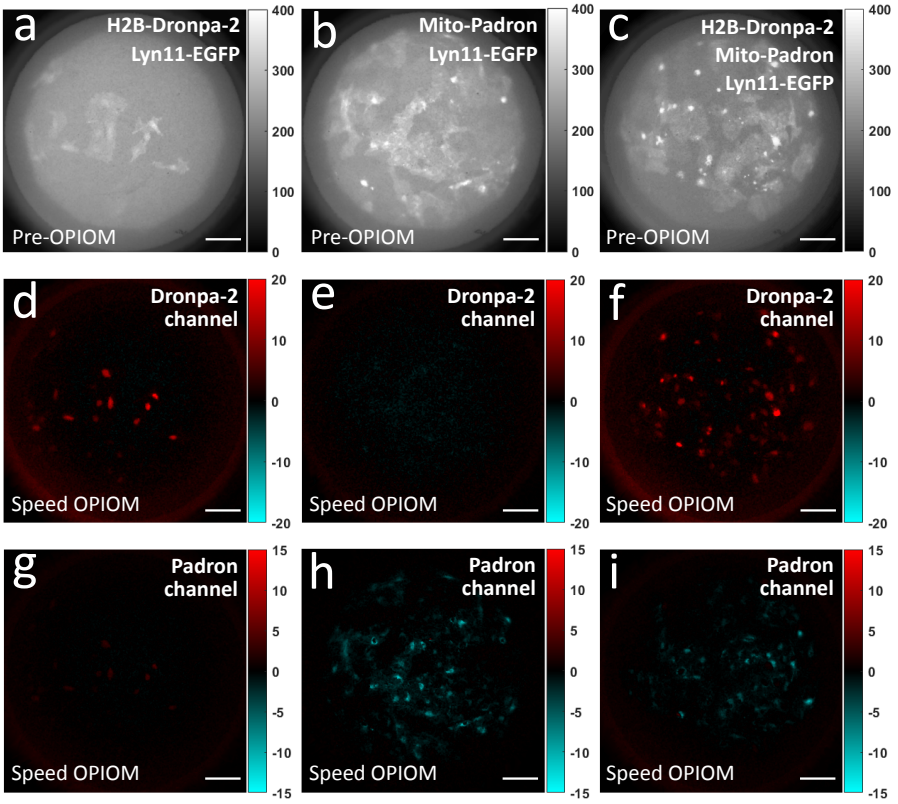

Figure 1.6 – *Speed OPIOM selectively discriminates RSFPs in fixed HeLa cells in the presence of a strong autofluorescent background*. **a**–**c**: Pre-OPIOM images; **d**–**i**: Speed OPIOM images collected under resonance conditions for Dronpa-2 (**d**–**f**) and for Padron (**g**–**i**). Systems: Fixed HeLa cells expressing Lyn11-eGFP tagging the cell membrane, H2B-Dronpa-2 tagging the nucleus, and Mito-Padron tagging the mitochondria as indicated in **a**–**c**. **a**,**d**,**g**: HeLa cells expressing H2B-Dronpa and Lyn11-EGFP; **b**,**e**,**h**: HeLa cells expressing Mito-Padron and Lyn11-EGFP; **c**,**f**,**i**: HeLa cells expressing H2B-Dronpa-2, Mito-Padron and Lyn11-EGFP. Images **e** and **g** act as negative controls to show the absence of spectral interference of (i) Padron and EGFP when using the resonance condition of Dronpa-2 and of (ii) Dronpa-2 and EGFP when using the resonance condition of Padron. *Scale bar*: 100 μm. See Supporting Information for the acquisition conditions.

1.3 Discussion

The preceding results have demonstrated that the application of the Speed OPIOM imaging protocol considerably improves the performances of an epifluorescent fiber bundle-based one-photon microendoscope. Without removing any of its advantages (cheap to construct, simple to use, and enabling full- and fast-frame rate fluorescence imaging), Speed OPIOM gives access to intrinsic optical sectioning, elimination of autofluorescence, and multiplexed observations by using a single absorption/emission channel. In the following paragraphs, we recapitulate its scope and limitations with respect to these issues.

In this account, we evidenced that the Speed OPIOM observable is relevant to endow a one-photon epifluorescence microendoscope with optical sectioning so as to significantly reduce the effective imaged volume by tuning the control parameters of illumination to resonance at the sample surface. If one adds that Speed OPIOM easily discriminates the signal from reversible photoswitchable fluorophores from autofluorescence, our configuration of fluorescence microendoscope appears especially well-suited to image superficial structures.[224] Hence one particular field of application could be imaging brain surfaces in freely moving animals. In fact, manipulating neural function with light and fast frame-rate *in vivo* imaging of neural activity are becoming increasingly important.[256,257] Speed OPIOM would eliminate the fluorescence background from out-of-focus and scattered fluorescence emissions generally encountered with conventional one-photon epi-fluorescence microendoscopy[224] (we provide further numerical simulations in Fig. S6a–d). In addition it would open an avenue to multiplexed endoscopic fluorescence observations[258] with only one wavelength channel to the most compact current setups, which are limited to imaging one genetically or anatomically defined population.[256] Eventually, it is worthy of note that our microendoscope is presently not optimized for optical sectioning with Speed OPIOM since its illumination profiles are essentially identical at 480 and 405 nm. Thus the Speed OPIOM resonance condition involving the ratio of light intensities is fulfilled along the whole illumination profile once it is satisfied in the focal plan. As a consequence, optical sectioning only relies on the departure of the second Speed OPIOM resonance condition, which involves matching light intensities and the radial frequency of the modulated light. In fact such a present limitation could be overcome by further shaping the light beams emerging from the fiber.[259–262]

Speed OPIOM has demonstrated its relevance to eliminate autofluorescence as well as spectral interferences. Yet it still suffers from the limited precision on phase retrieval when extracting the out-of-phase component of the fluorescence modulation. Indeed an error on phase retrieval will introduce into the measured signal a contribution from the in-phase component of the fluorescence modulation, which is now partially governed by the spectral interferences. We estimate our precision to $3\ 10^{-3}$ rad range, which enables us to enhance the contrast of the targeted fluorophore against spectral interferences by a factor 10^2-10^3. Another limitation may originate from the enhanced and intrinsic noise of the detector when the spectrally interfering signal is very strong.[143] Our equipment should presently allow us to specifically detect the OPIOM signal even in the presence of a 10^3 times stronger non-modulated photon source.

Eventually fluorescence microendoscopy traditionally exploits two categories of fluorescent labels depending on its applicative fields. Indocyanine green, Methylene blue, and Fluorescein can be presently used for clinical applications.[219] Biological applications are compatible with a broader library of fluorophores. In particular, the possibility to fluorescently tag biomolecules with absolute specificity through

genetic fusion provides attractive opportunities to report on gene expression, protein trafficking, and many other dynamic biochemical pathways.[1,151] OPIOM has to rely on fluorophores, which exhibit reversible photoswitching under illumination when they are exposed to light. The original OPIOM protocol exploiting resonant modulated monochromatic light can be used when the backward isomerization after forward photoswitching is thermally-driven.[140] Nevertheless the Speed OPIOM protocol[143] used in this study should be preferentially adopted when the forward and backward photoswitching processes of the reversibly photoswitchable fluorescent labels can be photochemically governed at two distinct wavelengths (e.g. in RSFPs,[123,159] cyanines,[121,132,180] and spirobenzopyrans[182]). Indeed the Speed OPIOM response is twice higher than the OPIOM one and accordingly provides a better signal-to-noise ratio. One should eventually notice that OPIOM can also be applied to non-photoswitching fluorophores, provided that they obey a photophysical mechanism, which can be dynamically reduced to a two-state model.[140] Eventually, with respect to multiplexed observations, one should underline that Speed OPIOM can already discriminate at least four spectrally similar genetically encodable fluorescent proteins. In particular, such a state-of-the art would be compatible with the endoscopic analysis of populations of microorganisms (e.g. in the rhizosphere[263] or the gut) at the single cell level in a noninvasive way.

1.4 Conclusion

In this work, we built up a fiber bundle-based fluorescent endoscopic system with modulatable one-photon excitations at two wavelengths. Upon adopting the Speed-OPIOM protocol, our cheap endoscope successively overcome the current limitations of lack of optical sectioning and autofluorescence arising from the samples or the optical components. Applying Speed-OPIOM protocol improved sensitivity both for biomonitoring and bio-imaging, as well as provided an unprecedented avenue for multiplexed fluorescent imaging. Already in the regular epifluorescence configuration, the superior performances of Speed OPIOM imaging over conventional fluorescence are likely to find applications in diverse areas such as bioprocessing, clinical diagnostics, plant observation, and surface imaging.

1.5 Supporting Information and Experimental Section

1.5.1 Endoscopic setup for fluorescence imaging

Setup configuration

The optical layout of the device is illustrated in Fig. 1.2. The setup uses two high power color LED chips (LXZ1-PB01, LHUV-0400, LXZ1-PX01; Lumileds, Amsterdam, Netherlands) as excitation lights. Their lights are collimated by optical condensors L1 (ACL2520U-A, f = 20 mm, Thorlabs, Newton, NJ) and filtered by band pass filters (ET470/40x, ET405/20x; Chroma Technology, Bellows Falls, VT). The UV and blue beams are combined by a dichroic mirror (T425LPXR, Chroma Technology) and sent to an afocal system, which consists of two convergent lenses (L2: AC254-100-A, f = 100 mm, L3: AC254-040-A, f = 40 mm; Thorlabs). An iris (SM1D12C, Φ_{max} = 12 mm, Thorlabs) is positioned at the exit pupil of the afocal system through which lights with different field angles pass. The iris is also at the focal plan of the lens L4 (AC254-100-A, f = 100 mm, Thorlabs), which is used to conjugate the iris stop to the focal

plan of the objective (10×, NA=0.5, Zeiss, Jena, Germany). The effective NA of the objective matches the NA of the fiber to secure a maximal light delivery. The imaging fiber (FIGH-30-850N, Fujikura, Tokyo, Japan) is a fused silica-based coherent fiber bundle, which consists of 30000 cores of about 5 μm in diameter with a core to core distance of around 7 μm. A GRIN lens (NEM-100-06-08-520-S, GrinTech, Jena, Germany) with a magnification of 1:1 is cemented onto the distal tip of the fiber. The fluorescence image transferred from the fiber is magnified by the objective, filtered by a emission filter (ET525/36m, Chroma Tech.) and focused onto the camera (3060cp, iDS, Obersulm, Germany) by a tube lens of f = 50 mm (AC254-050-A, Thorlabs). The effective magnification goes to 3X.

Video acquisition

In the imaging experiments, we record films for m periods of light modulation (m is an integer). The acquisition frequency of the camera is set so as to obtain $2N$(N is an integer) frames per period of modulation. Thus the acquisition frequency is $f_s = 2Nf_m$, where f_m is the modulation frequency of the excitation light. The fluorescence emission acquired at pixel(x,y) of the k^{th} frame is equal to

$$I_{\text{F}}(x,y,k) = T_s\left(\Im_{\text{F}}^{0}(x,y) + \sum_{n=1}^{N}\left\{\Im_{\text{F}}^{n,\sin}(x,y)\sin\left[\frac{\pi n f_s}{N}\left(\frac{k}{f_s}+\phi_{\text{acq}}\right)\right] + \Im_{\text{F}}^{n,\cos}(x,y)\cos\left[\frac{\pi n f_s}{N}\left(\frac{k}{f_s}+\phi_{\text{acq}}\right)\right]\right\}\right) \tag{1.1}$$

where $T_s = \frac{1}{f_s}$ refers to the exposure time of one frame, $\Im_{\text{F}}^{n,\sin}(x,y)$ and $\Im_{\text{F}}^{n,\cos}(x,y)$ are respectively the sinus and cosinus components of the fluorescence signal at harmonic n around the average value $\Im_{\text{F}}^{0}(x,y)$, and ϕ_{acq} is a time lag, which may originate from distinct starting times for the light modulation and the acquisition of the camera. ϕ_{acq} can be easily calibrated by using the fluorescence emission from instantaneously responding fluorophores (such as EGFP or Fluorescein).

Pre-processing has been performed over the video to compensate for possible photobleaching of the fluorophores. By assuming the photobleaching to exhibit a linear decay, the compensation factor has been calculated from the average of two successive periods:

$$K(x,y) = \frac{\langle I_{\text{F}}(x,y,k)\rangle_{k=2N}^{4N-1} - \langle I_{\text{F}}(x,y,k)\rangle_{k=0}^{2N-1}}{2N} \tag{1.2}$$

Then all the frames over the two periods are corrected as in Eq.(2.3)

$$I_{\text{F}}^{\text{corr}}(x,y,k) = I_{\text{F}}(x,y,k) - K(x,y)\times k \tag{1.3}$$

All the frames over the whole video have been corrected for photobleaching by applying the same algorithm for all the successive pairs of two periods.

The Pre-OPIOM image $\Im_{\text{F}}(x,y)$ is calculated by averaging the frames over the whole film and normalizing to unit time

$$\Im_{\text{F}}^{0}(x,y) = \frac{f_s}{2mN}\sum_{k=0}^{2\text{mN}-1} I_{\text{F}}^{\text{corr}}(x,y,k) \tag{1.4}$$

The demodulation is done by multiplying the k^{th} frame $I_{\text{F}}^{corr}(x,y,k)$ with $\cos\left[\frac{\pi n f_s}{N}\left(\frac{k}{f_s}+\phi_{\text{acq}}\right)\right]$ and by averaging over the whole film to get the first order cosinus component, namely the Speed OPIOM

image:

$$\Im_{\mathrm{F}}^{1,\cos} = \frac{f_s}{mN} \sum_{k=0}^{2\mathrm{mN}-1} \left\{ I_{\mathrm{F}}^{\mathrm{corr}}(x, y, k) \times \cos\left[\frac{\pi n f_s}{N} \left(\frac{k}{f_s} + \phi_{\mathrm{acq}} \right) \right] \right\} \tag{1.5}$$

Acquisition parameters used for Speed OPIOM imaging

Figure	Periods	f_s (Hz)	f_m (Hz)	$\lambda_{ex,1}$ nm	I_1^0 Ein.m^{-2}.s^{-1}	$\lambda_{ex,2}$ nm	I_2^0 Ein.m^{-2}.s^{-1}
1.3g,j	8	60	3.0	480	4.8×10^{-2}	405	2.3×10^{-2}
1.5a-d	8	60	3.0	480	4.8×10^{-2}	405	2.3×10^{-2}
1.6a,d-f	8	60	3.0	480	4.8×10^{-2}	405	2.3×10^{-3}
1.6b,c,g-i	2	10	1/8	480	5×10^{-2}	405	1.6×10^{-2}

Table S1 – Acquisition parameters used for Speed OPIOM imaging in Figures 1.3, 1.5, and 1.6 of the Main Text. f_s and f_m respectively refer to the sampling rate and to the modulation frequency of the excitation lights.

1.5.2 Reconstruction of the Pre-OPIOM and OPIOM images by removal of the comb pattern

The images shown in the Main Text have been corrected from the artifact originating from the comb structure of the fiber bundle by applying an algorithm based on spatial interpolation on the crude images (see Fig.S1).[248] The algorithm first localizes the centers of the individual fiber core through the image, which defines a set of local maximum points P_i identified by their coordinates and absolute fluorescence levels. The image is then segmented with a Voronoi diagram based on the set of points P_i so that the natural neighbours of any point in the rest of the image $Q \notin P_i$ can be easily defined. The fluorescence level at the point Q is eventually calculated as the weighted average of its neighbours, where the weight depends on its geometric relation to each neighbouring points.

Matlab Code to generate Speed OPIOM images with interpolation algorithm

```
%%% 'im' is the raw image.
ref=imgaussfilt(im,0.4);%pre-processing helps better find the regional maxima
BW=imregionalmax(ref,4);%find regional maxima of the image

im_core=im.*BW; %the maximal points representing the fiber cores are selected
[Xs,Ys,Vs]=find(im_core);% find the coordinates and the absolute values of the cores

% natural interpolation
F = scatteredInterpolant(Xs,Ys,Vs,'natural');
[Xq,Yq]=find(~BW);
Vq=F(Xq,Yq);
```

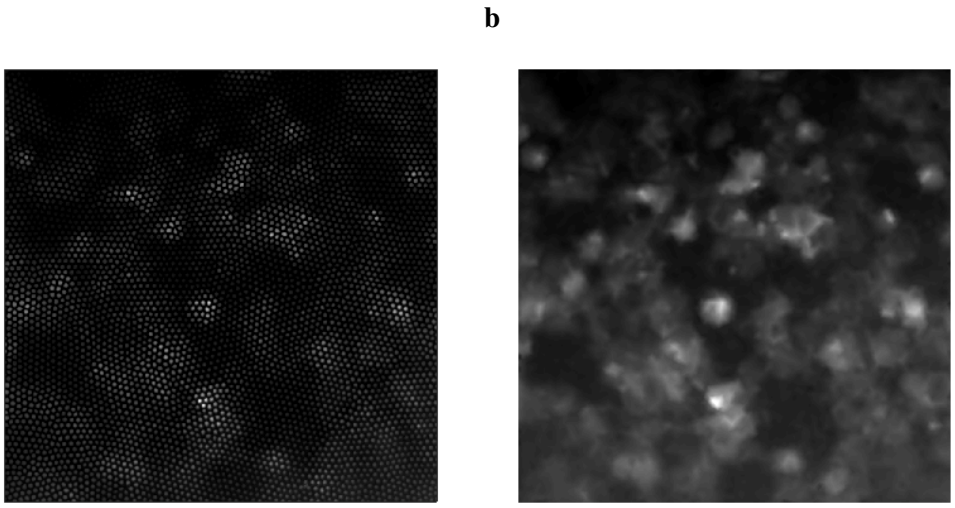

Figure S1 – Removal of the comb pattern in a Pre-OPIOM images acquired in endoscopy. **a**: Crude image acquired from the endoscope. **b**: Reconstructed image. Note that the algorithm retains the original fluorescence level imaged from the fiber and smooths the whole image without losing the lateral resolution defined by one bundle core. See Text for details.

```
%%%

%replace the other points with the calculated interpolation values
im_inter=zeros(size(im));
ind=sub2ind(size(im),Xq,Yq);
im_inter(ind)=Vq;
im_final=im_inter+im_core;% artifact-removed image
figure; h=imagesc(im_final);axis equal tight;axis off;
```

1.5.3 Simulation of the Pre-OPIOM and OPIOM signals in fluorescence microendoscopy

Calculation of the spatial profiles of exiting light intensity at the distal end of the fibers

Assumptions The emergent light from a 1X magnification GRIN lens[a] attached to the distal end of the fiber bundle plunging into a medium of refractive index n was computed by making several approximations:

- The intensity is considered to be constant across the distal surface of the fiber. This approximation results from uniformly illuminating the fiber thanks to the Köhler system (see Fig. 1.2d,e);

- The radiance L of the fiber distal end is angularly constant (Lambertian source) within the acceptance angle. Indeed, the radiance from each point of the LED source is homogeneous. After being imaged

[a]The magnification of the GRIN lens being 1, Abbe sine condition $y \cdot n\sin(\alpha) = y' \cdot n'\sin(\alpha')$, ($n, n'$: the refractive index of object space and image space, α, α': angle of the ray to the optical axis when it reaches object and image plan; y, y': object and image heights) implies that NA at the exit of the grin lens equals to that of the fiber ($NA = NA' = n\sin(\alpha_m) = n'\sin(\alpha'_m)$).

to infinity after the optics, the spatial homogeneity of the LED chip is transferred to the angular homogeneity of the radiance at the distal end;

- Absorption or scattering of light in the propagation medium can be characterized as: $I(\lambda) = I_0 10^{-\frac{\lambda}{\lambda_c}}$, where I designates light intensity. λ is the light path through the medium and λ_c is the characteristic length of penetration, after passing through which the intensity falls to $\frac{1}{10}$ of its value at the origin;

- The simulation starts from the focal plan, which can be considered close to the GRIN lens surface (<50 μm).

Calculation of the spatial intensity profile We first analyzed the spatial profile of the exiting light intensity at the distal end of a fiber of radius R_0. Since the light distribution is rotationally symmetric to the optical axis, we only computed the light irradiance I at medium points $(r, 0, z)$ identified by their cartesian coordinates with origin set at the center of the exit surface of the GRIN lens (see Fig. S2).

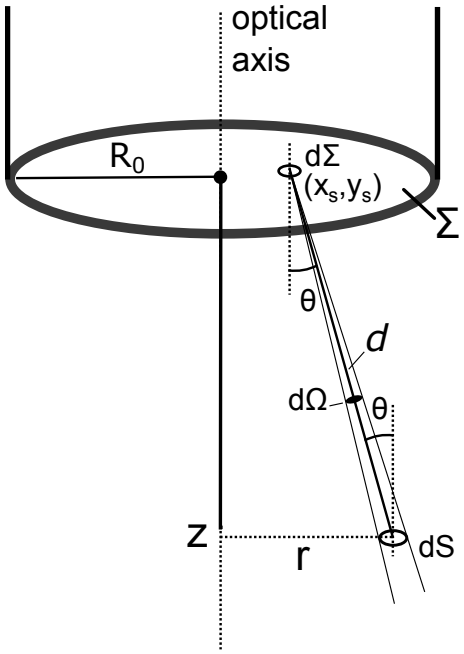

Figure S2 – Schematic representation of the fiber for simulation of the excitation light intensity at the distal end of the fiber as a function of the sample depth.

One has

$$I(r, 0, z) = \frac{\mathrm{d}\Phi_F(r, 0, z)}{\mathrm{d}S} \tag{1.6}$$

where r is the distance to the optical axis of the fiber, z is the depth from the end of the GRIN lens and $\Phi_F(r, 0, z)$ is the photon flux passing through an element of area $\mathrm{d}S$ at $(r, 0, z)$.

When analyzing the points $(r, 0, z)$ close to the fiber ($z \sim 2R_0$), the exit end of the fiber is considered as a surface source Σ. Each element of surface $\mathrm{d}\Sigma$ at $(x_s, y_s, 0)$ is considered lambertian within an

acceptance angle θ_m. The radiance can be expressed as:

$$L(\theta) = \begin{cases} L_s & \theta \leqslant \theta_m \\ 0 & \theta > \theta_m \end{cases}$$

where θ is the angle between the light ray and the normal of the surface Σ. The acceptance angle is defined by the numerical aperture of the fiber in use, NA= $n\sin(\theta_m) = 0.39$, where n is the refractive index of the medium around the fiber.

The flux received by dS at $(r, 0, z)$ from the source element dΣ at $(x_s, y_s, 0)$ is:

$$\mathrm{d}^2\Phi_F = L(\theta)10^{-\frac{d}{\lambda_c}}\mathrm{d}^2G = L(\theta)10^{-\frac{d}{\lambda_c}}\frac{\mathrm{d}S\mathrm{d}\Sigma\cos^2\theta}{d^2} = L(\theta)10^{-\frac{d}{\lambda_c}}\frac{\mathrm{d}S\mathrm{d}\Sigma\cos^4\theta}{z^2} \tag{1.7}$$

In Eq.(1.7), G is the *etendue* defined as

$$\mathrm{d}^2G = \mathrm{d}\Sigma\cos\theta\mathrm{d}\Omega_\Sigma = \frac{\mathrm{d}\Sigma\mathrm{d}S\cos^2\theta}{d^2} \tag{1.8}$$

where d is the distance between dΣ and dS, and $\cos\theta = \frac{z}{d} = \frac{z}{\sqrt{(r-x_s)^2+y_s^2+z^2}}$ (see Fig. S2).

Finally we get the irradiance at $(r, 0, z)$ from the entire surface Σ:

$$\begin{aligned} I(r,0,z) &= \frac{\mathrm{d}\Phi_F(r,0,z)}{\mathrm{d}S} = \frac{1}{\mathrm{d}S}\int_\Sigma \mathrm{d}^2\Phi_F(r,0,z) \\ &= \frac{1}{\mathrm{d}S}\int_\Sigma \frac{L(\theta)\mathrm{d}\Sigma\mathrm{d}S\cos^2\theta}{d^2}10^{-\frac{d}{\lambda_c}} = \int_\Sigma \frac{L(\theta)\cos^4\theta}{z^2}10^{-\frac{d}{\lambda_c}}\mathrm{d}\Sigma \end{aligned} \tag{1.9}$$

This general expression has been used to calculate the intensity pattern of a single fiber core of R_0=3 μm, and the entire fiber bundle of R_0=0.72 mm. Indeed, since the fiber cores are extremely small and tightly packed, the distal end of the fiber bundle can be considered as an entire light-emitting source regardless of the core structures.

Calculation of the Pre-OPIOM and OPIOM responses to the spatial profiles of exiting light intensity at the distal end of the fibers

In the following, we consider that the Speed OPIOM resonance is fulfilled in the focal plan ($z = 0$). We correspondingly adopt

$$\frac{I_1(0,0,0)}{I_2(0,0,0)} = \rho_I \tag{1.10}$$

$$\omega\tau_{12}^0(0,0,0) = 1 \tag{1.11}$$

where the ratio ρ_I depends on the photoswitching properties of the fluorescent label and $\tau_{12}^0(r,0,z)$ designates the relaxation time associated to photoswitching under illumination with $I_1(r,0,z)$ and $I_2(r,0,z)$ (see Eqs.(101,102) of the Supporting Information of the reference[143]). Neglecting any chromatic aberration of the fluorescence microendoscope and assuming that the medium exhibits similar absorption and scattering towards lights at the two wavelengths 480 and 405 nm, we then conclude that the ratio ρ_I is constant within the irradiance profile.

Equipped with the preceding information, one can easily calculate the spatial evolution of the Pre-OPIOM and Speed OPIOM response from the computed spatial profiles of light intensity. Indeed they exhibit a well-defined dependence on the light intensities I_1^0 and I_2^0, which are given in Eqs.(98,100) of the Supporting Information of the reference.[143]

- Pre-OPIOM response. At constant ratio ρ_I, the profile of Pre-OPIOM fluorescence intensity $\Im_F^0$ can be written

$$\Im_F^0 = \mathfrak{C}^0 \times I_1(r,0,z) \tag{1.12}$$

where $\mathfrak{C}^0$ designates a constant, which depends on the brightness of the fluorophore states, ρ_I, the cross sections for forward and backward photoswitching at both wavelengths, and the fluorophore concentration;

- Speed OPIOM response. At constant ratio ρ_I, the profile of Speed OPIOM fluorescence intensity $\Im_F^{1,cos}$ can be written

$$\Im_F^{1,cos} = \mathfrak{C}^{1,cos} \times I_1(0,0,0)\frac{[I_1(r,0,z)]^2}{[I_1(0,0,0)]^2 + [I_1(r,0,z)]^2} \tag{1.13}$$

where $\mathfrak{C}^{1,cos}$ designates a constant, which depends on the brightness of the fluorophore states, ρ_I, the cross sections for forward and backward photoswitching at both wavelengths, and the fluorophore concentration. The first Speed OPIOM resonance condition (1.10) is verified at each position of the illuminated zone since ρ_I remains there constant. In contrast, the second Speed OPIOM resonance condition (1.11) directly involves the light intensities (see Eqs.(13–16,18) of the Supporting Information of the reference[143]) and not anymore their ratio. As a consequence, it is only verified in the focal plane, which correspondingly generates a faster spatial decay of the response and an associated better axial selectivity in Speed OPIOM than in Pre-OPIOM.

Simulation of the collected Pre-OPIOM and Speed OPIOM signals from variable thickness of solution

In the following, we still assume that the Speed OPIOM resonance conditions are satisfied at the focal plan at $z = 0$. The fluorescence collected by the fiber arises from the solution under illumination of the fiber. We consider a dz-thick layer of fluorescent solution at depth z. The intensities of the Pre-OPIOM and Speed OPIOM signals generated from the layer are respectively given in Eqs.(1.14,1.15)

$$\mathrm{d}I_{PreOPIOM}(z) = \mathrm{d}z \cdot \int \mathfrak{C}^0 \cdot I_1(r,0,z) \cdot 2\pi r \mathrm{d}r \tag{1.14}$$

$$\mathrm{d}I_{OPIOM}(z) = \mathrm{d}z \cdot \int \mathfrak{C}^{1,cos} \cdot I_1(0,0,0)\frac{[I_1(r,0,z)]^2}{[I_1(0,0,0)]^2 + [I_1(r,0,z)]^2} \cdot 2\pi r \mathrm{d}r. \tag{1.15}$$

The fluorescence signals collected from the solution of depth z by the fiber with S_{fiber} detection surface integrate the contribution of all the layers within the depth of z. As the S_{fiber} and the illuminated layer at depth z, $S_{layer}(z)$, are small with respect to the distance z between them, we write

$$I_{PreOPIOM}(z) = \int_0^z \frac{S_{fiber}\mathrm{d}I_F(z)}{z^2} \tag{1.16}$$

$$I_{OPIOM}(z) = \int_0^z \frac{S_{fiber}\mathrm{d}I_{OPIOM}(z)}{z^2} \tag{1.17}$$

The calculation was performed using MatLab, the $\mathfrak{C}^0$ and $\mathfrak{C}^{1,cos}$ were deduced according to the experimental measurements of Pre-OPIOM and Speed OPIOM respectively.

Matlab Code for the calculation of Pre-OPIOM and Speed OPIOM responses at the exit of the fiber

```
% 'R0' is the radius of the fiber
% 'NA' is the numerical aperture of the fiber
% 'n_r' is the refractive index of the medium
% 'lambda' is the characteristic penetration length of the light in scattering medium

theta=asin(NA/n_r);% acceptance angle of the fiber
delta=0.0005; % size of the differential element on the distal end
xs=-r0:delta:r0;
ys=-r0:delta:r0;
[X,Y]=meshgrid(x,y);
fiber=sqrt(X.^2+Y.^2)<R0;% the fiber is round shape

%discretization of the coordinates (r,0,z)in the space
d_r=0.01;d_z=0.5;
r=0:d_r:20; r=r';
z=0.5:d_z:60; z=z';

m=length(r); n=length(z);
I=zeros(n,m);
for i=1:m
  for j=1:n
  D = sqrt((r(i)-X).^2+(Y).^2+z(j)^2);%distance between the two elementary surfaces
  cone = sqrt((X-r(i)).^2+Y.^2)<(z(j)*tan(theta));%acceptance cone
  surface = fiber&cone;
  %effective area of the fiber facet that contribute to the illumination of this point
  G = delta^2*(z(j)./D).^4./(z(j)^2).*10.^(-D/lambda);
  %solid angle and scattering coefficient
  I(j,i) = sum(G(surface)); irradiance on point (r,0,z)
  end
end

B=I(:,2:m);
B=fliplr(B);
I=[B I];%symmetrical extension

I0=max(I(:));% resonance condition occurs at the maximal intensity

I_opiom=I.*((I0.*I)./(I0^2+I.^2)); %calculation of the Speed OPIOM response
```

```
IN=I/max(I(:)); %normalization
IN_opiom=I_opiom/max(I_opiom(:));\normalization
```

1.5.4 Calibration of light intensity

Speed OPIOM implementation requires to determine the intensity of the two excitation lights at the sample (typically at 480 and 405 nm) so as to fulfill the resonant illumination conditions for the desired reversibly photoswitchable fluorescent proteins. Instead of using a powermeter, we directly exploited the dynamical photochemical properties of the RSFPs for calibrating the light intensities.

The principle of the calibration experiments is to measure the relaxation time associated to the conversion between the on and off RSFPs states by applying light jumps on a RSFP-containing sample. We typically used fixed Hela cells expressing Dronpa-2 or Padron as the calibrating sample put at the focal plan of the endoscope. In the first step, the sample was submitted to a light jump at 480 nm with constant light intensity I_1^0, in which the current of the LED source was set around 500 mA to give the maximal power. Upon illumination, the RSFP switched from its thermodynamically stable state to its photoisomerized state, and the fluorescence image was recorded as a function of time. The fluorescent signal (usually obtained by averaging over the image) was then plotted as a function of time (Fig. S3a, S4a) and was fitted with Eq.(2.6):

$$I_F(t) = I_F(0, \lambda_1) + \mathcal{A}_{\lambda_1}\left[1 - \exp\left(-\frac{t}{\tau_{\lambda_1}}\right)\right] \tag{1.18}$$

where $\mathcal{A}_{\lambda_1}$ is a pre-exponential term, which accounts for the molecular brightnesses of the ON and OFF states as well as their relative proportions (see[143]). τ_{λ_1} was extracted from the fit and I_1^0 could be then retrieved from Eq.(1.19):

$$\frac{1}{\tau_{\lambda_1}} = k_{21}^{\Delta} + (\sigma_{12,\lambda_1} + \sigma_{21,\lambda_1})I_1^0 \tag{1.19}$$

where σ_{12,λ_1} and σ_{21,λ_1} are respectively the molecular action cross-sections for photoisomerization, which converts **1** to **2** and **2** to **1** (see[143]). In the second step, while I_1^0 was still maintained at its original value, the sample was submitted to a light jump at 405 nm at constant light intensity I_2^0. A reversed switch took place. The temporal evolution of the fluorescence emission was recorded (see Fig. S3b,S4b) and fitted with Eq.(1.20):

$$I_F(t) = I_F(0, \lambda_1, \lambda_2) + \mathcal{A}_{\lambda_1\lambda_2}\left[1 - \exp\left(-\frac{t}{\tau_{\lambda_1\lambda_2}}\right)\right] \tag{1.20}$$

where $\mathcal{A}_{\lambda_1\lambda_2}$ is a pre-exponential term, which accounts for the molecular brightnesses of the ON and OFF states as well as their relative proportions (see[143]). $\tau_{\lambda_1\lambda_2}$ was extracted from the fit and I_2^0 could be then retrieved from Eq.(1.21):

$$\frac{1}{\tau_{\lambda_1\lambda_2}} = k_{21}^{\Delta} + (\sigma_{12,\lambda_1} + \sigma_{21,\lambda_1})I_1^0 + (\sigma_{12,\lambda_2} + \sigma_{21,\lambda_2})I_2^0 \tag{1.21}$$

where $\sigma_{12,\lambda_1} + \sigma_{21,\lambda_1}$ and $\sigma_{12,\lambda_2} + \sigma_{21,\lambda_2}$ are respectively the molecular action cross-sections for photoisomerization at wavelength λ_1 or λ_2, which converts **1** to **2** and **2** to **1**.

After repeating this experiment for several values of I_1^0 and I_2^0, we could use the reported values of $\sigma_{12,\lambda_1} + \sigma_{21,\lambda_1} = 196$ m^{2}mol^{-1} and $\sigma_{12,\lambda_2} + \sigma_{21,\lambda_2} = 413$ m^{2}mol^{-1} for Dronpa-2,[143] to finalize the calibration linking the current intensities applied to the LEDs with I_1^0 and I_2^0.

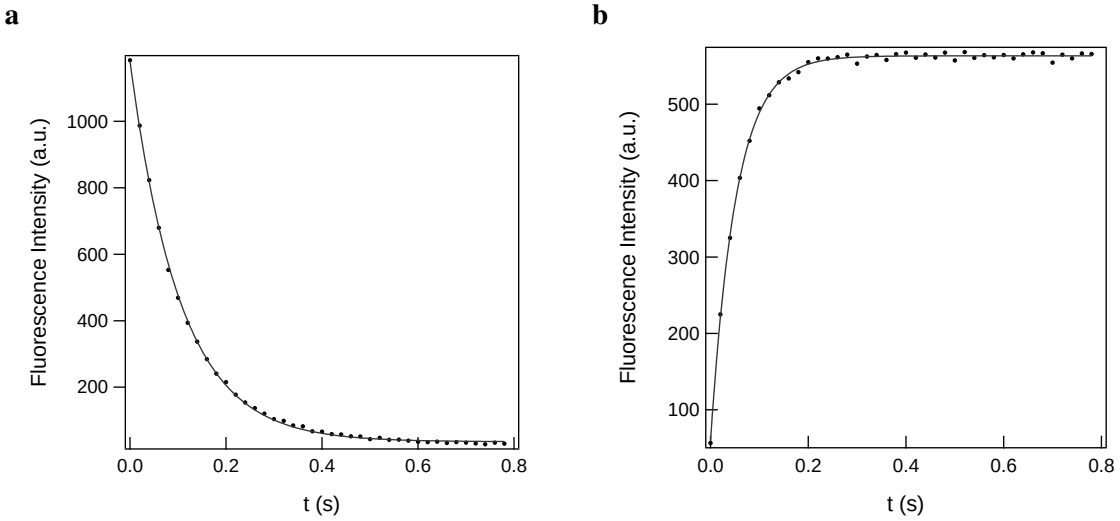

Figure S3 – Photoisomerization kinetics of Dronpa-2. **a**: Evolution of the fluorescence emission of Dronpa-2 upon illumination at 480 nm (I_1^0 = 4.8 × 10^{-2} Ein.$m^{-2}s^{-1}$); **b**: Evolution of the fluorescence emission of Dronpa-2 upon illumination at both 480 and 405 nm (I_1^0 = 4.8 × 10^{-2} Ein.$m^{-2}s^{-1}$ and I_2^0 = 2.3 × 10^{-2} Ein.$m^{-2}s^{-1}$).

1.5.5 Autofluorescence of the fiber bundle

The fiber bundle exhibits a significant autofluorescence under illumination in the UV range. For illustration, we imaged at 525 nm in the air the distal end of the fiber bundle upon reducing the illumination zone by the iris so that only the central area of the fiber bundle was illuminated with at 480 (I_1^0 = 4.8 × 10^{-2} Ein.$m^{-2}.s^{-1}$) and 405 (I_2^0 = 1.6 × 10^{-2} Ein.$m^{-2}.s^{-1}$) nm. After averaging 20 images, we obtained the image displayed in Fig.1.2f.

1.5.6 Materials

Reversibly photoswitchable fluorescent proteins

The RSFPs used in this study are Dronpa-2[141,172] and Padron,[173] which belong to the Dronpa[183] family. Dronpa-2 contains only one mutation M159T and Padron contains eight mutations: T59M, V60A, N94I, P141L, G155S, V157G, M159Y and F190S.

Plasmids

The plasmids for bacterial and cellular expression of Dronpa-2, Padron and EGFP, and the plants (*Camelina* and *Arabidopsis*) expression vector expressing p35S::Dronpa-2; pCVMV::DsRED construct have been previously described.[143]

Protein production and purification

The plasmid expressing Dronpa-2 carrying an N-terminal hexahistidine tag was transformed in *E. coli* DH10B strain. Cells were grown in Terrific Broth (TB). Expression was induced by addition of isopropyl

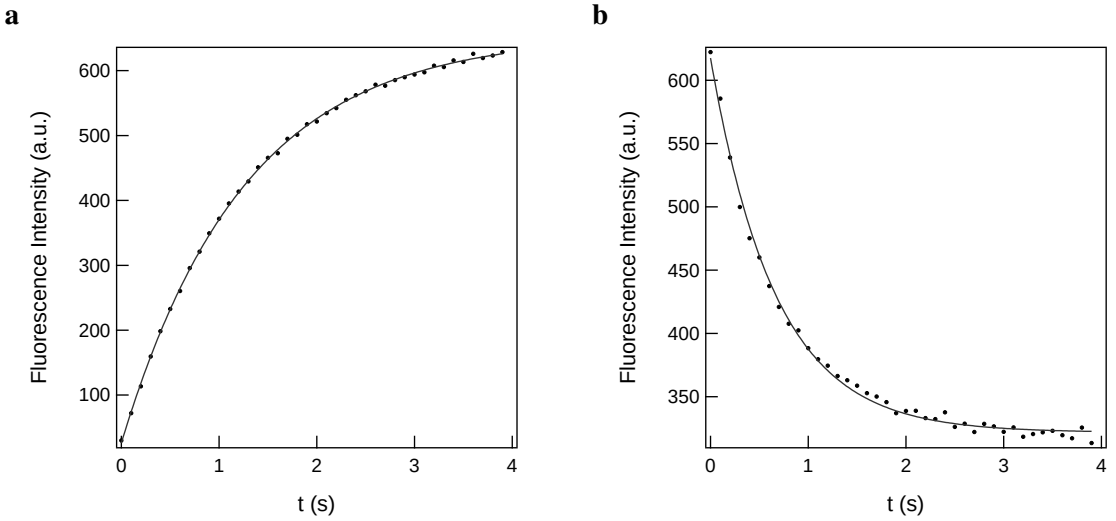

Figure S4 – Photoisomerization kinetics of Padron. **a**: Evolution of the fluorescence emission of Padron upon illumination at 480 nm ($I_1^0 = 5 \times 10^{-2}$ Ein.m^{-2}s^{-1}); **b**: Evolution of the fluorescence emission of Padron upon illumination at both 480 and 405 nm ($I_1^0 = 5 \times 10^{-2}$ Ein.m^{-2}s^{-1} and $I_2^0 = 1.6 \times 10^{-2}$ Ein.m^{-2}s^{-1}).

β-D-1-thiogalactopyranoside (IPTG) to a final concentration of 1 mM at OD(600 nm)=0.6. Cells were harvested after 16 h of expression and lysed by sonication in Lysis buffer (30/40 mM imidazole, 50 mM Tris/HCl at pH 7.5, 400 μM 1-(2-Aminoethyl) benzenesulfonyl fluoride hydrochloride, 5 mg/mL DNAse, 5 mM $MgCl_2$ and 1 mM dithiothreitol). Insoluble materials were removed by centrifugation and the soluble protein extract was batch absorbed onto Ni-NTA agarose resin (Thermofisher). The protein loaded Ni-NTA column was washed with 20 column volumes of 50 mM TRIS/HCl pH 7.5, 20 mM imidazole, 150 mM NaCl. Bound protein was eluted in 50 mM TRIS/HCl pH 7.5, 500 mM imidazole, 150 mM NaCl. Protein fractions were dialyzed on cassette Slide-A-Lyzer Dialysis Cassettes (Thermofisher) against 50 mM TRIS/H_2SO_4 pH 8.0.

Cultures of Escherichia coli

Dronpa-2 was expressed in E. coli BL21 strain. Cells were grown into 2 mL of lysogeny broth (LB) at 37°C, 220 RPM for 1 h. Cells were platted at low density on LB agar plates, and plates were incubated overnight at 37°C. Dronpa-2 single colonies were then separately transfered to LB-ampicillin media and incubated at 37°C, 220 RPM. Cells were then diluted and grown in LB at 37°C, 220 RPM. Expression was induced at 30°C by addition of isopropyl β-D-1-thiogalactopyranoside (IPTG) to final concentration of 1mM at OD(600)= 0.6.

Plant transformation and growth

Camelina sattiva(cv Celine) was transformed with *Arabidopsis* floral-dip method and transgenic were selected as described previously.[185] *Arabidopsis* and *Camelina* seeds were sown respectively on sucrose-supplemented medium[186] or water-soaked paper and grown for 7 days in a growth chamber under cycles of 16 h light / 8 h dark at 22°C.

Mammalian cell culture

U2OS HTB-96 (ATCC lot 64048673) cells were cultured in McCoy's 5A medium supplemented with phenol red and 10% (vol/vol) fetal calf serum (FCS), at 37 °C in a 5% CO_2 atmosphere. For imaging, cells were seeded in μDish IBIDI (Biovalley) coated with poly-L-lysine. Cells were then transiently transfected with 2 μg total DNA using Lipofectamine 2000 (Invitrogen) according to the manufacturer's protocol for 24 hours prior to fixing. Samples were washed with 1X DPBS and then fixed for 15 minutes in 4% paraformaldehyde. Imaging was performed in 1X DPBS.

1.5.7 Supplementary Figures

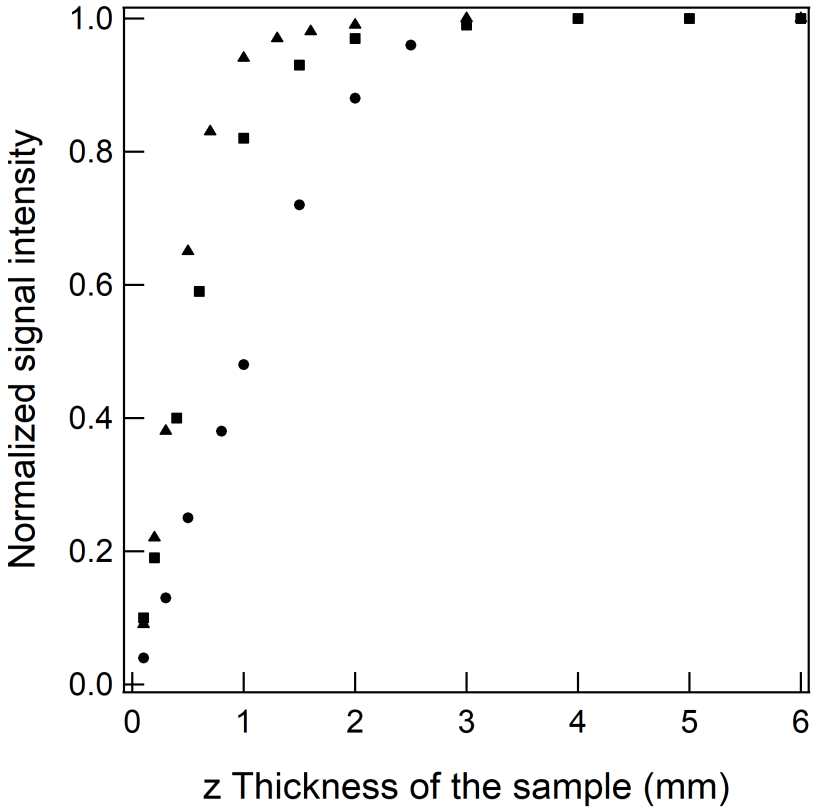

Figure S5 – Normalized Speed OPIOM signals collected from three Dronpa-2 containg samples exhibiting different opacities. •: Quasi-transparent Dronpa-2 solution; ■: Suspension of Dronpa-2-expressing bacteria; ▲: dense suspension of Dronpa-2-expressing bacteria after centrifugation. The Pre-OPIOM and Speed OPIOM signals have been obtained after spatial averaging over a disk of 50 pixels (equivalent to a disk 60 μm in the sample) of the Pre-OPIOM and Speed OPIOM images.

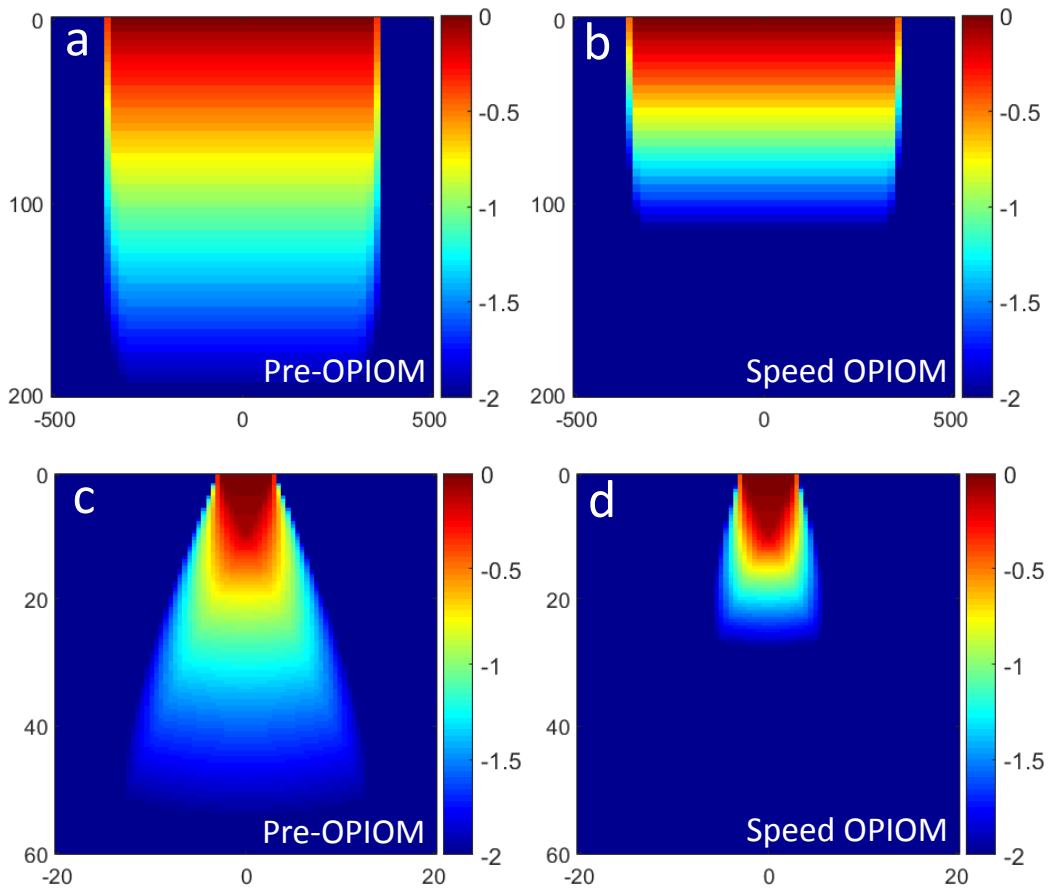

Figure S6 – Normalized Pre-OPIOM (**a,c**) and Speed OPIOM (**b,d**) responses to the spatial profiles of exiting light intensity at the distal end of the fiber bundle (**a**,**b**) or of a single microfiber (**c**,**d**) based on simulated illumination pattern through a scattering medium with a penetration length of λ_c=100 μm, which is representative of attenuation distances in the mice brain.[264] Intensities are displayed in common decimal logarithmic scale. *Axis unity: μm.*

Part IV

Conclusion and Perspectives

Chapter 1

General conclusion and perspectives

1.1 Conclusion

This PhD work has explored a variety of novel applications of Speed OPIOM for versatile biological observations, relying on the instrumental development of two imaging devices.

Instrumental development

In this work we independently developed a macroscope and a microendoscope for fluorescence observations at different scales, both of which were designed for selective imaging with the implementation of Speed OPIOM. The macroscope was an all home-built device with optimized dual-excitation and dual color fluorescence imaging. This device has been used for remote and selective fluorescence imaging of macro scale samples, allowing us for fast and efficient detection of targeted RSFP probes regardless of the lighting environment and the autofluorescence background from the sample. A simple microendoscope based on fiber bundles was subsequently built with a similar logic, but the dual-color excitation system was optimized for fiber-based illumination. Both of the instruments were experimentally validated of the optical and electronical robustness, which permit reliable measurements in diverse environments.

Valuation of Speed OPIOM

Speed OPIOM selective imaging against autofluorescence has been described in a previous work in the context of fluorescence microscopy. In this work, this point was further evidenced in macroscopic and endoscopic imaging of more complex biological or non-biological media. Experiments have also verified the ability of Speed OPIOM for multiplexed imaging as well as for quantification of targeted fluorescent probes in the presence of an interfering fluorescent background. It has also been validated to be a powerful tool for fluorescence imaging in the presence of ambient light (e.g. indoor light, artificial light in greenhouse, and out-door sunlight). More importantly, Speed OPIOM has been shown to significantly improve the sensitivity and signal-to-noise ratio for imaging fluorescent probes against autofluorescent media. Compared to traditional fluorescence detection methods, Speed OPIOM lowers the detection limit by 1-2 orders of magnitude and enhances the SNR by at least a factor of 10. Likewise, in the presence of constant ambient light illumination, Speed OPIOM permits to extract signal of interests which are 10^{-3}

less intense. Furthermore, with the endoscope setup, we have evaluated the possible application of Speed OPIOM in optical sectioning. It has been evidenced by numerical simulations as well as by experimental validations that the intensity decay of the excitation lights around the focal plan leads to a tightly confined Speed OPIOM response, which declines more rapidly outside the focus compared to the light-induced fluorescent signal. This fact suggests that Speed OPIOM might find applications in optically sectioned imaging with optimized axial resolution.

Observation of new biological systems

Thanks to the two innovative imaging devices built in this work, we were able to observe a series of biological samples at different scales, extending the application of Speed OPIOM to new areas. The macroscope has been used for imaging of fluorescent blots on strongly-autofluorescent nitrocellulose membranes, which has opened for Speed OPIOM an opportunity for sensitive and quantitative analysis of blotting assay. It was then found efficient in screening bacteria producing different fluorescent proteins, by selectively imaging bacterial colonies grown on highly autofluorescent culture media. In this work, the macroscope was principally adopted for the measurement of exogenous fluorescence emission in living plant leaves under outdoor conditions, through which the expression of stress-related gene could be quantified so as to achieve specific and sensitive detection of diverse biological and non-biological stresses. The fiber endoscopic device has found unprecedented application in bioprocess for real time bacterial production tracking, relying on a sensitive fluorescent detection of targeted FP probes among complex compounds from the culture media. It has also offered a new way for multiplexed cell imaging with optical fibers.

1.2 Perspectives

Following the organization of the preceding section, the three axes deserve further OPIOM developments.

Instrumental development

As far as instrumental developments are concerned, we are willing to adapt OPIOM to fluorescence imaging techniques, which exploit scanning for image acquisition (e. g. confocal microscopy). In particular, we will design and implement temporal control of light excitation and detection in scanning microscopies in order to add the option of dynamic contrast on commercial optical instruments, which are widely accessible on imaging platforms. Interestingly these scanning microscopy techniques rely on illumination with high light intensities, which should enable us to expand the collection of reversibly photoswitchable fluorescent labels beyond the ones engaged in photoisomerizations (e.g. fluorophores photoswitching between their first singlet and triplet states).

Valuation of Speed OPIOM

As far as Speed OPIOM developments are concerned, this PhD work has opened new perspectives with the observation of intrinsic optical sectioning in the fluorescence microendoscope. This feature seems

attractive to simplify the optical setups endowed with high spatial 3D resolution and it is under current evaluation in the group.

Observation of new biological systems

Eventually our application of Speed OPIOM to observe plants has motivated our interest to evaluate its application by relying on endogeneous fluorophores instead on exogeneous fluorescent labels. In the first place, we would be willing to evaluate whether the dynamic response of the fluorescence from the photosynthetic apparatus contains valuable information which could complement spectral analysis to read out the physiological status of plants.

Bibliography

[1] B. N. G. Giepmans, S. R. Adams, M. H. Ellisman, and R. Y. Tsien. The fluorescent toolbox for assessing protein location and function. *Science*, 312:217–224, 2006.

[2] C. Joo, H. Balci, Y. Ishitsuka, C. Buranachai, and T. Ha. Advances in single-molecule fluorescence methods for molecular biology. *Annual Review of Biochemistry*, 77:51–76, 2008.

[3] T. Xia, N. Li, and X. Fang. Single-molecule fluorescence imaging in living cells. *Annual Review of Physical Chemistry*, 64:459–480, 2013.

[4] D. E. Wolf, C. Samarasekera, and J. R. Swedlow. Quantitative analysis of digital microscope images. *Digital Microscopy, 3rd Edition*, 81:365 – 396, 2007.

[5] J. C. Waters. Accuracy and precision in quantitative fluorescence microscopy. *The Journal of cell biology*, 185:1135–48, 2009.

[6] J. R. Swedlow, K. Hu, P. D. Andrews, D. S. Roos, and J. M. Murray. Measuring tubulin content in toxoplasma gondii: A comparison of laser-scanning confocal and wide-field fluorescence microscopy. *Proceedings of the National Academy of Sciences*, 99:2014–2019, 2002.

[7] J. M. Murray, P. L. Appleton, J. R. Swedlow, and J. C. Waters. Evaluating performance in three-dimensional fluorescence microscopy. *Journal of Microscopy*, 228:390–405, 2007.

[8] S. Manley, J. Gillette, G. H Patterson, H. Shroff, H. F Hess, E. Betzig, and J. Lippincott-Schwartz. High-density mapping of single-molecule trajectories with photoactivated localization microscopy. *Nat. Methods*, 5:155–7, 2008.

[9] T. George, Y. Jung Sun, S. Kwang-Sup, S. Ralf, and N. Vasilis. Real-time intraoperative fluorescence imaging system using light-absorption correction. *J. Biomed. Opt.*, 14 6:064012, 2009.

[10] S. Troyan, V. Kianzad, S. L Gibbs-Strauss, S. Gioux, A. Matsui, R. Oketokoun, L. Ngo, A. Kamen, F. Azar, and J. V Frangioni. The flare intraoperative near-infrared fluorescence imaging system: A first-in-human clinical trial in breast cancer sentinel lymph node mapping. *Annals of surgical oncology*, 16:2943–52, 2009.

[11] R. R. Richards-Kortum and E. M. Sevick-Muraca. Quantitative optical spectroscopy for tissue diagnosis. *Annual review of physical chemistry*, 47:555–606, 1996.

[12] K. Koenig and H. Schneckenburger. Laser-induced autofluorescence for medical diagnosis. *Journal of Fluorescence*, 4:17–40, 1994.

[13] W. R. Zipfel, R. M. Williams, R. Christie, A. Y. Nikitin, B. T. Hyman, and W. W. Webb. Live tissue intrinsic emission microscopy using multiphoton-excited native fluorescence and second harmonic generation. *Proceedings of the National Academy of Sciences*, 100:7075–7080, 2003.

[14] M. Monici. Cell and tissue autofluorescence research and diagnostic applications. *Biotechnology annual review*, 11:227–56, 2005.

[15] P. Talamond, J. L. Verdeil, and G. Conéjéro. Secondary metabolite localization by autofluorescence in living plant cells. *Molecules*, 20 3:5024–37, 2015.

[16] R. H. Berg. Evaluation of spectral imaging for plant cell analysis. *Journal of Microscopy*, 214:174–181, 2004.

[17] M. T. M. Willemse. *Cell Wall Autofluorescence*. 1989.

[18] R. H. Goodwin. Fluorescent substances in plants. *Annual Review of Plant Physiology*, 4:283–304, 1953.

[19] B. Del Rosal, I. Villa, D. Jaque, and F. Sanz-Rodriguez. In vivo autofluorescence in the biological windows: The role of pigmentation. *Journal of biophotonics*, 9:1059–1067, 2015.

[20] R. Walmsley, N. Billinton, and W.-D. Heyer. Green fluorescent protein as a reporter for the dna damage-induced gene rad54 insaccharomyces cerevisiae. *Yeast*, 13:1535–1545, 1997.

[21] J. E. Aubin. Autofluorescence of viable cultured mammalian cells. *Journal of Histochemistry & Cytochemistry*, 27:36–43, 1979.

[22] L. Duysens and J. Amesz. Fluorescence spectrophotometry of reduced phosphopyridine nucleotide in intact cells in the near-ultraviolet and visible region. *Biochimica et Biophysica Acta*, 24:19–26, 1957.

[23] L. Duysens and G. Kronenberg. The fluorescence spectrum of the complex of reduced phosphopyridine nucleotide and alcohol dehydrogenase from yeast. *Biochimica et Biophysica Acta*, 26:437 – 438, 1957.

[24] J.-M. Salmon, E. Kohen, P. Viallet, J. G. Hirschberg, A. W. Wouters, C. Kohen, and B. Thorell. Microspectrofluorometric approach to the study of free/bound nad(p)h ratio as metabolic indicator in various cell types. *Photochemistry and Photobiology*, 36:585–593, 1982.

[25] O. Wolfbeis. The fluorescence of organic natural products. *Molecular Luminescence Spectroscopy. Part I: Methods and Applications*, pages 167–370, 1985.

[26] R. C. Benson, R. A. Meyer, M. E. Zaruba, and G. M. McKhann. Cellular autofluorescence–is it due to flavins? *Journal of Histochemistry & Cytochemistry*, 27:44–48, 1979.

[27] J. Blomfield and J. F. Farrar. The fluorescent properties of maturing arterial elastin. *Cardiovascular Research*, 3:161–170, 1969.

[28] A. C. Croce and G. Bottiroli. Autofluorescence spectroscopy and imaging: A tool for biomedical research and diagnosis. In *European journal of histochemistry : EJH*, 2014.

[29] R. Sohal. Assay of lipofuscin/ceroid pigment in vivo during aging. In *Oxygen Radicals in Biological Systems*, volume 105, pages 484 – 487. 1984.

[30] H. Shimasaki, N. Ueta, and O. S. Privett. Isolation and analysis of age-related fluorescent substances in rat testes. *Lipids*, 15:236–241, 1980.

[31] M. Tsuchida, T. Miura, and K. Aibara. Lipofuscin and lipofuscin-like substances. *Chemistry and Physics of Lipids*, 44:297 – 325, 1987.

[32] Y. Matsumoto. Lipofuscin pigmentation in pleomorphic adenoma of the palate. pages 299–302. 2001.

[33] Z. G. Cerovic, G. Samson, F. Morales, N. Tremblay, and I. Moya. Ultraviolet-induced fluorescence for plant monitoring: present state and prospects. *Agronomie*, 19:543–578, 1999.

[34] J. I. García-Plazaola, B. Fernández-Marín, S. O. Duke, A. Hernández, F. López-Arbeloa, and J. M. Becerril. Autofluorescence: Biological functions and technical applications. *Plant Science*, 236:136 – 145, 2015.

[35] P. Harris and R. Hartley. Detection of bound ferulic acid in cell walls of the gramineae by ultraviolet fluorescence microscopy. *Nature*, 259:508–510, 1976.

[36] H. K. Lichtenthaler and J. Schweiger. Cell wall bound ferulic acid, the major substance of the blue-green fluorescence emission of plants. *Journal of Plant Physiology*, 152:272 – 282, 1998.

[37] A. Policard. Etude sur les aspects offerts par des tumeurs expérimentales examinées à la lumière de wood. *Comptes Rendus Hebdomadaires des Séances Mémories la Société Biologie ses Filiales*, 91:1423, 1924.

[38] M. Inaguma and K. Hashimoto. Porphyrin-like fluorescence in oral cancer. *Cancer*, 86:2201–2211, 2000.

[39] C. Buschmann, G. Langsdorf, and H. Lichtenthaler. Imaging of the blue, green, and red fluorescence emission of plants: An overview. *Photosynthetica*, 38:483–491, 2000.

[40] B. Genty, J.-M. Briantais, and N. R. Baker. The relationship between the quantum yield of photosynthetic electron transport and quenching of chlorophyll fluorescence. *Biochimica et Biophysica Acta (BBA) - General Subjects*, 990:87 – 92, 1989.

[41] L. Chaerle, D. Hagenbeek, E. D. Bruyne, R. Valcke, and D. V. D. Straeten. Thermal and chlorophyll-fluorescence imaging distinguish plant-pathogen interactions at an early stage. *Plant & cell physiology*, 45 7:887–96, 2004.

[42] L. Chaerle, I. Leinonen, H. G. Jones, and D. Van Der Straeten. Monitoring and screening plant populations with combined thermal and chlorophyll fluorescence imaging. *Journal of Experimental Botany*, 58:773–784, 2007.

[43] R. P. Barbagallo, K. Oxborough, K. E. Pallett, and N. R. Baker. Rapid, noninvasive screening for perturbations of metabolism and plant growth using chlorophyll fluorescence imaging. *Plant physiology*, 132 2:485–93, 2003.

[44] J. Flexas, J.-M. Briantais, Z. Cerovic, H. Medrano, and I. Moya. Steady-state and maximum chlorophyll fluorescence responses to water stress in grapevine leaves: A new remote sensing system. *Remote Sensing of Environment*, 73:283 – 297, 2000.

[45] N. Billinton and A. W. Knight. Seeing the wood through the trees: A review of techniques for distinguishing green fluorescent protein from endogenous autofluorescence. *Analytical Biochemistry*, 291:175 – 197, 2001.

[46] G. A. Wagnieres, W. M. Star, and B. C. Wilson. In vivo fluorescence spectroscopy and imaging for oncological applications. *Photochemistry and Photobiology*, 68:603–632, 1998.

[47] J. A. Plascyk. The mk ii fraunhofer line discriminator (fld-ii) for airborne and orbital remote sensing of solar-stimulated luminescence. *Optical Engineering*, 14:339–346, 1975.

[48] L. GomezChova, L. AlonsoChorda, J. Amoros Lopez, J. Vila Frances, S. del ValleTascon, J. Calpe, and J. Moreno. Solar induced fluorescence measurements using a field spectroradiometer. *AIP Conference Proceedings*, 852:274–281, 2006.

[49] I. Moya, A. Ounis, N. Moise, and Y. Goulas. First airborne multiwavelength passive chlorophyll fluorescence measurements over la mancha (spain) fields. *Second Recent Advances in Quantitative Remote Sensing*, pages 820–825, 2006.

[50] L. Alonso, L. Gomez-Chova, J. Vila-Frances, J. Amoros-Lopez, L. Guanter, J. Calpe, and J. Moreno. Sensitivity analysis of the fraunhofer line discrimination method for the measurement of chlorophyll fluorescence using a field spectroradiometer. In *2007 IEEE International Geoscience and Remote Sensing Symposium*, pages 3756–3759, 2007.

[51] M. Mazzoni, G. Agati, G. Cecchi, G. Toci, and P. Mazzinghi. High resolution measurements of solar induced chlorophyll fluorescence in the fraunhofer oxigen bands. *Proc.SPIE*, 10567:10567 – 10567 – 5, 2017.

[52] T. Yamaguchi, Y. Sunaga, M. Haruta, M. Motoyama, Y. Ohta, H. Takehara, T. Noda, K. Sasagawa, T. Tokuda, and J. Ohta. Fluorescence imaging under background light with a self-reset complementary metal-oxide semiconductor image sensor. *The Journal of Engineering*, 2015:328–330(2), 2015.

[53] J. H. Norikane and K. Kurata. Water stress detection by monitoring fluorescence of plants under ambient light. *Transactions of the ASAE*, 44:1915–1922, 2001.

[54] C. H. Mazel. Underwater fluorescence photography in the presence of ambient light. *Limnology and Oceanography: Methods*, 3:499–510, 2005.

[55] E. Dominik, G. Daniel, R. Matthias, and B. Thomas. A compact multi-channel fluorescence sensor with ambient light suppression. *Measurement Science and Technology*, 23:035702, 2012.

[56] K. Sexton, S. C. Davis, D. McClatchy, P. A. Valdes, S. C. Kanick, K. D. Paulsen, D. W. Roberts, and B. W. Pogue. Pulsed-light imaging for fluorescence guided surgery under normal room lighting. *Opt. Lett.*, 38:3249–3252, 2013.

[57] L. Nedbal, J. Soukupová, D. Kaftan, J. Whitmarsh, and M. Trtílek. Kinetic imaging of chlorophyll fluorescence using modulated light. *Photosynthesis Research*, 66:3–12, 2000.

[58] K. J. Sexton, Y. Zhao, S. C. Davis, S. Jiang, and B. W. Pogue. Optimization of fluorescent imaging in the operating room through pulsed acquisition and gating to ambient background cycling. *Biomedical Optics Express*, 8:2635, 2017.

[59] S. Weinstein, D. Pane, L. A. Ernst, K. Warren-Rhodes, J. M. Dohm, A. N. Hock, J. L. Piatek, S. Emani, F. Lanni, M. Wagner, G. W. Fisher, E. Minkley, L. E. Dansey, T. Smith, E. A. Grin, K. Stubbs, G. Thomas, C. S. Cockell, L. Marinangeli, G. G. Ori, S. Heys, J. P. Teza, J. E. Moersch, P. Coppin, G. C. Diaz, D. S. Wettergreen, N. A. Cabrol, and A. S. Waggoner. Application of pulsed-excitation fluorescence imager for daylight detection of sparse life in tests in the atacama desert. *Journal of Geophysical Research: Biogeosciences*, 113, 2008.

[60] F. Lanni, D. Pane, S. J Weinstein, and A. Waggoner. Compact flashlamp-based fluorescence imager for use under ambient-light conditions. *The Review of scientific instruments*, 78:033702, 2007.

[61] B. Shimshon, Y.-k. Sharon, K. Yossef, K. Victor, S. Tali, A. Yonatan, Z.-P. Cheinat, R. Zahi, N. Amos, and J. A. Aharon. Remote detection of buried landmines using a bacterial sensor. *Nature Biotechnology*, 35:308–310, 2017.

[62] Z. Banghe, C. R. John, and M. S.-M. Eva. Non-invasive fluorescence imaging under ambient light conditions using a modulated iccd and laser diode. *Biomedical Optics Express*, 5:562–572, 2014.

[63] Z. Pincus, T. C. Mazer, and F. J. Slack. Autofluorescence as a measure of senescence in c. elegans: look to red, not blue or green. 8:1–10, 2016.

[64] L. Randers-Eichhorn, C. R. Albano, J. Sipior, W. E. Bentley, and G. Rao. On-line green fluorescent protein sensor with led excitation. *Biotechnology and Bioengineering*, 55:921–926.

[65] J. H. An and T. K. Blackwell. Skn-1 links c. elegans mesendodermal specification to a conserved oxidative stress response. *Genes & development*, 17 15:1882–93, 2003.

[66] T. J. Staughton, C. J. McGillicuddy, and P. D. Weinberg. Techniques for reducing the interfering effects of autofluorescence in fluorescence microscopy: improved detection of sulphorhodamine b-labelled albumin in arterial tissue. *Journal of microscopy*, 201 Pt 1:70–6, 2001.

[67] A. C. Teuscher and C. Y. Ewald. Overcoming autofluorescence to assess gfp expression during normal physiology and aging in caenorhabditis elegans. *Bio protocol*, 8:e2940, 2018.

[68] G. Patonay and M. D. Antoine. Near-infrared fluorogenic labels: New approach to an old problem. *Anal. Chem.*, 63:321A–327A, 1991.

[69] T. Troy, D. Jekic-McMullen, L. C. Sambucetti, and B. Rice. Quantitative comparison of the sensitivity of detection of fluorescent and bioluminescent reporters in animal models. *Molecular imaging*, 3 1:9–23, 2004.

[70] M. G. Müller, I. Georgakoudi, Q. Zhang, J. Wu, and M. S. Feld. Intrinsic fluorescence spectroscopy in turbid media: disentangling effects of scattering and absorption. *Appl. Opt.*, 40:4633–4646, 2001.

[71] S. Diao, G. Hong, A. L. Antaris, J. L. Blackburn, K. Cheng, Z. Cheng, and H. Dai. Biological imaging without autofluorescence in the second near-infrared region. *Nano Research*, 8:3027–3034, 2015.

[72] R. Weissleder and V. Ntziachristos. Shedding light onto live molecular targets. *Nature Medicine*, 6:79–93, 2002.

[73] S. John, S. Lucjan, and P. Gabor. Dna and protein applications of near-infrared dyes. *J. Biomed. Opt.*, 7:7 – 7 – 5, 2002.

[74] N. M. Cordina, N. Sayyadi, L. M. Parker, A. Everest-Dass, L. J. Brown, and N. H. Packer. Reduced background autofluorescence for cell imaging using nanodiamonds and lanthanide chelates. *Scientific Reports*, 8:4521, 2018.

[75] S.-G. Amy, Z. Yonghong, H. Todd, M. Dayle, and O. D. Michael. Quantitative, two-color western blot detection with infrared fluorescence. *LI-COR Biosciences*, 2004.

[76] G. Deng, S. Li, Z. Sun, W. Li, L. Zhou, J. Zhang, P. Gong, and L. Cai. Near-infrared fluorescence imaging in the largely unexplored window of 900-1,000 nm. *Theranostics*, 8:4116–4128, 2018.

[77] I. Mihalcescu, M. V.-M. Gateau, B. Chelli, C. Pinel, and J.-L. Ravanat. Green autofluorescence, a double edged monitoring tool for bacterial growth and activity in micro-plates. *Physical Biology*, 12:066016, 2015.

[78] P. A. Jaeger, C. McElfresh, L. R. Wong, and T. Ideker. Beyond agar: Gel substrates with improved optical clarity and drug efficiency and reduced autofluorescence for microbial growth experiments. *Applied and environmental microbiology*, 81 16:5639–49, 2015.

[79] V. A. Spencer, S. Kumar, B. Paszkiet, J. Fein, and J. F. Zmuda. Cell culture media for fluorescence imaging. *Genetic Engineering & Biotechnology News*, 34:16–18, 2014.

[80] B. Clancy and L. Cauller. Reduction of background autofluorescence in brain sections following immersion in sodium borohydride. *Journal of Neuroscience Methods*, 83:97 – 102, 1998.

[81] W. Baschong, R. Suetterlin, and R. H. Laeng. Control of autofluorescence of archival formaldehyde-fixed, paraffin-embedded tissue in confocal laser scanning microscopy (clsm). *The journal of histochemistry and cytochemistry : official journal of the Histochemistry Society*, 49 12:1565–72, 2001.

[82] A. S. Davis, A. Richter, S. Becker, J. E. Moyer, A. Sandouk, J. Skinner, and J. K. Taubenberger. Characterizing and diminishing autofluorescence in formalin-fixed paraffin-embedded human respiratory tissue. *The journal of histochemistry and cytochemistry : official journal of the Histochemistry Society*, 62 6:405–423, 2014.

[83] R. L. Metcalf. The storage and interaction of water soluble vitamins in the malpighian system of periplaneta americana (l.). *Arch. Biochem.*, 2:55–62, 1943.

[84] S. Schnell, W. Staines, and M. Wessendorf. Reduction of lipofuscin-like autofluorescence in fluorescently labeled tissue. *Journal of Histochemistry and Cytochemistry*, 47:719–730, 1999.

[85] K. A. Potter, J. S. Simon, B. Velagapudi, and J. R. Capadona. Reduction of autofluorescence at the microelectrode-cortical tissue interface improves antibody detection. *Journal of neuroscience methods*, 203 1:96–105, 2012.

[86] V. L. Mosiman, B. K. Patterson, L. Canterero, and C. L. Goolsby. Reducing cellular autofluorescence in flow cytometry: An in situ method. *Cytometry*, 30:151–156, 2002.

[87] G. K. Srivastava, R. Reinoso, A. K. Singh, I. Fernandez-Bueno, D. Hileeto, M. D. Martino, M. T. García-Gutiérrez, J. M. P. Merino, N. F. Alonso, A. Corell, and J. C. Pastor. Trypan blue staining method for quenching the autofluorescence of rpe cells for improving protein expression analysis. *Experimental eye research*, 93 6:956–62, 2011.

[88] U. Pfüller, H. Franz, and A. Preiß. Sudan black b: Chemical structure and histochemistry of the blue main components. *Histochemistry*, 54:237–250, 1977.

[89] V. C. Oliveira, R. C. V. Carrara, D. L. C. Simoes, F. P. Saggioro, C. G. Carlotti Jr, D. T. Covas, and L. Neder. Sudan black b treatment reduces autofluorescence and improves resolution of in situ hybridization specific fluorescent signals of brain sections. *Histology and Histopathology*, 25:1017–1024, 2010.

[90] Y. Sun, H. J. Yu, D. X. Zheng, Q. Cao, Y. Wang, D. Harris, and Y. Wang. Sudan black b reduces autofluorescence in murine renal tissue. *Archives of pathology & laboratory medicine*, 135 10:1335–42, 2011.

[91] L. Qi, E. K. Knapton, X. Zhang, T. Zhang, C. Gu, and Y. Zhao. Pre-culture sudan black b treatment suppresses autofluorescence signals emitted from polymer tissue scaffolds. *Scientific Reports*, 7:8361, 2017.

[92] M. S. Viegas, T. C. M. Martins, F. Seco, and A. D. carmo. An improved and cost-effective methodology for the reduction of autofluorescence in direct immunofluorescence studies on formalin-fixed paraffin-embedded tissues. *European journal of histochemistry : EJH*, 51 1:59–66, 2007.

[93] X. Yang, A. J. Vidunas, and E. Beniash. Optimizing immunostaining of enamel matrix: Application of sudan black b and minimization of false positives from normal sera and iggs. *Frontiers in Physiology*, 8:239, 2017.

[94] G. Puneet and K. Richa. A unique immunofluorescence protocol to detect protein expression in vascular tissues: Tacking a long standing pathological hitch. *Turk Patoloji Derg*, 34:57–65, 2017.

[95] T. Erben, R. Ossig, H. Y. Naim, and J. Schnekenburger. What to do with high autofluorescence background in pancreatic tissues - an efficient sudan black b quenching method for specific immunofluorescence labelling. *Histopathology*, 69:406–422, 2016.

[96] J. Yang, F. Yang, L. Campos, W. Mansfield, H. Skelton, Y. Hooks, and P. Liu. Quenching autofluorescence in tissue immunofluorescence [version 1; referees: 2 approved with reservations, 1 not approved]. *Wellcome Open Research*, 2(79), 2017.

[97] Y. Zhang, Y. Wang, W. Cao, K. Ma, W. Ji, Z. Han, J. Si, and L. Li. Spectral characteristics of autofluorescence in renal tissue and methods for reducing fluorescence background in confocal laser scanning microscopy. *Journal of Fluorescence*, 28:561–572, 2018.

[98] J. Widengren and R. Rigler. Mechanisms of photobleaching investigated by fluorescence correlation spectroscopy. *Bioimaging*, 4:149–157, 1996.

[99] M. F. Neumann and D. Gabel. Simple method for reduction of autofluorescence in fluorescence microscopy. *The journal of histochemistry and cytochemistry : official journal of the Histochemistry Society*, 50 3:437–9, 2002.

[100] H. Duong and M. Han. A multispectral led array for the reduction of background autofluorescence in brain tissue. *Journal of Neuroscience Methods*, 220:46–54, 2013.

[101] B. S. Kumar, S. Sandhyamani, s. S. Nazeer, and R. Jayasree. Rapid and simple method of photobleaching to reduce background autofluorescence in lung tissue sections. *Indian Journal of Biochemistry & Biophysics*, 52:107–110, 2015.

[102] Y. Sun, P. Ip, and A. Chakrabartty. Simple elimination of background fluorescence in formalin-fixed human brain tissue for immunofluorescence microscopy. *Journal of Visualized Experiments Jove*, 2017:e56188, 2017.

[103] A. B. Cubitt, R. Heim, S. R. Adams, A. E. Boyd, L. A. Gross, and R. Y. Tsien. Understanding, improving and using green fluorescent proteins. *Trends in Biochemical Sciences*, 20:448 – 455, 1995.

[104] R. Swaminathan, C. Hoang, and A. Verkman. Photobleaching recovery and anisotropy decay of green fluorescent protein gfp-s65t in solution and cells: cytoplasmic viscosity probed by green fluorescent protein translational and rotational diffusion. *Biophysical Journal*, 72:1900 – 1907, 1997.

[105] J. Quérard, T. L. Saux, A. Gautier, D. Alcor, V. Croquette, A. Lemarchand, C. Gosse, and L. Jullien. Kinetics of reactive modules adds discriminative dimensions for selective cell imaging. *ChemPhysChem*, 17:1396–1413, 2016.

[106] T. Oida, Y. Sako, and A. Kusumi. Fluorescence lifetime imaging microscopy (flimscopy). methodology development and application to studies of endosome fusion in single cells. *Biophysical journal*, 64 3:676–85, 1993.

[107] J. R. Lakowicz, H. Szmacinski, K. Nowaczyk, K. W. Berndt, and M. Jonson. Fluorescence lifetime imaging. *Analytical Biochemistry*, 202:316 – 330, 1992.

[108] G. Marriott, R. M. Clegg, D. J. Arndt-Jovin, and T. M. Jovin. Time resolved imaging microscopy. phosphorescence and delayed fluorescence imaging. *Biophys. J.*, 60:1374 – 1387, 1991.

[109] I. Bugiel, K. Konig, and H. Wabnitz. Investigation of cells by fluorescence laser scanning microscopy with subnanosecond time resolution. *Lasers Life Sci.*, 3:47–53, 1989.

[110] D. S. Elson, I. Munro, J. Requejo-Isidro, J. McGinty, C. Dunsby, N. Galletly, G. W. Stamp, M. A. A. Neil, M. J. Lever, P. A. Kellett, A. Dymoke-Bradshaw, J. Hares, and P. M. W. French. Real-time time-domain fluorescence lifetime imaging including single-shot acquisition with a segmented optical image intensifier. *New Journal of Physics*, 6:180, 2004.

[111] J. R. Lakowicz, H. Szmacinski, K. Nowaczyk, and M. L. Johnson. Fluorescence lifetime imaging of free and protein-bound nadh. *Proceedings of the National Academy of Sciences*, 89:1271–1275, 1992.

[112] G. H. Krause and E. Weis. Chlorophyll fluorescence and photosynthesis: The basics. *Annual Review of Plant Physiology and Plant Molecular Biology*, 42:313–349, 1991.

[113] H. Schneckenburger, M. Wagner, P. Weber, W. S. Strauss, and R. Sailer. Autofluorescence lifetime imaging of cultivated cells using a uv picosecond laser diode. *Journal of Fluorescence*, 14:649–654, 2004.

[114] D. Schweitzer, E. R. Gaillard, J. Dillon, R. F. Mullins, S. Russell, B. Hoffmann, S. Peters, M. Hammer, and C. Biskup. Time-resolved autofluorescence imaging of human donor retina tissue from donors with significant extramacular drusen. *Investigative Ophthalmology & Visual Science*, 53:3376, 2012.

[115] W. Becker. Fluorescence lifetime imaging – techniques and applications. *Journal of Microscopy*, 247:119–136, 2012.

[116] Y. Kodama. Time gating of chloroplast autofluorescence allows clearer fluorescence imaging in planta. *PLOS ONE*, 11:1–8, 2016.

[117] D. Jin and J. A. Piper. Time-gated luminescence microscopy allowing direct visual inspection of lanthanide-stained microorganisms in background-free condition. *Anal. Chem.*, 83:2294–2300, 2011.

[118] R. M. Rich, D. L. Stankowska, B. P. Maliwal, T. J. Sørensen, B. W. Laursen, R. R. Krishnamoorthy, Z. Gryczynski, J. Borejdo, I. Gryczynski, and R. Fudala. Elimination of autofluorescence background from fluorescence tissue images by use of time-gated detection and the azadioxatriangulenium (adota) fluorophore. *Analytical and Bioanalytical Chemistry*, 405:2065–2075, 2013.

[119] R. M. Rich, M. Mummert, Z. Gryczynski, J. Borejdo, T. J. Sørensen, B. W. Laursen, Z. Foldes-Papp, I. Gryczynski, and R. Fudala. Elimination of autofluorescence in fluorescence correlation spectroscopy using the azadioxatriangulenium (adota) fluorophore in combination with time-correlated single-photon counting (tcspc). *Analytical and Bioanalytical Chemistry*, 405:4887–4894, 2013.

[120] B. C. Fleischer, J. T. Petty, J. C. Hsiang, and R. M. Dickson. Optically activated delayed fluorescence. *The journal of physical chemistry letters*, 8 15:3536–3543, 2017.

[121] G. T. Dempsey, M. Bates, W. E. Kowtoniuk, D. R. Liu, R. Y. Tsien, and X. Zhuang. Photoswitching mechanism of cyanine dyes. *J. Am. Chem. Soc.*, 131:18192–18193, 2009.

[122] T. Fukaminato. Single-molecule fluorescence photoswitching : Design and synthesis of photoswitchable fluorescent molecules. *J. Photochem. Photobiol. C : Photochem. Rev.*, 12:177–208, 2011.

[123] D. Bourgeois and V. Adam. Reversible photoswitching in fluorescent proteins : A mechanistic view. *IUBMB Life*, 64:482–491, 2012.

[124] G. Marriott, S. Mao, T. Sakata, J. Ran, D. K. Jackson, C. Petchprayoon, T. J. Gomez, E. Warp, O. Tulyathan, H. L. Aaron, E. Y. Isacoff, and Y. Yan. Optical lock-in detection imaging microscopy for contrast-enhanced imaging in living cells. *Proc. Natl. Acad. Sci. U. S. A.*, 105:17789–17794, 2008.

[125] Y. Yan, M. E. Marriott, C. Petchprayoon, and G. Marriott. Optical switch probes and optical lock-in detection (OLID) imaging microscopy: high-contrast fluorescence imaging within living systems. *Biochem. J.*, 433:411–422, 2011.

[126] Y. Yan, C. Petchprayoon, S. Mao, and G. Marriott. Reversible optical control of cyanine fluorescence in fixed and living cells: optical lock-in detection immunofluorescence imaging microscopy. *Philos. Trans. R. Soc. Lond. B. Biol. Sci.*, 368:1–9, 2012.

[127] G. Du, G. Marriott, and Y. Yan. An improved optical lock-in detection method for contrast-enhanced imaging in living cells. In *4th International Conference on Bioinformatics and Biomedical Engineering (iCBBE)*, pages 1–5, June 2010.

[128] L. Wu, Y. Dai, X. Jiang, C. Petchprayoon, J. E. Lee, T. Jiang, Y. Yan, and G. Marriott. High-contrast fluorescence imaging in fixed and living cells using optimized optical switches. *PLoS ONE*, 8:e64738, 2013.

[129] Y. C. Chen, A. E. Jablonski, I. Issaeva, D. Bourassa, J. C. Hsiang, C. J. Fahrni, and R. M. Dickson. Optically modulated photoswitchable fluorescent proteins yield improved biological imaging sensitivity. *J. Am. Chem. Soc.*, 137:12764–12767, 2015.

[130] C. I. Richards, J. C. Hsiang, D. Senapati, S. Patel, J. Yu, T. Vosch, and R. M. Dickson. Optically modulated fluorophores for selective fluorescence signal recovery. *J. Am. Chem. Soc.*, 131:4619–4621, 2009.

[131] C. I. Richards, J. C. Hsiang, and R. M. Dickson. Synchronously amplified fluorescence image recovery (safire). *The Journal of Physical Chemistry B*, 114:660–665, 2010.

[132] C. Fan, J.-C. Hsiang, and R. M. Dickson. Optical modulation and selective recovery of Cy5 fluorescence. *ChemPhysChem*, 13:1023–1029, 2012.

[133] A. E. Jablonski, J. C. Hsiang, P. Bagchi, N. P. Hull, C. I. Richards, C. J. Fahrni, and R. M. Dickson. Signal discrimination between fluorescent proteins in live cells by long-wavelength optical modulation. *The journal of physical chemistry letters*, 3 23:3585–3591, 2012.

[134] A. E. Jablonski, R. B. Vegh, J. C. Hsiang, B. R. Bommarius, Y.-C. Chen, K. M. Solntsev, A. S. Bommarius, L. M. Tolbert, and R. M. Dickson. Optically modulatable blue fluorescent proteins. *J. Am. Chem. Soc.*, 135 44:16410–7, 2013.

[135] J.-C. Hsiang, A. E. Jablonski, and R. M. Dickson. Optically modulated fluorescence bioimaging: Visualizing obscured fluorophores in high background. *Acc. Chem. Res.*, 47:1545–1554, 2014.

[136] J. C. Hsiang, B. C. Fleischer, and R. M. Dickson. Dark state-modulated fluorescence correlation spectroscopy for quantitative signal recovery. *The Journal of Physical Chemistry Letters*, 7:2496–2501, 2016.

[137] C. I. Richards, J. C. Hsiang, A. M. Khalil, N. P. Hull, and R. M. Dickson. Fret-enabled optical modulation for high sensitivity fluorescence imaging. *J. Am. Chem. Soc.*, 132 18:6318–23, 2010.

[138] C. Fan, J. C. Hsiang, A. E. Jablonski, and R. M. Dickson. All-optical fluorescence image recovery using modulated stimulated emission depletion. *Chemical science*, 2 6:1080–1085, 2011.

[139] J. Quérard, A. Gautier, T. Le Saux, and L. Jullien. Expanding discriminative dimensions for analysis and imaging. *Chem. Sci.*, 6:2968–2978, 2015.

[140] J. Quérard, T.-Z. Markus, M.-A. Plamont, C. Gauron, P. Wang, A. Espagne, M. Volovitch, S. Vriz, V. Croquette, A. Gautier, T. Le Saux, and L. Jullien. Photoswitching kinetics and phase-sensitive detection add discriminative dimensions for selective fluorescence imaging. *Angew. Chem. Int. Ed.*, 127:2671–2675, 2015.

[141] R. Ando, C. Flors, H. Mizuno, J. Hofkens, and A. Miyawaki. Highlighted generation of fluorescence signals using simultaneous two-color irradiation on dronpa mutants. *Biophysical journal*, 92 12:L97–9, 2007.

[142] Y. C. Chen and R. M. Dickson. Improved fluorescent protein contrast and discrimination by optically controlling dark state lifetimes. *The journal of physical chemistry letters*, 8:733–736, 2017.

[143] J. Quérard, R. Zhang, Z. Kelemen, M.-A. Plamont, X. Xie, R. Chouket, I. Roemgens, Y. Korepina, S. Albright, E. Ipendey, M. Volovitch, H. L. Sladitschek, P. Neveu, L. Gissot, A. Gautier, J.-D. Faure, V. Croquette, T. L. Saux, and L. Jullien. Resonant out-of-phase fluorescence microscopy and remote imaging overcome spectral limitations. *Nat. Comm.*, 8:969, 2017.

[144] S. Jacquemoud and F. Baret. Prospect: A model of leaf optical properties spectra. *Remote Sensing of Environment*, 34:75 – 91, 1990.

[145] Q. Ling, W. Huang, and P. Jarvis. Use of a spad-502 meter to measure leaf chlorophyll concentration in arabidopsis thaliana. *Photosynthesis research*, 107:209–214, 2011.

[146] A. A. Gitelson, Y. Zur, O. B. Chivkunova, and M. N. Merzlyak. Assessing carotenoid content in plant leaves with reflectance spectroscopy¶. *Photochemistry and Photobiology*, 75:272–281, 2002.

[147] H. Poorter, U. Niinemets, L. Poorter, I. J. Wright, and R. Villar. Causes and consequences of variation in leaf mass per area (lma): a meta-analysis. *The New phytologist*, 182 3:565–88, 2009.

[148] R. M. Mohammad and B. F. Sayyed. Leaf equivalent water thickness assessment using reflectance at optimum wavelengths. *Theoretical and Experimental Plant Physiology*, 25(3):196–202, 2013.

[149] M. Cui, T. C. Vogelmann, and W. K. Smith. Chlorophyll and light gradients in sun and shade leaves of spinacia oleracea. *Plant, Cell & Environment*, 14:493–500, 1991.

[150] Y. Qi, S. Bai, T. C. Vogelmann, and G. Heisler. Penetration of uva, uv-b, blue, and red light into leaf tissues of pecan measured by a fiber optic microprobe system. *Proceedings of SPIE - The International Society for Optical Engineering*, 5156, 2003.

[151] D. M. Chudakov, M. V. Matz, S. Lukyanov, and K. A. Lukyanov. Fluorescent proteins and their applications in imaging living cells and tissues. *Physiol. Rev.*, 90:1103–1163, 2010.

[152] L. Jullien and A. Gautier. Fluorogen-based reporters for fluorescence imaging: A review. *Methods Appl. Fluoresc.*, 3:042007, 2015.

[153] J. R. Mansfield, K. W. Gossage, C. C. Hoyt, and R. M. Levenson. Autofluorescence removal, multiplexing, and automated analysis methods for in-vivo fluorescence imaging. *J. Biomed. Opt.*, 104:041207, 2005.

[154] L. Gao and R. T. Smith. Optical hyperspectral imaging in microscopy and spectroscopy - a review of data acquisition. *J. Biophotonics*, pages 1–16, 2014.

[155] P. I. Bastiaens and A. Squire. Fluorescence lifetime imaging microscopy: spatial resolution of biochemical processes in the cell. *Trends in Cell Biology*, 9:48–52, 1999.

[156] J. Yuan and G. Wang. Lanthanide complex-based fluorescence label for time-resolved fluorescence bioassay. *J. Fluorescence*, 15:559–568, 2005.

[157] C. A. Lichten, R. White, I. B. Clark, and P. S. Swain. Unmixing of fluorescence spectra to resolve quantitative time-series measurements of gene expression in plate readers. *BMC Biotechnology*, 14:11, 2014.

[158] C. Yun, J. You, J. Kim, J. Huh, and E. Kim. Photochromic fluorescence switching from diarylethenes and its applications. *J. Photochem. Photobiol. C, Photochem. Rev.*, 10:111–129, 2009.

[159] X. X. Zhou and M. Z. Lin. Photoswitchable fluorescent proteins: ten years of colorful chemistry and exciting applications. *Curr. Opin. Chem. Biol.*, 17:682–690, 2013.

[160] S. van de Linde and M. Sauer. How to switch a fluorophore: from undesired blinking to controlled photoswitching. *Chem. Soc. Rev.*, 43:1076–1087, 2014.

[161] R. L. Ornberg, T. F. Harper, and H. Liu. Western blot analysis with quantum dot fluorescence technology: a sensitive and quantitative method for multiplexed proteomics. *Nat. Methods*, 2:79–81, 2005.

[162] K. G. Shah and P. Yager. Wavelengths and lifetimes of paper autofluorescence: A simple substrate screening process to enhance the sensitivity of fluorescence-based assays in paper. *Anal. Chem.*, 89:12023–12029, 2017.

[163] N. Padmavathy, L. D. Ghosh, M. Sharma, M. S. Remanan, K. Chatterjee, and S. Bose. Ultrasensitive detection of proteins using chemically modified nanoporous pvdf membrane with attenuated near ir autofluorescence. *ChemistrySelect*, 3:3839 –3847, 2018.

[164] Y. Kondo, S. Higa, T. Iwasaki, T. Matsumoto, K. Maehara, A. Harada, Y. Baba, M. Fujita, and Y. Ohkawa. Sensitive detection of fluorescence in western blotting by merging images. *PLoS ONE*, 13:e0191532, 2018.

[165] A. A. Gowen, Y. Feng, E. Gaston, and V. Valdramidis. Recent applications of hyperspectral imaging in microbiology. *Talanta*, 137:43–54, 2015.

[166] W. Jun, M. S. Kim, B.-K. Cho, P. D. Millner, K. Chao, and D. E. Chan. Microbial biofilm detection on food contact surfaces by macro-scale fluorescence imaging. *J. Food Eng.*, 99:314–322, 2010.

[167] R. Chait, S. Shrestha, A. K. Shah, J.-B. Michel, and R. Kishony. A differential drug screen for compounds that select against antibiotic resistance. *PLoS ONE*, 5:e15179, 2010.

[168] X. Zhou, R. Carranco, S. Vitha, and T. C. Hall. The dark side of green fluorescent protein. *New Phytologist*, 168:313–322, 2005.

[169] W. Ckurshumova, A. E. Caragea, R. S. Goldstein, and T. Berleth. Glow in the dark: Fluorescent proteins as cell and tissue-specific markers in plants. *Molecular Plant*, 4:794–804, 2011.

[170] C. N. J. Stewart, R. J. Millwood, M. D. Halfhill, M. Ayalew, V. Cardoza, M. Kooshki, G. A. Capelle, K. R. Kyle, D. Piaseki, G. McCrum, and J. D. Benedetto. Laser-induced fluorescence imaging and spectroscopy of gfp transgenic plants. *J. Fluoresc.*, 15:697–705, 2005.

[171] Z. Kelemen and et al. To be submitted, 2018.

[172] A. C. Stiel, S. Trowitzsch, G. Weber, M. Andresen, C. Eggeling, S. W. Hell, S. Jakobs, and M. C. Wahl. 1.8 å bright-state structure of the reversibly switchable fluorescent protein Dronpa guides the generation of fast switching variants. *Biochem. J.*, 402:35–42, 2007.

[173] M. Andresen, A. C. Stiel, J. Follig, D. Wenzel, A. Schoenle, A. Egner, C. Eggeling, S. W. Hell, and S. Jakobs. Photoswitchable fluorescent proteins enable monochromatic multilabel imaging and dual color fluorescence nanoscopy. *Nat. Biotechnol.*, 26:1035–1040, 2008.

[174] A. Zelmer and T. Ward. Noninvasive fluorescence imaging of small animals. *J. Microscopy*, 252:8–15, 2013.

[175] J. T. Woolley. Reflectance and transmittance of light by leaves. *Plant Physiology*, 47(5):656–662, 1971.

[176] H. Bouas-Laurent and H. Dürr. Organic photochromism. *Pure Appl. Chem.*, 73:639–665, 2001.

[177] H. M. Bandara and S. C. Burdette. Photoisomerization in different classes of azobenzene. *Chem. Soc. Rev.*, 41:1809–1825, 2012.

[178] M. Dong, A. Babalhavaeji, S. Samanta, A. A. Beharry, and G. A. Woolley. Red-shifting azobenzene photoswitches for in vivo use. *Acc. Chem. Res.*, 48:2662–2670, 2015.

[179] D. Bleger and S. Hecht. Visible-light-activated molecular switches. *Angew. Chem., Int. Ed.*, 54:11338–11349, 2015.

[180] D. P. Mahoney, E. A. Owens, C. Fan, J.-C. Hsiang, M. M. Henary, and R. M. Dickson. Tailoring cyanine dark states for improved optically modulated fluorescence recovery. *J. Phys. Chem. B*, 119:4637–4643, 2015.

[181] K. Matsuda and M. Irie. Diarylethene as a photoswitching unit. *J. Photochem. Photobiol. C, Photochem. Rev.*, 5:169–182, 2004.

[182] R. Klajn. Spiropyran-based dynamic materials. *Chem. Soc. Rev.*, 43:148–184, 2014.

[183] R. Ando, H. Mizuno, and A. Miyawaki. Regulated fast nucleocytoplasmic shuttling observed by reversible protein highlighting. *Science*, 306:1370–1373, 2004.

[184] S. Kredel, K. Nienhaus, F. Oswald, M. Wolff, S. Ivanchenko, F. Cymer, A. Jeromin, F. J. Michel, K.-D. Spindler, R. Heilker, G. U. Nienhaus, and J. Wiedenmann. Optimized and far-red-emitting variants of fluorescent protein eqfp611. *Chemistry & Biology*, 15(3):224 – 233, 2008.

[185] C. Morineau, Y. Bellec, F. Tellier, L. Gissot, F. N. Z. Kelemen, and J.-D. Faure. Selective gene dosage by crispr-cas9 genome editing in hexaploid camelina sativa. *Plant Biotechnol. J.*, 15:729–739, 2017.

[186] M. A. Estelle and C. Somerville. Auxin-resistant mutants of arabidopsis thaliana with an altered morphology. *Molecular and General Genetics MGG*, 206(2):200–206, Feb 1987.

[187] R. T. Furbank and M. Tester. Phenomics - technologies to relieve the phenotyping bottleneck. *Trends in Plant Science*, 16:635–644, 2016.

[188] G. P. Asner, D. Nepstad, G. Cardinot, and D. Ray. Drought stress and carbon uptake in an amazon forest measured with spaceborne imaging spectroscopy. *Proc. Natl. Acad. Sci. U. S. A.*, 101:6039–6044, 2004.

[189] G. A. Blackburn. Hyperspectral remote sensing of plant pigments. *Journal of experimental botany*, 58:855–867, 2007.

[190] F. Baret, V. Houliès, and M. Guérif. Quantification of plant stress using remote sensing observations and crop models: The case of nitrogen management. *Journal of experimental botany*, 58:869–880, 2007.

[191] K. Omasa, F. Hosoi, and A. Konishi. 3d lidar imaging for detecting and understanding plant responses and canopy structure. *Journal of experimental botany*, 58:881–898, 2007.

[192] N. R. Baker. Chlorophyll fluorescence: A probe of photosynthesis in vivo. *Annu. Rev. Plant Biol.*, 59:89–113, 2008.

[193] L. Nedbal and V. Brezina. Complex metabolic oscillations in plants forced by harmonic irradiance. *Biophys. J.*, 83:2180–2189, 2002.

[194] E. Kaiser, A. Morales, J. Harbinson, J. Kromdijk, E. Heuvelink, and L. Marcelis. Dynamic photosynthesis in different environmental conditions. *Journal of Experimental Botany*, 66:2415–2426, 2015.

[195] A. M. Mutka and R. S. Bart. Image-based phenotyping of plant disease symptoms. *Front. Plant Sci.*, 5:734, 2014.

[196] M. M. Rahaman, D. Chen, Z. Gillani, C. Klukas, and M. Chen. Advanced phenotyping and phenotype data analysis for the study of plant growth and development. *Front. Plant Sci.*, 6:619, 2015.

[197] N. Fahlgren, M. A. Gehan, and I. Baxter. Lights, camera, action: High-throughput plant phenotyping is ready for a close-up. *Current Opinion in Plant Biology*, 24:93–99, 2015.

[198] P. Dedecker, F. C. De Schryver, and J. Hofkens. Fluorescent proteins: Shine on, you crazy diamond. *J. Am. Chem. Soc.*, 135:2387–2402, 2013.

[199] B. A. Krizek, V. Prost, R. M. Joshi, T. Stoming, and T. C. Glenn. Developing transgenic arabidopsis plants to be metal-specific bioindicators. *Environ. Toxicol. Chem.*, 22:175–181, 2003.

[200] M. Kooshki, A. Mentewab, and C. N. Stewart. Pathogen inducible reporting in transgenic tobacco using a gfp construct. *Plant Sci.*, 165:213–219, 2003.

[201] M. R. Perera and M. G. K. Jones. Expression of the peroxidase gene promoter (shpx6b) from stylosanthes humilis in transgenic plants during insect attack. *Entomol. Exp. Appl.*, 111:165–171, 2004.

[202] A.-L. Paul, A. C. Schuerger, M. P. Popp, J. T. Richards, M. S. Manak, and R. J. Ferl. Hypobaric biology: Arabidopsis gene expression at low atmospheric pressure. *Plant Physiology*, 134:215–223, 2004.

[203] K. Martin, K. Kopperud, R. Chakrabarty, R. Banerjee, R. Brooks, and M. M. Goodin. Transient expression in nicotiana benthamiana fluorescent marker lines provides enhanced definition of protein localization, movement and interactions in planta. *Plant J.*, 59:150–162, 2009.

[204] M. Lummer, F. Humpert, M. Wiedenlübbert, M. Sauer, M. Schüttpelz, and D. Staiger. A new set of reversibly photoswitchable fluorescent proteins for use in transgenic plants. *Molecular Plant*, 6:1518–1530, 2013.

[205] A. Sarrion-Perdigones, M. Vazquez-Vilar, J. Palaci, B. Castelijns, J. Forment, P. Ziarsolo, J. Blanca, A. Granell, and D. Orzaez. Goldenbraid 2.0: A comprehensive dna assembly framework for plant synthetic biology. *Plant Physiology*, 162:1618–1631, 2013.

[206] D. Huang, W. Wu, S. R. Abrams, and A. Cutler. The relationship of drought-related gene expression in arabidopsis thaliana to hormonal and environmental factors. *Journal of experimental botany*, 59:2991–3007, 2008.

[207] V. Lanquar, F. Lelievre, S. Bolte, C. Hames, C. Alcon, D. Neumann, G. Vansuyt, C. Curie, A. Schroder, U. Kramer, H. Barbier-Brygoo, and S. Thomine. Mobilization of vacuolar iron by atnramp3 and atnramp4 is essential for seed germination on low iron. *EMBO J.*, 24:4041–4051, 2005.

[208] S. Tisné, Y. Serrand, L. M. Bach, E. Gilbault, R. B. Ameur, H. Balasse, R. Voisin, D. Bouchez, M. Durand-Tardif, P. Guerche, G. Chareyron, J. D. Rugna, C. Camilleri, and O. Loudet. Phenoscope: an automated large-scale phenotyping platform offering high spatial homogeneity. *The Plant journal : for cell and molecular biology*, 74 3:534–44, 2013.

[209] M. Karimi, D. Inzé, and A. G. Depicker. Gateway vectors for agrobacterium-mediated plant transformation. *Trends in plant science*, 7 5:193–5, 2002.

[210] C. Grefen, N. Donald, K. Hashimoto, J. Kudla, K. Schumacher, and M. R. Blatt. A ubiquitin-10 promoter-based vector set for fluorescent protein tagging facilitates temporal stability and native protein distribution in transient and stable expression studies. *The Plant journal : for cell and molecular biology*, 64 2:355–65, 2010.

[211] H. T. Nguyen, J. C. e Silva, R. Podicheti, J. C. Macrander, W. Yang, T. J. Nazarenus, J. W. Nam, J. G. Jaworski, C. Lu, B. E. Scheffler, K. Mockaitis, and E. B. Cahoon. Camelina seed transcriptome: a tool for meal and oil improvement and translational research. *Plant biotechnology journal*, 11 6:759–69, 2013.

[212] M. D. Curtis and U. Grossniklaus. A gateway cloning vector set for high-throughput functional analysis of genes in planta. *Plant physiology*, 133 2:462–9, 2003.

[213] T. Nakagawa, T. Kurose, T. Hino, K. Tanaka, M. Kawamukai, Y. Niwa, K. Toyooka, K. Matsuoka, T. Jinbo, and T. Kimura. Development of series of gateway binary vectors, pgwbs, for realizing efficient construction of fusion genes for plant transformation. *Journal of bioscience and bioengineering*, 104 1:34–41, 2007.

[214] R. J. Oomen, J. Wu, F. Lelièvre, S. Blanchet, P. M. Richaud, H. Barbier-Brygoo, M. G. M. Aarts, and S. Thomine. Functional characterization of nramp3 and nramp4 from the metal hyperaccumulator thlaspi caerulescens. *The New phytologist*, 181 3:637–50, 2009.

[215] B. A. Flusberg, E. D. Cocker, W. Piyawattanametha, J. C. Jung, E. L. M. Cheung, and M. J. Schnitzer. Fiber-optic fluorescence imaging. *Nat. Methods*, 2:941–950, 2005.

[216] J. M. Jabbour, M. A. Saldua, J. N. Bixler, and K. C. Maitland. Confocal endomicroscopy: Instrumentation and medical applications. *Annals of Biomedical Engineering*, 40:378–397, 2012.

[217] T. J. Muldoon, D. Roblyer, M. D. Williams, V. M. Stepanek, R. Richards–Kortum, and A. M. Gillenwater. Noninvasive imaging of oral neoplasia with a high-resolution fiber-optic microendoscope. *Head & Neck*, 34(3):305–312, 2012.

[218] M. J. Landau, D. J. Gould, and K. M. Patel. Advances in fluorescent-image guided surgery. *Ann. Transl. Med.*, 4:392, 2016.

[219] T. Nagaya, Y. A. Nakamura, P. L. Choyke, and H. Kobayashi. Fluorescence-guided surgery. *Front. Oncol.*, 7:314, 2017.

[220] F. Nooshabadi, H.-J. Yang, J. N. Bixler, Y. Kong, J. D. Cirillo, and K. C. Maitland. Intravital fluorescence excitation in whole animal optical imaging. *PLoS ONE*, 11:e0149932, 2016.

[221] J. Vos and J. Groenwold. Estimation of root densities by observation tubes and endoscope. *Plant and Soil*, 74:295–300, 1983.

[222] M. Athmann, T. Kautz, R. Pude, and U. Köpke. Root growth in biopores - evaluation with in situ endoscopy. *Plant and Soil*, 371:179–190, 2013.

[223] B. A. Flusberg, J. C. Jung, E. D. Cocker, E. P. Anderson, and M. J. Schnitzer. In vivo brain imaging using a portable 3.9 gram two-photon fluorescence microendoscope. *Opt. Lett.*, 30:2272–2274, 2005.

[224] J. C. Jung, A. D. Mehta, E. Aksay, R. Stepnoski, and M. J. Schnitzer. In vivo mammalian brain imaging using one- and two-photon fluorescence microendoscopy. *J. Neurophysiol.*, 92:3121–3133, 2004.

[225] A. F. Gmitro and D. Aziz. Confocal microscopy through a fiber-optic imaging bundle. *Opt. Lett.*, 18(8):565–567, 1993.

[226] N. Bozinovic, C. Ventalon, T. Ford, and J. Mertz. Fluorescence endomicroscopy with structured illumination. *Opt. Express*, 16(11):8016–8025, 2008.

[227] W. Göbel, J. N. D. Kerr, A. Nimmerjahn, and F. Helmchen. Miniaturized two-photon microscope based on a flexible coherent fiber bundle and a gradient-index lens objective. *Opt. Lett.*, 29(21):2521–2523, 2004.

[228] A. R. Rouse and A. F. Gmitro. Multispectral imaging with a confocal microendoscope. *Opt. Lett.*, 25:1708–1710, 2000.

[229] J.-A. Conchello and J. W. Lichtman. Optical sectioning microscopy. *Nat. Methods*, 2:920–931, 2005.

[230] P. M. Lane, A. L. P. Dlugan, R. Richards-Kortum, and C. E. MacAulay. Fiber-optic confocal microscopy using a spatial light modulator. *Opt. Lett.*, 25(24):1780–1782, 2000.

[231] F. Jean, G. Bourg-Heckly, and B. Viellerobe. Fibered confocal spectroscopy and multicolor imaging system for in vivo fluorescence analysis. *Opt. Express*, 15(7):4008–4017, 2007.

[232] F. Helmchen and W. Denk. Deep tissue two-photon microscopy. *Nat. Methods*, 2:932–940, 2005.

[233] P. Kim, M. Puoris'haag, D. Coté, C. P. Lin, and S. H. Yun. In vivo confocal and multiphoton microendoscopy. *J. Biomed. Opt*, 13:010501, 2008.

[234] S. Santos, K. K. Chu, D. Lim, N. Bozinovic, T. N. Ford, C. Hourtoule, A. C. Bartoo, S. K. Singh, and J. Mertz. Optically sectioned fluorescence endomicroscopy with hybrid-illumination imaging through a flexible fiber bundle. *J. Biomed. Opt.*, 14:030502, 2009.

[235] T. N. Ford, D. Lim, and J. Mertz. Fast optically sectioned fluorescence hilo endomicroscopy. *J. Biomed. Opt.*, 17:17 – 17 – 8, 2012.

[236] D. Xu, T. Jiang, A. Li, B. Hu, Z. Feng, H. Gong, S. Zeng, and Q. Luo. Fast optical sectioning obtained by structured illumination microscopy using a digital mirror device. *J. Biomed. Opt.*, 18:060503, 2013.

[237] J. Ahn, H. Yoo, and D.-G. Gweon. Endoscopic focal modulation microscopy. *Journal of Microscopy*, 250:116–121, 2013.

[238] P. Keahey, P. Ramalingam, K. Schmeler, and R. R. Richards-Kortum. Differential structured illumination microendoscopy for in vivo imaging of molecular contrast agents. *Proceedings of the National Academy of Sciences*, 113(39):10769–10773, 2016.

[239] J. A. Udovich, N. D. Kirkpatrick, A. Kano, A. Tanbakuchi, U. Utzinger, and A. F. Gmitro. Spectral background and transmission characteristics of fiber optic imaging bundles. *Appl. Opt.*, 47(25):4560–4568, 2008.

[240] R. Baumgartner, H. Fisslinger, D. Jocham, H. Lenz, L. Ruprecht, H. Stepp, and E. Unsold. A fluorescence imaging device for endoscopic detection of early stage cancer - instrumental and experimental studies. *Photochemistry and Photobiology*, 46(5):759–763, 1987.

[241] G. Oh, E. Chung, and S. H. Yun. Optical fibers for high-resolution in vivo microendoscopic fluorescence imaging. *Optical Fiber Technology*, 19:760–771, 2013.

[242] D. L. Dickensheets and G. S. Kino. Scanned optical fiber confocal microscope. *Proc.SPIE*, 2184, 1994.

[243] E. J. Seibel and Q. Y. Smithwick. Unique features of optical scanning, single fiber endoscopy. *Lasers in Surgery and Medicine*, 30(3):177–183, 2002.

[244] H. Bao, J. Allen, R. Pattie, R. Vance, and M. Gu. Fast handheld two-photon fluorescence microendoscope with a 475 μm $\times$ 475 μm field of view for in vivo imaging. *Opt. Lett.*, 33(12):1333–1335, 2008.

[245] Y. Zhao, H. Nakamura, and R. J. Gordon. Development of a versatile two-photon endoscope for biological imaging. *Biomed. Opt. Express*, 1(4):1159–1172, 2010.

[246] M. Pierce, D. Yu, and R. Richards-Kortum. High-resolution fiber-optic microendoscopy for in situ cellular imaging. *J. Vis. Exp.*, 30, 2011.

[247] C. D. Saunter, S. Semprini, C. Buckley, J. Mullins, and J. M. Girkin. Micro-endoscope for in vivo widefield high spatial resolution fluorescent imaging. *Biomed. Opt. Exp.*, 3:1274–1278, 2012.

[248] C. Winter, T. Zerfaß, M. Elter, S. Rupp, and T. Wittenberg. *Physically Motivated Enhancement of Color Images for Fiber Endoscopy*. 2007.

[249] A. Leung, P. M. Shankar, and R. Mutharasan. A review of fiber-optic biosensors. *Sensors and Actuators B*, 125:688–703, 2007.

[250] K. M. Polizzi and C. Kontoravdi. Genetically-encoded biosensors for monitoring cellular stress in bioprocessing. *Current Opinion in Biotechnology*, 31:50 – 56, 2015.

[251] R. P. Harrison and V. M. Chauhan. Enhancing cell and gene therapy manufacture through the application of advanced fluorescent optical sensors (review). *Biointerphases*, page 01A301, 2018.

[252] L. Dekker and K. M. Polizzi. Sense and sensitivity in bioprocessing-detecting cellular metabolites with biosensors. *Current Opinion in Chemical Biology*, 40:31 – 36, 2017.

[253] E. M. Zhao, Y. Zhang, J. Mehl, H. Park, M. A. Lalwani, J. E. Toettcher, and J. L. Avalos. Optogenetic regulation of engineered cellular metabolism for microbial chemical production. *Nature*, 555:683–687, 2018.

[254] A. Zaslaver, A. Bren, M. Ronen, S. Itzkovitz, I. Kikoin, S. Shavit, W. Liebermeister, M. Surette, and U. Alon. A comprehensive library of fluorescent transcriptional reporters for escherichia coli. *Nat. Methods*, 3:623–8, 2006.

[255] S. Berthoumieux, H. de Jong, G. Baptist, C. Pinel, C. Ranquet, D. Ropers, and J. Geiselmann. Shared control of gene expression in bacteria by transcription factors and global physiology of the cell. *Molecular Systems Biology*, 9:634, 2013.

[256] Y. Ziv and K. K. Ghosh. Miniature microscopes for large-scale imaging of neuronal activity in freely behaving rodents. *Current Opinion in Neurobiology*, 32:141–147, 2015.

[257] W. Yang and R. Yuste. In vivo imaging of neural activity. *Nat. Methods*, 14:349–359, 2017.

[258] T. J. Muldoon, M. C. Pierce, D. L. Nida, M. D. Williams, A. Gillenwater, and R. Richards-Kortum. Subcellular-resolution molecular imaging within living tissue by fiber microendoscopy. *Opt. Express*, 15:16413–16423, 2007.

[259] U. Utzinger and R. R. Richards-Kortum. Fiber optic probes for biomedical optical spectroscopy. *J. Biomed. Opt.*, 8:121–147, 2003.

[260] J. Han, M. Sparkes, and W. O'Neill. Controlling the optical fiber output beam profile by focused ion beam machining of a phase hologram on fiber tip. *Appl. Opt.*, 54:890–894, 2015.

[261] G. Calafiore, A. Koshelev, F. I. Allen, S. Dhuey, S. Sassolini, E. Wong, P. Lum, K. Munechika, and S. Cabrini. Nanoimprint of a 3d structure on an optical fiber for light wavefront manipulation. *Nanotechnology*, 27:375301, 2016.

[262] R. S. R. Ribeiro, P. Dahal, A. Guereiro, P. Jorge, and J. Viegas. Optical fibers as beam shapers: from gaussian beams to optical vortices. *Opt. Lett.*, 41:2137–2140, 2016.

[263] G. V. Bloemberg, A. H. M. Wijfjes, G. E. M. Lamers, N. Stuurman, and B. J. J. Lugtenberg. Simultaneous imaging of pseudomonas fluorescens wcs365 populations expressing three different autofluorescent proteins in the rhizosphere: New perspectives for studying microbial communities. *MPMI*, 13:1170–1176, 2000.

[264] S. I. Al-Juboori, A. Dondzillo, E. A. Stubblefield, G. Felsen, T. C. Lei, and A. Klug. Light scattering properties vary across different regions of the adult mouse brain. *PLoS ONE*, 8:e67626, 2013.

Appendix A

Nature Communication Article

A.1 Article: Resonant out-of-phase fluorescence microscopy and remote imaging overcome spectral limitations

nature COMMUNICATIONS

ARTICLE

DOI: 10.1038/s41467-017-00847-3 OPEN

Resonant out-of-phase fluorescence microscopy and remote imaging overcome spectral limitations

Jérôme Quérard[1,2], Ruikang Zhang[1,2], Zsolt Kelemen[3], Marie-Aude Plamont[1,2], Xiaojiang Xie[1,2,4], Raja Chouket[1,2], Insa Roemgens[1,2], Yulia Korepina[1,2], Samantha Albright[1,2], Eliane Ipendey[1,2], Michel Volovitch[5,6], Hanna L. Sladitschek[7], Pierre Neveu[7], Lionel Gissot[3], Arnaud Gautier[1,2], Jean-Denis Faure[3], Vincent Croquette[8], Thomas Le Saux[1,2] & Ludovic Jullien[1,2]

We present speed out-of-phase imaging after optical modulation (OPIOM), which exploits reversible photoswitchable fluorophores as fluorescent labels and combines optimized periodic illumination with phase-sensitive detection to specifically retrieve the label signal. Speed OPIOM can extract the fluorescence emission from a targeted label in the presence of spectrally interfering fluorophores and autofluorescence. Up to four fluorescent proteins exhibiting a similar green fluorescence have been distinguished in cells either sequentially or in parallel. Speed OPIOM is compatible with imaging biological processes in real time in live cells. Finally speed OPIOM is not limited to microscopy but is relevant for remote imaging as well, in particular, under ambient light. Thus, speed OPIOM has proved to enable fast and quantitative live microscopic and remote-multiplexed fluorescence imaging of biological samples while filtering out noise, interfering fluorophores, as well as ambient light.

[1] PASTEUR, Département de Chimie, École Normale Supérieure, UPMC Univ Paris 06, CNRS, PSL Research University, 75005 Paris, France. [2] Sorbonne Universités, UPMC Univ Paris 06, École Normale Supérieure, CNRS, PASTEUR, 75005 Paris, France. [3] Institut Jean-Pierre Bourgin, INRA, AgroParisTech, CNRS, Saclay Plant Sciences (SPS), Universite Paris-Saclay, 78000 Versailles, France. [4] Department of Chemistry, Southern University of Science and Technology, Shenzhen 518055, China. [5] Centre for Interdisciplinary Research in Biology (CIRB) CNRS, INSERM, Labex MemoLife, PSL Research University, Collège de France, 75005 Paris, France. [6] École Normale Supérieure, Institute of Biology at the Ecole Normale Supérieure (IBENS), CNRS, INSERM, PSL Research University, 75005 Paris, France. [7] Cell Biology and Biophysics Unit, European Molecular Biology Laboratory, 69117 Heidelberg, Germany. [8] Ecole Normale Supérieure, Département de Physique and Département de Biologie, Laboratoire de Physique Statistique, CNRS, ENS, 75005 Paris, France. Correspondence and requests for materials should be addressed to T.S. (email: Thomas.Lesaux@ens.fr) or to L.J. (email: Ludovic.Jullien@ens.fr)

ARTICLE NATURE COMMUNICATIONS | DOI: 10.1038/s41467-017-00847-3

In fluorescence microscopy and remote imaging, the discrimination of a fluorophore usually results from optimizing its brightness and its spectral properties[1]. Despite the widespread use of fluorescence for labeling biological samples, this approach still suffers from limitations. First, extraction of a fluorescent signal is challenging in light-scattering and autofluorescent samples. Second, spectral deconvolution of overlapping absorption and emission bands can only discriminate a few labels, falling short from the several tens needed for advanced bioimaging[2, 3].

Following our previous works exploiting kinetic parameters for selective discrimination[4–8], we have introduced Out-of-Phase Imaging after Optical Modulation (OPIOM), an imaging technique enabling selective imaging of photoactive fluorescent labels such as reversibly photoswitchable fluorescent proteins (RSFPs)[9] using their photoswitching kinetics as discriminating parameters[10, 11]. Other imaging protocols have exploited RSFP photoswitching kinetics for selective fluorescence imaging. In optical lock-in detection (OLID), the observable is the correlation coefficient between the total fluorescence emission and a reference signal from the targeted photoswitchable fluorophore over several cycles of dual-wavelength-driven photoswitching[12, 13]. In synchronously amplified fluorescence image recovery (SAFIRe), the amplitude of the fluorescence modulation generated by modulating a secondary light source depopulating dark states of the fluorophore is used to build the image[14]. As SAFIRe, OPIOM relies on a periodically modulated illumination but it exploits phase-sensitive detection and easily predictable resonance conditions involving the illumination control parameters and the RSFP photoswitching dynamics to selectively retrieve the contribution of a fluorescent probe of interest from the amplitude of the overall out-of-phase fluorescence response. The requirements for driving RSFP photoswitching at a slow rate and non-optimized extent have limited however the use of OPIOM for live fluorescence imaging[10, 11].

Here we introduce a powerful protocol, speed OPIOM, for multiplexed imaging of fluorescent labels under adverse optical conditions. Like OPIOM, speed OPIOM combines periodic illumination matched with RSFP photoswitching kinetics and phase-sensitive detection. However, speed OPIOM differs from OPIOM by a much-optimized periodic illumination modality relying on an extensive theoretical background. Speed OPIOM correspondingly enables the fast and remote imaging of an RSFP expressed in a strongly autofluorescent biological sample under ambient light and the fast, quantitative and simultaneous microscopy imaging of several spectrally overlapping RSFPs in both fixed and live cells.

Results

Speed OPIOM principle. To drive RSFP photoswitching at optimal rate and extent, speed OPIOM does not use one modulated light source like the original OPIOM,[10] but two modulated light sources synchronized in antiphase at two wavelengths driving RSFP photoswitching between its bright and dark states (angular frequency of modulation $\omega = 2\pi/T$, where T is the period of light modulation; mean intensities $<I_1>$ and $<I_2>$) (Fig. 1a). Tens to hundreds images are acquired for at least two periods of light excitation. The speed OPIOM algebraic signal S is the out-of-phase component of the modulated fluorescence signal, which is directly retrieved without any further processing after lock-in detection with efficient noise rejection by Fourier transform of the acquired images (Fig. 1b). S exhibits a sharp resonant maximum when $<I_1>$ and $<I_2>$ are tuned to maximize sensitivity of the average concentrations of the exchanging RSFP states to changes of light intensities, and ω is matched with the inverse of the RSFP photoswitching relaxation time (Supplementary Note 1). Interestingly, this maximum is twice as high as in OPIOM[10, 11]. For a given RSFP, S is maximal only when the ratios $<I_2>/<I_1>$ and $\omega/<I_1>$ take specific values that depend only on the photochemical and kinetic properties of the RSFP, and is negligible otherwise. Each RSFP has singular photochemical and kinetic properties, and thus its own resonant conditions. Hence, tuning $<I_2>/<I_1>$ and $\omega/<I_1>$ to the resonant values of a specific RSFP allows to selectively image this RSFP (Fig. 1b), filtering out the contribution of non-resonant fluorophores as well as ambient light. In addition, in contrast to OPIOM, which has been limited by the thermally driven back conversion of the photo switched RSFP[10],

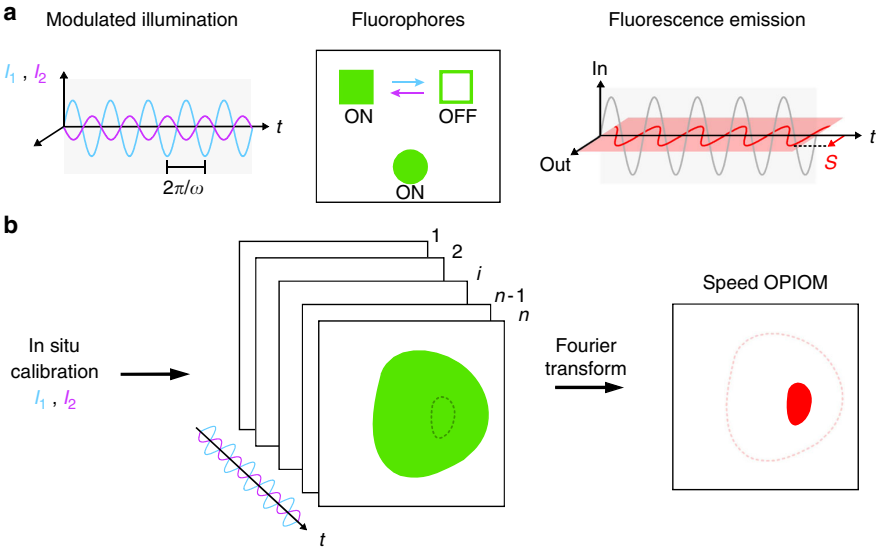

Fig. 1 Principle of speed OPIOM. **a** A sinusoidally modulated antiphase-synchronized dual illumination generates the quadrature-delayed component S (in *red*) of the fluorescence emission used for selective speed OPIOM imaging of RSFPs. **b** After in situ calibration, the fluorescence images are recorded under modulated illumination and processed to yield S after Fourier transform

NATURE COMMUNICATIONS | DOI: 10.1038/s41467-017-00847-3 ARTICLE

imaging speed can be simply increased by increasing the excitation light intensities, provided that RSFP photoconversion still obeys a two-state exchange.

Acquisition of the speed OPIOM discrimination map. To test the discriminative power of speed OPIOM, we used eight RFSPs: Dronpa[15], Dronpa-2[16], Dronpa-3[17], RSFastLime[16, 18], rsEFGP[19], rsEFGP2[20], Padron[18], and Kohinoor[21], which exhibit maximal emission in a narrow (505 nm; 522 nm) wavelength range[15–21] precluding spectral discrimination (Supplementary Fig. 1). Dronpa, Dronpa-2, Dronpa-3, RSFastLime, rsEFGP, and rsEFGP2 are switched to a dark or a bright state by blue and violet light, respectively (negative photochromism), whereas Padron and Kohinoor exhibit the opposite behavior (positive photochromism). We investigated the photoswitching behavior of these RSFPs and established that it obeys a two-state kinetic model at time scales longer than a few milliseconds, yielding robust photochemical and kinetic parameters with respect to environmental changes (Supplementary Note 2). Interestingly, resonant illumination conditions matching a specific RSFP could be easily determined directly on the imaging setup using a simple series of light jump experiments (Supplementary Note 3) and either purified RSFPs or fixed cells among others (Supplementary Note 2). We then computed the speed OPIOM response with varying illumination parameters for the eight assessed green RSFPs and determined that each RFSP had a distinct response maximum—analogous to an individual detection channel—in the parameter space of illumination intensities and frequencies (Fig. 2).

Speed OPIOM is a quantitative imaging protocol. To evidence that speed OPIOM provides quantitative information, we used a microfluidic device containing six chambers filled with Dronpa-2 solutions at five different concentrations and with the spectrally similar non-photoactive fluorescent protein EGFP. A home-built epifluorescence microscope equipped with two light emitting diodes (LEDs; Supplementary Fig. 2) driven for intensity, angular frequency of modulation, and phase was used to image the microfluidic device by tuning illumination to the Dronpa-2 resonance conditions. We recorded the processed speed OPIOM image together with the pre-OPIOM image (built from the average fluorescence intensity) (Supplementary Fig. 3). Dronpa-2 fluorescence emission was visible in both pre-OPIOM and speed OPIOM images. In contrast, as expected from the in-phase modulation of its fluorescence emission only, no EGFP signal could be detected on the speed OPIOM image, which evidenced the anticipated selective imaging of Dronpa-2 with speed OPIOM: for EGFP and Dronpa-2 at 3 and 6 µM concentrations, respectively, pre-OPIOM and speed OPIOM images with 1:0.8 and 1:7600 intensity ratios were obtained. Furthermore, the five chambers containing Dronpa-2 exhibited relative intensities directly reflecting their concentration, which demonstrated that the speed OPIOM signal is proportional to the probe concentration as theoretically predicted.

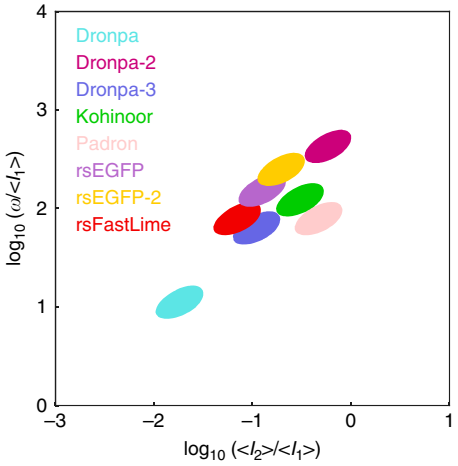

Fig. 2 Map of RSFP discrimination with speed OPIOM. The illumination parameters $\langle I_2\rangle/\langle I_1\rangle$ and $\omega/\langle I_1\rangle$ (here in rad Ein^{-1} m^2) can be tuned to single out the observable *S* from multiple RSFP targets (See Supplementary Note 2 for the RSFP photochemical and kinetic parameters). The contours correspond to >95% of the maximal *S* value with $\langle I_1\rangle = 1$ Ein s^{-1} m^{-2}

Speed OPIOM eliminates spectral interferences. We then showed that speed OPIOM could selectively retrieve a targeted RSFP signal in biological samples in the presence of interfering non-photoactive fluorophores and autofluorescence (Fig. 3). In microscopy of mammalian cells expressing both Dronpa-2 and EGFP (Fig. 3a), these two proteins could not be distinguished in the pre-OPIOM image (Fig. 3b), whereas only Dronpa-2 contributed to the speed OPIOM channel (Fig. 3c and Supplementary Fig. 4). Hence, speed OPIOM efficiently suppressed the signal from spectrally interfering non-photoactive fluorophores.

Speed OPIOM for fluorescence remote imaging under ambient light. We then showed that speed OPIOM is not limited to microscopy but is relevant for remote imaging as well, in particular, under ambient light (Fig. 3d). Hence, we implemented speed OPIOM on a home-built fluorescence remote imaging setup (Supplementary Fig. 5) and successfully discriminated an RSFP in the highly demanding situation of remote imaging of a labeled autofluorescent plant sample under ambient light: whereas Dronpa-2-expressing *Camelina* seedlings were undistinguishable from wild-type seedlings in the pre-OPIOM image (Fig. 3e), Dronpa-2 was unambiguously revealed in the speed OPIOM channel (Fig. 3f). Thus, speed OPIOM is appropriate for selective RSFP imaging against an autofluorescent background even in ambient light.

Speed OPIOM discriminates distinct spectrally similar RSFPs. We first discriminated RSFPs with close resonance conditions but opposite photoswitching behaviors using the sign of their speed OPIOM signal (Fig. 4a): RSFPs with negative photochromism like Dronpa-3 contribute positively to the signal, whereas RSFPs with positive photochromism like Kohinoor contribute negatively. Thus, unlike pre-OPIOM (Fig. 4b), speed OPIOM easily distinguished Dronpa-3 and Kohinoor (Fig. 4c, d and Supplementary Fig. 6).

RFSPs possessing distinct values of the resonant illumination parameters can be imaged sequentially by adjusting the illumination conditions to the resonant values of each RSFP (Fig. 4e). Accordingly, in contrast to pre-OPIOM (Fig. 4f), the spectrally undistinguishable Dronpa and Dronpa-2 could be imaged in a microfluidic device and in mammalian cells with high-contrast enhancement in their respective speed OPIOM channels (Fig. 4g–h; Supplementary Figs. 7 and 8). Hence, in the microdevice, the pre-OPIOM and speed OPIOM images of Dronpa and Dronpa-2 at concentrations of 1 and 18 µM yielded 1:1.2 and 1:27 intensity ratios with Dronpa-2 as the target (respectively, 1:2 and 1:8 with Dronpa as the target).

In speed OPIOM, multiplexed RSFP imaging is not limited to sequential modifications of the ($\langle I_1\rangle$, $\langle I_2\rangle$, ω) set but can be parallelized (and correspondingly further accelerated) for RSFPs

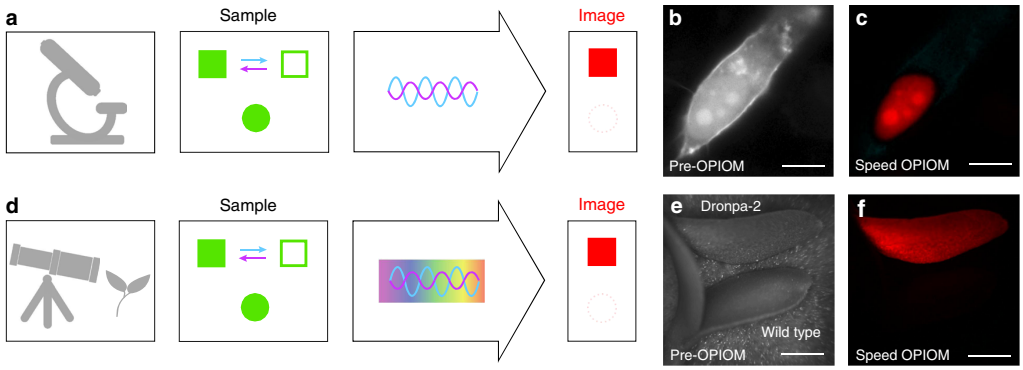

Fig. 3 Speed OPIOM selectively retrieves an RSFP signal in the presence of spectral interferences. In contrast to pre-OPIOM (**b**, **e**), speed OPIOM microscopy (**a**) and remote (**d**) imaging selectively unveils a RSFP target (*square* in **a**, **d**, Dronpa-2 in **c**–**f**) in cells (**a**) and *Camelina* seedlings (**d**) even in the presence of a spectrally interfering fluorophore (*disk* in **a**, **d**, EGFP in **b**, **c**), autofluorescence or ambient light (**d**) and (**e**, **f**). Systems: Fixed HeLa cells expressing H2B-Dronpa-2 (at the nucleus) and Lyn11-EGFP (at the cell membrane). **b**, **c** Camelina, ubiquitously expressing Dronpa-2 or wild type (respectively *top* and *down* in **e**, **f**). The images were recorded at 37 °C (**b**, **c**) and 20 °C (**e**, **f**). *Scale bars* (μm): 10 (**b**, **c**), 875 (**e**, **f**). See Supplementary Tables 1 and 3 for the acquisition conditions

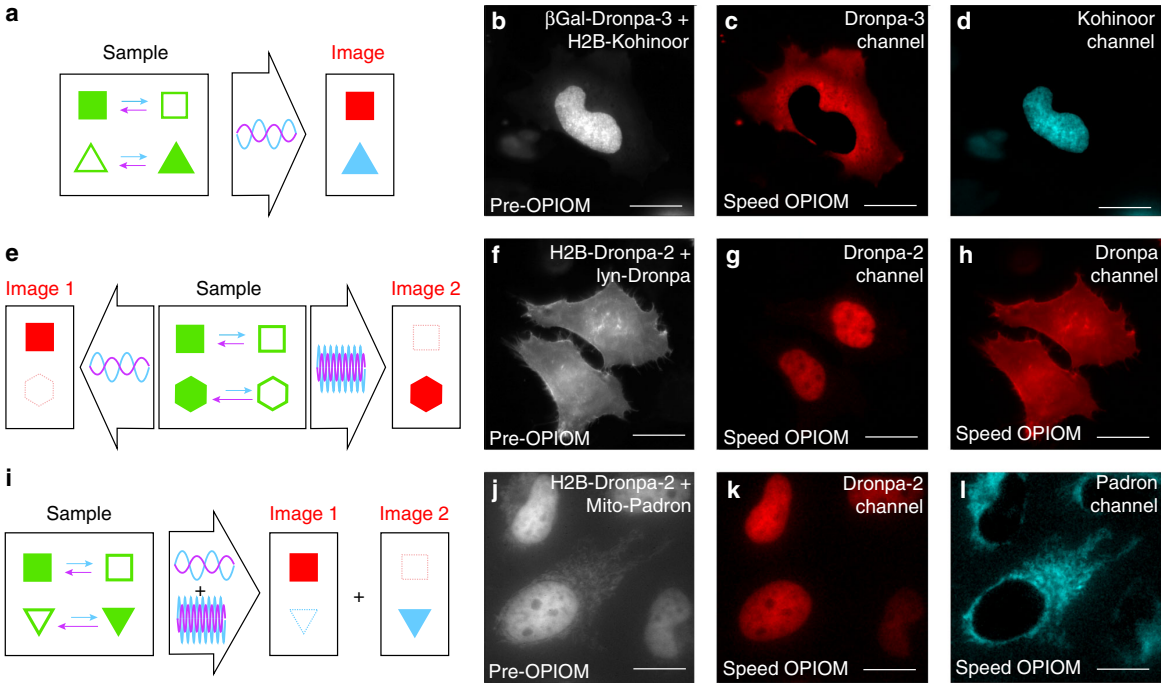

Fig. 4 Speed OPIOM selectively discriminates RSFP signals in the presence of interfering RSFPs. Tuning the illumination parameters enables the selective imaging of RSFPs exhibiting similar resonance conditions but opposite photochromism (**a**) or distinct resonance conditions using light modulation, either sequentially at one frequency (**e**) or simultaneously at multiple frequencies (**i**). Pre-OPIOM and speed OPIOM images tuned to the resonance of Dronpa-3 and Kohinoor (**b**–**d**), Dronpa-2 (**f**, **g**) and Dronpa (**h**), or tuned to optimize orthogonality between Dronpa-2 and Padron (**j**–**l**). Systems: Fixed HeLa cells expressing βGal-Dronpa-3 and H2B-Kohinoor (**b**–**d**), H2B-Dronpa-2 and Lyn11-Dronpa (**f**–**h**), or H2B-Dronpa-2 and Mito-Padron (**j**–**l**). Localizations: βGal (cytoplasm), H2B (nucleus), Lyn11 (cell membrane). The images were recorded at 37 °C. *Scale bars*: 20 μm. See Supplementary Tables 1 and 2 for the acquisition conditions

sharing identical resonance for $<I_2>/<I_1>$ by modulating illumination at multiple resonant modulation frequencies (Fig. 4i and Supplementary Note 1). Hence, Dronpa-2 and Padron (Fig. 2) could be imaged simultaneously in a single speed OPIOM acquisition superposing two periodic illumination regimes tuned to the resonant frequency of each RFSP (Fig. 4j–l and Supplementary Fig. 9).

Speed OPIOM for real time fluorescence imaging. In speed OPIOM, the frequency of image acquisition can be increased by increasing $<I_1>$ and $<I_2>$ at constant value of the $<I_2>/<I_1>$ ratio. Hence, speed OPIOM gives access to imaging biological processes in live cells. To illustrate this opportunity, we monitored the nuclear translocation of ERK2 fused to Kohinoor upon epidermal growth factor (EGF) stimulation in cells with an

NATURE COMMUNICATIONS | DOI: 10.1038/s41467-017-00847-3 ARTICLE

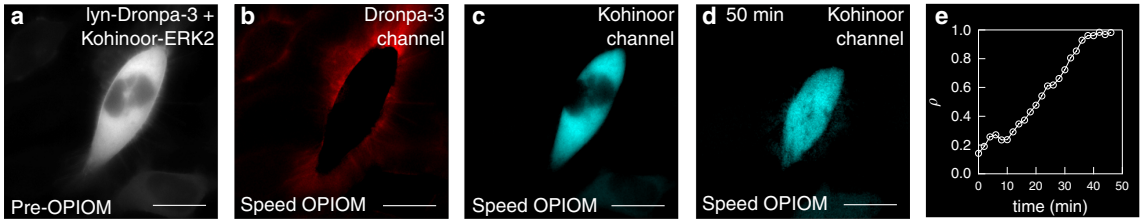

Fig. 5 Speed OPIOM can track quantitatively fast biological processes. Live HeLa cells expressing MEK1, Kohinoor-ERK2 (initially located in the cytoplasm) and Lyn11-Dronpa-3 before (**a**–**c**) and after (**d**) addition of epidermal growth factor (*EGF*). The figure in **e** displays the temporal evolution of the absolute value of the ratio ρ of the speed OPIOM Kohinoor signals in the nucleus and in the cytoplasm. Pre-OPIOM and speed OPIOM images tuned to the resonance of Dronpa-3 and Kohinoor (**a**–**e**). Localizations: Lyn11 (cell membrane). The images were recorded at 37 °C. *Scale bars*: 20 µm. See Supplementary Table 1 for the acquisition conditions

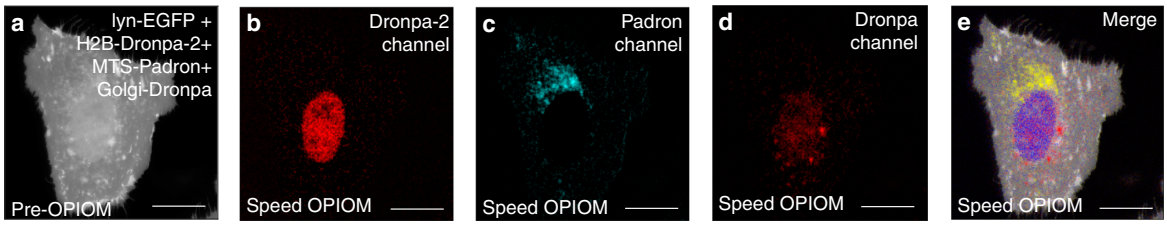

Fig. 6 Speed OPIOM can independently image four spectrally similar fluorescent proteins without high-contrast enhancement. Pre-OPIOM (**a**) and speed OPIOM images tuned to selectively image Dronpa-2 (**b**), Padron (**c**), and Dronpa (**d**). In **e**, overlay between the pre-OPIOM image from the Dronpa-2 acquisition and speed OPIOM images collected in (**b**–**d**). Systems: Fixed U2OS cells expressing H2B-Dronpa-2, Mito-Padron, Dronpa-GTS, and Lyn11-EGFP. Localizations: H2B (nucleus), Lyn11 (cell membrane), Mito (mitochondria), GTS (Golgi). The images were recorded at 37 °C. *Scale bars*: 20 µm. See Supplementary Table 1 for the acquisition conditions

interfering Dronpa-3 membrane label (Fig. 5a–d). Speed OPIOM allowed following the rapid Kohinoor-ERK2 nuclear translocation (Fig. 5e), demonstrating that speed OPIOM can be used to track quantitatively fast biological processes.

Speed OPIOM for multiplexed fluorescence imaging. Finally we demonstrated that speed OPIOM could overcome spectral limitations for multiplexed imaging. Hence, Dronpa, Dronpa-2, and Padron could be first imaged in a microdevice with high-contrast enhancement using three acquisitions involving different ($<I_1>$, $<I_2>$, ω) sets (Supplementary Note 5). They were subsequently imaged in cells (Fig. 6a–d and Supplementary Fig. 10) to build a merged image unambiguously displaying four spectrally similar fluorescent proteins—EGFP, Dronpa, Dronpa-2, and Padron (Fig. 6e).

Discussion

In this paper, we used RSFPs to show that speed OPIOM is a powerful approach for multiplexed fluorescence imaging against a background of spectral interferences. Speed OPIOM efficiently filters out autofluorescence, scattered and ambient light, opening up great prospects for remote fluorescence imaging within highly autofluorescent biological samples under broad daylight. Speed OPIOM has enabled live imaging of biological processes at the second time scale but is compatible with a speed of image acquisition of up to 50 Hz by adjusting the illumination light intensities. Eventually, as speed OPIOM only requires the modulation of illumination light and phase-sensitive detection of the fluorescence, such features could be easily implemented on existing fluorescence imaging setups in addition to optical filters for spectral discrimination.

Speed OPIOM distinguishes spectrally similar RSFPs (but other photoswitchable fluorophores[22–25] would be relevant as well) by leveraging their photochemical and kinetic characteristics. Thanks to its phase-sensitive detection scheme, speed OPIOM is both reference-free and band-pass-selective thereby overcoming some limitations encountered with SAFIRe and OLID (Supplementary Note 5). Despite intrinsic limitations associated to noise (Supplementary Note 6) and precision on phase retrieval (currently 3×10^{-3} rad), speed OPIOM imaging can typically enhance contrast of photoswitchable fluorophores against non-photoactive spectrally interfering fluorophores or ambient light by a 10^2–10^3 factor. Eventually, speed OPIOM application will be facilitated by the ever-expanded number of RSFPs developed for super-resolution microscopy; by requiring one order of magnitude departure of the photochemical properties for efficient discrimination, we estimate that speed OPIOM should soon give access to multiplexed imaging of five to ten distinct RSFPs. Hence, speed OPIOM should considerably expand the scope of fluorescence microscopy and remote imaging at video rate.

Methods

Reversibly photoswitchable fluorescent proteins. Most of the RSFPs used in this study take part to the Dronpa[15] family. Dronpa-2[16] and rsFastLime[16] contain only one mutation M159T and V157G respectively whereas Dronpa-3[17] has two mutations: V157I/M159A. Padron[18] carries eight mutations: T59M, V60A, N94I, P141L, G155S, V157G, M159Y, and F190S. Kohinoor[21] is a Padron variant containing seven mutations (according to the Padron sequence): N102I, L141P, F173S, S190D, D192V, K202R, and E218G. rsEGFP1 (EGFP(T65A, A206K)[19]) and rsEGFP2 (EGFP(T65A, Q69L, V163S, A206K)[20]) have been obtained from EGFP and contained two and four mutations, respectively.

Plasmids. The plasmids for bacterial expression of Dronpa-2[10], Dronpa-3[10], Dronpa[26], Kohinoor (pRSET-Kohinoor)[21], rsEGFP1 (pBAD-rsEGFP)[19], and rsEGFP2 (pBAD-rsEGFP2)[20] carrying an N-terminal hexahistidine tag were previously described. The plasmid for bacterial expression of rsFastLime was obtained by introducing the V157G mutation in that of Dronpa, using the QuickChange Site-Directed Mutagenesis Kit (Stratagene).

The plasmid pcDNA3-Kohinoor-H2B for mammalian expression of H2B-Kohinoor was previously described by Nagai and coworkers[21]. The plasmid for mammalian expression of Lyn11-EGFP (with a N-terminal MGCIKSKGKDSAGGGS sequence for membrane targeting) was previously described[10]. The plasmid pJWCAG90 for mammalian expression of MEK1 was previously described by Gautier et al[27]. The plasmid for mammalian expression of Dronpa and Dronpa-3 with a N-terminal MGCIKSKGKDSAGGGS sequence (Lyn11) for membrane targeting (Lyn11-Dronpa and Lyn11-Dronpa-3) were obtained by insertion of the genes encoding Lyn11-Dronpa and Lyn11-Dronpa-3 in the pIRES vector (Invitrogen) using *Bgl*II and *Not*I restriction sites. The plasmid for mammalian expression of Dronpa-2 fused at the C terminal of the histone H2B (H2B-Dronpa-2) was obtained by insertion of the genes encoding H2B-Dronpa-2 in the pIRES vector (Invitrogen) using *Bgl*II and *Not*I restriction sites. The plasmid for mammalian expression of Dronpa-3 fused to the C terminal of β-galactosidase (βGal-Dronpa-3) was obtained by inserting the genes encoding βGal-Dronpa-3 in the pIRES vector (Invitrogen) using *Bgl*II and *Not*I restriction sites. The plasmid for mammalian expression of Kohinoor fused to the N terminal of ERK2 (Kohinoor-ERK2) was obtained by inserting the genes encoding Kohinoor-ERK2 in the pEGFP-C vector (Clontech) using *Nhe*I and *Kpn*I restriction sites. The plasmids for the mammalian expression of EGFP fused to the membrane anchoring (lyn) peptide from the mouse tyrosine-protein kinase Lyn, Dronpa fused to a 25 aa Golgi-targeting signal (GTS) from human Golgi phosphoprotein 2 (GOLPH2), Padron fused to the N-terminal mitochondrial targeting signal (MTS) of either COX4 or COX8 and Dronpa-2 fused to human H2B for chromosomal location were assembled using MXS chaining[28]. We sequentially inserted a CMV promoter (or sCMV for Padron), the lyn (MGCIKSKRKDVEN), MTS (MLSLRQSIRFFKPATRTLCSSRYLL or MSVLTPLLLRGLTGSARRLPVPRAKIHSL), GTS (MKSPPLVLAALVACIIVLGFNYWIA) peptide tags or the H2B coding sequence to plasmids containing the coding sequences of EGFP, Dronpa, Padron, or Dronpa-2, respectively, coupled to the bovine growth hormone (BGHpA, alternatively SV40LpA for Padron) polyadenylation signal. The expression blocks CMV::GTS-Dronpa-BGHpA and CMV::Lyn-eGFP-BGHpA were further combined to give a bicistronic plasmid. CMV::MTS-Padron-BGHpA and CMV::H2B-Dronpa-2-BGHpA blocks were similarly combined.

The Camelina expression vector expressing p35S::Dronpa2 construct was achieved as follow. The gateway-cassette from pUBN-GFP-Dest[29] amplified by PCR using primers 5′-tgacgcgtaaggggatctagaatcacaagtttgtacaaaaaagctg-3′ and 5′-ttaatcacactcaccatctcgaggatcaccactttgtacaagaaag-3′ and Dronpa-2 coding sequence amplified from Dronpa-2pDONR207 with primers 5′-atggtgagtgtgatta aaccagaca-3′ and 5′-ggctgcggccgcctcgactacttggcctgcctcggcagctcag-3′ were cloned in one step in *Bam*HI *Xho*I-digested pBinGlyRed vector[30], creating pD2. The doubled CaMV 35 S promoter was amplified from pMDC83[31] with primers 5′-ggggacaag tttgtacaaaaaagcaggcttccagtgccaagcttggcgtgcct-3′ and 5′-ggggaccactttgtacaagaaagct gggtcgtcgaggtcctctccaaatgaaatg-3′, recombined into pDONR207 (Invitrogen) and eventually recombined into pD2.

Protein production and purification. The plasmids expressing Dronpa, Dronpa-2, Dronpa-3, rsFastLime, Padron, and Kohinoor carrying an N-terminal hexahistidine tag were transformed in *E. coli* DH10B strain. Cells were grown in Terrific Broth (TB). Expression was induced by addition of isopropyl β-D-1-thio-galactopyranoside (IPTG) to a final concentration of 1 mM at OD_{600} 0.6. Cells were harvested after 16 h of expression and lysed by sonication in Lysis buffer (30/40 mM imidazole, 50 mM TRIS/HCl at pH 7.5, 400 µM 4-(2-Aminoethyl) benzenesulfonyl fluoride hydrochloride, 5 mg ml^{-1} DNAse, 5 mM $MgCl_2$ and 1 mM dithiothreitol). Insoluble material was removed by centrifugation and the soluble protein extract was batch adsorbed onto Ni-NTA agarose resin (Thermofisher). The protein loaded Ni-NTA column was washed with 20 column volumes of 50 mM TRIS/HCl pH 7.5, 20 mM imidazole, 150 mM NaCl. Bound protein was eluted in 50 mM TRIS/HCl pH 7.5, 500 mM imidazole, 150 mM NaCl. Protein fractions were dialyzed on cassette Slide-A-Lyzer Dialysis Cassettes (Thermofisher) against 50 mM TRIS/H_2SO_4 pH 8.

The plasmids pBAD-rsEGFP and pBAD-rsEGFP2 were transformed in E. coli BL21 cells (Merck Millipore). Cells were grown in Lysogeny Broth (LB) supplemented with 0.1% glucose w/v. Expression was induced by addition of arabinose to 0.2% w/v at OD600 0.4. Cells were collected after 4 h of expression and lysed by sonication in 50 mM PBS pH 7.4, 150 mM NaCl and a cocktail of protease inhibitors (Sigma Aldrich). Insoluble material was removed by centrifugation and the soluble protein extract was batch adsorbed onto Ni-NTA agarose resin (Thermofisher). The protein loaded Ni-NTA column was washed with 20 column volumes of 50 mM PBS pH 7.4, 150 mM NaCl, 20 mM imidazole. Bound protein was eluted in 50 mM PBS pH 7.4, 150 mM NaCl, 0.5 M imidazole. Protein fractions were dialyzed on cassette Slide-A-Lyzer Dialysis Cassettes (Thermofisher) against 50 mM PBS pH 7.4, 150 mM NaCl.

Mammalian cell culture and transfection. HeLa and U2OS cells were grown at 37°C in 5% CO_2 atmosphere in DMEM with GlutaMAX-1 complemented with 10% fetal bovine serum (FBS) and 1% penicillin / streptomycin. Cells were transiently transfected with Genejuice (Merck) according to the manufacturer's protocol. Cells were washed with Dulbecco's phosphate-buffered saline (DPBS) and fixed with 2% paraformaldehyde (PFA) solution.

***Camelina sativa* transformation and growth**. *Camelina sativa* (cv Celine) was transformed following an improved method of the traditional *Arabidopsis* floral-dip method and transgenic were selected as described previously[32]. Seeds were sown on water-soaked paper and grow for 7 days in a growth chamber under cycles of 16 h light at 22°C/8 h dark at 16°C.

Reagents and solutions. All solutions were made up using purified water (Direct-Q 5 apparatus; Millipore, Billerica, MA). The Britton-Robinson buffer was prepared from acetic acid: 4 mM; phosphoric acid: 4 mM; AMPSO: 4 mM, NaCl: 150 mM. All experiments conducted to determine the photophysical and photochemical properties of the purified proteins were performed in Britton-Robinson buffer (pH 7.5) at 37 °C, using protein concentrations of 10 µM, unless stated otherwise.

pH measurements. By assimilating activity and concentration, the proton concentration was directly measured after calibration of the pH meter (Standard pH meter PHM210, Radiometer Analytical equipped with a Radiometer Analytical PHC3359-8 combination pH electrode (Hach, Loveland, CO).

Spectroscopic instruments. Absorption spectra of proteins were recorded at 37 °C on a Cary 300 UV/Vis spectrophotometer (Agilent Technologies, Santa Clara, CA), equipped with a Peltier 1 × 1 thermostated cell holder (Agilent Technologies). The samples were placed in 55 µl quartz cuvettes (0.3 cm × 0.3 cm light path; Hellma Optics, Jena, Germany). Fluorescence measurements used for kinetic analysis were acquired on a LPS 220 spectrofluorometer (PTI, Monmouth Junction, NJ), equipped with a TLC50 cuvette holder (Quantum Northwest, Liberty Lake, WA) thermoregulated at 37 °C. Light intensities were controlled by varying the current on two LED light sources. The first one (LXZ1-PB01 from Philips Lumileds, San Jose, CA) was filtered at 480 ± 20 nm (HQ 480-40 from Chroma Technology Corp, Rockingham, VT) whereas the second one (LHUV-0405, Philips Lumileds) was filtered at 405 ± 20 nm (F405-40; Semrock, Rodchester, NY). The LEDs were supplied by a DC4100 LED driver (Thorlabs, Newton, NJ). The two light sources were collimated with ACL2520U condenser lenses (Thorlabs) and beams were next combined thanks to a dichroic filter (T425LPXR, Chroma Technology Corp). Photon fluxes were measured with a Nova II powermeter (Laser Measurement Instruments).

Microfluidic devices. Each microdevice was composed of a circular glass coverslip (0.17 mm thick, 40 mm diameter; Menzel-Glaser, Braunschweig, Germany) and a PDMS stamp (RTV615; General Electrics, Fairfield, CT) including either four 400 µm × 400 µm × 20 µm square chambers separated by 150 µm × 20 µm walls or six 250 µm × 125 µm × 20 µm chambers separated by 100 µm × 20 µm walls. Each chamber was connected to a sample reservoir punched in the PDMS stamp through a 40 µm × 20 µm channel. Before assembly, the coverslip and the PDMS stamp were rinsed with ethanol and dried under a nitrogen flow. The bottom glass surface of the microdevice was placed on a 0.4 mm thick copper disk in which a 8 mm hole had been opened for further observation with the objective. To fill the micro-chambers with appropriate solutions, the air dissolved in the PDMS was pumped for 3 min at 50 mbar at room temperature and sample solutions were added to each reservoir, which resulted in the autonomous and controlled loading of the device.

Microscopy epifluorescence setup. We used a home-built epifluorescence microscopy setup (Supplementary Fig. 2). The samples were illuminated using a LXZ1-PB01 LED (Philips Lumileds) filtered at 480 ± 20 nm (F480-40; Semrock, Rochester, NY) and a LHUV-0405 (Philips Lumileds) LED filtered at 405 ± 20 nm (F405-40; Semrock, Rochester, NY) as light sources. Each LED was supplied by a LED driver (LEDD1B, Thorlabs, Newton, NJ) and modulated synchronously to each other by a waveform generator (33612 A, Keysight Technologies). A lens (ACL2520U; Thorlabs, Newton, NJ, f = 20 mm) was placed just after each diode to collimate the light sources. The two light beams were next combined thanks to a dichroic mirror (T425LPXR, Chroma, Bellows Falls, VT) and a second pair of lenses was used to focus the light at the back focal plane of the objective after being reflected by the dichroic filter (Di-FF506, Semrock, Rochester, NY). Fluorescence images at 525 ± 15 nm (F525-30; Semrock, Rochester, NY) were acquired for the microdevices with a 10 × fluar (NA 0.5, Carl Zeiss AG, Feldbach, Switzerland) objective and for cell imaging with a 60 × UPlanApo (NA 1.2, Olympus Corporation, Tokyo, Japan) objective. Objectives were mounted on a home-built microscope equipped with a Luca-R CCD camera (Andor Technology, Belfast, UK). The bottom surface of the imaged sample was placed on a 0.4 mm thick copper disk in which a hole of 8 mm in diameter had been opened for observation with the objective. This metal holder was itself mounted on an aluminum block thermostated at 37 ± 0.2 °C with two thermoelectric Peltier devices (CP 1.0-63-05 L-RTV; Melcor, Trenton, NJ). The stage temperature was monitored with a TCS610 thermistor (Wavelength Electronics, Bozeman, MT) and the feedback loop was driven by a MPT10000 temperature controller (Wavelength Electronics, Bozeman, MT). The average excitation intensities were calibrated in imaging conditions by measuring the relaxation times associated to the photoisomerizations of Dronpa-2 containing samples upon irradiation with one or two wavelengths

(Supplementary Note 3). Triggering of the camera acquisition was synchronized with the onset of the periodic excitation light (using the option "External start" in the Solis software, Andor Technology). A fixed phase delay ϕ_{acq} between the dates of camera recording and light excitation was observed accordingly (due to integration of the signal over the exposure time and the triggering of the camera). This phase delay has been previously calibrated using a microfluidic device filled with Fluorescein or using cells expressing EGFP:[10] the $I_F^{1,out}$ and $I_F^{1,in}$ first-order in- and out-of-phase components of temporal evolution of Fluorescein (or EGFP) emission were extracted (see the Matlab code given in Supplementary Note 4) and ϕ_{acq} was computed as $\phi_{acq} = \arctan(I_F^{1,out}/I_F^{1,in})$. This value was then used for further image analysis.

Setup for remote fluorescence imaging. We used a home-built remote sensing setup (Supplementary Fig. 5) for macro imaging. In addition to the two LED sources at 480 and 405 nm used in the microscopy setup, we introduced a LXZ1-PB01 LED (Philips Lumiled) filtered at 550 ± 15 nm (ET550/15×; Chroma, Bellows Falls, VT) to possibly excite red fluorescent emitters (for example DsRed). The three light beams were combined by three dichroic mirrors (T425LPXR, T505LPXR, 59004bs; Chroma, Bellows Falls, VT). A beam expander system consisted of one divergent lens (ACN254-040-A, $f = -40$ mm, Thorlabs, Newton, NJ) and two convergent lenses (AC508-100-A, $f = 100$ mm, Thorlabs, Newton, NJ) has been used so that the light is clearly focused at a distance of up to 130 mm away where the sample is placed. With this setup, we can detect both green (525 nm) and red (600 nm) fluorescence emissions. A specially designed objective with three elements has been correspondingly used to correct for the chromatism of these two channels. The sample image is acquired by a color CMOS camera (UI-3060CP, iDS Imaging Development Systems GmbH, Obersulm, DE). The sample is positioned on a *z*-axis translation stage, which allows us to find the focus. The average excitation intensities have been calibrated by measuring the relaxation time of the Dronpa-2 photoisomerization. The modulated signals are generated by the computer and applied to the LEDs through an Arduino microcontroller. The acquisition of the camera is synchronized with the modulated excitation light. A series of images of the red (DsRed) and the green (Dronpa-2) channel can be separately acquired by the camera and sent back to the computer for later processing. The *I*/*O* control system and the image processing are accomplished with a home-made software coded in C.

Softwares. Data treatment, image analysis, and theoretical computations were performed using Igor Pro (WaveMetrics), MATLAB (The MathWorks), and Gnuplot and Mathematica (Wolfram Research) softwares.

Data availability. Data available on request from the authors.

Received: 10 May 2017 Accepted: 1 August 2017
Published online: 17 October 2017

References

1. Giepmans, B., Adams, S., Ellisman, M. & Tsien, R. The fluorescent toolbox for assessing protein location and function. *Science* **312**, 217–224 (2006).
2. Weissleder, R. & Nahrendorf, M. Advancing biomedical imaging. *Proc. Natl Acad. Sci. USA* **112**, 14424–14428 (2015).
3. Grecco, H. E., Imtiaz, S. & Zamir, E. Multiplexed imaging of intracellular protein networks. *Cytometry A* **89A**, 761–775 (2016).
4. Alcor, D., Croquette, V., Jullien, L. & Lemarchand, A. Molecular sorting by stochastic resonance. *Proc. Natl Acad. Sci. USA* **101**, 8276–8280 (2004).
5. Charier, S. et al. Reactant concentrations from fluorescence correlation spectroscopy with tailored fluorescent probes. an example of local calibration-free pH measurement. *J. Am. Chem. Soc.* **127**, 15491–15505 (2005).
6. Berthoumieux, H., Antoine, C., Jullien, L. & Lemarchand, A. Resonant response to temperature modulation for enzymatic dynamics characterization. *Phys. Rev. E* **79**, 021906 (2009).
7. Zrelli, K. et al. Temperature modulation and quadrature detection for selective titration of two-state exchanging reactants. *Anal. Chem.* **83**, 2461–2468 (2011).
8. Quérard, J. et al. Kinetics of reactive modules adds discriminative dimensions for selective cell imaging. *Chemphyschem* **17**, 1396–1413 (2016).
9. Bourgeois, D. & Adam, V. Reversible photoswitching in fluorescent proteins: a mechanistic view. *IUBMB Life* **64**, 482–491 (2012).
10. Querard, J. et al. Photoswitching kinetics and phase sensitive detection add discriminative dimensions for selective fluorescence imaging. *Angew Chem. Int. Ed.* **54**, 2633–2637 (2015).
11. Croquette, V., *et al.* Method for the detection of reversibly photoconvertible fluorescent species. WO 2015075209 A1, PCT/EP2014/075336.
12. Marriott, G. et al. Optical lock-in detection imaging microscopy for contrast-enhanced imaging in living cells. *Proc. Natl Acad. Sci USA* **105**, 17789–17794 (2008).
13. Abbandonato, G., Storti, B., Signore, G., Beltram, F. & Bizzarri, R. Quantitative optical lock-in detection for quantitative imaging of switchable and non-switchable components. *Microsc. Res. Technol.* **79**, 929–937 (2016).
14. Hsiang, J.-C., Jablonski, A. E. & Dickson, R. M. Optically modulated fluorescence bioimaging: visualizing obscured fluorophores in high background. *Acc. Chem. Res.* **47**, 1545–1554 (2014).
15. Ando, R., Mizuno, H. & Miyawaki, A. Regulated fast nucleocytoplasmic shuttling observed by reversible protein highlighting. *Science* **306**, 1370–1373 (2004).
16. Stiel, A. C. et al. 1.8 Å bright-state structure of the reversibly switchable fluorescent protein Dronpa guides the generation of fast switching variants. *Biochem. J.* **402**, 35–42 (2007).
17. Ando, R., Flors, C., Mizuno, H., Hofkens, J. & Miyawaki, A. Highlighted generation of fluorescence signals using simultaneous two-color irradiation on Dronpa mutants. *Biophys. J.* **92**, L97–L99 (2007).
18. Andresen, M. et al. Photoswitchable fluorescent proteins enable monochromatic multilabel imaging and dual color fluorescence nanoscopy. *Nat. Biotechnol.* **26**, 1035–1040 (2008).
19. Grotjohann, T. et al. Diffraction-unlimited all-optical imaging and writing with a photochromic GFP. *Nature.* **478**, 204–208 (2011).
20. Grotjohann, T. et al. rsEGFP2 enables fast RESOLFT nanoscopy of living cells. *eLife* **1**, e00248 (2012).
21. Tiwari, D. K. et al. A fast- and positively photoswitchable fluorescent protein for ultralow-laser-power RESOLFT nanoscopy. *Nat. Methods* **12**, 515–518 (2015).
22. Tian, Z. & Li, A. Photoswitching-enabled novel optical imaging: innovative solutions for real-world challenges in fluorescence detections. *Acc. Chem. Res.* **46**, 269–279 (2013).
23. Chozinski, T. J., Gagnon, L. A. & Vaughan, J. C. Twinkle, twinkle little star: Photoswitchable fluorophores for super-resolution imaging. *FEBS Lett.* **588**, 3603–3612 (2014).
24. Van de Linde, S. & Sauer, M. How to switch a fluorophore: from undesired blinking to controlled photoswitching. *Chem. Soc. Rev.* **43**, 1076–1087 (2014).
25. Fukaminato, T. Single-molecule fluorescence photoswitching: Design and synthesis of photoswitchable fluorescent molecules. *J. Photochem. Photobiol. C* **12**, 177–208 (2011).
26. Yadav, D. et al. Real-time monitoring of chromophore isomerization and deprotonation during the photoactivation of the fluorescent protein Dronpa. *J. Phys. Chem. B* **119**, 2404–2414 (2015).
27. Gautier, A., Deiters, A. & Chin, J. W. Light-activated kinases enable temporal dissection of signaling networks in living cells. *J. Am. Chem. Soc.* **133**, 2124–2127 (2011).
28. Sladitschek, H. L. & Neveu, P. A. MXS-chaining: a highly efficient cloning platform for imaging and flow cytometry approaches in mammalian systems. *PLoS ONE* **10**, 0124958 (2015).
29. Grefen, C. et al. A ubiquitin-10 promoter-based vector set for fluorescent protein tagging facilitates temporal stability and native protein distribution in transient and stable expression studies. *Plant J.* **64**, 355–365 (2010).
30. Nguyen, H. T. et al. Camelina seed transcriptome: a tool for meal and oil improvement and translational research. *Plant Biotechnol. J.* **11**, 759–769 (2013).
31. Curtis, M. D. & Grossniklaus, U. A gateway cloning vector set for high-throughput functional analysis of genes in planta. *Plant Physiol.* **133**, 462–469 (2003).
32. Morineau, C. et al. Selective gene dosage by CRISPR-Cas9 genome editing in hexaploid *Camelina sativa*. *Plant Biotechnol. J.* **15**, 729–739 (2017).

Acknowledgements

We thank A. Miyawaki for providing the Dronpa-3 cDNA; S. Jakobs for providing the Dronpa-2, rsEGFP, and rsEGFP2 cDNAs; A. Espagne for providing the Dronpa, Padron, and rsFastLime cDNAs; and T. Nagai for providing the Kohinoor cDNA. We are also indebted to E. Billon-Denis (for help in preparing RSFPs), and O. Mesdjan and J. Fattaciolli (for access to clean rooms to fabricate the microdevices). This work was supported by the ANR (France BioImaging—ANR-10-INBS-04, Morphoscope2—ANR-11-EQPX-0029), the SATT Lutech (OPIOM), the Fondation de la Recherche Médicale (FRM DEI201512440), the LabEx Saclay Plant Sciences-SPS (ANR-10-LABX-0040-SPS) from the "Investments for the Future" program (ref. ANR-11-IDEX-0003-02), PSL Research University (ANR-10-IDEX-0001-02 PSL, SuperLINE project), and the Domaine d'Intérêt Majeur Analytics de la Région Ile de France (DREAM).

Author contributions

L.J. and T.L.S. conceived the speed OPIOM imaging protocol and supervised the project. J.Q., R.Z., X.X., R.C., I.R., Y.K., S.A., V.C., T.L.S., and L.J. designed and performed theoretical calculations and/or physicochemical experiments. Z.K., M.A.P.,

E.I., M.V., H.L.S., P.N., L.G., A.G., and J.-D.F. designed and prepared the biological samples.

Additional information

Supplementary Information accompanies this paper at doi:10.1038/s41467-017-00847-3.

Competing interests: The authors declare no competing financial interests.

Reprints and permission information is available online at http://npg.nature.com/reprintsandpermissions/

Change history: A correction to this article has been published and is linked from the HTML version of this paper.

Publisher's note: Springer Nature remains neutral with regard to jurisdictional claims in published maps and institutional affiliations.

A.2 Electronic Supplementary Material

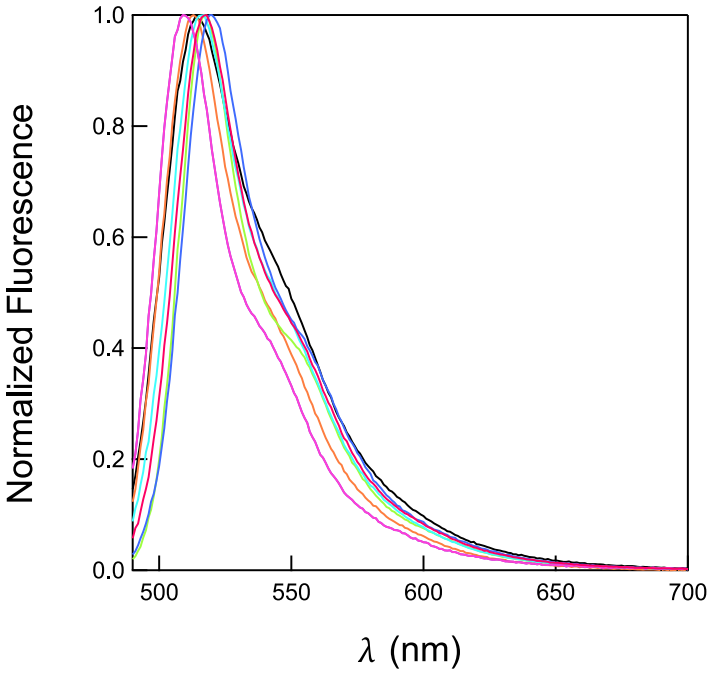

Supplementary Figure 1: Normalized emission ($\lambda_{exc} = 480$ nm) spectra of the RSFPs, which have been used in this study. Solvent: Britton-Robinson buffer (pH 7.5); T = 310 K.

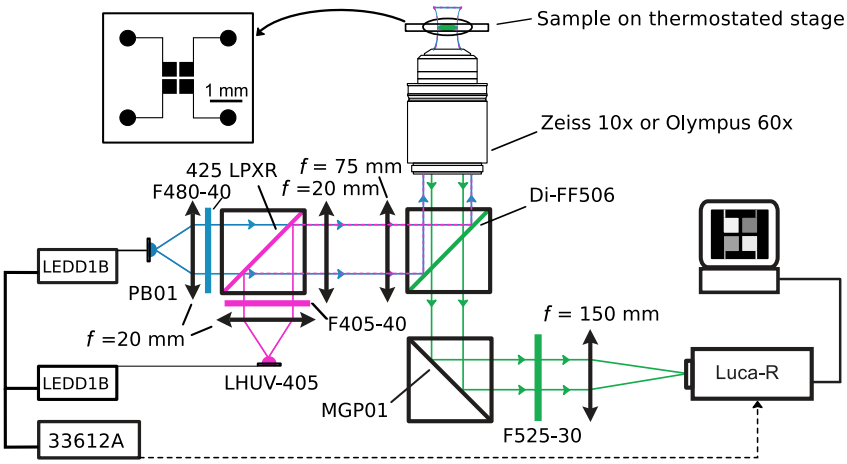

Supplementary Figure 2: Epifluorescence setup for Speed OPIOM and PDMS Imaging device.

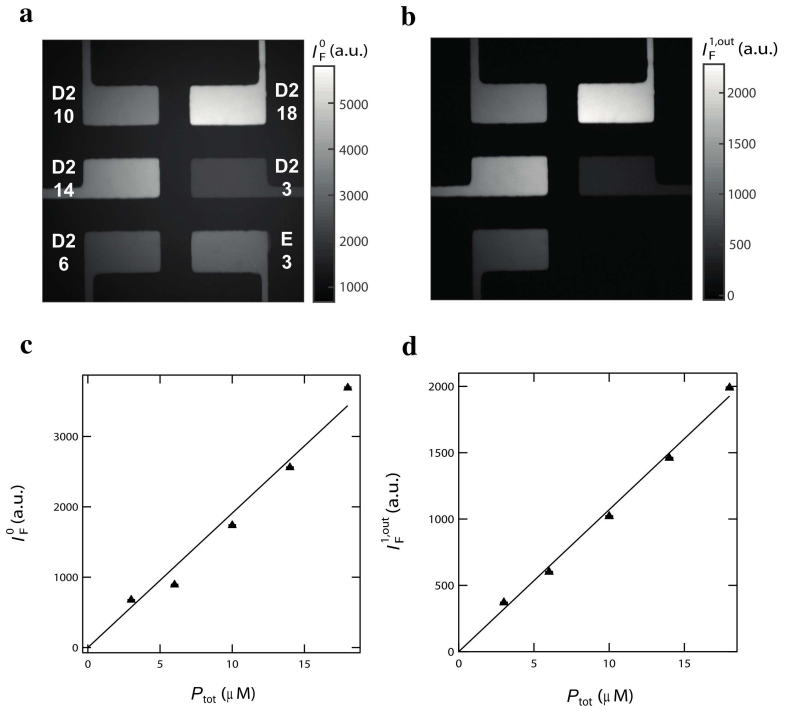

Supplementary Figure 3: Quantitative imaging of Dronpa-2. A microfluidic device with six rectangular chambers ($250\times125\times20$ μm^3) was filled with solutions of Dronpa-2 (D2) or EGFP (E) (the numbers in **a** indicate the concentrations in μM). The images recorded with a 10 × objective correspond to the pre-OPIOM (**a**) and Speed OPIOM (**b**) images resulting from imaging the microfluidic device at $\lambda_{\rm em}$ = 525 nm by sinusoidally modulating dual illumination tuned to the resonance of Dronpa-2 ($\lambda_{\rm exc,1}$; I_1^0; ω; f; α) = (480 nm; 7.1×10^{-3} Ein m^{-2} s^{-1}; 2.8 rad s^{-1}; 0.44 Hz; 100%), ($\lambda_{\rm exc,2}$; I_2^0; ω; f; α) = (405 nm; 3.4×10^{-3} Ein m^{-2} s^{-1}; 2.8 rad s^{-1}; 0.44 Hz; 100%); Average fluorescence intensity, $\langle I_{\rm F}^0\rangle$ (**c**), and average amplitude of the out-of-phase response, $\langle I_{\rm F}^{1,{\rm out}}\rangle$ (**d**), in function of the total concentration $P_{\rm tot}$ = [Dronpa-2]$_{\rm tot}$ of Dronpa-2. Experiments were performed at 37°C in pH 7.5 50 mM HEPES buffer. Dronpa-2 fluorescence emission can be detected in both pre-OPIOM and Speed OPIOM images. In contrast, as expected from the absence of an out-of-phase contribution in its fluorescence emission, EGFP only gives a signal on the pre-OPIOM image, thus demonstrating the expected selective Speed OPIOM imaging. Furthermore the five chambers filled with Dronpa-2 show relative intensities directly reflecting their concentration in both pre-OPIOM and Speed OPIOM images, which confirms the theoretical prediction that the Speed OPIOM signal is proportional to the label concentration.

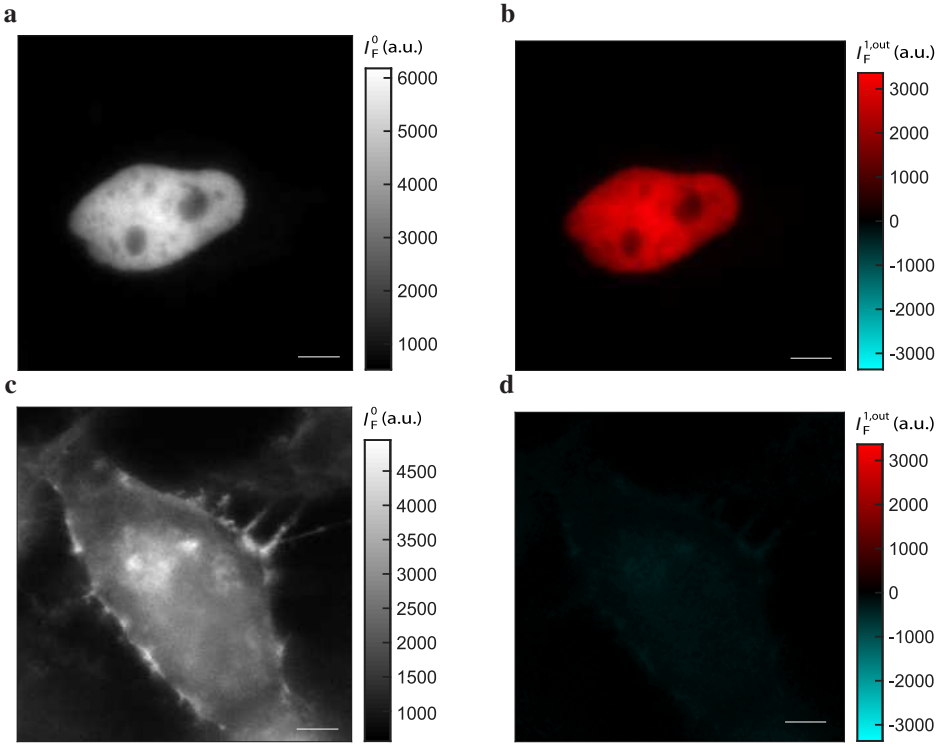

Supplementary Figure 4: Control experiment. Fixed Hela cells expressing either H2B-Dronpa-2 (**a**,**b**) or (**c**,**d**) Lyn11-EGFP. Pre-OPIOM (**a**,**c**) and Speed OPIOM (**b**,**d**) images result from analyzing a movie recorded with a 60 $\times$ objective at 525 nm under sinusoidal light modulation at a single angular frequency of modulation tuned on the resonance of Dronpa-2 ($\lambda_{\text{exc},1}$; I_1^0; ω; f; α) = (480 nm; 6.4×10^{-2} Ein m^{-2} s^{-1}; 25 rad s^{-1}; f = 4 Hz; 100%), ($\lambda_{\text{exc},2}$; I_2^0; ω; f; α) = (405 nm; 3.0×10^{-2} Ein m^{-2} s^{-1}; 25 rad s^{-1}; f = 4 Hz; 100%). Experiments were performed at 37°C. Dronpa-2 fluorescence emission is detected in both pre-OPIOM (**a**) and Speed OPIOM (**b**) images. In contrast, as expected from the absence of an out-of-phase contribution in its fluorescence emission, EGFP gives a signal on the pre-OPIOM image (**c**) but not on the Speed OPIOM one (**d**). Scale bars: 5 µm.

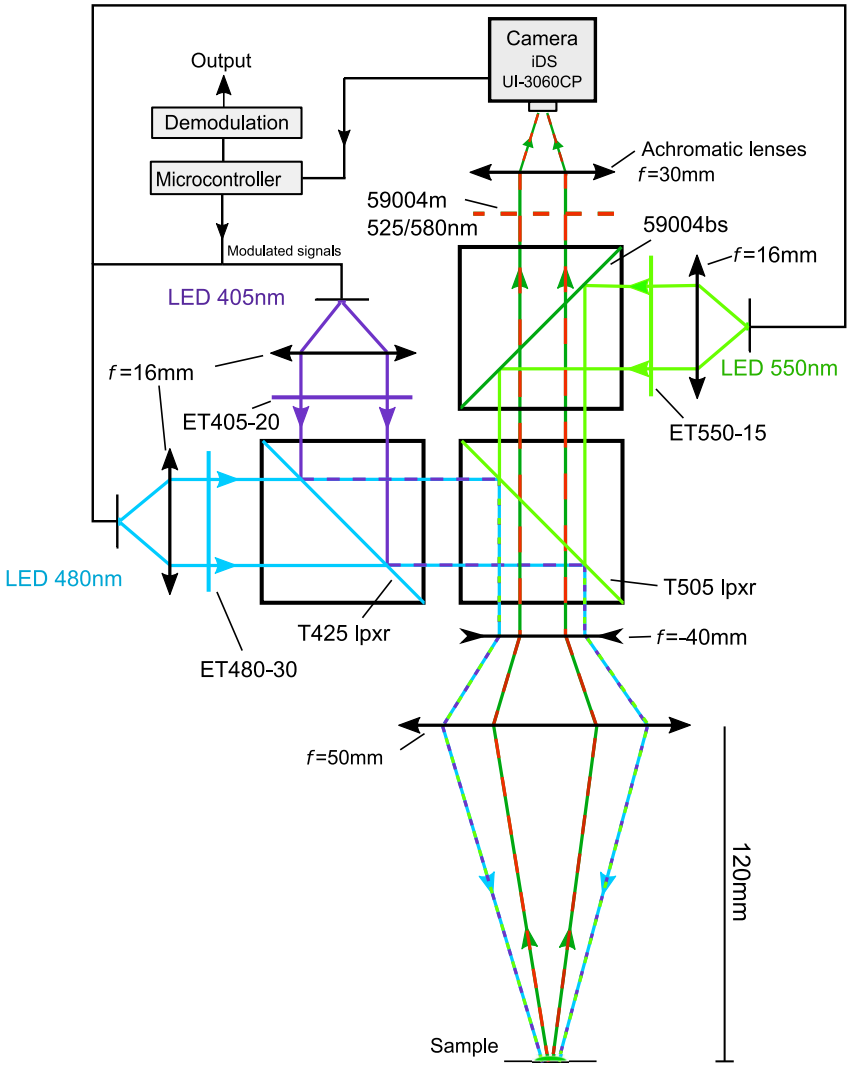

Supplementary Figure 5: Remote imaging fluorescence setup for Speed OPIOM.

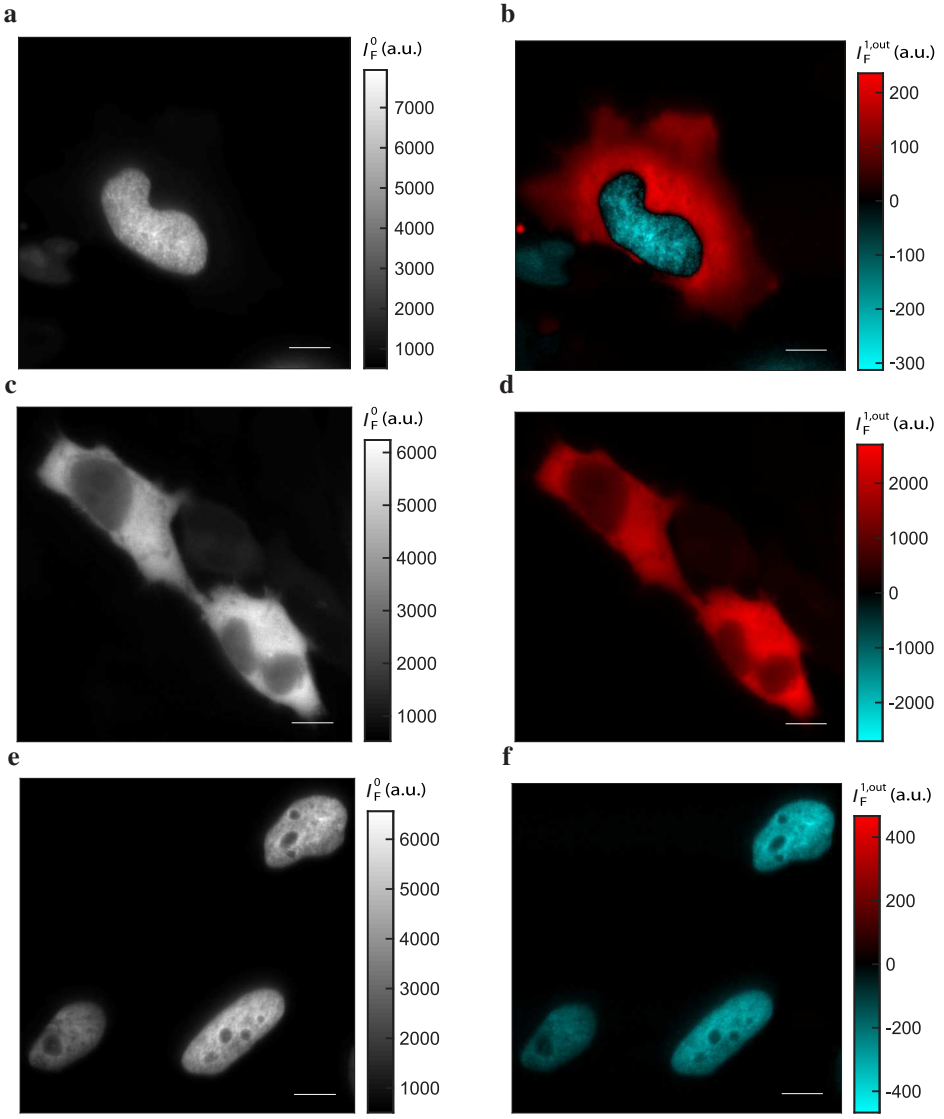

Supplementary Figure 6: Fixed Hela cells expressing βGal-Dronpa3 and H2B-Kohinoor (**a**,**b**), βGal-Dronpa3 (**c**,**d**) or H2B-Kohinoor (**e**,**f**). Pre-OPIOM (**a**,**c**,**e**) and Speed OPIOM (**b**,**d**,**f**) images result from analyzing a movie recorded with a 60 $\times$ objective at 525 nm under sinusoidal light modulation ($\lambda_{\text{exc},1}$; I_1^0; ω; f; α) = (480 nm; 2.8×10^{-1} Ein m^{-2} s^{-1}; 25 rad s^{-1}; 4 Hz; 100%), ($\lambda_{\text{exc},2}$; I_2^0; ω; f; α) = (405 nm; 1.0×10^{-2} Ein m^{-2} s^{-1}; 25 rad s^{-1}; 4 Hz; 100%). Experiments were performed at 37°C. Dronpa-3 and Kohinoor cannot be discriminated in the pre-OPIOM image. In contrast, they are easily distinguished in the Speed OPIOM image where they exhibit a positive and a negative signal respectively. Scale bars: 10 µm.

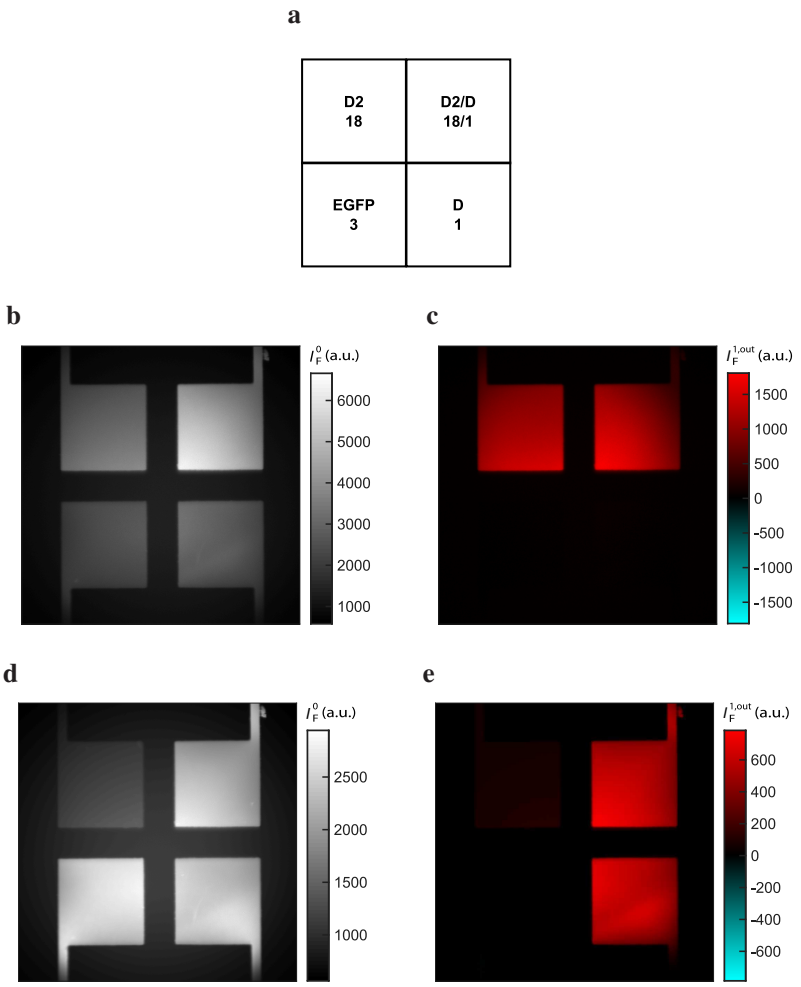

Supplementary Figure 7: Selective and quantitative Speed OPIOM imaging of Dronpa-2 or Dronpa. A microfluidic device with four square chambers (400×400×20 µm^3) was filled with solutions of Dronpa-2, Dronpa or EGFP as described on the scheme (**a**; the numbers indicate the concentrations in µM). The pre-OPIOM (**b**,**d**) and Speed OPIOM (**c**, **e**) images result from imaging with a 10 × objective the microfluidic device at λ_{em} = 525 nm by sinusoidally modulating dual illumination tuned to the resonance of either (**b**, **c**) Dronpa-2 ($\lambda_{exc,1}$; I_1^0; ω; f; α) = (480 nm; 1.5×10^{-2} Ein m^{-2} s^{-1}; 6.28 rad s^{-1}; 1 Hz; 100%), ($\lambda_{exc,2}$; I_2^0; ω; f; α) = (405 nm; 8.6×10^{-3} Ein m^{-2} s^{-1}; 6.28 rad s^{-1}; 1 Hz; 100%) or (**d**, **e**) Dronpa ($\lambda_{exc,1}$; I_1^0; ω; f; α) = (480 nm; 5.0×10^{-2} Ein m^{-2} s^{-1}; 0.63 rad s^{-1}; 0.1 Hz; 100%), ($\lambda_{exc,2}$; I_2^0; ω; f; α) = (405 nm; 1.0×10^{-3} Ein m^{-2} s^{-1}; 0.63 rad s^{-1}; 0.1 Hz; 100%). Experiments were performed at 37°C in pH 7.4 HEPES buffer. Dronpa and Dronpa-2 cannot be discriminated in the pre-OPIOM image. In contrast, they are orthogonally distinguished in the Speed OPIOM images targetting Dronpa and Dronpa-2 respectively.

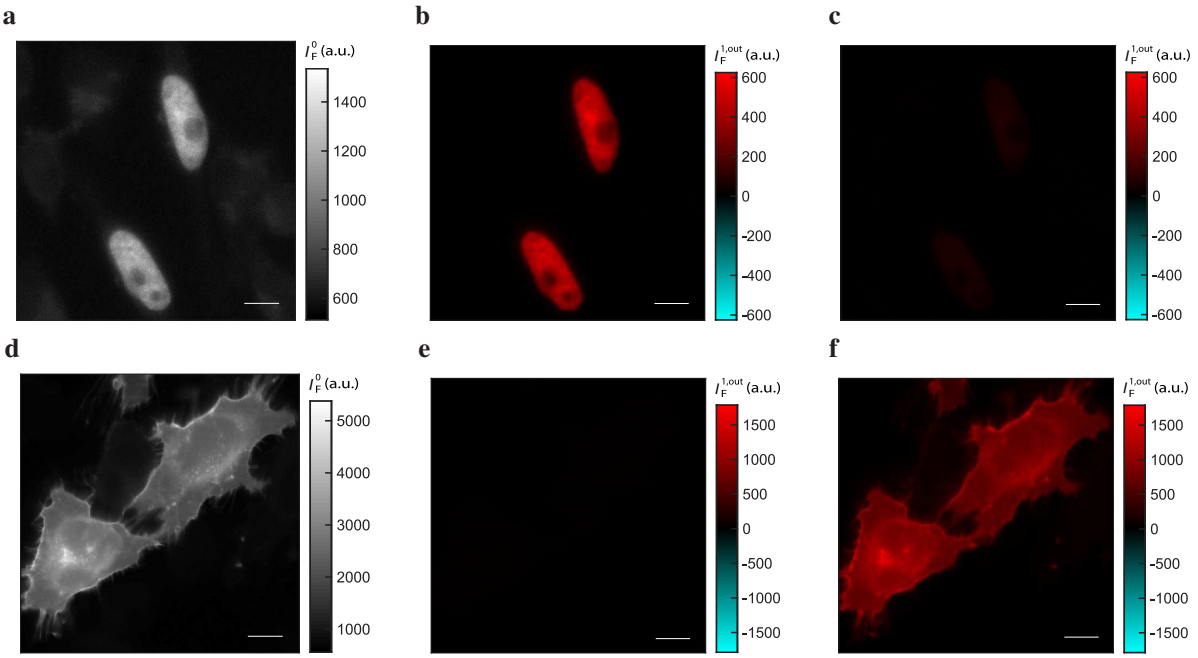

Supplementary Figure 8: Control experiment. Fixed Hela cells expressing either H2B-Dronpa-2 (**a**,**b**,**c**) or Lyn11-Dronpa (**d**,**e**,**f**). Pre-OPIOM (**a**,**d**) and Speed OPIOM (**b**,**c**,**e**,**f**) images result from analyzing a movie recorded with a 60 $\times$ objective at 525 nm under sinusoidal light modulation ($\lambda_{\mathrm{exc},1}$; I_1^0; ω; f; α) = (**a**,**b**,**e**: 480 nm; 1.5×10^{-2} Ein m^{-2} s^{-1}; 6.3 rad s^{-1}; 1 Hz; 100%) and (**c**,**d**,**f**: 480 nm; 5.7×10^{-2} Ein m^{-2} s^{-1}; 0.63 rad s^{-1}; 1 Hz; 100%), ($\lambda_{\mathrm{exc},2}$; I_2^0; ω; f; α) = (**a**,**b**,**e**: 405 nm; 8.7×10^{-3} Ein m^{-2} s^{-1}; 6.3 rad s^{-1};1 Hz; 100%) and (**c**,**d**,**f**: 405 nm; 1.0×10^{-3} Ein m^{-2} s^{-1}; 0.63 rad s^{-1}; 0.1 Hz; 100%). Experiments were performed at 37°C. Dronpa and Dronpa-2 cannot be discriminated in the pre-OPIOM image. In contrast, they are orthogonally distinguished in the Speed OPIOM images targetting Dronpa and Dronpa-2 respectively. Scale bars: 10 µm.

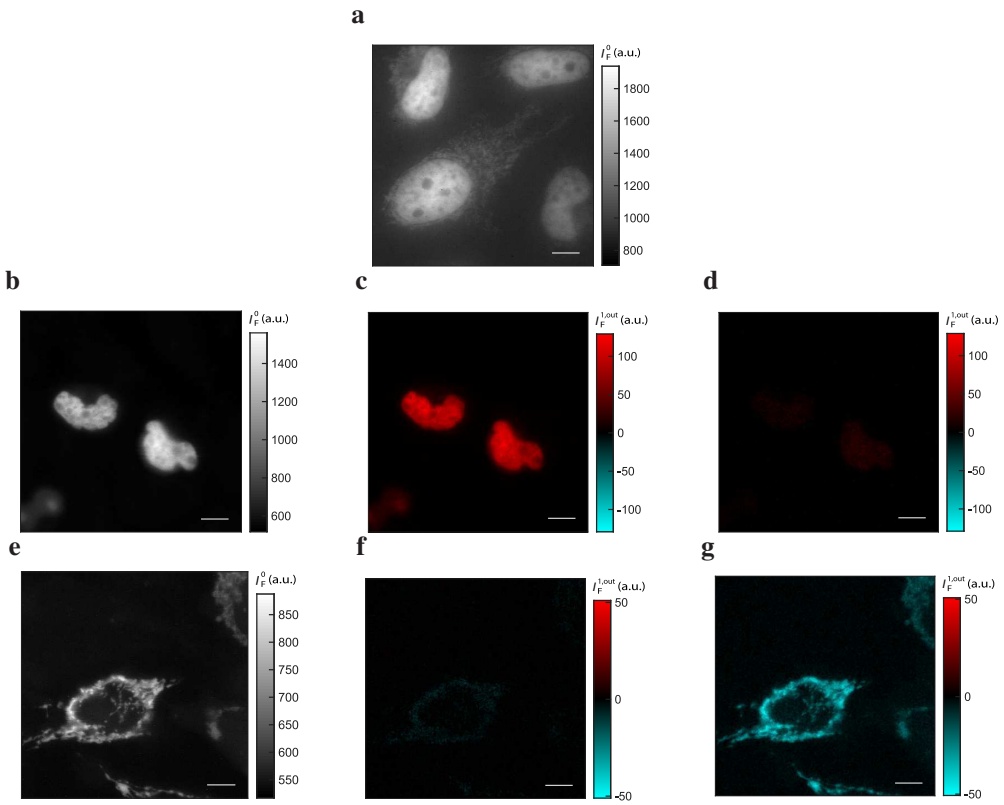

Supplementary Figure 9: **a**: Pre-OPIOM image of fixed Hela cells expressing H2B-Dronpa-2 and Mito-Padron; **b-g**: Control experiment. Multiplexed imaging of fixed Hela cells expressing either Dronpa-2-H2B (**a**, **b**, **c**) or Padron-Mito (**d**, **e**, **f**). Pre-OPIOM (**b**, **e**) and Speed OPIOM (**c**,**d**, **f**, **g**) images result from analyzing at ω_1 (**c**, **f**) or ω_2 (**d**, **g**) a movie recorded with a 60 $\times$ objective at 525 nm under sinusoidal light modulation at two modulation frequencies ($\lambda_{\text{exc},1}$; I_1^0; ω_1; f_1; ω_2; f_2; α; β) = (480 nm; 1.0×10^{-2} Ein m^{-2} s^{-1}; 0.2 rad s^{-1}; 0.032 Hz; 15.8 rad s^{-1}; 2.52 Hz; 50%; 100%), ($\lambda_{\text{exc},2}$; I_2^0; ω_1; f_1; ω_2; f_2; α; β) = (405 nm; 1.0×10^{-2} Ein m^{-2} s^{-1}; 0.2 rad s^{-1}; 0.032 Hz; 15.8 rad s^{-1}; 2.52 Hz; 50%; 100%). Experiments were performed at 37°C. Dronpa-2 and Padron cannot be discriminated in the pre-OPIOM image. In contrast, they are orthogonally distinguished in the Speed OPIOM images targetting Dronpa-2 and Padron respectively. Scale bars: 10 µm.

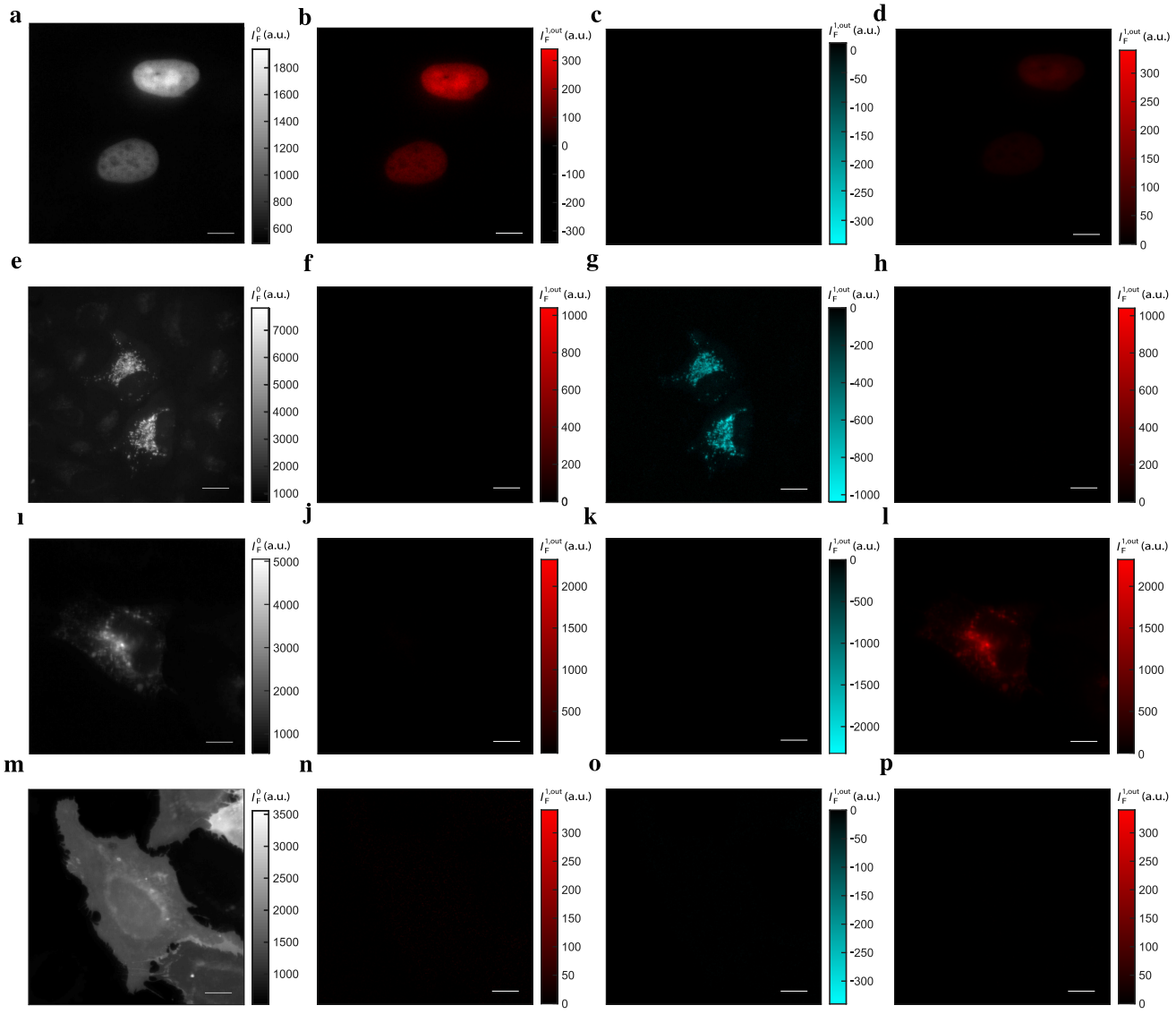

Supplementary Figure 10: Images of fixed UO2S cells expressing either H2B-Dronpa-2 (**a**-**d**), Mito-Padron (**e**-**h**), Dronpa-GTS (**i**-**l**), and Lyn11-EGFP (**m**-**p**); Control experiments. Pre-OPIOM (**a**,**e**,**i**,**m**) and Speed OPIOM (**b**-**d**,**f**-**h**,**j**-**l**,**n**-**p**) images result from analyzing a movie recorded with a 60 × objective at 525 nm under three different sinusoidal light modulations (**b**,**f**,**j**,**n**: ($\lambda_{\text{exc},1}$; I_1^0; ω; f; α) = (480 nm; 2.5×10^{-3} Ein m^{-2} s^{-1}; 6.3 rad s^{-1}; 1 Hz; 100%), ($\lambda_{\text{exc},2}$; I_2^0; ω; f; α) = (405 nm; 1.9×10^{-3} Ein m^{-2} s^{-1}; 6.3 rad s^{-1}; 1 Hz; 100%); **c**,**g**,**k**,**o**: ($\lambda_{\text{exc},1}$; I_1^0; ω; f; α) = (480 nm; 2.3×10^{-2} Ein m^{-2} s^{-1}; 0.6 rad s^{-1}; 0.1 Hz; 100%), ($\lambda_{\text{exc},2}$; I_2^0; ω; f; α) = (405 nm; 4.3×10^{-2} Ein m^{-2} s^{-1}; 0.6 rad s^{-1}; 0.1 Hz; 100%); **d**,**h**,**l**,**p**: ($\lambda_{\text{exc},1}$; I_1^0; ω; f; α) = (480 nm; 2.4×10^{-2} Ein m^{-2} s^{-1}; 0.2 rad s^{-1}; 0.03 Hz; 100%), ($\lambda_{\text{exc},2}$; I_2^0; ω; f; α) = (405 nm; 2.8×10^{-4} Ein m^{-2} s^{-1}; 0.2 rad s^{-1}; 0.03 Hz; 100%). Experiments were performed at 37°C. Dronpa, Dronpa-2, and Padron cannot be discriminated in the pre-OPIOM image. In contrast, they are orthogonally distinguished in the Speed OPIOM images targetting Dronpa, Dronpa-2 and Padron respectively. Scale bars: 10 µm.

Supplementary Methods

Video acquisition

In the imaging experiments, we recorded movies over an integer number of periods of light modulation (in general $2m$ periods, where m is an integer). The acquisition frequency of the camera was set in order to transfer $2n$ (n is an integer) frames per period of light excitation, which triggered CCD acquisition start. Thus, using Eq. (80), the fluorescence emission at pixel (*x*,*y*) of the k^{th} frame is equal to

$$I_{\mathrm{F}}(x,y,k) = \mathfrak{I}_{\mathrm{F}}^{0}(x,y) + \sum_{n=1}^{\infty}\left\{\mathfrak{I}_{\mathrm{F}}^{n,\sin}(x,y)\sin\left[n\left(\frac{k\pi}{n}+\phi_{\mathrm{acq}}\right)\right] + \mathfrak{I}_{\mathrm{F}}^{n,\cos}(x,y)\cos\left[n\left(\frac{k\pi}{n}+\phi_{\mathrm{acq}}\right)\right]\right\} \tag{1}$$

In Eq.(1), the constant phase lag ϕ_{acq} reflects the fact that light modulation do not share the same starting date with CCD recording which integrates the signal over exposure time. ϕ_{acq} can be easily calibrated by using the fluorescence emission from an instantaneously responding fluorophore (for example Fluorescein, EGFP). Acquisition in quadrature was subsequently achieved through phase sensitive detection.[1]–[5] The pre-OPIOM image corresponding to the average signal over the whole movie, equal to $\mathfrak{I}_{\mathrm{F}}^{0}(x,y)$, was first computed using Eq.(2)

$$\langle I_{\mathrm{F}}(x,y,k)\rangle_{k=0}^{4\mathrm{nm}-1} = \frac{1}{4nm}\sum_{k=0}^{4\mathrm{nm}-1} I_{\mathrm{F}}(x,y,k). \tag{2}$$

Using Eq.(161), the k^{th} frames $I_{\mathrm{F}}(x,y,k)$ were next multiplied by $\cos\left(\frac{k\pi}{n}+\phi_{\mathrm{acq}}\right)$ and averaged over the whole duration of the movie to give rise to the Speed OPIOM image :

$$\mathfrak{I}_{\mathrm{F}}^{1,\cos}(x,y) = \frac{1}{2nm}\sum_{k=0}^{4\mathrm{nm}-1}\left[(I_{\mathrm{F}}(x,y,k))\times\cos\left(\frac{k\pi}{n}+\phi_{\mathrm{acq}}\right)\right] \tag{3}$$

In the presence of photobleaching of the probe, image analysis has to be modified to correct from bleaching.[6], [7] Assuming a linear decay of the fluorescence signal due to photobleaching, the recorded emission signal at pixel (*x*,*y*) of the k^{th} frame $I_{\mathrm{F}}^{\mathrm{raw}}(x,y,k)$ was written using Eq.(1)

$$I_{\mathrm{F}}^{\mathrm{raw}}(x,y,k) = I_{\mathrm{F}}(x,y,k) + B(x,y)\times k. \tag{4}$$

$B(x,y)$ was calculated from the average signals $\langle I_{\mathrm{F}}^{\mathrm{raw}}(x,y,k)\rangle_{k=0}^{2\mathrm{nm}-1}$ and $\langle I_{\mathrm{F}}^{\mathrm{raw}}(x,y,k)\rangle_{k=2\mathrm{nm}}^{4\mathrm{nm}-1}$ computed over the first and last m periods

$$B(x,y) = \frac{\langle I_{\mathrm{F}}^{\mathrm{raw}}(x,y,k)\rangle_{k=2\mathrm{nm}}^{4\mathrm{nm}-1} - \langle I_{\mathrm{F}}^{\mathrm{raw}}(x,y,k)\rangle_{k=0}^{2\mathrm{nm}-1}}{2\mathrm{nm}} \tag{5}$$

Then, all frames were corrected for photobleaching using :

$$I_{\mathrm{F}}^{\mathrm{corr}}(x,y,k) = I_{\mathrm{F}}^{\mathrm{raw}}(x,y,k) - B(x,y)\times k. \tag{6}$$

$I_{\mathrm{F}}^{\mathrm{corr}}(x,y,k)$ was subsequently processed as $I_{\mathrm{F}}(x,y,k)$ above to extract the Speed OPIOM image.

In section , we provide the Matlab code, which we used to compute $\mathfrak{I}_{\mathrm{F}}^{1,\cos}(x,y)$ (Speed OPIOM image) in our imaging experiments.

Cell imaging with epifluorescence microscopy

This series of experiments has been performed upon applying sinusoidal 480 nm and 405 nm light modulations of large amplitude (100%) and in antiphase. Otherwise indicated, the temporal dependence of the fluorescence intensity $I_{\mathrm{F}}(x, y, t)$ of each image pixel was analyzed with Eqs.(2–6) to provide the $\mathfrak{I}_{\mathrm{F}}^{\mathrm{o}}(x, y)$ (pre-OPIOM) and the $\mathfrak{I}_{\mathrm{F}}^{1,\mathrm{cos}}(x, y)$ (Speed OPIOM) images. To reduce noise, the processed images have been subsequently filtered upon applying a 3 pixels $\times$ 3 pixels median filter. The acquisition parameters, which have been used for Speed OPIOM imaging of cells are reported in Supplementary Tables 1 and 2.

Remote fluorescence imaging of Camelina sativa seedlings

This series of experiments has been performed upon applying sinusoidal ($f = 2.5$ Hz) 480 nm ($I_1^0 = 3.8\ 10^{-2}$ Ein $\mathrm{m}^{-2}\ \mathrm{s}^{-1}$) and 405 nm ($I_2^0 = 2.2\ 10^{-2}$ Ein $\mathrm{m}^{-2}\ \mathrm{s}^{-1}$) light modulations of large amplitude (100%) and in antiphase. Otherwise indicated, the temporal dependence of the fluorescence intensity $I_{\mathrm{F}}(x, y, t)$ of each image pixel was analyzed over 8 periods with Eqs.(2–6) to provide the $\mathfrak{I}_{\mathrm{F}}^{\mathrm{o}}(x, y)$ (pre-OPIOM) and the $\mathfrak{I}_{\mathrm{F}}^{1,\mathrm{cos}}(x, y)$ (Speed OPIOM) images. The acquisition parameters, which have been used for Speed OPIOM remote imaging of Camelina seedlings are reported in Supplementary Table 3.

Acquisition parameters used for Speed OPIOM imaging

The acquisition parameters, which have been used for Speed OPIOM imaging of cells are reported in Supplementary Tables 1 and 2. The acquisition parameters, which have been used for Speed OPIOM remote imaging of Camelina seedlings are reported in Supplementary Table 3.

Supplementary Table 1: Acquisition parameters used to image Dronpa, Dronpa-2, Dronpa-3, and Kohinoor at 37°C in Figures 3–6 of the Main Text (MT) and in Supplementary Figures 4, 6, 8, and 10 (SI).

Figure MT;SI	Objective	Periods : Images	$\lambda_{\mathrm{exc},1}$ (nm)	I_1^0 (Ein m^{-2} s^{-1})	$\lambda_{\mathrm{exc},2}$ (nm)	I_2^0 (Ein m^{-2} s^{-1})	ω (rad s^{-1})	f (Hz)	α %
3b,c;4	60×	10 : 160	480	$6.0\ 10^{-2}$	405	$3.5\ 10^{-2}$	25.1	4	100
4b–d,5a–d;6	60×	10 : 100	480	$7.2\ 10^{-2}$	405	$1.3\ 10^{-2}$	6.3	1	100
4f,g;8	60×	10 : 100	480	$1.5\ 10^{-2}$	405	$8.7\ 10^{-3}$	6.3	1	100
4h;8	60×	2 : 200	480	$5.7\ 10^{-2}$	405	$1.0\ 10^{-3}$	0.63	0.1	100
6a,b;10	60×	10 : 100	480	$2.5\ 10^{-3}$	405	$1.9\ 10^{-3}$	6.3	1	100
6c;10	60×	2 : 80	480	$2.3\ 10^{-2}$	405	$4.3\ 10^{-2}$	0.6	0.1	100
6d;10	60×	2 : 400	480	$2.4\ 10^{-2}$	405	$2.8\ 10^{-4}$	0.2	0.03	100

Supplementary Table 2: Acquisition parameters used to simultaneously image Dronpa-2 and Padron with a 60× objective at 37°C in Figure 4 of the Main Text (MT) and Supplementary Figure 9 (SI).

Figure MT;SI	$\lambda_{\mathrm{exc},1}$ (nm)	I_1^0 (Ein m^{-2} s^{-1})	$\lambda_{\mathrm{exc},2}$ (nm)	I_2^0 (Ein m^{-2} s^{-1})	ω_1 (rad s^{-1})	f_1 (Hz)	α %	ω_2 (rad s^{-1})	f_2 (Hz)	β %
4j–l;9	480	$1.0\ 10^{-2}$	405	$1.0\ 10^{-2}$	0.2	0.032	50	16	2.5	100

Supplementary Table 3: Acquisition parameters used to image Dronpa-2 under its resonant conditions at 20°C in Figure 3e,f of the Main Text (MT).

Figure MT	Periods : Images	$\lambda_{\mathrm{exc},1}$ (nm)	I_1^0 (Ein m^{-2} s^{-1})	$\lambda_{\mathrm{exc},2}$ (nm)	I_2^0 (Ein m^{-2} s^{-1})	ω (rad s^{-1})	f (Hz)	α %
3e,f	8 : 160	480	$3.8\ 10^{-2}$	405	$2.2\ 10^{-2}$	15.8	2.5	100

Evaluation of the contrast enhancement associated to Speed OPIOM image processing The contrast enhancement $\chi_{\mathrm{t/i}}$ associated to Speed OPIOM image processing was calculated from the signals $\mathfrak{I}^{\mathrm{o}}_{\mathrm{F,t}}$, $\mathfrak{I}^{\mathrm{1,cos}}_{\mathrm{F,t}}$, $\mathfrak{I}^{\mathrm{o}}_{\mathrm{F,i}}$, $\mathfrak{I}^{\mathrm{1,cos}}_{\mathrm{F,i}}$ originating from areas containing the targeted RSFP and the spectrally interfering fluorophore

$$\chi_{\mathrm{t/i}} = \frac{\frac{\mathfrak{I}^{\mathrm{1,cos}}_{\mathrm{F,t}}}{\mathfrak{I}^{\mathrm{1,cos}}_{\mathrm{F,i}}}}{\frac{\mathfrak{I}^{\mathrm{o}}_{\mathrm{F,t}}}{\mathfrak{I}^{\mathrm{o}}_{\mathrm{F,i}}}}. \tag{7}$$

In the case of microdevice imaging, $\mathfrak{I}^{\mathrm{o}}_{\mathrm{F,t}}$, $\mathfrak{I}^{\mathrm{1,cos}}_{\mathrm{F,t}}$, $\mathfrak{I}^{\mathrm{o}}_{\mathrm{F,i}}$, $\mathfrak{I}^{\mathrm{1,cos}}_{\mathrm{F,i}}$ were extracted from signal integration over the chambers containing the targeted or the interfering species.

Supplementary Note 1: Photoswitchable fluorophore responses to dual illuminations

The model

The dynamic behavior of a reversibly photoswitchable probe P illuminated with a light of intensity $I(t)$ involving two components $I_1(t)$ and $I_2(t)$ at wavelengths λ_1 and λ_2 is assumed to be reliably described by the two-state exchange (8)

$$\mathsf{1} \underset{k_{21}(t)}{\overset{k_{12}(t)}{\rightleftharpoons}} \mathsf{2} \tag{8}$$

where the thermodynamically most stable state 1 is photochemically converted to the thermodynamically less stable state 2 at rate constant $k_{12}(t) = \sigma_{12,1}I_1(t) + \sigma_{12,2}I_2(t)$ from which it can relax back to the initial state 1 either by a photochemically- or a thermally-driven process at rate constant $k_{21}(t) = \sigma_{21,1}I_1(t) + \sigma_{21,2}I_2(t) + k_{21}^{\Delta}$ where $\sigma_{12,1}I_1(t)$, $\sigma_{12,2}I_2(t)$, $\sigma_{21,1}I_1(t)$, $\sigma_{21,2}I_2(t)$, and k_{21}^{Δ} are respectively the photochemical and the thermal contributions of the rate constants. In that case, the molecular action cross-sections for photoisomerization $\sigma_{12,1}$ and $\sigma_{21,1}$ (at λ_1), $\sigma_{12,2}$ and $\sigma_{21,2}$ (at λ_2), and the thermal rate constant k_{21}^{Δ} fully define the behavior of the photoswitchable probe.

We assume that the system is either uniformly illuminated or that it can be considered homogeneous at any time of its evolution. Then we rely on the two-state exchange (8) to write Eqs.(9–10) describing the concentration evolutions:

$$\frac{d1}{dt} = -k_{12}(t)\ 1 + k_{21}(t)\ 2 \tag{9}$$

$$\frac{d2}{dt} = k_{12}(t)\ 1 - k_{21}(t)\ 2. \tag{10}$$

Response to light jumps

In relation to the experiments aiming to acquire the photochemical properties of the investigated reversibly photoswitchable fluorescent proteins (RSFPs), we first consider two types of light jump experiments: (i) sudden illumination at λ_1 and λ_2; (ii) sudden change of illumination at λ_1 and λ_2.

Sudden illumination at λ_1 and λ_2

When the system is suddenly submitted to a constant illumination defined by the intensity $I(t) = I_1^0 + I_2^0 = I^0$, the forward and backward rate constants become

$$k_{12}(t) = k_{12}^0 = k_{12,1}^0 + k_{12,2}^0 \tag{11}$$

$$k_{21}(t) = k_{21}^0 = k_{21,1}^0 + k_{21,2}^0 + k_{21}^{\Delta}. \tag{12}$$

where

$$k^0_{12,1} = \sigma_{12,1} I^0_1 \tag{13}$$

$$k^0_{21,1} = \sigma_{21,1} I^0_1 \tag{14}$$

$$k^0_{12,2} = \sigma_{12,2} I^0_2 \tag{15}$$

$$k^0_{21,2} = \sigma_{21,2} I^0_2 \tag{16}$$

Starting from the thermodynamically stable state 1, the temporal evolution of the concentrations in 1 and 2 evolves as

$$2 - 2^0 = 1^0 - 1 = -2^0 \exp\left(-\frac{t}{\tau^0_{12}}\right) \tag{17}$$

where

$$\tau^0_{12} = \frac{1}{k^0_{12} + k^0_{21}} \tag{18}$$

designates the relaxation time of the photoswitchable fluorophore and 1^0 and 2^0 the concentrations of 1 and 2 at the photostationnary state reached after τ^0_{12}

$$1^0 = P_{\rm tot} - 2^0 = \frac{1}{1 + K^0_{12}} P_{\rm tot} \tag{19}$$

where

$$K^0_{12} = \frac{k^0_{12}}{k^0_{21}} \tag{20}$$

and the total concentration in reversibly photoswitchable probe P, $P_{\rm tot} = 1 + 2$.

The fluorescence emission $I_{\rm F}(t)$ results then from the individual contributions of the species 1 and 2. It can be written

$$I_{\rm F}(t) = \left[Q_{1,1} 1(t) + Q_{2,1} 2(t)\right] I_1(t) + \left[Q_{1,2} 1(t) + Q_{2,2} 2(t)\right] I_2(t) \tag{21}$$

where $Q_{1,1}$ and $Q_{2,1}$, and $Q_{1,2}$ and $Q_{2,2}$ are the molecular brightnesses of 1 and 2 at the wavelengths λ_1 and λ_2 respectively. From Eqs.(17,19), one subsequently derives

$$\frac{I_{\rm F}(t)}{I_{\rm F}(0)} = 1 + \frac{\left(Q_{2,1} - Q_{1,1}\right) I^0_1 + \left(Q_{2,2} - Q_{1,2}\right) I^0_2}{I_{\rm F}(0)} \frac{K^0_{12}}{1 + K^0_{12}} P_{\rm tot} \left[1 - \exp\left(-\frac{t}{\tau^0_{12}}\right)\right] \tag{22}$$

where

$$I_{\rm F}(0) = \left(Q_{1,1} I^0_1 + Q_{1,2} I^0_2\right) P_{\rm tot}. \tag{23}$$

Starting from $I_{\rm F}(0)$, the fluorescence emission exponentially decays toward

$$I_{\rm F}(\infty) = \left[\left(Q_{1,1} \frac{1}{1 + K^0_{12}} + Q_{2,1} \frac{K^0_{12}}{1 + K^0_{12}}\right) I^0_1 + \left(Q_{1,2} \frac{1}{1 + K^0_{12}} + Q_{2,2} \frac{K^0_{12}}{1 + K^0_{12}}\right) I^0_2\right] P_{\rm tot}. \tag{24}$$

In particular, when the light jump is made at λ_1 alone, the expressions (22–24) become

$$\frac{I_{\rm F}(t)}{I_{\rm F}(0)} = 1 + \left(\frac{Q_{2,1}}{Q_{1,1}} - 1\right) \frac{K_{12}^0}{1+K_{12}^0} \left[1 - \exp\left(-\frac{t}{\tau_{12}^0}\right)\right] \tag{25}$$

with

$$I_{\rm F}(0) = Q_{1,1} I_1^0 P_{\rm tot} \tag{26}$$

$$I_{\rm F}(\infty) = \left(Q_{1,1}\frac{1}{1+K_{12}^0} + Q_{2,1}\frac{K_{12}^0}{1+K_{12}^0}\right) I_1^0 P_{\rm tot}. \tag{27}$$

Sudden change of illumination at λ_1 and λ_2

We now assume that the system is first illuminated at λ_1 and λ_2 with intensity $I^{0,1} = I_1^{0,1} + I_2^{0,1}$. As shown above, its composition exponentially evolves toward the steady-state given in Eq.(28)

$$1^{\infty,1} = P_{\rm tot} - 2^{\infty,1} = \frac{1}{1+K_{12}^{0,1}} P_{\rm tot} \tag{28}$$

with

$$K_{12}^{0,1} = \frac{k_{12}^{0,1}}{k_{21}^{0,1}} \tag{29}$$

and

$$k_{12}^{0,1} = \sigma_{12,1} I_1^{0,1} + \sigma_{12,2} I_2^{0,1} \tag{30}$$

$$k_{21}^{0,1} = \sigma_{21,1} I_1^{0,1} + \sigma_{21,2} I_2^{0,1} + k_{21}^{\Delta}, \tag{31}$$

which is typically reached beyond $\tau_{12}^{0,1}$ given in Eq.(32)

$$\tau_{12}^{0,1} = \frac{1}{k_{12}^{0,1} + k_{21}^{0,1}}. \tag{32}$$

Then the system is suddenly submitted to a change of constant illumination at λ_1 and λ_2 defined by the final intensity $I^{0,2} = I_1^{0,2} + I_2^{0,2}$. During this second kinetic regime, the forward and backward rate constants become

$$k_{12}(t) = k_{12}^{0,2} = \sigma_{12,1} I_1^{0,2} + \sigma_{12,2} I_2^{0,2} \tag{33}$$

$$k_{21}(t) = k_{21}^{0,2} = \sigma_{21,1} I_1^{0,2} + \sigma_{21,2} I_2^{0,2} + k_{21}^{\Delta} \tag{34}$$

and the temporal evolution of the concentrations in 1 and 2 evolves as

$$2 - 2^{\infty,2} = 1^{\infty,2} - 1 = \left(2^{\infty,1} - 2^{\infty,2}\right) \exp\left(-\frac{t}{\tau_{12}^{0,2}}\right) \tag{35}$$

where

$$\tau_{12}^{0,2} = \frac{1}{k_{12}^{0,2} + k_{21}^{0,2}} \tag{36}$$

designates the relaxation time of the photoswitchable fluorophore in the second kinetic regime and $1^{\infty,2}$ and $2^{\infty,2}$ the concentrations of 1 and 2 at the second photostationnary state typically reached in the second kinetic regime after $\tau_{12}^{0,2}$

$$1^{\infty,2} = P_{\rm tot} - 2^{\infty,2} = \frac{1}{1+K_{12}^{0,2}} P_{\rm tot} \tag{37}$$

where

$$K_{12}^{0,2} = \frac{k_{12}^{0,2}}{k_{21}^{0,2}}. \tag{38}$$

The fluorescence emission $I_{\rm F}(t)$ is again given in Eq.(21). From Eqs.(35,37), one subsequently derives

$$\frac{I_{\rm F}(t)}{I_{\rm F}^2(0)} = 1 + \frac{\left[(Q_{2,1}-Q_{1,1})\, I_1^{0,2} + (Q_{2,2}-Q_{1,2})\, I_2^{0,2}\right]}{I_{\rm F}^2(0)} \left(\frac{K_{12}^{0,2}}{1+K_{12}^{0,2}} - \frac{K_{12}^{0,1}}{1+K_{12}^{0,1}}\right) P_{\rm tot} \left[1 - \exp\left(-\frac{t}{\tau_{12}^{0,2}}\right)\right] \tag{39}$$

where

$$I_{\rm F}^2(0) = \left(Q_{1,1}1^{\infty,1} + Q_{2,1}2^{\infty,1}\right) I_1^{0,2} + \left(Q_{1,2}1^{\infty,1} + Q_{2,2}2^{\infty,1}\right) I_2^{0,2} \tag{40}$$

Starting from $I_{\rm F}^2(0)$, the fluorescence emission exponentially decays toward

$$I_{\rm F}^2(\infty) = \left(Q_{1,1}1^{\infty,2} + Q_{2,1}2^{\infty,2}\right) I_1^{0,2} + \left(Q_{1,2}1^{\infty,2} + Q_{2,2}2^{\infty,2}\right) I_2^{0,2} \tag{41}$$

Response to periodic dual light modulation

In the following subsections, we analyze the response of the fluorescence emission from the reversibly photoswitchable fluorescent probe P when it is submitted to various periodic dual light modulations. We first introduce the principle of theoretical analysis, which is common to all the presently considered periodic dual light modulations. Then we apply this theoretical analysis to specific cases.

Principle of the theoretical analysis

Master equation We consider that the reversibly photoswitchable fluorescent probe P is submitted to dual illumination involving two components: a periodic illumination $I_1(t)$ at wavelength λ_1 with average light intensity I_1^0 and a periodic illumination $I_2(t)$ at wavelength λ_2 with average light intensity I_2^0. In the most general case, we write

$$I(t) = I_1(t) + I_2(t) \tag{42}$$

$$I_j(t) = I_j^0 \left[1 + \alpha h_j(t)\right] \tag{43}$$

with j = 1 or 2. In Eq.(43), α measures the amplitude of light modulation and the $h_j(t)$ designate periodic functions. Eqs.(42,43) are used to express the rate constants with Eqs.(44,45)

$$k_{12}(t) = k_{12,1}^0 \left[1 + \alpha h_1(t)\right] + k_{12,2}^0 \left[1 + \alpha h_2(t)\right] \tag{44}$$

$$k_{21}(t) = k_{21,1}^0 \left[1 + \alpha h_1(t)\right] + k_{21,2}^0 \left[1 + \alpha h_2(t)\right] + k_{21}^{\Delta}. \tag{45}$$

Upon expanding the concentration expressions by introducing the function $f\left(t\right)$,

$$2 = 2^0 + \alpha f\left(t\right) \tag{46}$$

$$1 = 1^0 - \alpha f\left(t\right), \tag{47}$$

the system of differential equations governing the temporal evolution of the concentrations in 1 and 2 is solved with Eqs.(9,10) to yield

$$\frac{df\left(x\right)}{dx} = -f\left(x\right) + \left[\mathfrak{a}_1 - \mathfrak{b}_1 f\left(x\right)\right] h_1(x) + \left[\mathfrak{a}_2 - \mathfrak{b}_2 f\left(x\right)\right] h_2(x) \tag{48}$$

where

$$x = \frac{t}{\tau_{12}^0} \tag{49}$$

$$\mathfrak{a}_1 = \rho_{12}^0 \Delta_{12,1}^0 \tau_{12}^0 \tag{50}$$

$$\mathfrak{b}_1 = \alpha\left(\sigma_{12,1} + \sigma_{21,1}\right) I_1^0 \tau_{12}^0 \tag{51}$$

$$\mathfrak{a}_2 = \rho_{12}^0 \Delta_{12,2}^0 \tau_{12}^0 \tag{52}$$

$$\mathfrak{b}_2 = \alpha\left(\sigma_{12,2} + \sigma_{21,2}\right) I_2^0 \tau_{12}^0 \tag{53}$$

and

$$\rho_{12}^0 = k_{12}^0 1^0 = k_{21}^0 2^0 \tag{54}$$

$$\Delta_{12,1}^0 = \frac{k_{12,1}^0}{k_{12,1}^0 + k_{12,2}^0} - \frac{k_{21,1}^0}{k_{21,1}^0 + k_{21,2}^0 + k_{21}^{\Delta}} \tag{55}$$

$$\Delta_{12,2}^0 = \frac{k_{12,2}^0}{k_{12,1}^0 + k_{12,2}^0} - \frac{k_{21,2}^0}{k_{21,1}^0 + k_{21,2}^0 + k_{21}^{\Delta}} \tag{56}$$

designate the steady-state rate of reaction (8) (with 1^0 and 2^0 given in Eq.(19)) and the differences of the relative contributions of the average of the modulated light (I_1^0 and I_2^0 respectively) to drive the transition from 1 to 2 or from 2 to 1 respectively.

Expression of the concentrations Beyond the relaxation time τ_{12}^0, one enters into a permanent regime in which $f\left(x\right)$ is a continuous periodic function. In the cases considered in this work, light modulation involves one (denoted ω) or two (denoted ω_1 and ω_2) fundamental modulation frequencies.

In the first situation, the Fourier series associated to $f\left(x\right)$ can be written

$$f(\theta x) = a^0 + \sum_{n=1}^{+\infty} \left[a^{n,\cos} \cos\left(n\theta x\right) + b^{n,\sin} \sin\left(n\theta x\right)\right] \tag{57}$$

where

$$\theta = \omega \tau_{12}^0, \tag{58}$$

and $a^{n,\cos}$ and $b^{n,\sin}$ designate the amplitudes of the n-th components of the Fourier series.

In contrast, in the second situation, the Fourier series associated to $f(x)$ can be expressed as

$$f(\theta_1 x, \theta_2 x) = a^0 + \sum_{n=-\infty}^{+\infty} \sum_{m=-\infty}^{+\infty} \left\{ a^{n,m,\cos} \cos\left[(n\theta_1 + m\theta_2)\, x\right] + b^{n,m,\sin} \sin\left[(n\theta_1 + m\theta_2)\, x\right] \right\} \tag{59}$$

where

$$\theta_1 = \omega_1 \tau_{12}^0 \tag{60}$$

$$\theta_2 = \omega_2 \tau_{12}^0 \tag{61}$$

and a^0, $a^{n,m,\cos}$, and $b^{n,m,\sin}$ designate the amplitudes of the zeroth and $\{n,m\}$-th components of the Fourier series.

Either the $a^{n,\cos}$ and $b^{n,\sin}$, or the a^0, $a^{n,m,\cos}$, and $b^{n,m,\sin}$ terms can be extracted from Eq.(48) upon identifying the amplitudes of the components of the same order. The resulting set of equations can then be transformed to explicit the amplitudes of the concentration modulations at all modulation frequencies. Thus we write either

$$2 = 2^{\circ} + \alpha \sum_{n=1}^{+\infty} \left[2^{n,\sin} \sin(n\theta x) + 2^{n,\cos} \cos(n\theta x) \right] \tag{62}$$

$$1 = 1^{\circ} - \alpha \sum_{n=1}^{+\infty} \left[2^{n,\sin} \sin(n\theta x) + 2^{n,\cos} \cos(n\theta x) \right] \tag{63}$$

where

$$2^{\circ} = 2^0 + \alpha a^0 \tag{64}$$

$$1^{\circ} = 1^0 - \alpha a^0 \tag{65}$$

$$2^{n,\sin} = -1^{n,\sin} = b^{n,\sin} \tag{66}$$

$$2^{n,\cos} = -1^{n,\cos} = a^{n,\cos}. \tag{67}$$

or

$$2 = 2^{\circ} + \alpha \sum_{n=-\infty}^{+\infty} \sum_{m=-\infty}^{+\infty} \left\{ 2^{n,m,\sin} \sin\left[(n\theta_1 + m\theta_2)\, x\right] + 2^{n,m,\cos} \cos\left[(n\theta_1 + m\theta_2)\, x\right] \right\} \tag{68}$$

$$1 = 1^{\circ} - \alpha \sum_{n=-\infty}^{+\infty} \sum_{m=-\infty}^{+\infty} \left\{ 2^{n,m,\sin} \sin\left[(n\theta_1 + m\theta_2)\, x\right] + 2^{n,m,\cos} \cos\left[(n\theta_1 + m\theta_2)\, x\right] \right\} \tag{69}$$

where

$$2^{\circ} = 2^0 + \alpha a^0 \tag{70}$$

$$1^{\circ} = 1^0 - \alpha a^0 \tag{71}$$

$$2^{n,m,\sin} = -1^{n,m,\sin} = b^{n,m,\sin} \tag{72}$$

$$2^{n,m,\cos} = -1^{n,m,\cos} = a^{n,m,\cos}. \tag{73}$$

Expression of the fluorescence intensity We first defined in Eq.(74) the observable O_j associated to the observation at the wavelength λ_j with j = 1 or 2

$$O_j(t) \quad = \quad Q_{1,j}1(t) + Q_{2,j}2(t). \tag{74}$$

Then we subsequently extracted fluorescence emission $I_{\rm F}(t)$ from Eq.(75)

$$I_{\rm F}(t) \quad = \quad O_1(t)I_1(t) + O_2(t)I_2(t). \tag{75}$$

When the temporal dependence of $1(t)$ and $2(t)$ is given in Eqs.(62,63)

$$O_j(t) = \mathfrak{O}_{\rm j}^{\rm o} + \sum_{n=1}^{\infty} \left[\mathfrak{O}_{\rm j}^{\rm n,sin} \sin\left(n\theta x\right) + \mathfrak{O}_{\rm j}^{\rm n,cos} \cos\left(n\theta x\right) \right]. \tag{76}$$

with

$$\mathfrak{O}_{\rm j}^{\rm o} \quad = \quad Q_{1,j}1^{\rm o} + Q_{2,j}2^{\rm o} = Q_{1,j}1^0 + Q_{2,j}2^0 + \left(Q_{2,j} - Q_{1,j}\right)\alpha a^0 \tag{77}$$

$$\mathfrak{O}_{\rm j}^{\rm n,sin} \quad = \quad \left(Q_{2,j} - Q_{1,j}\right)\alpha b^{n,\sin} \tag{78}$$

$$\mathfrak{O}_{\rm j}^{\rm n,cos} \quad = \quad \left(Q_{2,j} - Q_{1,j}\right)\alpha a^{n,\cos} \tag{79}$$

and

$$I_{\rm F}(t) = \mathfrak{I}_{\rm F}^{\rm o} + \sum_{n=1}^{\infty} \left[\mathfrak{I}_{\rm F}^{\rm n,sin} \sin\left(n\theta x\right) + \mathfrak{I}_{\rm F}^{\rm n,cos} \cos\left(n\theta x\right) \right]. \tag{80}$$

In contrast to the expressions of the amplitudes of the $O_j(t)$ terms which are generic, the expressions of the amplitudes of the $I_{\rm F}(t)$ terms depend on the temporal dependence of the illumination.

When the temporal dependence of $1(t)$ and $2(t)$ is given in Eqs.(68,69)

$$O_j(t) = \mathfrak{O}_{\rm j}^{\rm o} + \sum_{n=-\infty}^{+\infty} \sum_{m=-\infty}^{+\infty} \left\{ \mathfrak{O}_{\rm j}^{\rm n,m,sin} \sin\left[\left(n\theta_1 + m\theta_2\right)x\right] + \mathfrak{O}_{\rm j}^{\rm n,m,cos} \cos\left[\left(n\theta_1 + m\theta_2\right)x\right] \right\} \tag{81}$$

with

$$\mathfrak{O}_{\rm j}^{\rm o} \quad = \quad Q_{1,j}1^0 + Q_{2,j}2^0 + \left(Q_{2,j} - Q_{1,j}\right)\alpha a^0 \tag{82}$$

$$\mathfrak{O}_{\rm j}^{\rm n,m,sin} \quad = \quad \left(Q_{2,j} - Q_{1,j}\right)\alpha b^{n,m,\sin} \tag{83}$$

$$\mathfrak{O}_{\rm j}^{\rm n,m,cos} \quad = \quad \left(Q_{2,j} - Q_{1,j}\right)\alpha a^{n,m,\cos} \tag{84}$$

and

$$I_{\rm F}(t) = \mathfrak{I}_{\rm F}^{\rm o} + \sum_{n=-\infty}^{+\infty} \sum_{m=-\infty}^{+\infty} \left\{ \mathfrak{I}_{\rm F}^{\rm n,m,sin} \sin\left[\left(n\theta_1 + m\theta_2\right)x\right] + \mathfrak{I}_{\rm F}^{\rm n,m,cos} \cos\left[\left(n\theta_1 + m\theta_2\right)x\right] \right\}. \tag{85}$$

Again, whereas the expressions of the amplitudes of the $O_j(t)$ terms are generic, the expressions of the amplitudes of the $I_{\rm F}(t)$ terms depend on the temporal dependence of the illumination.

Periodic dual light modulations of small amplitude

In a first subsection, we consider the cases of dual light modulations of small amplitude denoted ε instead of α in the following. In these cases, the general master equation can be linearized, which permits to derive analytic expressions.

Sinusoidal modulation at a single angular frequency of modulation at two wavelengths

Derivation of the theoretical expressions We first considered for $I(t)$ the superposition of two sinusoidal modulations of small amplitude: i) at wavelength λ_1 around the averaged value I_1^0 at angular frequency of modulation ω and ii) at wavelength λ_2 around the averaged value I_2^0 at the same angular frequency of modulation ω but with a phase delay φ. We adopted

$$I(t) = I_1^0 [1 + \varepsilon h_1(t)] + I_2^0 [1 + \varepsilon h_2(t)] \quad (86)$$

$$h_1(t) = \sin(\omega t) \quad (87)$$

$$h_2(t) = \sin(\omega t + \varphi) \quad (88)$$

with $\varepsilon \ll 1$. At the first-order expansion in the light perturbation, $f(x) = f_1(\theta x) + f_2(\theta x)$ is solution of Eq.(48) when $f_1(\theta x)$ and $f_2(\theta x)$ are solutions of Eq.(89)

$$\frac{df_j(\theta x)}{dx} = -f_j(\theta x) + \mathfrak{a}_j h_j(\theta x) \quad (89)$$

with $j = 1$ or 2 respectively. Beyond the relaxation time τ_{12}^0 given in Eq.(18), we derived

$$\mathfrak{2}^{\circ} = 2^0 \quad (90)$$

$$\mathfrak{1}^{\circ} = 1^0 \quad (91)$$

$$\mathfrak{2}^{1,\sin} = -\mathfrak{1}^{1,\sin} = \frac{\mathfrak{a}_1}{1+\theta^2} + \frac{\mathfrak{a}_2 (\cos\varphi + \theta \sin\varphi)}{1+\theta^2} \quad (92)$$

$$\mathfrak{2}^{1,\cos} = -\mathfrak{1}^{1,\cos} = -\frac{\mathfrak{a}_1 \theta}{1+\theta^2} + \frac{\mathfrak{a}_2 (\sin\varphi - \theta \cos\varphi)}{1+\theta^2} \quad (93)$$

In the specific case of the RSFPs considered in this work, the photochemically driven transition from the state $\mathsf{1}$ to the state $\mathsf{2}$ (respectively from the state $\mathsf{2}$ to the state $\mathsf{1}$) is exclusively governed by illumination at wavelength λ_1 (respectively λ_2). Upon considering that the rate of the $\mathsf{2}$ to $\mathsf{1}$ conversion is mainly governed by photochemistry, one then deduces $\mathfrak{a}_1 = -\mathfrak{a}_2$. Under such conditions, Eqs.(92,93) become

$$\mathfrak{2}^{1,\sin} = -\mathfrak{1}^{1,\sin} = \frac{\mathfrak{a}_1}{1+\theta^2} [(1 - \cos\varphi) - \theta \sin\varphi] \quad (94)$$

$$\mathfrak{2}^{1,\cos} = -\mathfrak{1}^{1,\cos} = -\frac{\mathfrak{a}_1}{1+\theta^2} [\theta (1 - \cos\varphi) + \sin\varphi] . \quad (95)$$

Eqs.(94,95) show that $\varphi = \pi$ is especially favorable to increase the amplitudes of the fluorescence response to light modulation. This φ value has been adopted in Speed OPIOM. Eqs.(94,95) yield

$$\mathfrak{2}^{\mathfrak{1},\sin} = -\mathfrak{1}^{\mathfrak{1},\sin} = \frac{2\mathfrak{a}_{\mathfrak{1}}}{1+\theta^2} = 2\rho_{12}^0\tau_{12}^0\Delta_{12,1}^0\frac{1}{1+\left(\omega\tau_{12}^0\right)^2} = 2\Delta_{12,1}^0\frac{K_{12}^0}{\left(1+K_{12}^0\right)^2}\frac{1}{1+\left(\omega\tau_{12}^0\right)^2}P_{\rm tot} \tag{96}$$

$$\mathfrak{2}^{\mathfrak{1},\cos} = -\mathfrak{1}^{\mathfrak{1},\cos} = -\frac{2\mathfrak{a}_{\mathfrak{1}}\theta}{1+\theta^2} = -2\rho_{12}^0\tau_{12}^0\Delta_{12,1}^0\frac{\omega\tau_{12}^0}{1+\left(\omega\tau_{12}^0\right)^2} = -2\Delta_{12,1}^0\frac{K_{12}^0}{\left(1+K_{12}^0\right)^2}\frac{\omega\tau_{12}^0}{1+\left(\omega\tau_{12}^0\right)^2}P_{\rm tot} \tag{97}$$

and the terms of the fluorescence intensities are

$$\mathfrak{I}_{\rm F}^{\circ} = \left(Q_{1,1}1^0 + Q_{2,1}2^0\right)I_1^0 + \left(Q_{1,2}1^0 + Q_{2,2}2^0\right)I_2^0 \tag{98}$$

$$\mathfrak{I}_{\rm F}^{\mathfrak{1},\sin} = \varepsilon\left\{\left[\left(Q_{1,1}1^0 + Q_{2,1}2^0\right)I_1^0 - \left(Q_{1,2}1^0 + Q_{2,2}2^0\right)I_2^0\right]\right\} + \varepsilon\left\{\left[\left(Q_{1,1}-Q_{2,1}\right)I_1^0 + \left(Q_{1,2}-Q_{2,2}\right)I_2^0\right]\mathfrak{1}^{\mathfrak{1},\sin}\right\} \tag{99}$$

$$\mathfrak{I}_{\rm F}^{\mathfrak{1},\cos} = \varepsilon\left[\left(Q_{1,1}-Q_{2,1}\right)I_1^0 + \left(Q_{1,2}-Q_{2,2}\right)I_2^0\right]\mathfrak{1}^{\mathfrak{1},\cos}. \tag{100}$$

Optimal out-of-phase response Speed OPIOM differs from (one-color) OPIOM in the limit where the exchange between the states $\mathsf{1}$ and $\mathsf{2}$ is essentially driven by the photochemical contributions. We correspondingly chose to focus the subsequent analysis in a range of light intensities (I_1^0,I_2^0) such that $\sigma_{21,1}I_1^0+\sigma_{21,2}I_2^0 \gg k_{21}^{\Delta}$. Moreover, we adopted the Dronpa-2 values of the kinetic parameters to draw the following theoretical figures. The resulting normalized out-of-phase amplitude, $|\mathfrak{1}_{\rm norm}^{\mathfrak{1},\cos}| = |\mathfrak{1}^{\mathfrak{1},\cos}/P_{\rm tot}|$, as a function of the control parameters I_2^0/I_1^0 and ω/I_1^0 is plotted in Supplementary Figure 11a.

$|\mathfrak{1}_{\rm norm}^{\mathfrak{1},\cos}|$ exhibits a single optimum when the two resonance conditions (101,102) are fulfilled

$$\left(\sigma_{12,1}+\sigma_{21,1}\right)I_1^0 = \left(\sigma_{12,2}+\sigma_{21,2}\right)I_2^0 \tag{101}$$

$$\omega = 2\left(\sigma_{12,1}+\sigma_{21,1}\right)I_1^0. \tag{102}$$

The optimization of $\mathfrak{1}_{\rm norm}^{\mathfrak{1},\cos}$ results from the independent optimisation of the terms $\mathfrak{a}_{\mathfrak{1}}$ and $\theta/[1+\theta^2]$ in Eq.(97). $\mathfrak{a}_{\mathfrak{1}}$ measures the composition shift $\Delta 2^0$ from the steady-state 2^0 after a light intensity jump of amplitude $\Delta I_1^0 = \varepsilon I_1^0$.[1] It is maximized when Eq.(101) is fulfilled. The second term, $\theta/[1+\theta^2]$, is maximized upon matching the angular frequency of modulation of the light modulation ω with the exchange relaxation time τ_{12}^0 so that $\theta = 1$. When $\omega \gg 1/\tau_{12}^0$, the exchange is slow compared to the light variations and the couple $\{\mathsf{1},\mathsf{2}\}$ has not enough time to respond: both $\mathfrak{i}^{\mathfrak{1},\sin}$ and $\mathfrak{i}^{\mathfrak{1},\cos}$ vanish. Conversely, when $\omega \ll 1/\tau_{12}^0$, $\mathfrak{i}^{\mathfrak{1},\cos}$ cancels and the concentrations of $\mathsf{1}$ and $\mathsf{2}$ oscillate in phase with the light modulation.

[1] From the expression (19), one can show that $\frac{d2^0}{dLnI_1^0} = \frac{\Delta 2^0}{\varepsilon} = \Delta_{12,1}^0 K_{12}^0 P_{\rm tot}/\left(1+K_{12}^0\right)^2$ using $K_{12}^0 = k_{12}^0/k_{21}^0$ with the expressions of k_{12}^0 and k_{21}^0 given in Eqs.(11,12).

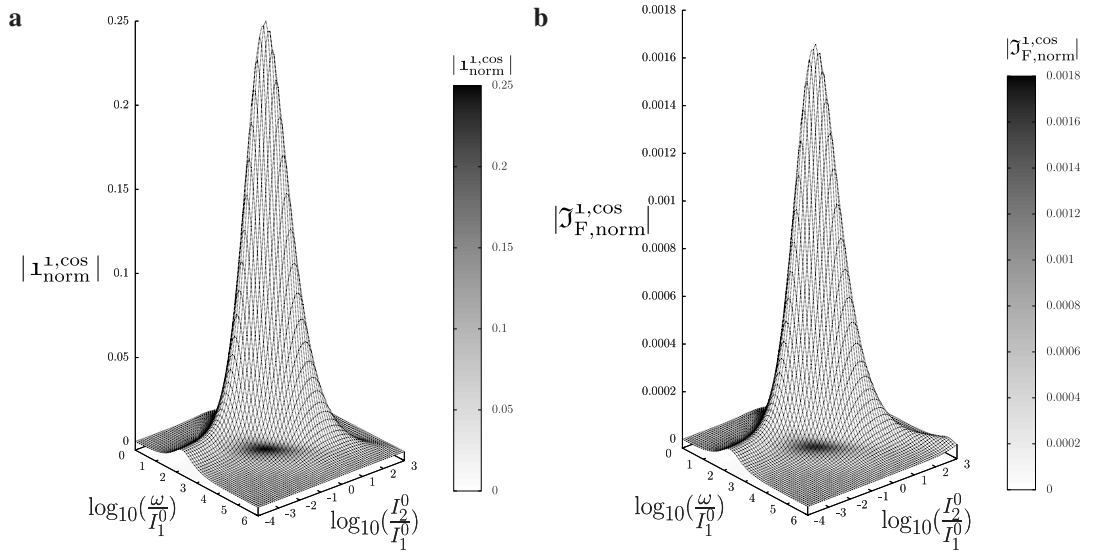

Supplementary Figure 11: Theoretical computation of the response of a photoswitchable fluorophore $\mathsf{1} \rightleftharpoons \mathsf{2}$ submitted to dual light harmonic forcing of small amplitude given in Eq.(86) with $\varphi = \pi$. The normalized amplitude of the out-of-phase oscillations in $\mathsf{1}$ concentration $|\mathfrak{1}^{1,\cos}_{\rm norm}|$ (**a**) and the normalized Speed OPIOM signal $|\mathfrak{I}^{1,\cos}_{\rm F}/(\varepsilon P_{\rm tot})|$ (**b**) are plotted versus the ratios I_2^0/I_1^0 and ω/I_1^0 (in rad Ein^{-1} m^2) when $I_1^0 = 100\frac{k_{21}^{\Delta}}{\sigma_{12,1}+\sigma_{21,1}}$. $\sigma_{12,1}$ = 196 m^2 mol^{-1}, $\sigma_{21,1}$ = 0 m^2 mol^{-1}, $\sigma_{12,2}$ = 0 m^2 mol^{-1}, $\sigma_{21,2}$ = 413 m^2 mol^{-1}, $k_{21}^{\Delta} = 1.4 \times 10^{-2}$ s^{-1}.

Sinusoidal modulation at two modulation frequencies at two wavelengths Then we considered for $I(t)$ the superposition of two sinusoidal modulations of small amplitude at modulation frequencies ω_1 and ω_2 (i) around the averaged value I_1^0 at wavelength λ_1 and (ii) around the averaged value I_2^0 at wavelength λ_2. We adopted

$$I(t) = I_1^0\left[1+\varepsilon h_1(t)\right] + I_2^0\left[1+\varepsilon h_2(t)\right] \tag{103}$$

$$h_1(t) = \sin(\omega_1 t) + \beta\sin(\omega_2 t) \tag{104}$$

$$h_2(t) = -\sin(\omega_1 t) - \beta\sin(\omega_2 t) \tag{105}$$

with $\varepsilon \ll 1$. At the first-order expansion in the light perturbation, $f(x) = f_1(\theta_1 x) + \beta f_2(\theta_2 x)$ is solution of Eq.(48) when $f_1(\theta_1 x)$ and $f_2(\theta_2 x)$ are solutions of Eq.(106)

$$\frac{df_j(\theta_j x)}{dx} = -f_j(\theta_j x) + (\mathfrak{a}_1 - \mathfrak{a}_2)\sin(\theta_j x) \tag{106}$$

with $j = 1$ or 2 respectively. Beyond the relaxation time τ_{12}^0 given in Eq.(18), we derived

$$\mathtt{2}^{\mathtt{0}} = 2^0 \tag{107}$$

$$\mathtt{1}^{\mathtt{0}} = 1^0 \tag{108}$$

$$\mathtt{2}^{\mathtt{1},\mathtt{0},\sin} = -\mathtt{1}^{\mathtt{1},\mathtt{0},\sin} = \frac{(\mathfrak{a}_1 - \mathfrak{a}_2)}{1+\theta_1^2} \tag{109}$$

$$\mathtt{2}^{\mathtt{1},\mathtt{0},\cos} = -\mathtt{1}^{\mathtt{1},\mathtt{0},\cos} = -\frac{(\mathfrak{a}_1 - \mathfrak{a}_2)\,\theta_1}{1+\theta_1^2} \tag{110}$$

$$\mathtt{2}^{\mathtt{0},\mathtt{1},\sin} = -\mathtt{1}^{\mathtt{0},\mathtt{1},\sin} = \beta\frac{(\mathfrak{a}_1 - \mathfrak{a}_2)}{1+\theta_2^2} \tag{111}$$

$$\mathtt{2}^{\mathtt{0},\mathtt{1},\cos} = -\mathtt{1}^{\mathtt{0},\mathtt{1},\cos} = -\beta\frac{(\mathfrak{a}_1 - \mathfrak{a}_2)\,\theta_2}{1+\theta_2^2} \tag{112}$$

In the specific case of the RSFPs considered in this work and by considering that the rate of the $\mathsf{2}$ to $\mathsf{1}$ conversion is mainly governed by photochemistry, one has $\mathfrak{a}_1 = -\mathfrak{a}_2$ and Eqs.(109,112) become

$$\mathtt{2}^{\mathtt{1},\mathtt{0},\sin} = -\mathtt{1}^{\mathtt{1},\mathtt{0},\sin} = \frac{2\mathfrak{a}_1}{1+\theta_1^2} \tag{113}$$

$$\mathtt{2}^{\mathtt{1},\mathtt{0},\cos} = -\mathtt{1}^{\mathtt{1},\mathtt{0},\cos} = -\frac{2\mathfrak{a}_1\theta_1}{1+\theta_1^2} \tag{114}$$

$$\mathtt{2}^{\mathtt{0},\mathtt{1},\sin} = -\mathtt{1}^{\mathtt{0},\mathtt{1},\sin} = \beta\frac{2\mathfrak{a}_1}{1+\theta_2^2} \tag{115}$$

$$\mathtt{2}^{\mathtt{0},\mathtt{1},\cos} = -\mathtt{1}^{\mathtt{0},\mathtt{1},\cos} = -\beta\frac{2\mathfrak{a}_1\theta_2}{1+\theta_2^2} \tag{116}$$

and the associated terms of the oscillating fluorescence emission are

$$\mathfrak{I}_{\mathrm{F}}^{\mathtt{0}} = \left(Q_{1,1}1^0 + Q_{2,1}2^0\right) I_1^0 + \left(Q_{1,2}1^0 + Q_{2,2}2^0\right) I_2^0 \tag{117}$$

$$\begin{aligned}\mathfrak{I}_{\mathrm{F}}^{\mathtt{1},\mathtt{0},\sin} = {} & \varepsilon\left\{\left(Q_{1,1}1^0 + Q_{2,1}2^0\right) I_1^0 - \left(Q_{1,2}1^0 + Q_{2,2}2^0\right) I_2^0\right\} + \\ & \varepsilon\left\{\left[(Q_{1,1} - Q_{2,1})\, I_1^0 + (Q_{1,2} - Q_{2,2})\, I_2^0\right] \mathtt{1}^{\mathtt{1},\mathtt{0},\sin}\right\}\end{aligned} \tag{118}$$

$$\mathfrak{I}_{\mathrm{F}}^{\mathtt{1},\mathtt{0},\cos} = \varepsilon\left[(Q_{1,1} - Q_{2,1})\, I_1^0 + (Q_{1,2} - Q_{2,2})\, I_2^0\right] \mathtt{1}^{\mathtt{1},\mathtt{0},\cos} \tag{119}$$

$$\begin{aligned}\mathfrak{I}_{\mathrm{F}}^{\mathtt{0},\mathtt{1},\sin} = {} & \varepsilon\beta\left\{\left(Q_{1,1}1^0 + Q_{2,1}2^0\right) I_1^0 - \left(Q_{1,2}1^0 + Q_{2,2}2^0\right) I_2^0\right\} + \\ & \varepsilon\left\{\left[(Q_{1,1} - Q_{2,1})\, I_1^0 + (Q_{1,2} - Q_{2,2})\, I_2^0\right] \mathtt{1}^{\mathtt{0},\mathtt{1},\sin}\right\}\end{aligned} \tag{120}$$

$$\mathfrak{I}_{\mathrm{F}}^{\mathtt{0},\mathtt{1},\cos} = \varepsilon\left[(Q_{1,1} - Q_{2,1})\, I_1^0 + (Q_{1,2} - Q_{2,2})\, I_2^0\right] \mathtt{1}^{\mathtt{0},\mathtt{1},\cos}. \tag{121}$$

Hence the Speed OPIOM signal from the superposition of two antiphase-related sinusoidal modulations of small amplitude around the averaged values I_1^0 and I_2^0 at two different modulation frequencies, ω_1 and ω_2, is equal to the sum of the Speed OPIOM signals from sinusoidal modulations of small amplitude around the averaged values I_1^0 and I_2^0 at the modulation frequencies ω_1 and ω_2. This dual frequency excitation is correspondingly relevant to selectively and simultaneously image two different reversibly photoswitchable fluorophores sharing an identical resonance condition (101) for the intensities I_1^0 and I_2^0 but associated to different resonant modulation frequencies ω_1 and ω_2 given in Eq.(102).

Periodic dual light modulations of large amplitude

The use of sinusoidal modulations of small amplitude is favorable to derive simple analytical expressions. However, it generates only weak variations of the probe signal because of the small modulations, which is a drawback to reliably extract the out-of-phase amplitude of the first order response. To circumvent this limitation, we also analyzed the response of a reversibly photoswitchable probe to periodic modulations of large amplitude.

Sinusoidal modulation at a single angular frequency of modulation at two wavelengths Following the analysis performed in the corresponding regime of sinusoidal modulation of small amplitude, we considered for $I(t)$ the superposition of two sinusoidal modulations of large amplitude at a same angular frequency of modulation ω in phase opposition at wavelengths λ_1 (around the averaged value I_1^0) and λ_2 (around the averaged value I_2^0):

$$I(t) = I_1^0 \left[1 + \alpha h_1(t)\right] + I_2^0 \left[1 + \alpha h_2(t)\right] \tag{122}$$

$$h_1(t) = \sin(\omega t) \tag{123}$$

$$h_2(t) = -h_1(t) = -\sin(\omega t)\,. \tag{124}$$

Following the general derivation given in subsection , we used the differential equation (125)

$$\frac{df(\theta x)}{dx} = -f(\theta x) + \left[(\mathfrak{a}_1 - \mathfrak{a}_2) - (\mathfrak{b}_1 - \mathfrak{b}_2) f(\theta x)\right] h_1(\theta x) \tag{125}$$

governing the temporal evolution of the concentrations in 1 and 2 to derive the $a^{n,\cos}$ and $b^{n,\sin}$ terms beyond the relaxation time τ_{12}^0.

- Zeroth order:

$$a^0 = -(\mathfrak{b}_1 - \mathfrak{b}_2)\frac{b^{1,\sin}}{2} \tag{126}$$

- First order:

$$-a^{1,\cos}\theta = -b^{1,\sin} + (\mathfrak{a}_1 - \mathfrak{a}_2) - (\mathfrak{b}_1 - \mathfrak{b}_2)\, a^0 + (\mathfrak{b}_1 - \mathfrak{b}_2)\frac{a^{2,\cos}}{2} \tag{127}$$

$$b^{1,\sin}\theta = -a^{1,\cos} - (\mathfrak{b}_1 - \mathfrak{b}_2)\frac{b^{2,\sin}}{2} \tag{128}$$

- Order $n > 1$:

$$a^{n,\cos}n\theta = b^{n,\sin} - \frac{(\mathfrak{b}_1 - \mathfrak{b}_2)}{2}\left(a^{n+1,\cos} - a^{n-1,\cos}\right) \tag{129}$$

$$b^{n,\sin}n\theta = -a^{n,\cos} - \frac{(\mathfrak{b}_1 - \mathfrak{b}_2)}{2}\left(b^{n+1,\sin} - b^{n-1,\sin}\right) \tag{130}$$

from which we obtained the expressions of the concentration terms for 1 and 2 with Eqs.(64–67).

To analyze the dependence of $\mathfrak{1}^{1,\cos} = -\mathfrak{2}^{1,\cos}$ on the control parameters I_2^0/I_1^0 and ω/I_1^0, we first analytically retrieved the $2n+1$ unknown parameters (a^0,...,$a^{n,\cos}$,$b^{n,\sin}$) upon truncating the Fourier expansion (57) at increasing orders n. Supplementary Figure 12 displays representative results, which have been obtained with $n = 5$. One can notice that the first order parameters $a^{1,cos}$ and $b^{1,sin}$ totally dominate the temporal response of the concentrations in 1 and 2.

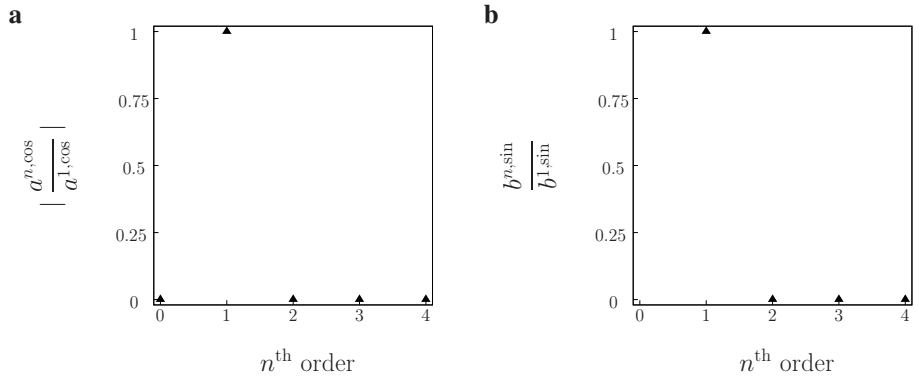

Supplementary Figure 12: Computation of the amplitudes of the Fourier terms, $a^{n,\cos}$ (**a**) and $b^{n,\sin}$ (**b**) for a reversibly photoswitchable fluorophore $1 \rightleftharpoons 2$ submitted to light harmonic forcing given in Eqs.(122–124). The numerical computation has been performed upon truncating the Fourier f expansion at the fifth order ($n = 5$). $\sigma_{12,1}$ = 196 m^2 mol^{-1}, $\sigma_{21,1}$ = 0 m^2 mol^{-1}, $\sigma_{12,2}$ = 0 m^2 mol^{-1}, $\sigma_{21,2}$ = 413 m^2 mol^{-1}, $k_{21}^{\Delta} = 1.4 \times 10^{-2}$ s^{-1}; $I_1^0 = 100\frac{k_{21}^{\Delta}}{\sigma_{12,1}+\sigma_{21,1}}$, $I_2^0 = 3.3 \times 10^{-3}$ Ein s^{-1} m^{-2} and ω = 2.78 rad s^{-1}.

Supplementary Figure 13 displays the dependence of the normalized amplitude, $|\ \mathfrak{1}_{\text{norm}}^{1,\cos}\ | = |\ \mathfrak{1}^{1,\cos}/P_{\text{tot}}\ |$, on I_2^0/I_1^0 and ω/I_1^0 when $\alpha = 1$. Truncation of the Fourier expansion of the $f(\theta x)$ function at the fifth order ($n = 5$) is sufficient to yield convergence: the dependence of $|\ \mathfrak{1}_{\text{norm}}^{1,\cos}\ |$ on I_2^0/I_1^0 and ω/I_1^0 does not significantly evolve beyond $n = 3$. $|\ \mathfrak{1}_{\text{norm}}^{1,\cos}\ |$ exhibits an optimum in the space (I_2^0/I_1^0,ω/I_1^0), whose position and amplitude are very close to those observed with a sinusoidal modulation of small amplitude (Supplementary Table 4).

Note that the error done when taking the analytical expression of the resonance conditions, valid only for a modulation of small amplitude, is vanishing, no matter which amplitude α is used.

Adopting the expression (76) for the observable O_j, we used the expression (122) for the light intensity to derive

$$\mathfrak{I}_{\text{F}}^{\circ} = \left(\mathfrak{O}_{\mathfrak{1}}^{\circ} + \frac{1}{2}\alpha\mathfrak{O}_{\mathfrak{1}}^{1,\sin}\right) I_1^0 + \left(\mathfrak{O}_{\mathfrak{2}}^{\circ} - \frac{1}{2}\alpha\mathfrak{O}_{\mathfrak{2}}^{1,\sin}\right) I_2^0 \tag{131}$$

$$\mathfrak{I}_{\text{F}}^{1,\sin} = \left(\alpha\mathfrak{O}_{\mathfrak{1}}^{\circ} + \mathfrak{O}_{\mathfrak{1}}^{1,\sin} - \frac{1}{2}\alpha\mathfrak{O}_{\mathfrak{1}}^{2,\cos}\right) I_1^0 + \left(-\alpha\mathfrak{O}_{\mathfrak{2}}^{\circ} + \mathfrak{O}_{\mathfrak{2}}^{1,\sin} + \frac{1}{2}\alpha\mathfrak{O}_{\mathfrak{2}}^{2,\cos}\right) I_2^0 \tag{132}$$

$$\mathfrak{I}_{\text{F}}^{1,\cos} = \left(\mathfrak{O}_{\mathfrak{1}}^{1,\cos} + \frac{1}{2}\alpha\mathfrak{O}_{\mathfrak{1}}^{2,\sin}\right) I_1^0 + \left(\mathfrak{O}_{\mathfrak{2}}^{1,\cos} - \frac{1}{2}\alpha\mathfrak{O}_{\mathfrak{2}}^{2,\sin}\right) I_2^0 \tag{133}$$

$$\mathfrak{I}_{\text{F}}^{\mathfrak{n},\sin} = \left[\mathfrak{O}_{\mathfrak{1}}^{\mathfrak{n},\sin} + \frac{1}{2}\alpha\left(\mathfrak{O}_{\mathfrak{1}}^{\mathfrak{n}-1,\cos} - \mathfrak{O}_{\mathfrak{1}}^{\mathfrak{n}+1,\cos}\right)\right] I_1^0 + \left[\mathfrak{O}_{\mathfrak{2}}^{\mathfrak{n},\sin} - \frac{1}{2}\alpha\left(\mathfrak{O}_{\mathfrak{2}}^{\mathfrak{n}-1,\cos} - \mathfrak{O}_{\mathfrak{2}}^{\mathfrak{n}+1,\cos}\right)\right] I_2^0 \tag{134}$$

$$\mathfrak{I}_{\text{F}}^{\mathfrak{n},\cos} = \left[\mathfrak{O}_{\mathfrak{1}}^{\mathfrak{n},\cos} + \frac{1}{2}\alpha\left(\mathfrak{O}_{\mathfrak{1}}^{\mathfrak{n}+1,\sin} - \mathfrak{O}_{\mathfrak{1}}^{\mathfrak{n}-1,\sin}\right)\right] I_1^0 + \left[\mathfrak{O}_{\mathfrak{2}}^{\mathfrak{n},\cos} - \frac{1}{2}\alpha\left(\mathfrak{O}_{\mathfrak{2}}^{\mathfrak{n}+1,\sin} - \mathfrak{O}_{\mathfrak{2}}^{\mathfrak{n}-1,\sin}\right)\right] I_2^0 \tag{135}$$

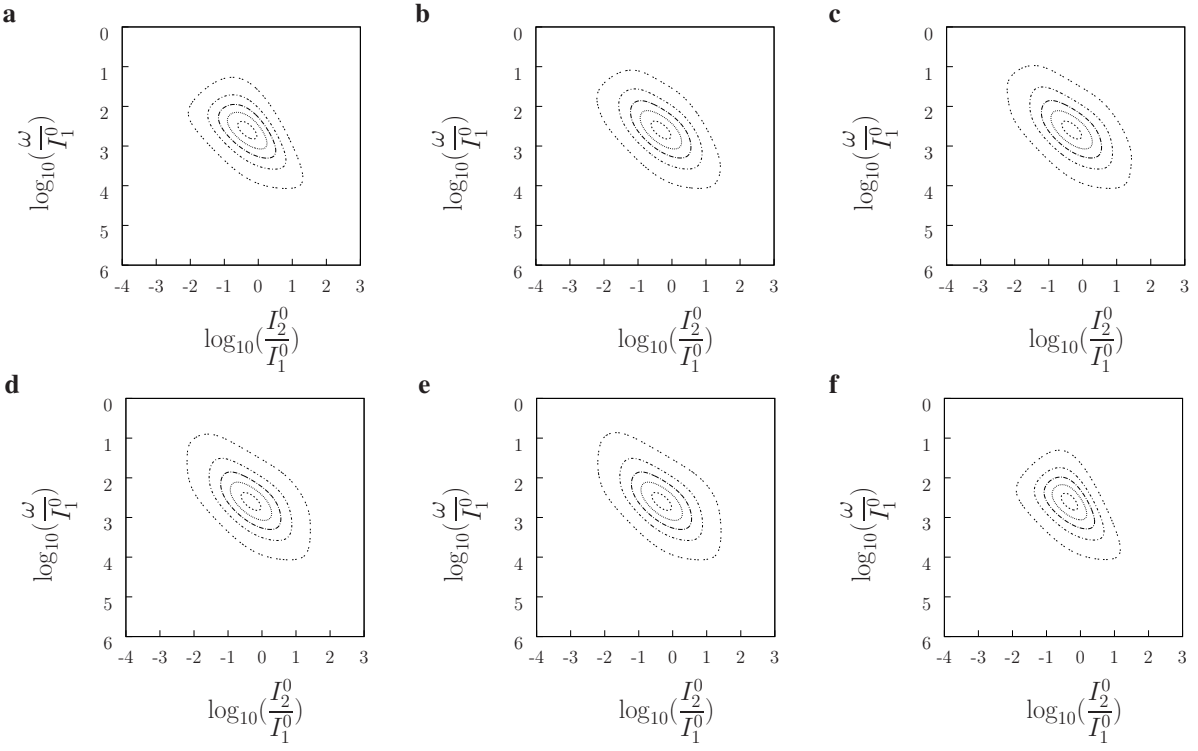

Supplementary Figure 13: Theoretical dependence of the normalized amplitude of the out-of-phase oscillations in 1 concentration, $\mid \imath^{1,\cos}_{\rm norm} \mid = \mid \imath^{1,\cos}/P_{\rm tot} \mid$, of a reversibly photoswitchable fluorophore $1 \rightleftharpoons 2$ submitted to light harmonic forcing given in Eqs.(122–124) on I_2^0/I_1^0 and ω/I_1^0 (in rad Ein^{-1} m^2). The numerical computation has been performed upon truncating the Fourier $f(\theta x)$ expansion at various orders n (**a**: 1, **b**: 2, **c**: 3, **d**: 4, **e**: 5). The dependence observed in a regime of small amplitude modulation, $\mid 1^{1,\cos}_{\rm norm} \mid$, is shown in **f**. $\sigma_{12,1}$ = 196 m^2 mol^{-1}, $\sigma_{21,1}$ = 0 m^2 mol^{-1}, $\sigma_{12,2}$ = 0 m^2 mol^{-1}, $\sigma_{21,2}$ = 413 m^2 mol^{-1}, $k_{21}^{\Delta} = 1.4 \times 10^{-2}$ s^{-1}; $I_1^0 = 100\frac{k_{21}^{\Delta}}{\sigma_{12,1}+\sigma_{21,1}}$. The markers correspond to isodensity curves : 0.03 (double-dash), 0.08 (dot small-dash), 0.13 (dot long-dash), 0.18 (dot) and 0.23 (dash).

for $n > 1$.

Supplementary Figure 14 compares the dependence of the absolute value of the normalized out-of-phase first-order amplitude $\mid \mathfrak{I}^{1,\cos}_{\rm F,norm} \mid = \mid \mathfrak{I}^{1,\cos}_{\rm F}/\{[(Q_{2,1} - Q_{1,1})I_1^0 + (Q_{2,2} - Q_{1,2})I_2^0]\alpha P_{\rm tot}\} \mid$ on I_2^0/I_1^0 and ω/I_1^0 obtained in the case of the largest amplitude modulation (computed using Eq.(133) with $\alpha = 1$) with that obtained for a modulation of small amplitude (computed using Eq.(100) with $\alpha = \varepsilon = 1$). The position and the amplitude of the optimum are similar in both cases: using $I_1^0 = 100\frac{k_{21}^{\Delta}}{\sigma_{12,1}+\sigma_{21,1}}$, we found $I_2^{0,R} = 4.4 \times 10^{-3}$ Ein s^{-1} m^{-2}, $\omega^R = 2.99$ rad s^{-1}, and $\mid \mathfrak{I}^{1,\cos}_{\rm F,norm} \mid = 2.59 \times 10^{-1}$ in the case of a sinusoidal modulation of large amplitude, and $I_2^{0,R} = 3.6 \times 10^{-3}$ Ein s^{-1} m^{-2}, $\omega^R = 2.90$ rad s^{-1}, and $\mid \mathfrak{I}^{1,\cos}_{\rm F,norm} \mid = 2.56 \times 10^{-1}$ in the case of a sinusoidal modulation of small amplitude.

Sinusoidal modulation at two modulation frequencies at two wavelengths We then considered for $I(t)$ the superposition of two antiphase sinusoidal modulations of large amplitude at modulation frequencies ω_1 and ω_2 at wavelength λ_1

Amplitude	n	$\frac{I_2^{0,R}}{I_1^{0,R}}$	$\frac{\omega^R}{I_1^{0,R}}$ (rad Ein^{-1} m^2)	$10^1\times \mid \mathfrak{1}_{\rm norm}^{\mathfrak{1},\cos} \mid$
Small	–	0.47	394	2.49
Large	1	0.47	394	2.49
Large	2	0.47	394	2.49
Large	3	0.47	394	2.49
Large	4	0.47	394	2.49
Large	5	0.47	394	2.49

Supplementary Table 4: Coordinates and amplitude of the $\mid \mathfrak{1}_{\rm norm}^{\mathfrak{1},\cos} \mid$ extremum from a reversibly photoswitchable fluorophore $\mathsf{1} \rightleftharpoons \mathsf{2}$ submitted to light harmonic forcing given in Eqs.(122–124) (with $\alpha = 1$) as a function of the truncation order n of the Fourier expansion of the $f(\theta x)$ function. The Table also provides the coordinates and the amplitude of $\mid \mathfrak{1}_{\rm norm}^{\mathfrak{1},\cos} \mid$ extremum observed in the corresponding regime of small amplitude modulation.

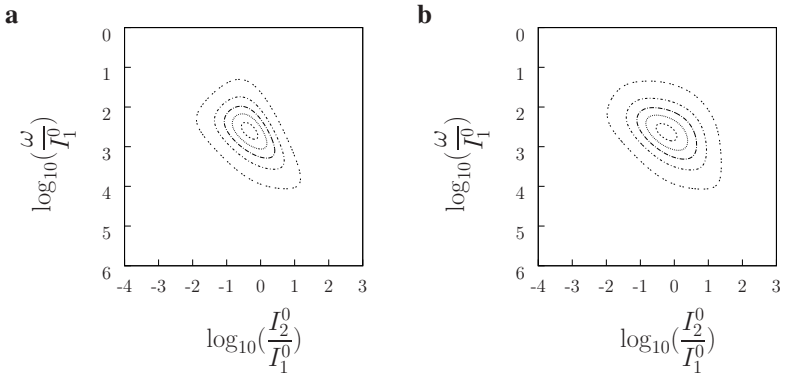

Supplementary Figure 14: Theoretical dependence of the absolute value of the normalized amplitude of the out-of-phase oscillations of fluorescence intensity, $\mid \mathfrak{I}_{\rm F,norm}^{\mathfrak{1},\cos} \mid = \mid \mathfrak{I}_{\rm F}^{\mathfrak{1},\cos}/\{[(Q_{2,1}-Q_{1,1})I_1^0 + (Q_{2,2}-Q_{1,2})I_2^0]\alpha P_{\rm tot}\} \mid$ for a reversibly photoswitchable fluorophore $\mathsf{1} \rightleftharpoons \mathsf{2}$ submitted to superposition of light harmonic forcing given in Eq.(86) with $\varphi = \pi$ (**a**) or in Eqs.(122–124) (**b**; α = 1) on I_2^0/I_1^0 and ω/I_1^0 (in rad Ein^{-1} m^2). The numerical computation has been performed upon truncating the Fourier f expansion at the fifth order ($n = 5$). $Q_{2,1}/Q_{1,1} = 0.01$, $Q_{2,2}/Q_{1,2} = 0.01$, and $Q_{1,1}/Q_{1,2} = 15$; $\sigma_{12,1}$ = 196 m^2 mol^{-1}, $\sigma_{21,1}$ = 0 m^2 mol^{-1}, $\sigma_{12,2}$ = 0 m^2 mol^{-1}, $\sigma_{21,2}$ = 413 m^2 mol^{-1}, $k_{21}^{\Delta} = 1.4\times10^{-2}$ s^{-1}; $I_1^0 = 100\frac{k_{21}^{\Delta}}{\sigma_{12,1}+\sigma_{21,1}}$. The markers correspond to isodensity curves : 0.03 (double-dash), 0.08 (dot small-dash), 0.13 (dot long-dash), 0.18 (dot) and 0.23 (dash).

(around the averaged value I_1^0) and λ_2 (around the averaged value I_2^0). We adopted

$$I(t) = I_1^0\,[1+\alpha h_1(t)] + I_2^0\,[1+\alpha h_2(t)] \tag{136}$$

$$h_1(t) = \sin(\omega_1 t) + \beta \sin(\omega_2 t) \tag{137}$$

$$h_2(t) = -\sin(\omega_1 t) - \beta \sin(\omega_2 t) \tag{138}$$

with $\alpha\,(1+\beta) \leq 1$. The dual frequency excitation has been considered to simultaneously image two different reversibly photoswitchable fluorophores sharing identical resonance condition (101) for the intensities I_1^0 and I_2^0, but significantly differing in their resonant angular frequency of modulation given in Eq.(102). Considering the typical one order of mag-

nitude wide bandwidth of the resonance phenomenon along the angular frequency of modulation axis (see Supplementary Figure 11), we denoted ω_1 the smallest angular frequency of modulation and assumed the ratio ω_2/ω_1 to be an integer n. Beyond the relaxation time τ_{12}^0, we relied on Eq.(48) to extract the amplitudes a_n and b_n of the Fourier series given in Eq.(57). We derived

- Zeroth order:

$$a^0 = -\frac{(\mathfrak{b}_1 - \mathfrak{b}_2)}{2}\left(b^{1,\sin} + \beta b^{n,\sin}\right) \tag{139}$$

- First order:

$$-a^{1,\cos}\theta = -b^{1,\sin} + (\mathfrak{a}_1 - \mathfrak{a}_2) - a^0(\mathfrak{b}_1 - \mathfrak{b}_2) + \frac{(\mathfrak{b}_1 - \mathfrak{b}_2)}{2}\left[a^{2,\cos} + \beta\left(a^{n+1,\cos} - a^{n-1,\cos}\right)\right] \tag{140}$$

$$b^{1,\sin}\theta = -a^{1,\cos} - \frac{(\mathfrak{b}_1 - \mathfrak{b}_2)}{2}\left[b^{2,\sin} + \beta\left(b^{n+1,\sin} + b^{n-1,\sin}\right)\right] \tag{141}$$

- Order $2 \leq i \leq n-1$:

$$a^{i,\cos}i\theta = b^{i,\sin} + \frac{(\mathfrak{b}_1 - \mathfrak{b}_2)}{2}\left[\left(a^{i-1,\cos} - a^{i+1,\cos}\right) + \beta\left(a^{n-i,\cos} - a^{n+i,\cos}\right)\right] \tag{142}$$

$$b^{i,\sin}i\theta = -a^{i,\cos} - \frac{(\mathfrak{b}_1 - \mathfrak{b}_2)}{2}\left[\left(b^{i+1,\sin} - b^{i-1,\sin}\right) + \beta\left(b^{n+i,\sin} + b^{n-i,\sin}\right)\right] \tag{143}$$

- n$^{\text{th}}$ order:

$$-a^{n,\cos}n\theta = -b^{n,\sin} + \beta(\mathfrak{a}_1 - \mathfrak{a}_2) - \beta a^0(\mathfrak{b}_1 - \mathfrak{b}_2) + \frac{(\mathfrak{b}_1 - \mathfrak{b}_2)}{2}\left[\beta a^{2n,\cos} + \left(a^{n+1,\cos} - a^{n-1,\cos}\right)\right] \tag{144}$$

$$b^{n,\sin}n\theta = -a^{n,\cos} - \frac{(\mathfrak{b}_1 - \mathfrak{b}_2)}{2}\left[\beta b^{2n,\sin} + \left(b^{n+1,\sin} - b^{n-1,\sin}\right)\right] \tag{145}$$

- Order $n+1 \leq i \leq +\infty$:

$$a^{i,\cos}i\theta = b^{i,\sin} + \frac{(\mathfrak{b}_1 - \mathfrak{b}_2)}{2}\left[\left(a^{i-1,\cos} - a^{i+1,\cos}\right) + \beta\left(a^{i-n,\cos} - a^{i+n,\cos}\right)\right] \tag{146}$$

$$b^{i,\sin}i\theta = -a^{i,\cos} - \frac{(\mathfrak{b}_1 - \mathfrak{b}_2)}{2}\left[\left(b^{i+1,\sin} - b^{i-1,\sin}\right) + \beta\left(b^{i+n,\sin} - b^{i-n,\sin}\right)\right] \tag{147}$$

from which we retrieved the expressions of the concentrations in 1 and 2 using Eqs.(62–67).

For each reversibly photoswitchable fluorophore, we evaluated the n-dependence of the interference of the sinusoidal light modulation at the out of resonance angular frequency of modulation. To proceed, we only retained in Eqs.(139–147) the amplitudes $a^{i,\cos}$ and $b^{i,\sin}$ with $i = 0, 1, 2, n-1, n, n+1, 2n$. Indeed they *directly* originate from the linear and non-linear terms in Eq.(48) and were correspondingly expected to dominate the amplitude values of main Speed OPIOM interest.

The n-dependence of the analytically retrieved unknown parameters ($a^{i,\cos}$,$b^{i,\sin}$) with $i = 0, 1, 2, n-1, n, n+1, 2n$ is displayed in Supplementary Figure 15 for $4 \leq n \leq 500$ for a reversibly photoswitchable fluorophore exhibiting the

Dronpa-2 photochemical parameters (*vide infra*) when it is resonant at ω (Supplementary Figure 15a,c,e) or $n\omega$ (Supplementary Figure 15b,d,f) angular frequency of modulation. The corresponding parameters ($a^{i,\cos}$,$b^{i,\sin}$) are compared with the ones associated to the same reversibly photoswitchable fluorophore, when it is submitted to a large sinusoidal modulation of illumination at its resonant angular frequency of modulation.

As shown in Supplementary Figure 15, the Speed OPIOM-relevant amplitudes $a^{1,\cos}$ and $a^{n,\cos}$ exhibit orthogonal behavior as soon as $n \geq 10$: In an equimolar mixture of two reversibly photoswitchable fluorophores sharing identical resonance condition for the intensities I_1^0 and I_2^0 but different resonant modulation frequencies respectively equal to ω and $n\omega$, $a^{1,\cos}$ and $a^{n,\cos}$ would be respectively dominated by the species resonating at ω and $n\omega$. Moreover the values of $a^{1,\cos}$ and $a^{n,\cos}$ observed with sinusoidal modulation of large amplitude at two modulation frequencies, resonant and non-resonant, fairly compare with the values obtained with a large sinusoidal modulation of illumination at the single resonant angular frequency of modulation, which underlines the robustness of these observables.

The amplitudes of the observable $O_j(t)$ terms can be obtained from Eqs.(76,77,78,79). Then fluorescence emission $I_{\rm F}(t)$ is extracted from Eq.(80) by using the temporal dependence (136) of the exciting light source with $\omega_2 = n\omega_1$ and the expression of $O_j(t)$ given in Eq.(76). Upon retaining the dominating terms $\mathfrak{O}_{\mathfrak{j}}^{\mathfrak{o}}$, $\mathfrak{O}_{\mathfrak{j}}^{\mathfrak{i},\sin}$ and $\mathfrak{O}_{\mathfrak{j}}^{\mathfrak{i},\cos}$ in Eq.(76) with $i = 0, 1, 2, n-1, n, n+1, 2n$ and $j = 1, 2$, we derived

- Zeroth order:

$$\mathfrak{I}_{\rm F}^{\mathfrak{o}} = \left(\mathfrak{O}_{\mathfrak{1}}^{\mathfrak{o}} + \frac{\alpha}{2}\mathfrak{O}_{\mathfrak{1}}^{\mathfrak{1},\sin} + \frac{\alpha\beta}{2}\mathfrak{O}_{\mathfrak{1}}^{\mathfrak{n},\sin}\right) I_1^0 + \left(\mathfrak{O}_{\mathfrak{2}}^{\mathfrak{o}} - \frac{\alpha}{2}\mathfrak{O}_{\mathfrak{2}}^{\mathfrak{1},\sin} - \frac{\alpha\beta}{2}\mathfrak{O}_{\mathfrak{2}}^{\mathfrak{n},\sin}\right) I_2^0 \tag{148}$$

- First order:

$$\begin{aligned}
\mathfrak{I}_{\rm F}^{\mathfrak{1},\sin} &= \left[\mathfrak{O}_{\mathfrak{1}}^{\mathfrak{1},\sin} + \alpha\mathfrak{O}_{\mathfrak{1}}^{\mathfrak{o}} - \frac{\alpha}{2}\mathfrak{O}_{\mathfrak{1}}^{\mathfrak{2},\cos} + \frac{\alpha\beta}{2}\left(\mathfrak{O}_{\mathfrak{1}}^{\mathfrak{n}-\mathfrak{1},\cos} - \mathfrak{O}_{\mathfrak{1}}^{\mathfrak{n}+\mathfrak{1},\cos}\right)\right] I_1^0 \\
&\quad + \left[\mathfrak{O}_{\mathfrak{2}}^{\mathfrak{1},\sin} - \alpha\mathfrak{O}_{\mathfrak{2}}^{\mathfrak{o}} + \frac{\alpha}{2}\mathfrak{O}_{\mathfrak{2}}^{\mathfrak{2},\cos} + \frac{\alpha\beta}{2}\left(\mathfrak{O}_{\mathfrak{2}}^{\mathfrak{n}+\mathfrak{1},\cos} - \mathfrak{O}_{\mathfrak{2}}^{\mathfrak{n}-\mathfrak{1},\cos}\right)\right] I_2^0 \\
\mathfrak{I}_{\rm F}^{\mathfrak{1},\cos} &= \left[\mathfrak{O}_{\mathfrak{1}}^{\mathfrak{1},\cos} + \frac{\alpha}{2}\mathfrak{O}_{\mathfrak{1}}^{\mathfrak{2},\sin} + \frac{\alpha\beta}{2}\left(\mathfrak{O}_{\mathfrak{1}}^{\mathfrak{n}+\mathfrak{1},\sin} + \mathfrak{O}_{\mathfrak{1}}^{\mathfrak{n}-\mathfrak{1},\sin}\right)\right] I_1^0 \\
&\quad + \left[\mathfrak{O}_{\mathfrak{2}}^{\mathfrak{1},\cos} - \frac{\alpha}{2}\mathfrak{O}_{\mathfrak{2}}^{\mathfrak{2},\sin} - \frac{\alpha\beta}{2}\left(\mathfrak{O}_{\mathfrak{2}}^{\mathfrak{n}+\mathfrak{1},\sin} + \mathfrak{O}_{\mathfrak{2}}^{\mathfrak{n}-\mathfrak{1},\sin}\right)\right] I_2^0
\end{aligned} \tag{149}$$

- Second order:

$$\mathfrak{I}_{\rm F}^{\mathfrak{2},\sin} = \left(\mathfrak{O}_{\mathfrak{1}}^{\mathfrak{2},\sin} + \frac{\alpha}{2}\mathfrak{O}_{\mathfrak{1}}^{\mathfrak{1},\cos}\right) I_1^0 + \left(\mathfrak{O}_{\mathfrak{2}}^{\mathfrak{2},\sin} - \frac{\alpha}{2}\mathfrak{O}_{\mathfrak{2}}^{\mathfrak{1},\cos}\right) I_2^0 \tag{150}$$

$$\mathfrak{I}_{\rm F}^{\mathfrak{2},\cos} = \left(\mathfrak{O}_{\mathfrak{1}}^{\mathfrak{2},\cos} - \frac{\alpha}{2}\mathfrak{O}_{\mathfrak{1}}^{\mathfrak{1},\sin}\right) I_1^0 + \left(\mathfrak{O}_{\mathfrak{2}}^{\mathfrak{2},\cos} + \frac{\alpha}{2}\mathfrak{O}_{\mathfrak{2}}^{\mathfrak{1},\sin}\right) I_2^0 \tag{151}$$

- $(n-1)^{\text{th}}$ order:

$$\mathfrak{I}_{\rm F}^{\mathfrak{n}-\mathfrak{1},\sin} = \left(\mathfrak{O}_{\mathfrak{1}}^{\mathfrak{n}-\mathfrak{1},\sin} - \frac{\alpha}{2}\mathfrak{O}_{\mathfrak{1}}^{\mathfrak{n},\cos} + \frac{\alpha\beta}{2}\mathfrak{O}_{\mathfrak{1}}^{\mathfrak{1},\cos}\right) I_1^0 + \left(\mathfrak{O}_{\mathfrak{2}}^{\mathfrak{n}-\mathfrak{1},\sin} + \frac{\alpha}{2}\mathfrak{O}_{\mathfrak{2}}^{\mathfrak{n},\cos} - \frac{\alpha\beta}{2}\mathfrak{O}_{\mathfrak{2}}^{\mathfrak{1},\cos}\right) I_2^0 \tag{152}$$

$$\mathfrak{I}_{\rm F}^{\mathfrak{n}-\mathfrak{1},\cos} = \left(\mathfrak{O}_{\mathfrak{1}}^{\mathfrak{n}-\mathfrak{1},\cos} + \frac{\alpha}{2}\mathfrak{O}_{\mathfrak{1}}^{\mathfrak{n},\sin} + \frac{\alpha\beta}{2}\mathfrak{O}_{\mathfrak{1}}^{\mathfrak{1},\sin}\right) I_1^0 + \left(\mathfrak{O}_{\mathfrak{2}}^{\mathfrak{n}-\mathfrak{1},\cos} - \frac{\alpha}{2}\mathfrak{O}_{\mathfrak{2}}^{\mathfrak{n},\sin} - \frac{\alpha\beta}{2}\mathfrak{O}_{\mathfrak{2}}^{\mathfrak{1},\sin}\right) I_2^0 \tag{153}$$

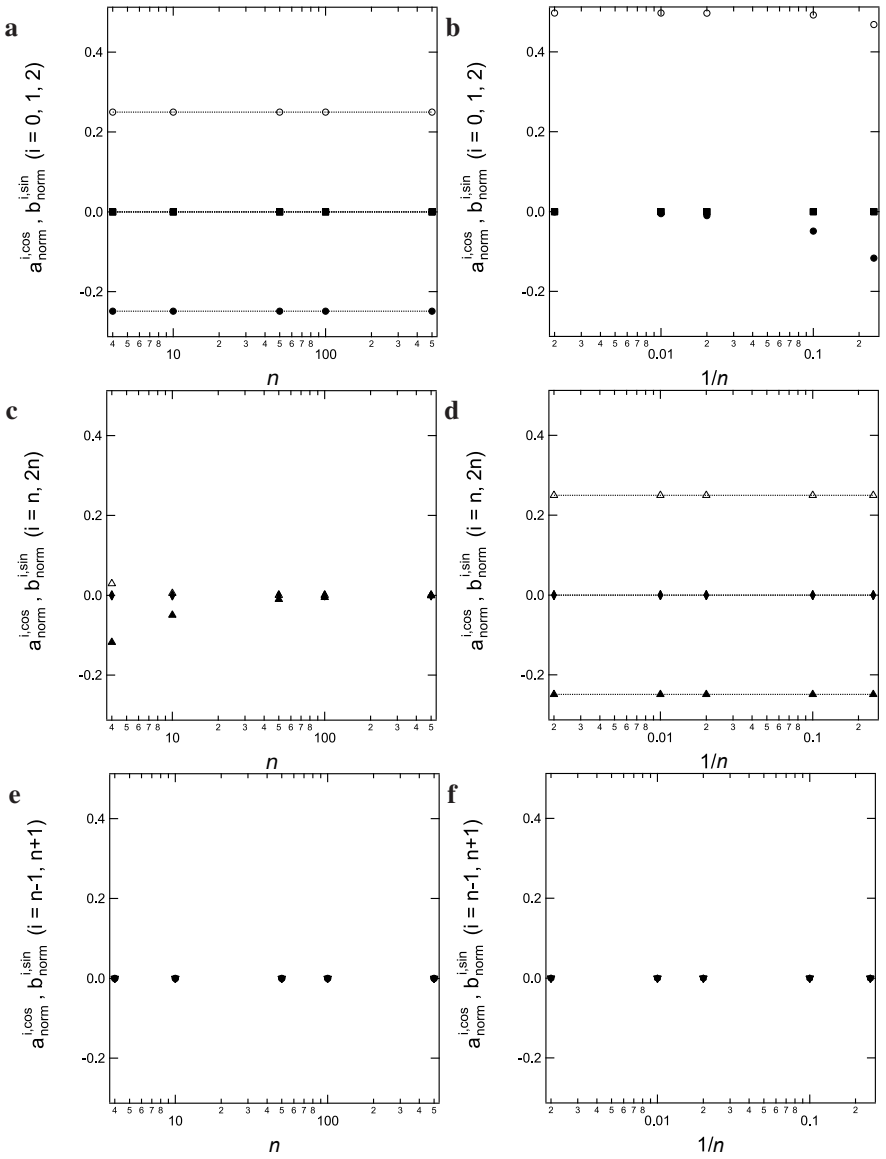

Supplementary Figure 15: Computation of the amplitudes of the Fourier terms, $a^{i,\cos}_{\rm norm} = a^{i,\cos}/P_{\rm tot}$ (filled markers) and $b^{i,\sin}_{\rm norm} = b^{i,\sin}/P_{\rm tot}$ (empty markers) ($i = 0$ (stars), 1 (circles), 2 (squares), $n-1$ (hexagons), n (triangles up), $n+1$ (triangles down), $2n$ (diamonds)), for a reversibly photoswitchable fluorophore $1 \rightleftharpoons 2$ submitted to superposition of light harmonic forcing at two modulation frequencies ω and $n\omega$ given in Eq.(136) (α = 0.5, $\beta = 1$) upon fulfilling the resonance condition (101) for the intensities I_1^0 and I_2^0. The computed parameters ($a^{i,\cos}$, $b^{i,\sin}$) obtained for the reversibly photoswitchable fluorophore under identical resonance condition for the intensities I_1^0 and I_2^0, when it is submitted to a large sinusoidal modulation of illumination at its single resonant angular frequency of modulation are shown as dotted lines. $\sigma_{12,1}$ = 196 m^2 mol^{-1}, $\sigma_{21,1}$ = 0 m^2 mol^{-1}, $\sigma_{12,2}$ = 0 m^2 mol^{-1}, $\sigma_{21,2}$ = 413 m^2 mol^{-1}, $k_{21}^{\Delta} = 1.4 \times 10^{-2}$ s^{-1}; $I_1^0 = 100\frac{k_{21}^{\Delta}}{\sigma_{12,1}+\sigma_{21,1}}$, and $I_2^0 = 3.3\times10^{-3}$ Ein s^{-1} m^{-2}. The resonant angular frequency of modulation for the considered reversibly photoswitchable fluorophore equal to 2.78 rad s^{-1} is ω (**a**, **c**, **e**) or $n\omega$ (**b**, **d**, **f**) to cover both cases when the non-resonant frequency is either larger (**a**, **c**, **e**) or smaller (**b**, **d**, **f**) than the resonant one.

- n^{th} order:

$$\begin{aligned}
\mathfrak{I}_{\mathrm{F}}^{\mathfrak{n},\sin} &= \left[\mathfrak{O}_{\mathfrak{1}}^{\mathfrak{n},\sin} + \alpha\beta\mathfrak{O}_{\mathfrak{1}}^{\mathfrak{o}} + \frac{\alpha}{2}\left(\mathfrak{O}_{\mathfrak{1}}^{\mathfrak{n}-\mathfrak{1},\cos} - \mathfrak{O}_{\mathfrak{1}}^{\mathfrak{n}+\mathfrak{1},\cos}\right) - \frac{\alpha\beta}{2}\mathfrak{O}_{\mathfrak{1}}^{\mathfrak{2n},\cos}\right] I_1^0 \\
&+ \left[\mathfrak{O}_{\mathfrak{2}}^{\mathfrak{n},\sin} - \alpha\beta\mathfrak{O}_{\mathfrak{2}}^{\mathfrak{o}} + \frac{\alpha}{2}\left(\mathfrak{O}_{\mathfrak{2}}^{\mathfrak{n}+\mathfrak{1},\cos} - \mathfrak{O}_{\mathfrak{2}}^{\mathfrak{n}-\mathfrak{1},\cos}\right) + \frac{\alpha\beta}{2}\mathfrak{O}_{\mathfrak{2}}^{\mathfrak{2n},\cos}\right] I_2^0 \\
\mathfrak{I}_{\mathrm{F}}^{\mathfrak{n},\cos} &= \left[\mathfrak{O}_{\mathfrak{1}}^{\mathfrak{n},\cos} - \frac{\alpha}{2}\mathfrak{O}_{\mathfrak{1}}^{\mathfrak{n}-\mathfrak{1},\sin} + \frac{\alpha\beta}{2}\left(\mathfrak{O}_{\mathfrak{1}}^{\mathfrak{2n},\sin} + \mathfrak{O}_{\mathfrak{1}}^{\mathfrak{n}+\mathfrak{1},\sin}\right)\right] I_1^0 \\
&+ \left[\mathfrak{O}_{\mathfrak{2}}^{\mathfrak{n},\cos} + \frac{\alpha}{2}\mathfrak{O}_{\mathfrak{2}}^{\mathfrak{n}-\mathfrak{1},\sin} - \frac{\alpha\beta}{2}\left(\mathfrak{O}_{\mathfrak{2}}^{\mathfrak{2n},\sin} + \mathfrak{O}_{\mathfrak{2}}^{\mathfrak{n}+\mathfrak{1},\sin}\right)\right] I_2^0
\end{aligned} \tag{154}$$

- $(n+1)^{\text{th}}$ order:

$$\mathfrak{I}_{\mathrm{F}}^{\mathfrak{n}+\mathfrak{1},\sin} = \left(\mathfrak{O}_{\mathfrak{1}}^{\mathfrak{n}+\mathfrak{1},\sin} + \frac{\alpha}{2}\mathfrak{O}_{\mathfrak{1}}^{\mathfrak{n},\cos} + \frac{\alpha\beta}{2}\mathfrak{O}_{\mathfrak{1}}^{\mathfrak{1},\cos}\right) I_1^0 + \left(\mathfrak{O}_{\mathfrak{2}}^{\mathfrak{n}+\mathfrak{1},\sin} - \frac{\alpha}{2}\mathfrak{O}_{\mathfrak{2}}^{\mathfrak{n},\cos} - \frac{\alpha\beta}{2}\mathfrak{O}_{\mathfrak{2}}^{\mathfrak{1},\cos}\right) I_2^0 \tag{155}$$

$$\mathfrak{I}_{\mathrm{F}}^{\mathfrak{n}+\mathfrak{1},\cos} = \left(\mathfrak{O}_{\mathfrak{1}}^{\mathfrak{n}+\mathfrak{1},\cos} - \frac{\alpha}{2}\mathfrak{O}_{\mathfrak{1}}^{\mathfrak{n},\sin} - \frac{\alpha\beta}{2}\mathfrak{O}_{\mathfrak{1}}^{\mathfrak{1},\sin}\right) I_1^0 + \left(\mathfrak{O}_{\mathfrak{2}}^{\mathfrak{n}+\mathfrak{1},\cos} + \frac{\alpha}{2}\mathfrak{O}_{\mathfrak{2}}^{\mathfrak{n},\sin} + \frac{\alpha\beta}{2}\mathfrak{O}_{\mathfrak{2}}^{\mathfrak{1},\sin}\right) I_2^0 \tag{156}$$

- $2n^{\text{th}}$ order:

$$\mathfrak{I}_{\mathrm{F}}^{\mathfrak{2n},\sin} = \left(\mathfrak{O}_{\mathfrak{1}}^{\mathfrak{2n},\sin} + \frac{\alpha\beta}{2}\mathfrak{O}_{\mathfrak{1}}^{\mathfrak{n},\cos}\right) I_1^0 + \left(\mathfrak{O}_{\mathfrak{2}}^{\mathfrak{2n},\sin} - \frac{\alpha\beta}{2}\mathfrak{O}_{\mathfrak{2}}^{\mathfrak{n},\cos}\right) I_2^0 \tag{157}$$

$$\mathfrak{I}_{\mathrm{F}}^{\mathfrak{2n},\cos} = \left(\mathfrak{O}_{\mathfrak{1}}^{\mathfrak{2n},\cos} - \frac{\alpha\beta}{2}\mathfrak{O}_{\mathfrak{1}}^{\mathfrak{n},\sin}\right) I_1^0 + \left(\mathfrak{O}_{\mathfrak{2}}^{\mathfrak{2n},\cos} + \frac{\alpha\beta}{2}\mathfrak{O}_{\mathfrak{2}}^{\mathfrak{n},\sin}\right) I_2^0 \tag{158}$$

The n-dependence of the analytically retrieved unknown parameters ($\mathfrak{I}_{\mathrm{F}}^{\mathfrak{i},\sin}$,$\mathfrak{I}_{\mathrm{F}}^{\mathfrak{i},\cos}$) with $i = 0, 1, 2, n-1, n, n+1, 2n$ is displayed in Supplementary Figure 16 for $4 \leq n \leq 500$ for a reversibly photoswitchable fluorophore exhibiting the Dronpa-2 photochemical parameters (*vide infra*) when it is resonant at ω (Supplementary Figure 16a,c,e) or $n\omega$ (Supplementary Figure 16b,d,f) angular frequency of modulation. The corresponding parameters ($\mathfrak{I}_{\mathrm{F}}^{\mathfrak{i},\sin}$,$\mathfrak{I}_{\mathrm{F}}^{\mathfrak{i},\cos}$) are compared with the ones associated to the same reversibly photoswitchable fluorophore, when it is submitted to a large sinusoidal modulation of illumination at its resonant angular frequency of modulation.

Supplementary Figure 17 further compares the dependence of the absolute value of the normalized out-of-phase first-order amplitudes $\mid \mathfrak{I}_{\mathrm{F,norm}}^{\mathfrak{1},\cos} \mid = \mid \mathfrak{I}_{\mathrm{F}}^{\mathfrak{1},\cos}/\{[(Q_{2,1}-Q_{1,1})I_1^0 + (Q_{2,2}-Q_{1,2})I_2^0]\alpha P_{\mathrm{tot}}\} \mid$ and $\mid \mathfrak{I}_{\mathrm{F,norm}}^{\mathfrak{n},\cos} \mid = \mid \mathfrak{I}_{\mathrm{F}}^{\mathfrak{n},\cos}/\{[(Q_{2,1}-Q_{1,1})I_1^0 + (Q_{2,2}-Q_{1,2})I_2^0]\alpha P_{\mathrm{tot}}\} \mid$ on I_2^0/I_1^0 and ω/I_1^0 in the case of a reversibly photoswitchable fluorophore submitted to the sinusoidal modulation of large amplitude at two modulation frequencies ω and $n\omega$ ($n = 10$, $\alpha = 0.5$ and $\beta = 1$) with that obtained for a large sinusoidal modulation of illumination at a single angular frequency of modulation for the same α value. The position of the optimum is similar in both cases: using $I_1^0 = 100\frac{k_{21}^{\Delta}}{\sigma_{12,1}+\sigma_{21,1}}$, we found $I_2^{0,R} = 3.5 \times 10^{-3}$ Ein s^{-1} m^{-2}, $\omega^R = 2.87$ rad s^{-1} for $\mid \mathfrak{I}_{\mathrm{F,norm}}^{\mathfrak{1},\cos} \mid$ and $I_2^{0,R} = 5.0 \times 10^{-3}$ Ein s^{-1} m^{-2}, $n\omega^R = 33,2$ rad s^{-1} for $\mid \mathfrak{I}_{\mathrm{F,norm}}^{\mathfrak{n},\cos} \mid$ in the case of the sinusoidal modulation of large amplitude at two modulation frequencies, and $I_2^{0,R} = 3.5 \times 10^{-3}$ Ein s^{-1} m^{-2}, $\omega^R = 2.87$ rad s^{-1} for $\mid \mathfrak{I}_{\mathrm{F,norm}}^{\mathfrak{1},\cos} \mid$ and $I_2^{0,R} = 3.5 \times 10^{-3}$ Ein s^{-1} m^{-2}, $\omega^R = 28.7$ rad s^{-1} for $\mid \mathfrak{I}_{\mathrm{F,norm}}^{\mathfrak{n},\cos} \mid$ in the case of a large sinusoidal modulation of illumination at a single angular frequency of modulation. The amplitudes of the optimum fairly compare as well: we computed $\mid \mathfrak{I}_{\mathrm{F,norm}}^{\mathfrak{1},\cos} \mid = 2.49 \times 10^{-1}$ and $\mid \mathfrak{I}_{\mathrm{F,norm}}^{\mathfrak{n},\cos} \mid = 2.55 \times 10^{-1}$ for the dual frequency modulation, and $\mid \mathfrak{I}_{\mathrm{F,norm}}^{\mathfrak{1},\cos} \mid = 2.49 \times 10^{-1}$ and $\mid \mathfrak{I}_{\mathrm{F,norm}}^{\mathfrak{n},\cos} \mid = 2.49 \times 10^{-1}$ for the single frequency modulation.

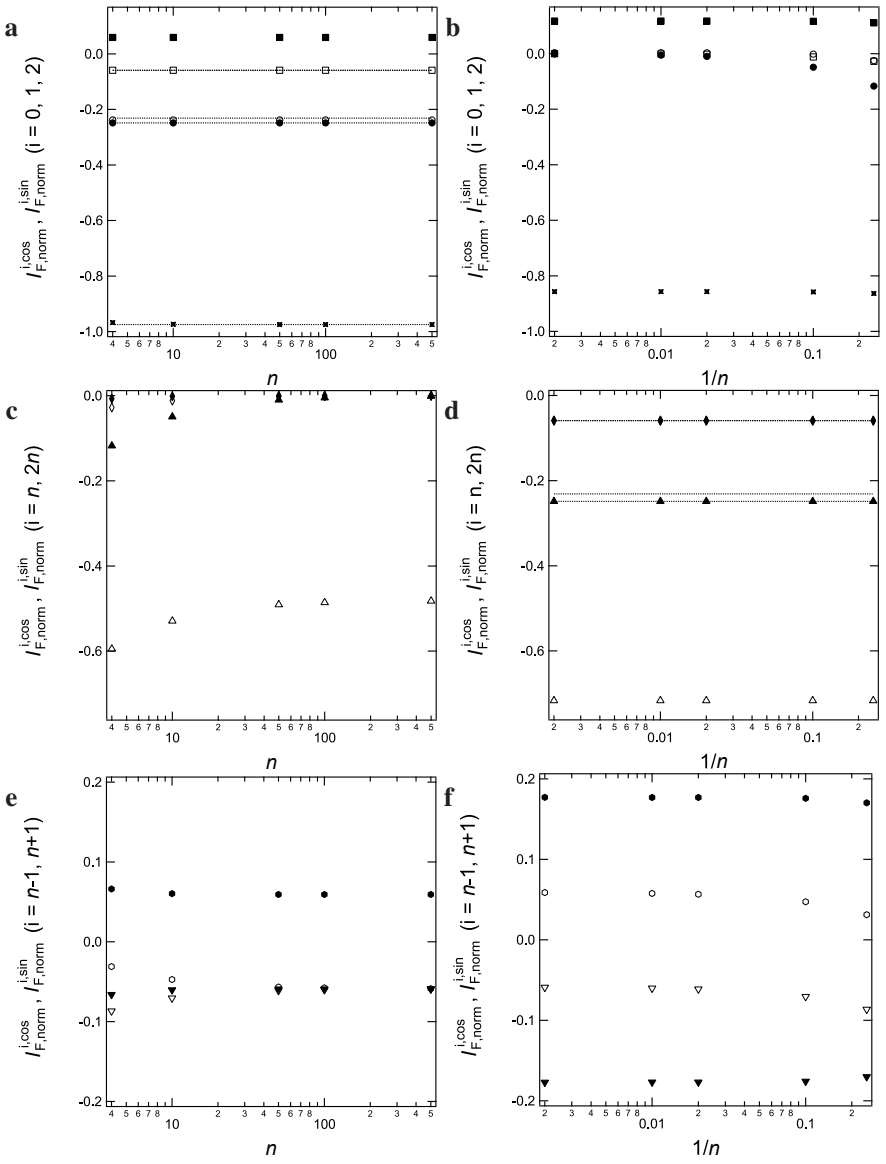

Supplementary Figure 16: Computation of the amplitudes of the Fourier terms, $\mathfrak{I}^{\mathrm{i,sin}}_{\mathrm{F,norm}}$ (empty markers) and $\mathfrak{I}^{\mathrm{i,cos}}_{\mathrm{F,norm}}$ (filled markers) ($i = 0$ (stars), 1 (circles) , 2 (squares), $n - 1$ (hexagons), n (triangles up), $n + 1$ (triangles down), $2n$ (diamonds)), for a reversibly photoswitchable fluorophore $1 \rightleftharpoons 2$ submitted to superposition of light harmonic forcing at two modulation frequencies ω and $n\omega$ given in Eq.(136) (α = 0.5, $\beta = 1$) upon fulfilling the resonance condition (101) for the intensities I_1^0 and I_2^0. $Q_{2,1}/Q_{1,1} = 0.01$, $Q_{2,2}/Q_{1,2} = 0.01$, and $Q_{1,1}/Q_{1,2} = 15$; $\sigma_{12,1}$ = 196 m^2 mol^{-1}, $\sigma_{21,1}$ = 0 m^2 mol^{-1}, $\sigma_{12,2}$ = 0 m^2 mol^{-1}, $\sigma_{21,2}$ = 413 m^2 mol^{-1}, $k_{21}^{\Delta} = 1.4 \times 10^{-2}$ s^{-1}; $I_1^0 = 100\frac{k_{21}^{\Delta}}{\sigma_{12,1}+\sigma_{21,1}}$, $I_2^0 = 3.3 \times 10^{-3}$ Ein s^{-1} m^{-2}. The resonant angular frequency of modulation for the considered reversibly photoswitchable fluorophore equal to 2.78 rad s^{-1} is ω (**a**, **c**, **e**) or $n\omega$ (**b**, **d**, **f**) to cover both cases when the non-resonant frequency is either larger (**a**, **c**, **e**) or smaller (**b**, **d**, **f**) than the resonant one.

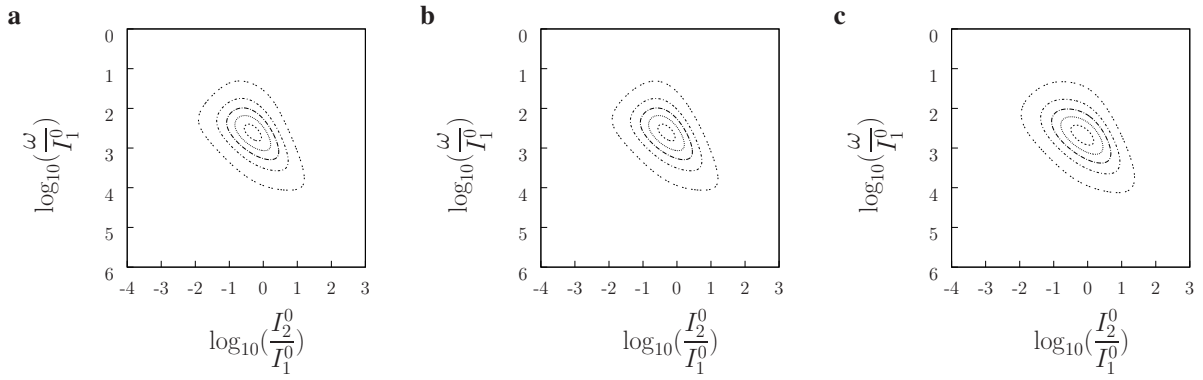

Supplementary Figure 17: Theoretical dependence of the absolute value of the normalized amplitude of the out-of-phase oscillation of fluorescence intensity, $\mid \Im_{\mathrm{F,norm}}^{1,\cos} \mid = \mid \Im_{\mathrm{F}}^{1,\cos}/\{[(Q_{2,1}-Q_{1,1})I_1^0+(Q_{2,2}-Q_{1,2})I_2^0]\alpha P_{\mathrm{tot}}\} \mid$, for a reversibly photoswitchable fluorophore $1 \rightleftharpoons 2$ resonant at angular frequency of modulation ω (**a**,**b**) or $n\omega$ (**c**) and submitted to modulated illumination given in Eq.(136) with $\omega_2 = n\omega_1$ (**a**,**c**) or Eq.(122) (**b**) on I_2^0/I_1^0 and ω/I_1^0 (in rad Ein^{-1} m^2). $I_1^0 = 100\frac{k_{21}^{\Delta}}{\sigma_{12,1}+\sigma_{21,1}}$; $Q_{2,1}/Q_{1,1} = 0.01$, $Q_{2,2}/Q_{1,2} = 0.01$, and $Q_{1,1}/Q_{1,2} = 15$; $n = 10$, α = 0.5, $\beta = 1$, $\sigma_{12,1}$ = 196 m^2 mol^{-1}, $\sigma_{21,1}$ = 0 m^2 mol^{-1}, $\sigma_{12,2}$ = 0 m^2 mol^{-1}, $\sigma_{21,2}$ = 413 m^2 mol^{-1}, $k_{21}^{\Delta} = 1.4 \times 10^{-2}$ s^{-1}. The markers correspond to isodensity curves : 0.03 (double-dash), 0.08 (dot small dash), 0.13 (dot long dash), 0.18 (dot) and 0.23 (dash). Note that the theoretical dependence of the absolute value of the normalized amplitude of the out-of-phase oscillation of fluorescence intensity, $\mid \Im_{\mathrm{F,norm}}^{1,\cos} \mid = \mid \Im_{\mathrm{F}}^{1,\cos}/\{[(Q_{2,1}-Q_{1,1})I_1^0+(Q_{2,2}-Q_{1,2})I_2^0]\alpha P_{\mathrm{tot}}\} \mid$, for a reversibly photoswitchable fluorophore $1 \rightleftharpoons 2$ resonant at angular frequency of modulation $n\omega$ and submitted to modulated illumination given in Eq.(122) on I_2^0/I_1^0 and ω/I_1^0 is the same as displayed in **b**.

Supplementary Figures 16 and 17 show that the amplitudes $\Im_{\mathrm{F}}^{1,\cos}$ and $\Im_{\mathrm{F}}^{\mathrm{n},\cos}$ observed with sinusoidal modulation of large amplitude at two modulation frequencies fairly compare with the values obtained with a large sinusoidal modulation of illumination at a single angular frequency of modulation as soon as $n \geq 10$. Hence, it is possible to perform simultaneous and selective imaging of two different reversibly photoswitchable fluorescent proteins provided that they share identical resonance conditions for the intensities I_1^0 and I_2^0 but resonant modulation frequencies differing by at least one order of magnitude.

Retrieval of concentrations from the fluorescence intensity

Extraction of $\Im_{\mathrm{F}}^{\circ}$, $\Im_{\mathrm{F}}^{1,\sin}$, $\Im_{\mathrm{F}}^{1,\cos}$ from the overall signal $I_{\mathrm{F}}(t)$

In the cases experimentally addressed in this manuscript, the fluorescence intensity associated to the photoswitchable probe adopts the general expression (80) by modulating light. $\Im_{\mathrm{F}}^{\circ}$, $\Im_{\mathrm{F}}^{1,\sin}$, and $\Im_{\mathrm{F}}^{1,\cos}$ can be easily retrieved from the experimental trace of the observed signal $I_{\mathrm{F}}(t)$ (either global or from each analyzed pixel).

$\Im_{\mathrm{F}}^{\circ}$ can be obtained upon averaging $I_{\mathrm{F}}(t)$ over an integer number k of the period $T = 2\pi/\omega$ of the modulated illumination

$$Int^0 = \frac{1}{kT}\int_0^{kT} I_{\mathrm{F}}(t)dt = \Im_{\mathrm{F}}^{\circ}. \tag{159}$$

The first-order amplitudes $\mathfrak{I}_{\rm F}^{1,\sin}$ and $\mathfrak{I}_{\rm F}^{1,\cos}$ can be extracted from the fluorescence signal upon computing the integrals $Int^{1,\sin}$ and $Int^{1,\cos}$

$$Int^{1,\sin} = \frac{2}{kT}\int_0^{kT} I_{\rm F}(t)\sin(\omega t)\,dt = \mathfrak{I}_{\rm F}^{1,\sin} \quad (160)$$

$$Int^{1,\cos} = \frac{2}{kT}\int_0^{kT} I_{\rm F}(t)\cos(\omega t)\,dt = \mathfrak{I}_{\rm F}^{1,\cos}. \quad (161)$$

Eqs.(160,161) illustrate orthogonality between the various components of the fluorescence intensity in Eq. (80). In particular, the computed integral $Int^{1,\cos}$ used to extract the Speed OPIOM image does not contain any contribution from the constant amplitude $\mathfrak{I}_{\rm F}^{\circ}$ as well as from the in-phase amplitude $\mathfrak{I}_{\rm F}^{1,\sin}$. This mathematical property is crucial to eliminate the contributions of non-photoactive fluorescent interfering species, which fluorescence response contains constant and in-phase terms only.

Quantifying a targeted photoswitchable probe

In the presence of light modulation, $\mathfrak{I}_{\rm F}^{1,\cos}$ can be reliably evaluated from its expression in the case of a sinusoidal light modulation of small amplitude given in Eqs.(97,100). However this approach requires the effort to acquire the values of all parameters involved in this expression. Alternatively, quantification can proceed by calibration with the pure reversibly photoswitchable probe at a reference concentration. Eq.(97,100) shows that $\mathfrak{I}_{\rm F}^{1,\cos}$ is proportional to the overall concentration in reversibly photoswitchable probe. Thus quantification can be simply achieved by recording the fluorescence intensity from a calibrating solution of the reversibly photoswitchable probe at a known concentration $P_{\rm tot}^{\rm cal}$. The concentration of the reversibly photoswitchable probe, which is retrieved at first-order is

$$P_{\rm tot}^{1,\cos} = \frac{\mathfrak{I}_{\rm F}^{1,\cos}}{\mathfrak{I}_{\rm F}^{1,\cos,{\rm cal}}} P_{\rm tot}^{\rm cal}. \quad (162)$$

Supplementary Note 2: Determination of the RSFP kinetic parameters

The photochemical behavior of the RSFPs has been already extensively investigated.[8]–[19] At short time scales, the detailed mechanisms involved in the photoisomerization process are quite complex and not yet fully established. In the present study, we did not attempt to bring any additional mechanistic information. In contrast, we aimed at building two-state models relevant to account for the dynamic behavior of the investigated RSFP at the second time scale in the physiological pH range.

We applied cycles of photoisomerization on RSFP solutions at micromolar concentrations in Britton-Robinson pH 7.5 buffer[20] (acetic acid: 4 mM; phosphoric acid: 4 mM; AMPSO: 4 mM). The solutions have been illuminated at 480 nm at constant light intensity up to the photosteady state upon recording the temporal evolution of the fluorescence emission at 522 nm. Then the solutions were submitted to a 405 nm light source at constant light intensity upon recording again the temporal evolution of the fluorescence emission at 522 nm. This series of experiments has been reproduced at various light intensities (Supplementary Figures 18–25).

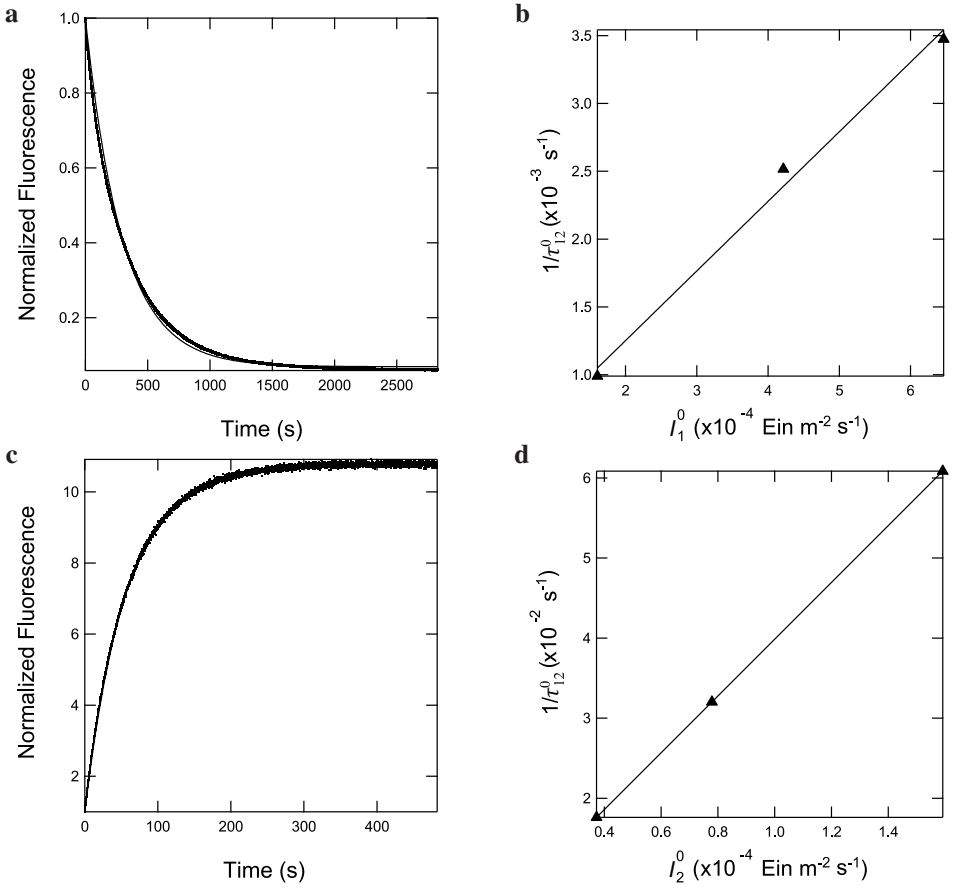

Supplementary Figure 18: Photoisomerization kinetics of Dronpa. **a**,**c**: Temporal evolution of the normalized fluorescence emission at 522 nm of Dronpa solutions (10 µM) upon illumination at 480 (**a**: I_1^0 = 6.4×10^{-4} Ein s^{-1} m^{-2}) and 405 and 480 (**c**: I_1^0 = 6.4×10^{-4} Ein s^{-1} m^{-2}, I_2^0 = 3.7×10^{-5} Ein s^{-1} m^{-2}) nm. The exponential fits with Eqs.(25) (**a**) and (39) (**c**) are shown as solid lines; **b**,**d**: Dependence of the inverse of the relaxation time $1/\tau_{12}^0$ on the light intensities I_1^0 (**b**, refering to $1/\tau_{12}^{0,1}$) and I_2^0 (**d**, refering to $1/\tau_{12}^{0,2}$). Linear fit (solid line) enables to extract $\sigma_{\overline{12},480} + \sigma_{\overline{21},480}$ from the slope and an order of magnitude of $k^{\Delta}_{\overline{21}}$ from the value on the y-axis for $I_1^0 = 0$ (**b**) and $\sigma_{\overline{12},405} + \sigma_{\overline{21},405}$ from the slope (**d**). $T = 37°$C in pH 7.5 buffer.

Analyses of the relaxation times associated to photoisomerizations at 480 nm

At pH 7.5, the temporal evolution of the fluorescence emission of the 480 nm-illuminated solutions was shown to satisfactorily obey the exponential behaviour predicted in Eq.(25) for all the investigated RSFPs and at all studied 480 nm light intensities (Supplementary Figures 18–25). We correspondingly extracted from a global fit:

- The relaxation time $\tau_{12}^{0,1}$ from the curvature of the temporal evolution. Then we used its linear dependence on light intensity I_1^0 given in Eq.(163) derived from Eq.(18)

$$\frac{1}{\tau_{12}^{0,1}} = \left(\sigma_{\overline{12},1} + \sigma_{\overline{21},1}\right) I_1^0 + k^{\Delta}_{\overline{21}} \tag{163}$$

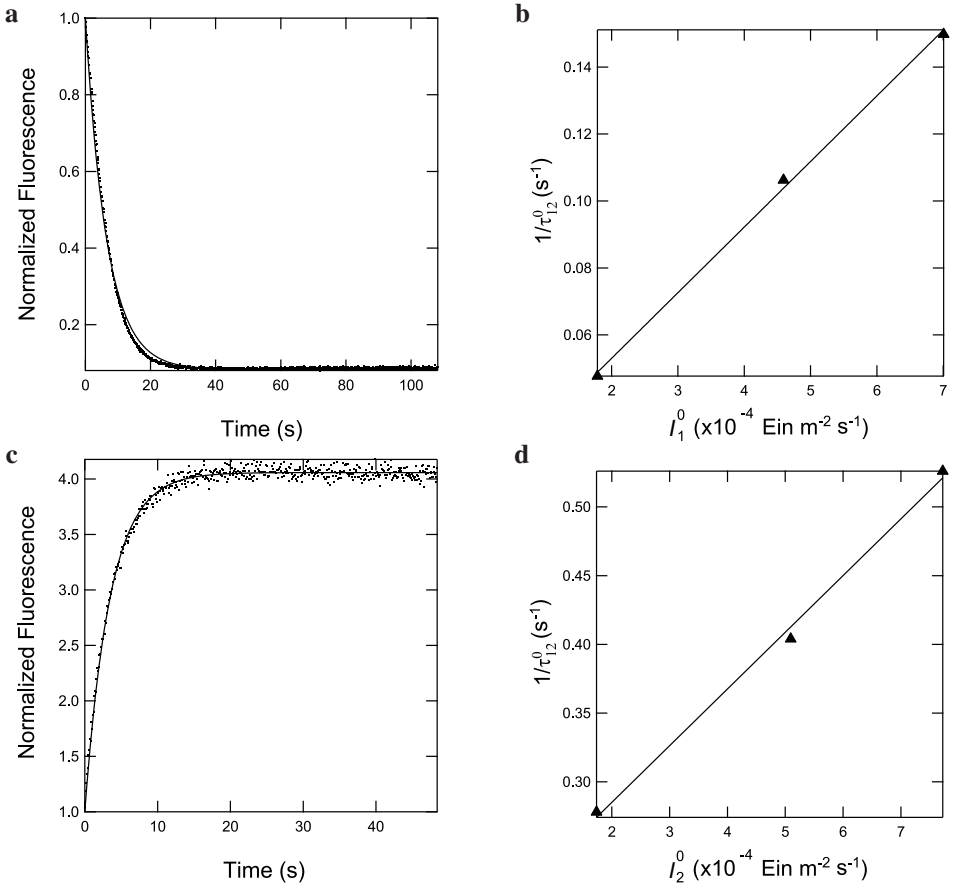

Supplementary Figure 19: Photoisomerization kinetics of Dronpa-2. **a**,**c**: Temporal evolution of the normalized fluorescence emission at 522 nm of Dronpa-2 solutions (10 μM) upon illumination at 480 (**a**: I_1^0 = 7.0×10^{-4} Ein s^{-1} m^{-2}) and 405 and 480 (**c**: I_1^0 = 7.0×10^{-4} Ein s^{-1} m^{-2}, I_2^0 = 2.0×10^{-4} Ein s^{-1} m^{-2}) nm. The exponential fits with Eqs.(25) (**a**) and (39) (**c**) are shown as solid lines; **b**,**d**: Dependence of the inverse of the relaxation time $1/\tau_{12}^0$ on the light intensities I_1^0 (**b**, refering to $1/\tau_{12}^{0,1}$) and I_2^0 (**d**, refering to $1/\tau_{12}^{0,2}$). Linear fit (solid line) enables to extract $\sigma_{\overline{12},480} + \sigma_{\overline{21},480}$ from the slope and an order of magnitude of $k_{\overline{21}}^{\Delta}$ from the value on the y-axis for $I_1^0 = 0$ (**b**) and $\sigma_{\overline{12},405} + \sigma_{\overline{21},405}$ from the slope (**d**). $T = 37°$C in pH 7.5 buffer.

to extract $\sigma_{\overline{12},480} + \sigma_{\overline{21},480}$[2] and an order of magnitude of $k_{\overline{21}}^{\Delta}$;

- The relative brightness $Q_{\overline{2},480}/Q_{\overline{1},480}$ measured upon illuminating at 480 nm and collecting fluorescence at 522 nm, from the amplitude of the temporal evolution.

Supplementary Figures 18–25 display the results, which have been obtained for Dronpa, Dronpa-2, Dronpa-3, RS-FastLime, rsEFGP, rsEFGP2, Padron and Kohinoor. The values of the extracted photochemical and kinetic parameters are given in Supplementary Table 5 together with data from the literature.

[2]In this subsection, we overlined the states $\overline{1}$ and $\overline{2}$ to emphasize that the possibly pH dependent values of the cross section for photoisomerization, the rate constant for thermally-driven relaxation as well as the brightness have been measured at pH 7.5.

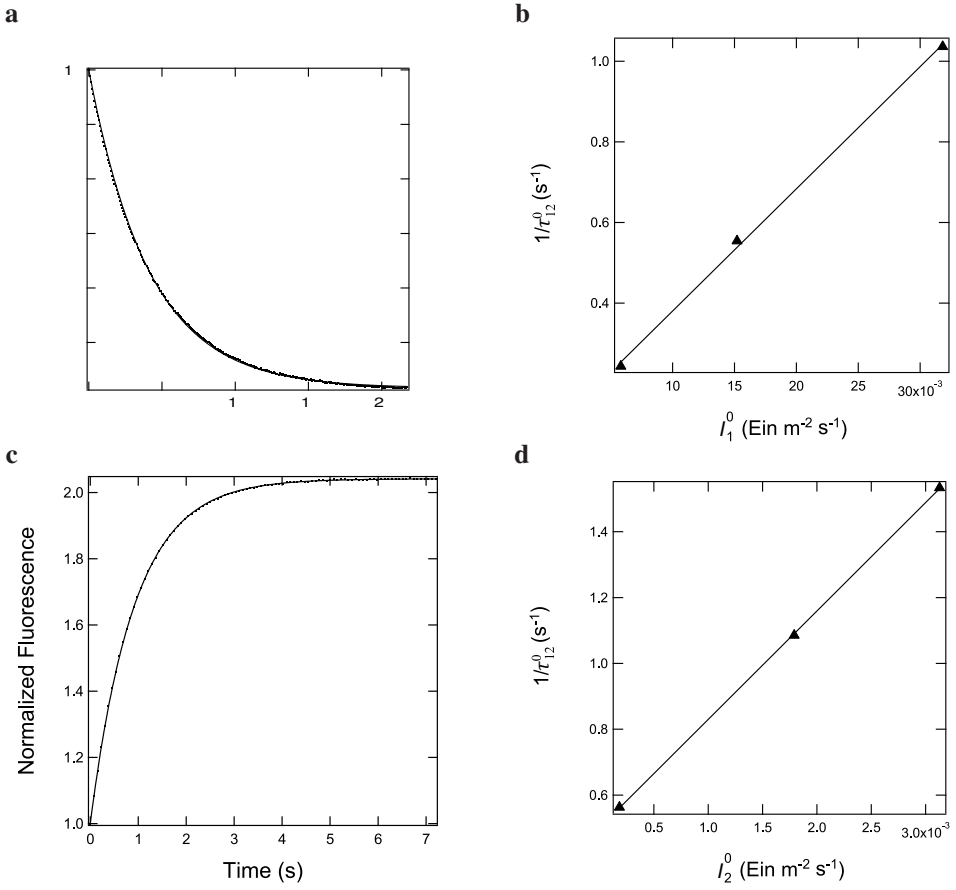

Supplementary Figure 20: Photoisomerization kinetics of Dronpa-3. **a**,**c**: Temporal evolution of the normalized fluorescence emission at 522 nm of Dronpa-3 solutions (10 µM) upon illumination at 480 (**a**: I_1^0 = 5.8×10^{-3} Ein s^{-1} m^{-2}) and 405 and 480 (**c**: I_1^0 = 1.5×10^{-2} Ein s^{-1} m^{-2}, I_2^0 = 1.8×10^{-3} Ein s^{-1} m^{-2}) nm. The exponential fits with Eqs.(25) (**a**) and (39) (**c**) are shown as solid lines; **b**,**d**: Dependence of the inverse of the relaxation time $1/\tau_{12}^0$ on the light intensities I_1^0 (**b**, refering to $1/\tau_{12}^{0,1}$) and I_2^0 (**d**, refering to $1/\tau_{12}^{0,2}$). Linear fit (solid line) enables to extract $\sigma_{\overline{12},480} + \sigma_{\overline{21},480}$ from the slope and an order of magnitude of $k_{\overline{21}}^{\Delta}$ from the value on the y-axis for $I_1^0 = 0$ (**b**) and $\sigma_{\overline{12},405} + \sigma_{\overline{21},405}$ from the slope (**d**). $T = 37°$C in pH 7.5 buffer.

Analyses of the relaxation times associated to photoisomerizations upon illumination at 405 and 480 nm

At pH 7.5, the temporal evolution of the fluorescence emission of the 405/488 nm-illuminated solutions was shown to satisfactorily obey the exponential behaviour given in Eq.(39) for all the investigated RSFPs and at all studied 405 nm light intensities (480 nm light intensity remaining fixed to a constant value). We correspondingly extracted from a global fit the relaxation time $\tau_{12}^{0,2}$ from the curvature of the temporal evolution. Then we used the linear dependence of its inverse value on light intensity I_2^0 given in Eq.(164) derived from Eq.(18)

$$\frac{1}{\tau_{12}^{0,2}} = \left(\sigma_{\overline{12},1} + \sigma_{\overline{21},1}\right) I_1^0 + \left(\sigma_{\overline{12},2} + \sigma_{\overline{21},2}\right) I_2^0 + k_{\overline{21}}^{\Delta} \tag{164}$$

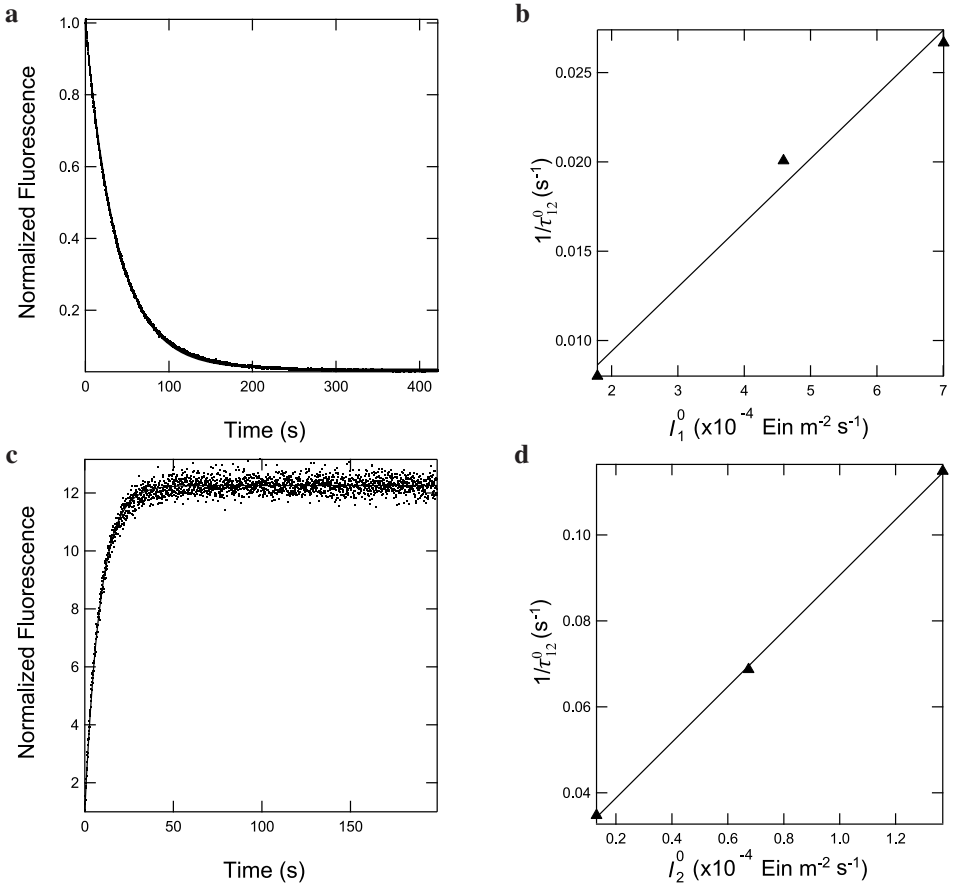

Supplementary Figure 21: Photoisomerization kinetics of rsFastLime. **a**,**c**: Temporal evolution of the normalized fluorescence emission at 522 nm of RSFastLime solutions (10 µM) upon illumination at 480 (**a**: $I_1^0 = 7.0\times10^{-4}$ Ein s^{-1} m^{-2}) and 405 and 480 (**c**: $I_1^0 = 7.0\times10^{-4}$ Ein s^{-1} m^{-2}, $I_2^0 = 1.4\times10^{-4}$ Ein s^{-1} m^{-2}) nm. The exponential fits with Eqs.(25) (**a**) and (39) (**c**) are shown as solid lines; **b**,**d**: Dependence of the inverse of the relaxation time $1/\tau_{12}^0$ on the light intensities I_1^0 (**b**, refering to $1/\tau_{12}^{0,1}$) and I_2^0 (**d**, refering to $1/\tau_{12}^{0,2}$). Linear fit (solid line) enables to extract $\sigma_{\overline{12},480} + \sigma_{\overline{21},480}$ from the slope and an order of magnitude of $k^{\Delta}_{\overline{21}}$ from the value on the y-axis for $I_1^0 = 0$ (**b**) and $\sigma_{\overline{12},405} + \sigma_{\overline{21},405}$ from the slope (**d**). $T = 37°$C in pH 7.5 buffer.

to extract $\sigma_{\overline{12},405} + \sigma_{\overline{21},405}$.[3,4] Supplementary Figures 18–25 display the results, which have been obtained for Dronpa, Dronpa-2, Dronpa-3, RSFastLime, rsEFGP, rsEFGP2, Padron and Kohinoor. The values of the extracted photochemical

[3]In view of literature analysis of the photoisomerization process for RSFPs,[8]–[17] we have considered for the numerical simulations that photoisomerization at 405 nm totally exhausted the 480 nm photoswitched-on state $\overline{2}$ so as to adopt

$$\sigma_{\overline{12},405} \sim 0 \text{ m}^2 \text{ mol}^{-1}. \tag{165}$$

for all the investigated RSFP. In fact, a deviation from the null value for $\sigma_{\overline{12},405}$ does not alter the values of the light intensities and angular frequency of modulation at resonance, but only the absolute values of the RSFP response to the light modulation. Hence, equipped with the $\sigma_{\overline{12},405} + \sigma_{\overline{21},405}$ value, we could derive an estimate of $\sigma_{\overline{12},405}$ by using Eq.(165).

[4]Although we could directly access the relative brightness $Q_{\overline{1},480}/Q_{\overline{1},405}$ from an independent experiment upon collecting fluorescence at 522 nm (see Supplementary Table 5), the global fit relying on Eq.(39) proved too constraining in order to reliably retrieve the relative brightness $Q_{\overline{2},405}/Q_{\overline{1},405}$ measured upon illuminating at 405 nm and collecting fluorescence at 522 nm. Therefore we have adopted the value of the ratio $Q_{\overline{2},480}/Q_{\overline{1},480}$ as an order of magnitude of $Q_{\overline{2},405}/Q_{\overline{1},405}$. The estimates of $Q_{\overline{2},480}/Q_{\overline{1},480}$, $Q_{\overline{2},405}/Q_{\overline{1},405}$, and $Q_{\overline{1},480}/Q_{\overline{1},405}$ for Dronpa-2 have been used to draw the Supplementary Figures.

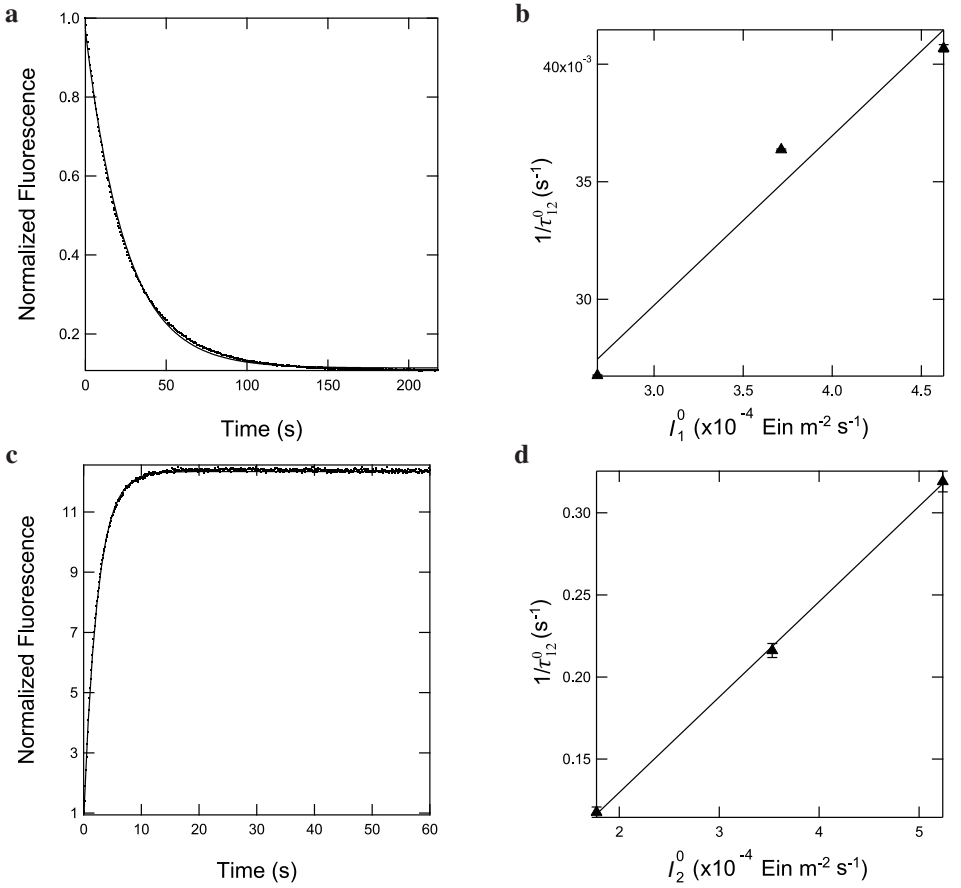

Supplementary Figure 22: Photoisomerization kinetics of rsEGFP. **a**,**c**: Temporal evolution of the normalized fluorescence emission at 522 nm of rsEGFP solutions (10 µM) upon illumination at 480 (**a**: I_1^0 = 4.6×10^{-4} Ein s^{-1} m^{-2}) and 405 and 480 (**c**: I_1^0 = 4.6×10^{-4} Ein s^{-1} m^{-2}, I_2^0 = 5.2×10^{-4} Ein s^{-1} m^{-2}) nm. The exponential fits with Eqs.(25) (**a**) and (39) (**c**) are shown as solid lines; **b**,**d**: Dependence of the inverse of the relaxation time $1/\tau_{12}^0$ on the light intensities I_1^0 (**b**, refering to $1/\tau_{12}^{0,1}$) and I_2^0 (**d**, refering to $1/\tau_{12}^{0,2}$). Linear fit (solid line) enables to extract $\sigma_{\overline{12},480} + \sigma_{\overline{21},480}$ from the slope and an order of magnitude of $k_{\overline{21}}^{\Delta}$ from the value on the y-axis for $I_1^0 = 0$ (**b**) and $\sigma_{\overline{12},405} + \sigma_{\overline{21},405}$ from the slope (**d**). $T = 37$°C in pH 7.5 buffer.

and kinetic parameters are given in Supplementary Table 5 together with data from the literature.

Robustness of the RSFP photochemical behavior

Robustness towards environmental changes

The relaxation times $\tau_{12}^{0,1}$ and $\tau_{12}^{0,2}$ determine the resonance conditions for Speed OPIOM. To evaluate their robustness, we measured the values of the relaxation times $\tau_{12}^{0,1}$ and $\tau_{12}^{0,2}$ of Dronpa-2 and at 37 °C in various environments: (i) an aqueous solution at pH 7.5; (ii) the cytoplasm of live cells; (iii) the cytoplasm of fixed cells. The results are shown in Supplementary Table 6. They evidence the absence of any significant variation of $\tau_{12}^{0,1}$ and $\tau_{12}^{0,2}$ among the three

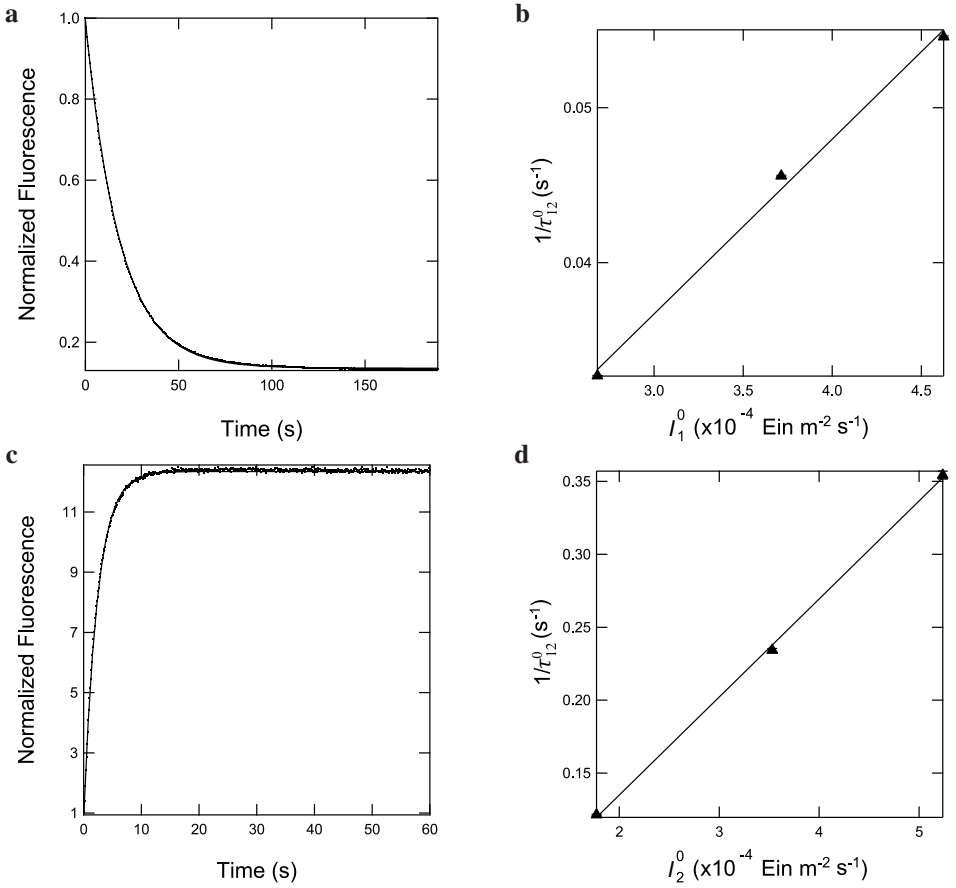

Supplementary Figure 23: Photoisomerization kinetics of rsEGFP2. **a**,**c**: Temporal evolution of the normalized fluorescence emission at 522 nm of rsEGFP2 solutions (10 µM) upon illumination at 480 (**a**: I_1^0 = 4.6×10^{-4} Ein s^{-1} m^{-2}) and 405 and 480 (**c**: I_1^0 = 4.6×10^{-4} Ein s^{-1} m^{-2}, I_2^0 = 5.2×10^{-4} Ein s^{-1} m^{-2}) nm. The exponential fits with Eqs.(25) (**a**) and (39) (**c**) are shown as solid lines; **b**,**d**: Dependence of the inverse of the relaxation time $1/\tau_{12}^0$ on the light intensities I_1^0 (**b**, refering to $1/\tau_{12}^{0,1}$) and I_2^0 (**d**, refering to $1/\tau_{12}^{0,2}$). Linear fit (solid line) enables to extract $\sigma_{\overline{12},480} + \sigma_{\overline{21},480}$ from the slope and an order of magnitude of $k_{\overline{21}}^{\Delta}$ from the value on the y-axis for $I_1^0 = 0$ (**b**) and $\sigma_{\overline{12},405} + \sigma_{\overline{21},405}$ from the slope (**d**). $T = 37°$C in pH 7.5 buffer.

investigated experimental conditions, which suggests resonance conditions for Speed OPIOM to be robust.

We did not observe any significant change of $\tau_{12}^{0,1}$ and $\tau_{12}^{0,2}$ in the three investigated conditions. From Eqs.(163,164), we correspondingly concluded that the RSFP photochemical parameters $\sigma_{\overline{12},480} + \sigma_{\overline{21},480}$, $\sigma_{\overline{12},405} + \sigma_{\overline{21},405}$, and $k_{\overline{21}}^{\Delta}$ were not markedly sensitive to the environment at a same pH.

Robustness towards changes of the image acquisition frequency

Eqs.(101,102) suggest that increasing I_1^0 and I_2^0 at constant I_1^0/I_2^0 ratio would enable us to increase ω (and correspondingly the image acquisition frequency) while maintaining the resonance condition. However, this prediction is only relevant as long as the photoswitching behavior of the RSFPs is correctly accounted for by the two-state model (8). To

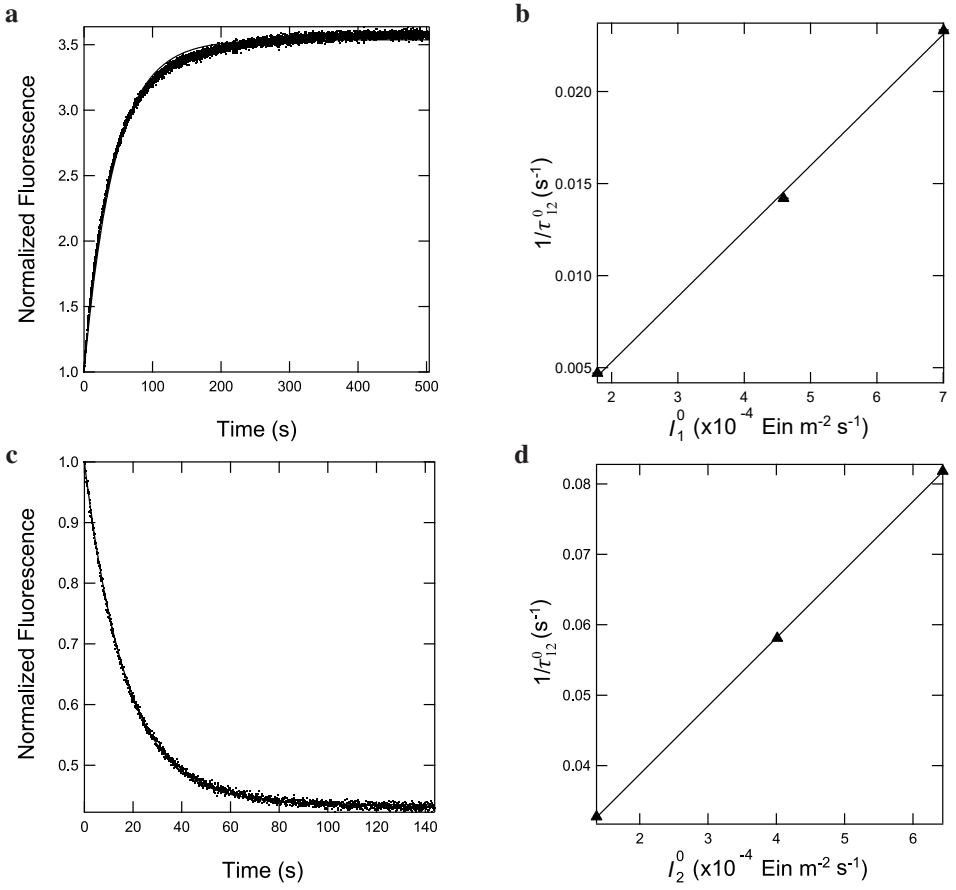

Supplementary Figure 24: Photoisomerization kinetics of Padron. **a**,**c**: Temporal evolution of the normalized fluorescence emission at 522 nm of Padron solutions (10 µM) upon illumination at 480 (**a**: I_1^0 = 7.0×10^{-4} Ein s^{-1} m^{-2}) and 405 and 480 (**c**: I_1^0 = 7.0×10^{-4} Ein s^{-1} m^{-2}, I_2^0 = 4.8×10^{-4} Ein s^{-1} m^{-2}) nm. The exponential fits with Eqs.(25) (**a**) and (39) (**c**) are shown as solid lines; **b**,**d**: Dependence of the inverse of the relaxation time $1/\tau_{12}^0$ on the light intensities I_1^0 (**b**, refering to $1/\tau_{12}^{0,1}$) and I_2^0 (**d**, refering to $1/\tau_{12}^{0,2}$). Linear fit (solid line) enables to extract $\sigma_{\overline{12},480} + \sigma_{\overline{21},480}$ from the slope and an order of magnitude of $k^{\Delta}_{\overline{21}}$ from the value on the y-axis for $I_1^0 = 0$ (**b**) and $\sigma_{\overline{12},405} + \sigma_{\overline{21},405}$ from the slope (**d**). $T = 37°$C in pH 7.5 buffer.

evaluate the scope of its relevance, we submitted fixed H2B-Dronpa-2 cells labelled at the nucleus to light jump experiments at larger light intensities than done above by using our microscope instead of our fluorimeter for illumination (Supplementary Figure 26).

Even at the highest investigated 480 nm light intensity giving rise to fluorescence drops at the millisecond time scale, the temporal evolution of the fluorescence emission of the illuminated cells was shown to satisfactorily obey the exponential behaviour predicted by the two-state kinetic model in Eq.(25) (Supplementary Figure 26a). Moreover we could observe the theoretically predicted linear dependence of the inverse of the relaxation time $1/\tau_{12}^0$ on the light intensities I_1^0 (Supplementary Figure 26b) with the same $\sigma_{\overline{12},480} + \sigma_{\overline{21},480}$ value as observed in Supplementary Figure 19. We similarly

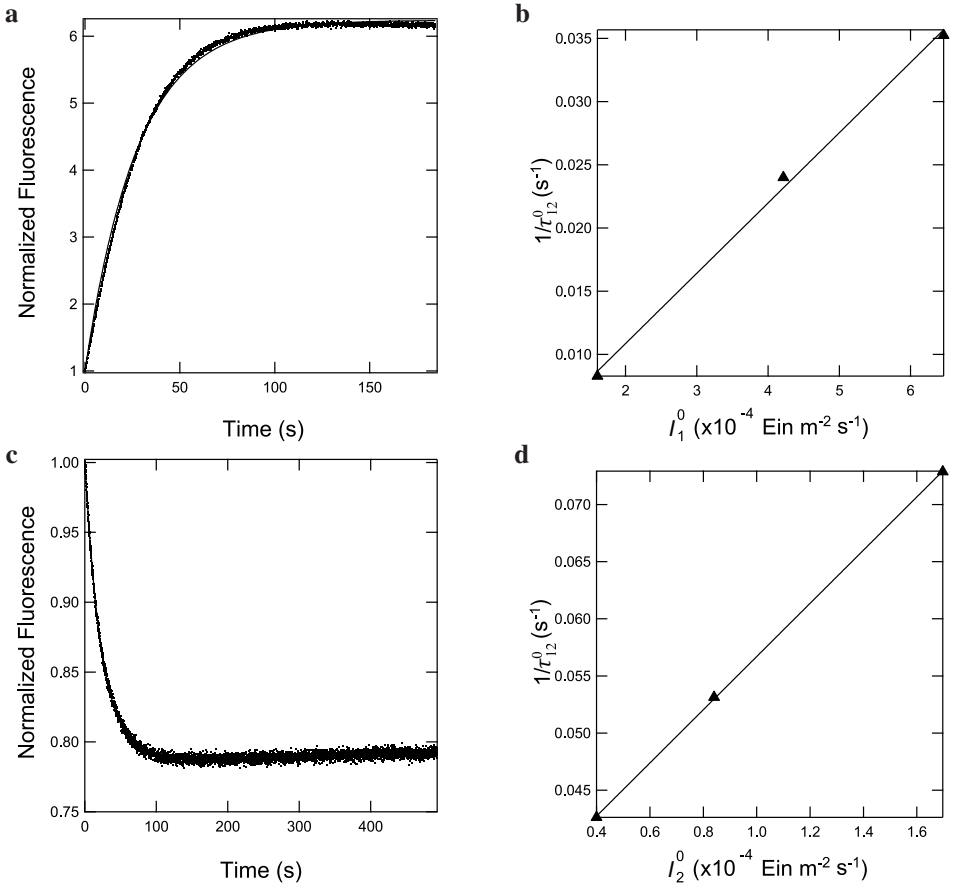

Supplementary Figure 25: Photoisomerization kinetics of Kohinoor. **a**,**c**: Temporal evolution of the normalized fluorescence emission at 522 nm of Kohinoor solutions (10 µM) upon illumination at 480 (**a**: I_1^0 = 6.4×10^{-4} Ein s^{-1} m^{-2}) and 405 and 480 (**c**: I_1^0 = 6.4×10^{-4} Ein s^{-1} m^{-2}, I_2^0 = 3.7×10^{-5} Ein s^{-1} m^{-2}) nm. The exponential fits with Eqs.(25) (**a**) and (39) (**c**) are shown as solid lines; **b**,**d**: Dependence of the inverse of the relaxation time $1/\tau_{12}^0$ on the light intensities I_1^0 (**b**, refering to $1/\tau_{12}^{0,1}$) and I_2^0 (**d**, refering to $1/\tau_{12}^{0,2}$). Linear fit (solid line) enables to extract $\sigma_{\overline{12},480} + \sigma_{\overline{21},480}$ from the slope and an order of magnitude of $k^{\Delta}_{\overline{21}}$ from the value on the y-axis for $I_1^0 = 0$ (**b**) and $\sigma_{\overline{12},405} + \sigma_{\overline{21},405}$ from the slope (**d**). $T = 37°$C in pH 7.5 buffer.

observed that the fluorescence emission from 405/488 nm-illuminated cells satisfactorily exhibited the exponential behaviour predicted with the two-state kinetic model in Eq.(39) at all studied 405 nm light intensities (480 nm light intensity remaining fixed to a constant value). Gratefully the linear dependence of the inverse of the relaxation time $\tau_{12}^{0,2}$ on light intensity I_2^0 given in Eq.(164) derived from Eq.(18) provided the same $\sigma_{\overline{12},405} + \sigma_{\overline{21},405}$ value than observed at lower light intensities.

Hence we could conclude that the two-state kinetic model used to model the RSFP photoswitching behavior is relevant down to the millisecond time scale, which suggests that image acquisition frequencies as high as 50 Hz could be used with Speed OPIOM.

Supplementary Table 5: Photochemical and kinetic parameters of Dronpa, Dronpa-2, Dronpa-3, RSFastLime, rsEGFP, rsEGFP2, Padron, and Kohinoor at pH 7.5 and at 37 °C.

RSFP	$\frac{Q_{\overline{2},480}}{Q_{\overline{1},480}}$	$\sigma_{\overline{12},480} + \sigma_{\overline{21},480}$ (m^2 mol^{-1})	$\sigma_{\overline{12},405} + \sigma_{\overline{21},405}$ (m^2 mol^{-1})	$\frac{Q_{\overline{1},480}}{Q_{\overline{1},405}}$	k_{21}^{Δ} (s^{-1})
Dronpa	~ 0.01 [a]	5.1 ± 0.5	354.5 ± 0.1	$\sim$31	$(2 \pm 2) \times 10^{-4}$ [b]
Dronpa-2	~ 0.01	196 ± 8 [c]	413 ± 25	$\sim$13	$(14 \pm 4) \times 10^{-3}$ [d]
Dronpa-3	~ 0.01	29 ± 2 [e]	331 ± 4	$\sim$12	$(1.0 \pm 0.3) \times 10^{-1}$ [f]
rsFastLime	~ 0.01 [g]	36 ± 5	648 ± 11	$\sim$18	$(2 \pm 2) \times 10^{-3}$ [h]
rsEGFP	~ 0.01	72 ± 13	581 ± 13	~ 11	$(8 \pm 5) \times 10^{-3}$ [i]
rsEGFP2	~ 0.01	113 ± 8	672 ± 18	~ 5	$(3 \pm 3) \times 10^{-3}$
Padron	~ 6	36 ± 1	96.8 ± 0.6	$\sim$6	$(0 \pm 6) \times 10^{-4}$ [j]
Kohinoor	~ 6	56 ± 3	233 ± 2	~ 17	$(0 \pm 1) \times 10^{-3}$ [k]

[a] 0.06 is given in;[11] [b] 2 10^{-5} s^{-1} is reported in;[9],[11] [c] 157 m^2 mol^{-1} in;[6] [d] 3 10^{-2} and 1.5 10^{-2} s^{-1} are respectively reported in[9] and;[6] [e] 21 m^2 mol^{-1} in;[6] [f] 0.17 s^{-1} in;[6] [g] 0.015 is given in;[11] [h] 2 10^{-3} s^{-1} is reported in;[9],[11] [i] 7 10^{-4} is reported in;[18] [j] 1 10^{-4} s^{-1} is reported in;[11] [k] 1 10^{-4} s^{-1} is reported in.[17]

Supplementary Table 6: Dependence of the relaxation times $\tau_{12}^{0,1}$ and $\tau_{12}^{0,2}$ of Dronpa-2 on the environment at pH 7.5 and at 37°C. For fixed and live cells, the measurement was performed on ten different cells in the same field of view.

Sample	$\tau_{12}^{0,1}$ (ms)	$\tau_{12}^{0,2}$ (ms)
in vitro	359 ± 1	163 ± 1
Fixed cells	338 ± 9	157 ± 7
Live cells	350 ± 9	162 ± 7

Supplementary Note 3: Speed OPIOM implementation

The implementation of Speed OPIOM requires (i) to determine the light intensities at the sample of the two light sources used for RSFP photoswitching (typically 480 and 405 nm) and (ii) to set up the relevant illumination conditions to target the desired reversibly photoswitchable fluorescent proteins (RSFPs).

Measurement of light intensities

Instead of using a powermeter (which is not always accessible in a laboratory of Biology), we propose to directly exploit the photochemical properties of the RSFPs which have been measured during this study and which are expected to be used for Speed OPIOM imaging. The principle of the calibrating experiments is to apply light jumps on RSFP-containing samples and to analyze the temporal evolution of the collected fluorescence emission to extract the light intensities sought for. We recommend to use calibrating samples at the closest to the original samples to be subsequently observed with Speed OPIOM. We typically use fixed cells expressing Dronpa-2 in the nucleus for most of our experiments. Such a calibrating sample has been shown photochemically reliable beyond the month timescale.

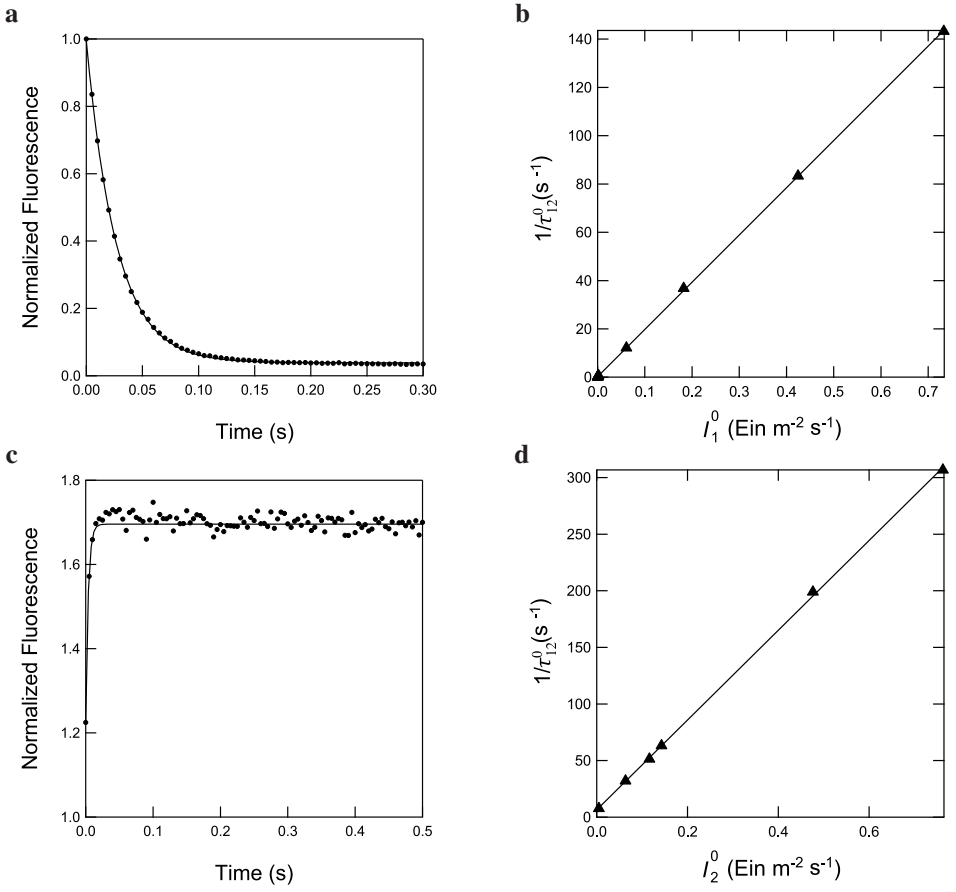

Supplementary Figure 26: Photoisomerization kinetics of Dronpa-2 at large light intensities. **a**,**c**: Temporal evolution of the normalized fluorescence emission of fixed H2B-Dronpa-2 labelled cells upon illumination at 480 (**a**: $I_1^0 = 1.8\times10^{-1}$ Ein s^{-1} m^{-2}) and 405 and 480 (**c**: $I_1^0 = 3\times10^{-2}$ Ein s^{-1} m^{-2}, $I_2^0 = 7.6\times10^{-1}$ Ein s^{-1} m^{-2}) nm. The exponential fits with Eqs.(25) (**a**) and (39) (**c**) are shown as solid lines; **b**,**d**: Dependence of the inverse of the relaxation time $1/\tau_{12}^0$ on the light intensities I_1^0 (**b**, refering to $1/\tau_{12}^{0,1}$) and I_2^0 (**d**, refering to $1/\tau_{12}^{0,2}$). Linear fit (solid line) enables to extract $\sigma_{\overline{12},480}+\sigma_{\overline{21},480}$ from the slope (**b**) and $\sigma_{\overline{12},405}+\sigma_{\overline{21},405}$ from the slope (**d**). $T = 37°$C.

In a first step, the RSFP-containing sample is briefly illuminated (typically at 405 nm) to restore the RSFP thermodynamically stable state (denoted 1 in Section).[5] The sample is then submitted to a light jump (typically at 480 nm) at constant light intensity I_1^0 and the fluorescence image is collected as a function of time. The fluorescence signal (obtained by integration over the RSFP-containing zone) is then plotted as a function of time. One should typically observe the temporal dependence observed in Supplementary Figure 19a when using Dronpa-2 (or the corresponding figures for the other RSFPs). This temporal dependence is subsequently fitted in the time window where the fluorescence signal varies

[5]Indeed, the calibrating sample may have been exposed to sunlight so as to yield some photoswitched state (denoted 2 in Section).

from its initial steady-state value $I_{\mathrm{F}}(0,\lambda_1)$ with the law given in Eq.(166)

$$I_{\mathrm{F}}(t) \;=\; I_{\mathrm{F}}(0,\lambda_1) + \mathcal{A}_{\lambda_1}\left[1-\exp\left(-\frac{t}{\tau_{\lambda_1}}\right)\right] \tag{166}$$

which derivation is given in subsection . τ_{λ_1} is extracted from the fit and I_1^0 is subsequently derived from Eq.(167)

$$I_1^0 \;=\; \frac{\left(\frac{1}{\tau_{\lambda_1}} - k^{\Delta}_{\overline{21}}\right)}{\left(\sigma_{\overline{12},\lambda_1} + \sigma_{\overline{21},\lambda_1}\right)} \tag{167}$$

by expressing τ_{λ_1} in second and by using the values of $k^{\Delta}_{\overline{21}}$ and $\left(\sigma_{\overline{12},\lambda_1} + \sigma_{\overline{21},\lambda_1}\right)$, which are given in Supplementary Table 5. This experiment can be reproduced for several values of the light powers in order to calibrate the light source at λ_1.

In a second step, the RSFP-containing sample is illuminated (typically at 480 nm) at constant light intensity I_1^0. It is then submitted to a light jump (typically at 405 nm) at constant light intensity I_2^0 while maintaining light intensity I_1^0 at a constant value. The fluorescence image is again collected as a function of time and the temporal dependence of the fluorescence signal (obtained by integration over the RSFP-containing zone) is subsequently plotted. One should typically observe the temporal dependence observed in Supplementary Figure 19c when using Dronpa-2 (or the corresponding figures for the other RSFPs). This temporal dependence is subsequently fitted in the time window where the fluorescence signal now varies (starting from the steady-state value $I_{\mathrm{F}}(0,\lambda_1\lambda_2)$ reached before application of the I_2^0 jump) with the law given in Eq.(168)

$$I_{\mathrm{F}}(t) \;=\; I_{\mathrm{F}}(0,\lambda_1\lambda_2) + \mathcal{A}_{\lambda_1\lambda_2}\left[1-\exp\left(-\frac{t}{\tau_{\lambda_1\lambda_2}}\right)\right]. \tag{168}$$

$\tau_{\lambda_1\lambda_2}$ is extracted from the fit and I_2^0 is subsequently derived from Eq.(169).

$$I_2^0 \;=\; \frac{\left[\frac{1}{\tau_{\lambda_1\lambda_2}} - \left(\sigma_{\overline{12},\lambda_1} + \sigma_{\overline{21},\lambda_1}\right) I_1^0 - k^{\Delta}_{\overline{21}}\right]}{\left(\sigma_{\overline{12},\lambda_2} + \sigma_{\overline{21},\lambda_2}\right)} \tag{169}$$

by expressing $\tau_{\lambda_1\lambda_2}$ in second, and by using the values of I_1^0 (obtained from the calibration indicated above) and $k^{\Delta}_{\overline{21}}$, $\left(\sigma_{\overline{12},\lambda_1} + \sigma_{\overline{21},\lambda_1}\right)$, and $\left(\sigma_{\overline{12},\lambda_2} + \sigma_{\overline{21},\lambda_2}\right)$ which are given in Supplementary Table 5. This experiment can be reproduced at several powers of the second light source in order to calibrate the light source at λ_2.

Setting up illumination to target RSFPs

Once the light sources have been calibrated, it is possible to determine the illumination conditions to be used to specifically target the RSFPs in the sample. We successively consider two situations:

- *The sample contains one RSFP and the goal is to eliminate the fluorescence signal from interfering species (for example auto-fluorescence, ambient light, non-photoactive fluorophores).* In such a situation, it is worth to adopt

the resonance conditions (101,102) for the targeted RSFP since they maximize the Speed OPIOM RSFP signal while maintaining an exclusive contrast against optical interferences. One should preferentially adopt the highest available light intensities compatible with resonance in order to increase both the temporal resolution of Speed OPIOM imaging and the signal to noise ratio. Denoting $I_1^{\max}$ and $I_2^{\max}$ for the highest available intensities of the two light sources and using data given in Supplementary Table 5 for the values of $\sigma_{12,\lambda_1}+\sigma_{21,\lambda_1}$ and $\sigma_{12,\lambda_2}+\sigma_{21,\lambda_2}$, one should adopt

–

$$I_1^0 = \frac{I_1^{\max}}{2} \tag{170}$$

$$I_2^0 = \frac{\left(\sigma_{12,\lambda_1}+\sigma_{21,\lambda_1}\right)}{\left(\sigma_{12,\lambda_2}+\sigma_{21,\lambda_2}\right)}\frac{I_1^{\max}}{2} \tag{171}$$

if $\left(\sigma_{12,\lambda_1}+\sigma_{21,\lambda_1}\right) I_1^{\max} \leqslant \left(\sigma_{12,\lambda_2}+\sigma_{21,\lambda_2}\right) I_2^{\max}$;

–

$$I_1^0 = \frac{\left(\sigma_{12,\lambda_2}+\sigma_{21,\lambda_2}\right)}{\left(\sigma_{12,\lambda_1}+\sigma_{21,\lambda_1}\right)}\frac{I_2^{\max}}{2} \tag{172}$$

$$I_2^0 = \frac{I_2^{\max}}{2} \tag{173}$$

if $\left(\sigma_{12,\lambda_1}+\sigma_{21,\lambda_1}\right) I_1^{\max} \geqslant \left(\sigma_{12,\lambda_2}+\sigma_{21,\lambda_2}\right) I_2^{\max}$.

Then the resonant angular frequency of modulation of the illumination modulation is equal to

$$\omega = \min\left[\left(\sigma_{12,\lambda_1}+\sigma_{21,\lambda_1}\right) I_1^{\max}, \left(\sigma_{12,\lambda_2}+\sigma_{21,\lambda_2}\right) I_2^{\max}\right], \tag{174}$$

and the corresponding period T equal to

$$T = \frac{2\pi}{\min\left[\left(\sigma_{12,\lambda_1}+\sigma_{21,\lambda_1}\right) I_1^{\max}, \left(\sigma_{12,\lambda_2}+\sigma_{21,\lambda_2}\right) I_2^{\max}\right]} \tag{175}$$

gives the Speed OPIOM temporal resolution, which is equal to one period of illumination modulation;

- *The sample contains several RSFPs and the goal is to discriminate their individual contributions (still by eliminating optical interferences).* In such situations, the goal is to set illumination conditions so as to maximize the normalized response ($\mid \Im_{\mathrm{F,norm}}^{1,\cos} \mid = \mid \Im_{\mathrm{F}}^{1,\cos}/\{[(Q_{2,1}-Q_{1,1})I_1^0+(Q_{2,2}-Q_{1,2})I_2^0]\alpha P_{\mathrm{tot}}\} \mid$) of the desired RSFP while keeping the normalized responses from others RSFPs below a threshold (typically 10%). We provide a Mathematica computable document (Speed OPIOM.cdf) where the user can enter the desired responses from the RSFPs among the eight RSFPs described in the paper to identify set(s) of I_1^0, I_2^0 and ω values where the desired imaging conditions are fulfilled. This application can be opened using Mathematica CDF player which is freely available at `https://www.wolfram.com/cdf-player/` after registration.

Supplementary Note 4: Matlab code for OPIOM imaging

```
function [IF0,IF1out,IF1outmed,Phase]=opiom_(filename,period,phi_acq,n_per,skip_per)
% Computes pre-OPIOM (IF0), OPIOM (IF1out), OPIOM
% median-filtered (IF1outmed) and phase (Phase) images
% We assume movie acquired is already loaded in Matlab
% (as camera manufacturer usually provide code to import files)
% 'filename' is the matrix to be treated
% 'period' is the period of the light excitation defined as frame number
% 'phi_acq' is the phase delay between the dates of camera recording
% and light excitation previously calibrated with fluorescein or EGFP
% 'n_per' is the total number of periods used for calculation
% 'skip_per' is the number of periods to skip before calculation
%

npts = period*n_per;
first = skip_per*period;
[X,Y,Z]=size(filename);
Holder = zeros(X,Y,npts);
IF1out = zeros(X,Y);
IF1in  = zeros(X,Y);

for i=1:npts
   Holder(:,:,i)=filename(:,:,i+first);
end

%%%%%% Photobleaching correction assuming a linear decay%%%%%%
% Calculate the average signal over the first half of periods
 linePoint1=mean(Holder(:,:,1:((npts)/2)),3);
%Calculate the average signal over the last half of periods
 linePoint2=mean(Holder(:,:,((npts)/2+1):end),3);
% Calculate the slope B(x,y) (See Eq. XXX)
 slope=(linePoint2-linePoint1)/(npts/2);
%Correction for photobleaching
```

```
 for i=1:npts
     Holder(:,:,i)=(Holder(:,:,i)-slope.*i);
 end

%%%%%% Data processing %%%%%%

% Compute pre-OPIOM image
IF0 = mean(Holder,3);

% Compute OPIOM image
for i=1:npts
   IF1out(:,:) = (IF1out(:,:) + (Holder(:,:,i)).*cos(pi*(2*i-1)/period + phi_acq));
   IF1in (:,:) = (IF1in(:,:) + (Holder(:,:,i)).*sin(pi*(2*i-1)/period + phi_acq));
end

IF1out = 2.*IF1out ./ npts;
IF1in = 2.*IF1in ./ npts;
IF1outmed=medfilt2(IF1out,[3,3]);
Phase = atan(IF1out./IF1in);

%%% Display Pre-Opiom image
figure;imagesc(IF0);colormap(gray(4096));colorbar;

%%% Display Opiom image
figure;imagesc(IF1outmed);
colormap(gray(4096));
colorbar;
```

Supplementary Note 5: Comparison of the selective contrasts obtained with Speed OPIOM, SAFIRe and OLID

To compare the selective contrasts obtained with Speed OPIOM, SAFIRe and OLID, we recorded a movie from a microfluidic device with four rectangular chambers filled with solutions of the spectrally similar Dronpa-2, Padron, Dronpa, or EGFP under the three resonant conditions associated to each RSFP. The movie has been subsequently used to build the

Speed OPIOM, SAFIRe and OLID images from which we eventually analyzed the contrasts of the targeted RSFP against the various spectrally interfering fluorescent proteins.

Acquisition conditions

Supplementary Table 7 displays the acquisition parameters used to image Dronpa-2, Padron, Dronpa and EGFP in Supplementary Figure 27.

Supplementary Table 7: Acquisition parameters used to image Dronpa-2, Padron, Dronpa and EGFP at 37°C in Supplementary Figure 27.

Figure 27	Objective	Periods : Images	$\lambda_{\text{exc},1}$ (nm)	I_1^0 (Ein m^{-2} s^{-1})	$\lambda_{\text{exc},2}$ (nm)	I_2^0 (Ein m^{-2} s^{-1})	ω (rad s^{-1})	f (Hz)	α %
a,b,c,d	10×	10 : 100	480	2.5 10^{-3}	405	1.9 10^{-3}	6.3	1	100
e,f,g,h	10×	2 : 80	480	2.3 10^{-2}	405	4.3 10^{-2}	0.6	0.1	100
i,j,k,l	10×	2 : 400	480	2.4 10^{-2}	405	2.8 10^{-4}	0.2	0.03	100

Computation of the SAFIRe and OLID images

SAFIRe

The SAFIRe images were computed from the time series of the Speed OPIOM experiment as:

$$\mathcal{S}(x,y) = \sqrt{\mathfrak{I}_{\mathrm{F}}^{1,\sin}(x,y)^2 + \mathfrak{I}_{\mathrm{F}}^{1,\cos}(x,y)^2} \tag{176}$$

where $\mathfrak{I}_{\mathrm{F}}^{1,\cos}(x,y)$ and $\mathfrak{I}_{\mathrm{F}}^{1,\sin}(x,y)$ were respectively given in Eqs.(3) and (177)

$$\mathfrak{I}_{\mathrm{F}}^{1,\sin}(x,y) = \frac{1}{2nm} \sum_{k=0}^{4\mathrm{nm}-1} \left[(I_{\mathrm{F}}(x,y,k)) \times \sin\left(\frac{k\pi}{n} + \phi_{\mathrm{acq}}\right) \right]. \tag{177}$$

OLID

The OLID images were computed from the time series of the Speed OPIOM experiment as:

$$\rho(x,y) = \sum_{k=0}^{4\mathrm{nm}-1} \frac{(I_{\mathrm{F}}(x,y,k) - \langle I_{\mathrm{F}}(x,y,k)\rangle_{k=0}^{4\mathrm{nm}-1})(I_{F,R}(x,y,k) - \langle I_{F,R}(x,y,k)\rangle_{k=0}^{4\mathrm{nm}-1})}{\sigma_{x,y}\ \sigma_{x,y,R}} \tag{178}$$

where $I_{\mathrm{F}}(x,y,k)$ (resp. $I_{F,R}(x,y,k)$) is the fluorescence intensity at pixel (x,y) (resp. (x_{ref}, y_{ref}), for example within the reference) of the k^{th} frame during the photoconversion cycle. $\langle I_{\mathrm{F}}(x,y,k)\rangle_{k=0}^{4\mathrm{nm}-1}$ and $\langle I_{F,R}(x,y,k)\rangle_{k=0}^{4\mathrm{nm}-1}$, and $\sigma_{x,y}$ and $\sigma_{x,y,R}$ respectively designate the mean values and the standard deviation (std) values of the fluorescence intensity at the considered pixels.

Speed OPIOM, SAFIRe and OLID images

Results

Supplementary Figure 27 displays the obtained Speed OPIOM, SAFIRe and OLID images.

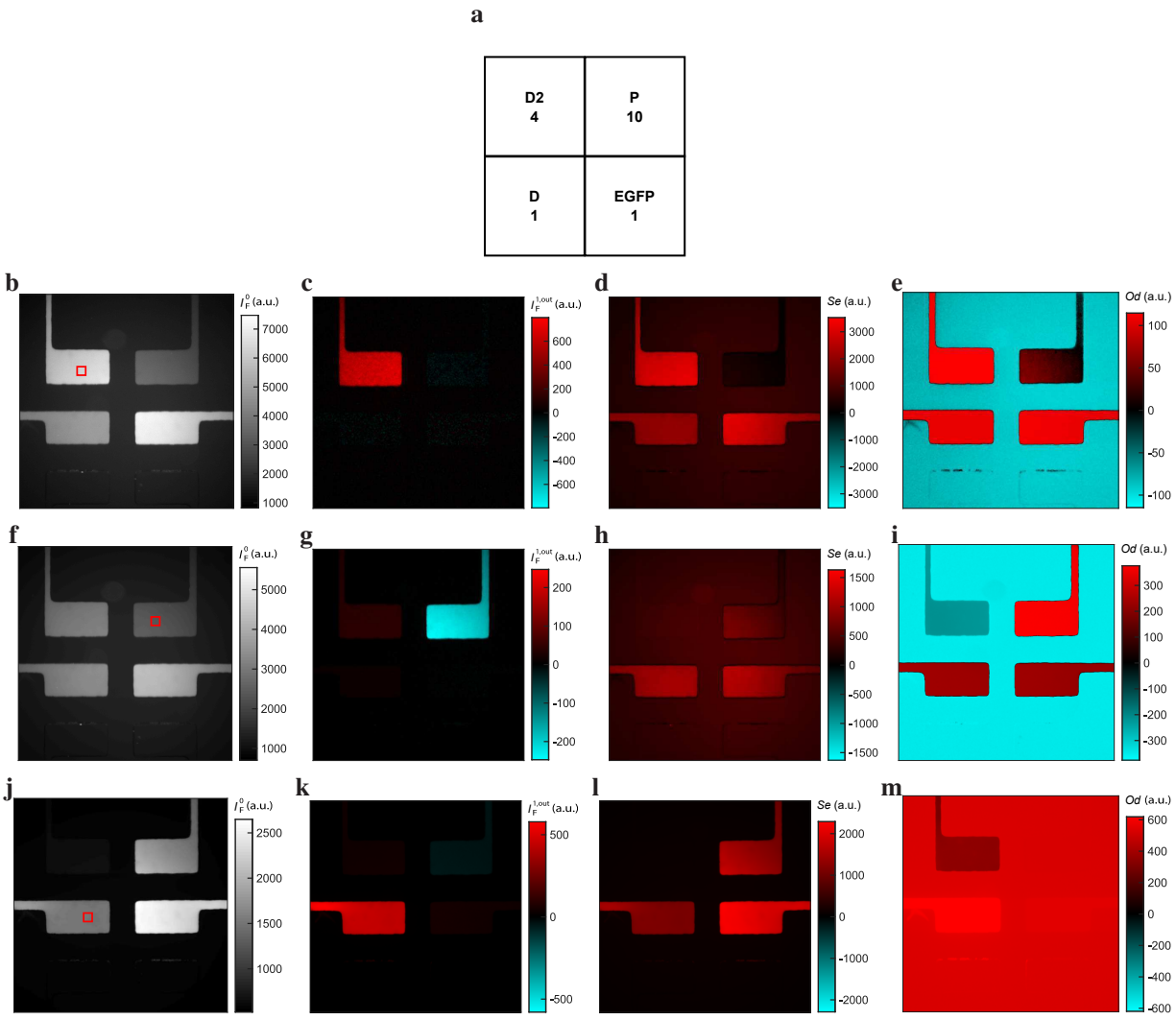

Supplementary Figure 27: Comparison of the selective contrasts obtained with Speed OPIOM, SAFIRe and OLID. A microfluidic device with four rectangular chambers (250×125×20 µm^3) was filled with solutions of Dronpa-2 (D2), Padron (P), Dronpa (D), or EGFP (E) (the numbers in **a** indicate the concentrations in µM). The pre-OPIOM (**b,f,j**), Speed OPIOM (**c,g,k**), SAFIRe (**d,h,l**) and OLID (**e,i,m**) images have been recorded with a 10 × objective at λ_{em} = 525 nm by sinusoidally modulating dual illumination tuned to the resonance of Dronpa-2 (**b,c,d,e**; $\lambda_{exc,1}$; I_1^0; ω; f; α) = (480 nm; 2.5×10^{-3} Ein m^{-2} s^{-1}; 6.3 rad s^{-1}; 1 Hz; 100%), ($\lambda_{exc,2}$; I_2^0; ω; f; α) = (405 nm; 1.9×10^{-3} Ein m^{-2} s^{-1}; 6.3 rad s^{-1}; 1 Hz; 100%), Padron (**f,g,h,i**; $\lambda_{exc,1}$; I_1^0; ω; f; α) = (480 nm; 2.3×10^{-2} Ein m^{-2} s^{-1}; 0.6 rad s^{-1}; 0.1 Hz; 100%), ($\lambda_{exc,2}$; I_2^0; ω; f; α) = (405 nm; 4.3×10^{-2} Ein m^{-2} s^{-1}; 0.6 rad s^{-1}; 0.1 Hz; 100%) and Dronpa (**j,k,l,m**; $\lambda_{exc,1}$; I_1^0; ω; f; α) = (480 nm; 2.4×10^{-2} Ein m^{-2} s^{-1}; 0.2 rad s^{-1}; 0.03 Hz; 100%), ($\lambda_{exc,2}$; I_2^0; ω; f; α) = (405 nm; 2.8×10^{-4} Ein m^{-2} s^{-1}; 0.2 rad s^{-1}; 0.03 Hz; 100%); Solvent: pH 7.5 50 mM HEPES buffer; T = 310 K. For OLID, we used as the reference signal the time-averaged fluorescence emission from a 20 × 20 pixels area (displayed as a red square in the pre-OPIOM image series) from the microfluidic chamber containing the targeted protein.

Discussion

As expected, Speed OPIOM selectively provides the image of the targeted RSFP while erasing the signals from non-targeted RSFPs as well as from non-photoactive fluorophores. More precisely, significant contrast enhancements have been obtained in Supplementary Figure 27 as displayed in Supplementary Table 8.

Supplementary Table 8: Contrast enhancements $\chi_{\mathrm{t/i}}$ (defined in Eq.(7)) obtained with Speed OPIOM imaging in a mixture containing Dronpa-2, Padron, Dronpa and EGFP at 37°C (see Supplementary Figure 27).

Figure27	t	i	$\chi_{\mathrm{t/i}}$
b,c,	Dronpa-2	EGFP	220
b,c	Dronpa-2	Dronpa	13
b,c	Dronpa-2	Padron	67
f,g	Dronpa	EGFP	210
f,g	Dronpa	Dronpa-2	4.9
f,g	Dronpa	Padron	11
j,k	Padron	EGFP	170
j,k	Padron	Dronpa-2	2.0
j,k	Padron	Dronpa	16

SAFIRe is not under optimal conditions to eliminate the signal from spectrally interfering fluorophores since the modulated light intensity at 480 nm is also the wavelength for exciting all the fluorophores.[6] Hence the SAFIRe image is mainly dominated by the zeroth order term which is present in the $\mathfrak{I}_{\mathrm{F}}^{1,\sin}$ contribution (see Eqs.(99,131)) of Eq.(176) and the final SAFIRe image exhibits a strong similarity with the pre-OPIOM image.

Eventually, the extracted OLID images underline the significance of the angular frequency of modulation of the periodically modulated illumination to govern the OLID relevance to selectively discriminate a targeted RSFP from spectrally interfering fluorophores. It is only when the phase lag between the targeted RSFP and the interfering fluorophore is equal to $\pi/2$ or $3\pi/2$ (which is not strictly the case in Supplementary Figure 27) that OLID can efficiently eliminate the interfering contributions. In particular, this condition cannot be simultaneously met when the spectral interferences originate from a mixture of RSFPs and non-photoactive fluorophores since they are associated to different phase lags.[7]

[6] To benefit at most from SAFIRe, image recovery is achieved through selective fluorescence enhancement via modulating a secondary excitation light source at much lower energy than the observed emission.

[7] Under our experimental conditions, the fluorescence emission from all the fluorescent proteins experience a sinusoidal temporal modulation at steady-state. For the targeted RSFP ($f = t$, $k = n$) and for the interfering fluorophore ($f = i$, $k = m$), we adopt

$$I_{\mathrm{F},f}(t) \quad = \quad \mathfrak{I}_{\mathrm{F},f}^{0}\left[1+\sum_{k=1}^{+\infty}\frac{\mathfrak{I}_{\mathrm{F},f}^{k}}{\mathfrak{I}_{\mathrm{F},f}^{0}}\sin\left(k\theta x+\phi_{n,f}\right)\right] \tag{179}$$

where k is an integer, $\phi_{n,t}$ is fixed to zero, and $\phi_{m,i} \neq 0$. In the case of RSFPs,

$$\mathfrak{I}_{\mathrm{F},f}^{n}=\sqrt{\left(\mathfrak{I}_{\mathrm{F},f}^{n,\sin}\right)^{2}+\left(\mathfrak{I}_{\mathrm{F},f}^{n,\cos}\right)^{2}} \tag{180}$$

whereas $\mathfrak{I}_{\mathrm{F},f}^{1}=\mathfrak{I}_{\mathrm{F},f}^{1,\sin}$ and $\mathfrak{I}_{\mathrm{F},f}^{n}=0$ ($n \geq 2$) in the case of non-photoactive fluorophores. Then Eq.(178) yields ρ

This feature explains the incomplete discrimination of the targeted RSFPs against the spectrally interfering fluorophores in Supplementary Figure 27.[8]

Supplementary Note 6: Speed OPIOM limitations arising from noise considerations

All modulation-based techniques such as Speed OPIOM are limited by the enhanced and intrinsic noise of the detector. We have correspondingly measured the noise of the instrument alone and under a constant non-modulated illumination using the Sony IMX174 camera on our home built setup for remote Speed OPIOM imaging as an example. We eventually derived an order of magnitude of the minimal OPIOM signal, which can be reliably extracted in the presence of an interfering non-modulated signal.

Theoretical derivations

The data treatment of the camera consists of averaging N_c periods of signal at the modulation frequency f_m; it is equivalent to applying a narrow band-pass filter having a width f_m/N_c. When the camera receives a non-modulated stray light component, we consider that n_s electrons are produced at each camera frame. It gives rise to a current $I_s = n_s.e.f_c$ where f_c designates the acquisition frequency of the camera. Speed OPIOM filters out this signal. However this light also produces photon noise at all frequency components that will blur the actual Speed OPIOM signal. For a mean level n_s (evaluated by the current $I_s = n_s.e.f_c$), the photon noise (evaluated by the square of the current $I_n = n_n.e.f_c$ or similarly by the square of the electron number n_n) that appears on the entire bandwidth is given by Schottky noise formula $I_n^2 = 2I_s.e.f_m/N_c$, where e is the electron charge. We correspondingly derive $(n_n.e.f_c)^2 = 2.n_s.e.f_c.e.f_m/N_c$ and finally $n_n^2 = 2.n_s f_m/f_c.N_c$. Even when no light is sent to the camera, a noise remains corresponding to the reading noise of each pixel of the camera. By introducing n_r as the number of electrons injected as noise in each frame in each pixel, we derive the intrinsic camera read noise as $n_r^2 f_m/\left(f_c.N_c\right)$. We eventually extract the expression of the global noise in

- Interfering RSFPs

$$\rho \quad = \quad \frac{1}{2\sigma_{x,y}\sigma_{x,y,R}} \sum_{n=1}^{+\infty} \mathfrak{I}_{\mathrm{F,t}}^{\mathrm{n}} \mathfrak{I}_{\mathrm{F,i}}^{\mathrm{n}} \left\langle \cos \phi_n \right\rangle \tag{181}$$

- Non-photoactive fluorophores

$$\rho \quad = \quad \frac{1}{2\sigma_{x,y}\sigma_{x,y,R}} \mathfrak{I}_{\mathrm{F,t}}^{\mathrm{1}} \mathfrak{I}_{\mathrm{F,i}}^{\mathrm{1}} \left\langle \cos \phi_1 \right\rangle . \tag{182}$$

Two features are worth to be pointed out:

- At a given angular frequency of modulation, the phase lags ϕ_i depend on the photoswitching kinetics of the spectrally interfering fluorophores. In particular, they cannot be simultaneously fixed to $\pi/2$ or $3\pi/2$ for all interfering fluorophores;
- The dominating $\mathfrak{I}_{\mathrm{F,t}}^{\mathrm{1}}$ and $\mathfrak{I}_{\mathrm{F,i}}^{\mathrm{1}}$ terms in Eqs.(181,182) contains zeroth order contributions from the $\mathfrak{I}_{\mathrm{F,t}}^{\mathrm{1,sin}}$ and $\mathfrak{I}_{\mathrm{F,i}}^{\mathrm{1,sin}}$ terms, which are non-vanishing for the interfering fluorophores.

Thus, in contrast to Speed OPIOM, OLID cannot simultaneously eliminate kinetically distinct interfering fluorophores

[8] In particular, note that the PDMS autofluorescence (especially when excited at 405 nm) generates non-vanishing OLID signals.

Eq.(183):

$$n_n^2 \quad = \quad [f_m/\left(f_c.N_c\right)] \,.\left(n_r^2 + 2.n_s\right) \tag{183}$$

We now respectively call O and S (in electrons per second on a single pixel) the OPIOM signal and the non-modulated light (they respectively yield O/f_c and S/f_c electrons per image) and we choose the camera frequency $f_c = 2.S/n_s$ so that the camera is half way to saturation (n_s). By considering that Eq.(183) gives $n_n^2 = [f_m/\left(f_c.N_c\right)]\,.2.n_s$ at high light intensity, we can evaluate the minimal OPIOM detectable signal O_{min} against the non-modulated signal S as

$$O_{min} \quad = \quad 2\sqrt{\frac{S.f_m}{N_c}} \tag{184}$$

Noise measurement

Supplementary Figure 28 displays our measurement of the total noise after demodulation of our Sony IMX174 camera, which has been illuminated with a non-modulated light source either with 1/4, 1/2, or nearly full light capacity of the camera.

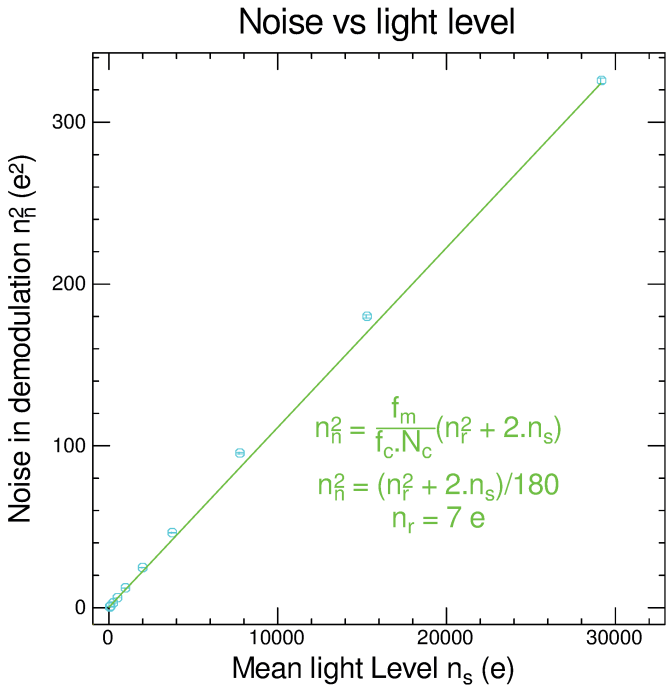

Supplementary Figure 28: Measurement of the noise from the Sony IMX174 camera on our home built setup for remote Speed OPIOM imaging. Markers: experimental points; line: theoretical prediction based on the n_r value provided by the manufacturer ($n_r = 7.e$).

Eq.(183) describes correctly the observed behavior. With $n_s = 32000e$, $f_m/f_c = 20$ and $N_c = 9$, we got an excellent agreement between the observed behavior and the one predicted using the value indicated by the manufacturer.

Derivation of the minimal OPIOM contribution to the fluorescence signal

In practice, f_c can span 1 to 100 Hz with $n_s = 32000e$ (well depth of the IMX174 camera). Then S can be in the range of 3.2×10^4 to 3.2×10^6 e s^{-1} on a single pixel (for example 1.53×10^{-14} to 1.53×10^{-12} W), which yields $O_{min} = 120$ to 1200 e s^{-1} (corresponding to 5.76×10^{-17} to 5.76×10^{-15}W. Thus at the maximum non-modulated light illumination, we can reliably detect an OPIOM signal which is 2666 times smaller (with a 100 times smaller non-modulated light illumination, the accessible ratio is still 266). Finally it is worth of note that all these numbers have been computed for a single pixel. However averaging data on 10×10 pixels would already increase the signal quality by a factor 10.

Supplementary References

[1] Fringeli, U. P., Baurecht, D. & Günthard H. H. in *Infrared and Raman Spectroscopy of Biological Materials* (Eds.: Gremlich, H.-U. & Yan B.), Marcel Dekker, New-York, 143–191 (2000) .

[2] Baurecht, D., & Fringeli, U. P. Quantitative modulated excitation Fourier transform infrared spectroscopy. *Rev. Sci. Inst.* **72**, 3782–3792 (2001).

[3] Urakawa, A., Bürgi, T., & Baiker, A. Sensitivity enhancement and dynamic behavior analysis by modulation excitation spectroscopy: Principle and application in heterogeneous catalysis. *Chem. Eng. Sci.* **63**, 4902–4909 (2008).

[4] McGown, L., & Bright, F. Phase-Resolved Fluorescence Spectroscopy. *Anal. Chem* **56**, 1400A–1417A (1984).

[5] Scofield, J. H. Frequency-domain description of a lock-in amplifier. *Am. J. Phys.* **62**, 129–133 (1994).

[6] Querard, J. *et al*. Photoswitching kinetics and phase sensitive detection add discriminative dimensions for selective fluorescence imaging. *Angew. Chem. Int. Ed.* 2633–2637 (2015).

[7] Querard, J., Gautier, A., Le Saux, T., & Jullien, L. Expanding discriminative dimensions for analysis and imaging. *Chem. Sci.* **6**, 2968–2978 (2015).

[8] Ando, R., Mizuno, H., & Miyawaki, A. Regulated fast nucleocytoplasmic shuttling observed by reversible protein highlighting. *Science* **306**, 1370–1373 (2004).

[9] Stiel, A. C. *et al*. 1.8 Å bright-state structure of the reversibly switchable fluorescent protein Dronpa guides the generation of fast switching variants. *Biochem. J.* **402**, 35–42 (2007).

[10] Ando, R., Flors, C., Mizuno, H., Hofkens, J., & Miyawaki, A. Highlighted Generation of Fluorescence Signals Using Simultaneous Two-Color Irradiation on Dronpa Mutants. *Biophys. J. Biophys. Lett.* L97–L99 (2007).

[11] Andresen, M. *et al*. Photoswitchable fluorescent proteins enable monochromatic multilabel imaging and dual color fluorescence nanoscopy. *Nat. Biotech.* **26**, 1035–1040 (2008).

[12] Brakemann, T. *et al*. Molecular Basis of the Light-driven Switching of the Photochromic Fluorescent Protein Padron. *J. Biol. Chem.* **285**, 14603–14609 (2010).

[13] Regis Faro, A. *et al*. Low-Temperature Chromophore Isomerization Reveals the Photoswitching Mechanism of the Fluorescent Protein Padron. *J. Am. Chem. Soc.* **133**, 16362–16365 (2011).

[14] Kaucikas, M., Tros, M., van Thor, J. J. Photoisomerization and Proton Transfer in the Forward and Reverse Photoswitching of the Fast-Switching M159T Mutant of the Dronpa Fluorescent Protein. *J. Phys. Chem. B* **119**, 2350–2362 (2015).

[15] Yadav, D. *et al*. Real-Time Monitoring of Chromophore Isomerization and Deprotonation during the Photoactivation of the Fluorescent Protein Dronpa. *J. Phys. Chem. B* **119**, 2404–2414 (2015).

[16] Walter, A., Andresen, M., Jakobs, S., Schroeder, J., & Schwarzer, D. Primary Light-Induced Reaction Steps of Reversibly Photoswitchable Fluorescent Protein Padron0.9 Investigated by Femtosecond Spectroscopy. *J. Phys. Chem. B* **119**, 5136–5144 (2015).

[17] Tiwari, D. K., *et al*. A fast- and positively photoswitchable fluorescent protein for ultralow-laser-power RESOLFT nanoscopy. *Nat. Meth.* **12**, 515–518 (2015).

[18] Grotjohann, T., *et al*. Diffraction-unlimited all-optical imaging and writing with a photochromic GFP, *Nature* **478**, 204–208 (2011).

[19] Grotjohann, T., *et al*. rsEGFP2 enables fast RESOLFT nanoscopy of living cells. *eLife* **1**, e00248 (2012).

[20] Frugoni, C. Tampone universale di Britton e Robinson a forza ionica costante. *Gazz. Chim. Ital.* **87**, 403–407 (1957).

Résumé

L'analyse de l'émission de fluorescence sur un modèle foliaire a permis de mettre au point un premier dispositif optique pour la macro-imagerie par fluorescence qui met en œuvre le protocole Speed OPIOM (Out of Phase Imaging after Optical Modulation) pour observer la fluorescence de plantes vivantes marquées avec des protéines fluorescentes réversiblement photo-commutables génétiquement encodées. Ce système optique a été conçu pour obtenir une image de bonne qualité des canaux d'émission rouge et vert sur une surface d'environ 4×4 mm2. Il a permis aux biologistes de mesurer le niveau d'expression des sondes fluorescentes dans les plantes vivantes, sans interférence de l'autofluorescence et de la lumière ambiante, même en plein soleil. Ce macroscope de fluorescence a également trouvé d'autres applications en macro-imagerie de fluorescence, par exemple l'analyse de Western blots et la sélection bactérienne sur des supports fortement autofluorescents. Un endoscope à faisceau de fibres optiques intégrant Speed OPIOM a également été construit. Ce second dispositif optique a également amélioré le contraste de l'image sur un fond autofluorescent. De plus, il a été utilisé pour mettre en évidence un phénomène de sectionnement optique à l'aide d'une série de simulations numériques et de mesures expérimentales.

Mots-clés : macro imagerie, plante sentinelle, autofluorescence, lumière ambiante, endoscopie, sectionnement optique.

Abstract

Based on an analysis of the fluorescent emission on a leaf model, a first optical setup has been built for macro-scale fluorescence imaging, which implements the Speed OPIOM (Out of Phase Imaging after Optical Modulation) protocol to observe the fluorescence of living plants labeled with genetically-encoded reversibly photoswitchable fluorescent proteins. The optical system was designed to image both the red and green emission channels with good quality over an area of about 4×4 mm2. This setup allowed biologists to measure the level of expression of fluorescent probes in living plants, without interference from autofluorescence and ambient light, even under sunlight. This fluorescence macroscope also found other applications in fluorescence macro-imaging, e.g. western blot analysis & bacterial selection, against the autofluorescence of the substrate. A fiber bundle-based endoscope incorporating Speed OPIOM has also been built. This second optical setup improved as well the contrast of the image against an autofluorescent background. In addition, it has been used to evidence optical sectioning by a series of numerical simulations and experimental measurements.

Keywords : macro imaging, sensor plant, autofluorescence, ambient light, endoscopy, optical sectioning.